Galactic Windmills

Spectroscopical and Timing studies of three X-ray binaries.

Galaktische Windmühlen: Energie- und zeitaufgelöste Untersuchungen von drei Röntgendoppelsternen.

Der Naturwissenschaftlichen Fakultät
der Friedrich-Alexander-Universität
Erlangen-Nürnberg

zur

Erlangung des Doktorgrades Dr. rer. nat.

vorgelegt von

Felix Fürst
aus Stuttgart

Als Dissertation genehmigt
von der Naturwissenschaftlichen Fakultät
der Friedrich-Alexander Universität Erlangen-Nürnberg

Tag der mündlichen Prüfung: 19. Dezember 2011

Vorsitzender der Promotionskommission:	Prof. Dr. Rainer Fink
Erstberichterstatter:	Prof. Dr. Jörn Wilms
Zweitberichterstatter:	Dr. Norbert S. Schulz

The small image on the title page shows the sun dial of the Dr. Karl-Remeis-Observatory in Bamberg, Germany.

Zusammenfassung

DAS Thema dieser Arbeit sind Neutronensterne in Binärsystemen, sogenannte Röntgendoppelsterne. Neutronensterne sind die Überreste massiver Sterne und besitzen eine extreme Dichte und extreme Magnetfelder. Sie haben typischerweise Massen von etwa 1.4 Sonnenmassen und dabei einen Radius von nur etwa 10 km, während ihre Magnetfelder eine Stärke im Bereich von 10^{12} G und mehr erreichen können. In einem Röntgendoppelstern umkreisen sich ein Neutronenstern und ein optischer Begleiter, ein Stern, welcher seine Energie durch nukleare Fusion erzeugt. Durch seine immense Gravitationskraft akkretiert der Neutronenstern Materie von diesem Begleiter. Die potentielle Energie der akkretierten Materie wird in Strahlung, hauptsächlich im Bereich der Röntgenstrahlung, umgewandelt. Die hohe Röntgenleuchtkraft ist auch der Grund für den Namen Röntgendoppelstern. Die Röntgenstrahlung wechselwirkt mit dem umgebenden Medium, welches größtenteils aus dem Wind des Begleiters stammt. In diesem Medium werden die Röntgenstrahlen absorbiert und erzeugen Fluoreszenzlinien. Daher kann man mit ihrer Hilfe sowohl Informationen über den Neutronenstern als auch über das absorbierende Medium erhalten.

In dieser Arbeit werden Röntgendaten von den satellitengestützten Observatorien *XMM-Newton*, *Suzaku*, *INTEGRAL*, *RXTE* und *Swift* benutzt, um drei Röntgendoppelsterne zu untersuchen: 3A 1954+319, 4U 1909+07 und GX 301−2. Durch die Messung der zeitlichen Veränderung und der Energieverteilung ihrer Strahlung können Erkenntnisse über die physikalischen Zustände nahe am Neutronenstern gewonnen werden. Dort sind Gravitationskräfte und elektromagnetische Kräfte am Werk, deren Stärke um viele Grössenordnungen über die hinausgeht, die in Laboren erzeugbar ist. Untersuchungen von Neutronensternen erlauben es daher, physikalische Theorien unter extremen Bedingungen zu testen.

Die Analyse von regelmäßigen Beobachtungen von 3A 1954+319 zwischen 2006 und 2010 ergibt, dass die Periode des Neutronensterns, sichtbar als regelmäßiger Puls in der Röntgenlichtkurve, sich in Zeiten geringen Flusses kontinuierlich vergrößert. Dagegen verringerte sie sich sehr schnell während eines Ausbruchs im November 2008. Diese Veränderungen der Periode an sich sowie ihre Stärke können durch einen besonderen Akkretionsprozess, der quasi-sphärischen Akkretion, erklärt werden. Das Breitbandspektrum von 3A 1954+319 kann sehr gut mit einem Comptonisierungs-Modell beschrieben werden, welches auch die Spektren vieler anderer Neutronensterne in Röntgendoppelsternen beschreibt.

Die Pulsperiodenentwicklung von 4U 1909+07 verläuft anders als die von 3A 1954+319. Statt eines kontinuierlichen, flussabhängigen Verlaufs verändert sich die Periode von 4U 1909+07 zufällig und folgt einem "Random Walk", wie man in regelmäßigen Beobachtungen zwischen 2003 und 2011 sieht. Dieses Verhalten weist klar auf eine direkte Akkretion des Sternwindes des Begleiters hin. Das Spektrum von 4U 1909+07 kann ebenfalls mit bekannten phänomenologischen Röntgenpulsarmodellen beschrieben werden. Durch pulsphasenaufgelöste Spektroskopie kann eine starke Veränderung der spektralen Parameter, besonders in der Schwarzkörperkomponente, sichtbar gemacht werden. Diese Veränderungen können durch Geometrien der Akkretionssäule erklärt werden, bei denen ihr heißer Boden nur zu bestimmten Phasen sichtbar ist.

Zur Untersuchung von GX 301−2 werden sehr hochaufgelöste Daten von Beobachtungen aus den Jahren 2008 und 2009 verwendet. In diesen Daten wurden starke Fluoreszenzlinien von Eisen und Nickel gefunden, so wie zum ersten Mal in Röntgendoppelsternen auch eine Fluoreszenzlinie von Chrom. Der Fluss und die Spektren von GX 301−2 sind hochvariabel. Durch Spektroskopie von einzelnen Pulsen wurden starke Änderungen der Absorptionssäule sowie des Flusses der Fluoreszenzlinien auf Zeitskalen von wenigen 100 Sekunden gefunden. Die Lichtkurve weist einen Zeitraum mit stark verringertem Fluss auf, in der keinerlei Pulsationen zu sehen sind. Dieser Abfall ist vermutlich darauf zurückzuführen, dass der Neutronenstern eine sehr dünne Stelle im Wind passierte und dass dabei die Akkretion zusammenbrach.

Zusammenfassend lässt sich sagen, dass obwohl alle drei untersuchten Systeme windakkretierende Neutronensterne sind, sie doch alle ihre Besonderheiten haben. Ein Vergleich der Systeme zeigt das breite Spektrum an Helligkeiten und Verhalten auf, welche stark durch den optischen Begleiter und die orbitalen Parameter beeinflusst werden.

Abstract

THE topic of this thesis are neutron stars in binary systems, so-called X-ray binaries. Neutron stars are remnants of massive stars and have extreme densities and magnetic fields. They have typical masses around 1.4 times the solar mass and radii of only 10 km and their magnetic fields can reach values of 10^{12} G and more. In an X-ray binary the neutron star is in orbit with an optical companion, a star powered by nuclear fusion. From this companion the neutron star accretes matter due to its very strong gravitational pull. The potential energy of the accreted matter is transferred into radiation, mainly in the X-ray regime, hence the name X-ray binary. The X-rays interact with the surrounding medium, which originates mainly from the stellar wind of the companion. In this medium the X-ray radiation gets absorbed and gives rise to fluorescence lines. X-rays can therefore be used to obtain not only information about the neutron star itself, but also about the surrounding medium. In the vicinity of neutron stars gravitational and electro-magnetic powers are at work, which can not be reproduced in a laboratory. Investigations of neutron stars allow therefore to test physical theories under extreme conditions.

In this work X-ray data from the satellite-based observatories *XMM-Newton*, *Suzaku*, *INTEGRAL*, *RXTE*, and *Swift* are used to analyze three X-ray binaries: 3A 1954+319, 4U 1909+07, and GX 301−2. By measuring the temporal variance and energy dependence of the X-ray flux, knowledge about the physical conditions close to the neutron star is gained.

The analysis of monitoring data of 3A 1954+319 between 2006 and 2010 shows that the period of the neutron star, visible as regular pulses in the X-ray lightcurve, increases continuously during phases of low flux. Contrary to that, an analysis of a bright flare in 2008 shows a rapid decrease in the pulse period. These changes and their magnitudes are explainable using a specific accretion process, the quasi-spherical accretion. The broadband X-ray spectrum of 3A 1954+319 can be very well described by a thermal Comptonization model, commonly used to describe the spectra of neutron stars in X-ray binaries.

4U 1909+07 shows a different pulse period evolution than 3A 1954+319. Instead of a continuous, flux-dependent variation, 4U 1909+07 shows a random walk like behavior, as visible in the analysis of monitoring data taken between 2003 and 2011. This behavior is a clear indicator that the source accretes matter directly from the stellar wind of its companion. The spectrum of 4U 1909+07 can also be described by standard phenomenological X-ray pulsar models. In pulse phase resolved spectroscopy a strong change of the spectral parameters is evident, especially in the blackbody component. This behavior is used to constrain the geometries of the accretion column, so that its hot bottom is only visible at specific phases.

For the investigation of GX 301−2 very highly resolved data, taken in 2008 and 2009, is used. In these data, strong fluorescence lines from iron and nickel are found, as well as for the first time in an X-ray binary a fluorescence line from chromium. The flux and the spectra of GX 301−2 are highly variable. By performing pulse-to-pulse spectroscopy

large changes in the absorption column and the flux of the fluorescent lines on timescales of a few 100 seconds are found. The lightcurve includes an epoch of drastically reduced flux, during which no pulsations are measured. This dip is likely due to the neutron star passing through a thin area of the wind, which led to a cessation of accretion.

In conclusion it becomes clear that despite all three systems being wind-accreting neutron stars, they all have their own peculiarities. In comparing the systems the broad range of luminosities and behavior becomes evident, which are strongly influenced by the optical companion and the orbital parameters.

Contents

Obey Gravity. It's the law!

(The Gravity Police)

1

Introduction

ALBERT Einstein once said: "The laws of gravity cannot be held responsible for people falling in love." This statement is of course true, but only in a very direct way. Without gravity, any two people will have a rather hard time falling in love with each other, as all our lives depend on the laws of gravity. A romantic dinner for example is only romantic as long as the candles stay on the table and the table on the floor, which only happens because table and candles are pulled gravitationally down to the ground. Without gravity they would be floating around, like seen on the *International Space Station (ISS)* where the gravitational force is canceled out by the centrifugal force resulting from the fast movement of the station around Earth. Not only would all furniture be floating around, but also the atmosphere we need to breathe would not stay close to the surface of our planet and instead dissipate freely into empty space. Furthermore, watching the sun set over the ocean would be impossible, not only because there would be no ocean but also because the earth would not be in orbit with the sun but drifting lonely through the vastness of space. Even more, the sun itself would be non-existent. It is only the large gravitational force of the atoms it consists of that makes it dense and hot enough to produce enough heat and radiation that we on Earth can live a happy life. All stars and celestial bodies owe their existence to the laws of gravity, even our own galaxy, Milky Way, and all other galaxies and clusters of galaxies exist only because of gravity. So that "The laws of gravity cannot be held responsible for people falling in love" might be true at first glance, but without gravity nobody would fall in love.

Even though everything in the universe depends upon gravity, the gravitational force is very weak compared to the other basic forces of nature, namely the strong, the weak, and the electromagnetic force. The strong and weak force act only on the scales of atomic nuclei and atoms, but gravity and the electromagnetic force have an infinite action range. However, the electromagnetic is a factor of 10^{25} stronger than gravitation. So why is gravity even measurable and more, so important for the stability of the universe? One part of the answer lies in the fact that the electromagnetic force only acts on electric charges and neutral bodies are not affected by it. Furthermore the electric charge knows two opposite signs, plus and minus. Only charges of opposite signs are attracted to each other, while particles with the same sign are repelled. These effects mean that the electromagnetic force can work in two directions, and that as soon as equal amounts of positive and negative charges are put together, they become neutral and no force is present anymore. Gravity on the other side is a much more global force, as it acts on all matter with mass, including all baryonic and dark matter. Furthermore no signs exits for gravity and it is always attractive. Consequently gravity is acting always and everywhere and there can be no neutralization of “gravitational charges”.

In Einstein’s theory of relativity (Einstein, 1916) gravitation and mass become even more fundamental, as masses are assumed to influence space and time. Space is warped close to bodies of mass, which means that even massless particles, like photons, feel the influence of large masses nearby and change their path and energy compared to an Euclidean geometry. This effect leads to the existence of gravitational lenses, where light from a source behind a large mass is bent around this mass and the observer sees a distorted image of the source (see Walsh et al., 1979, and references therein).

The electromagnetic force is nonetheless very important for many processes in the world and the universe. The most direct evidence of the importance of it is light, describable as photons, the carriers of the electromagnetic force. Light is what enables us to perceive the world in the way we do, and at energies not visible to humans, such as radio waves or X-rays, modern detectors allow us to enhance our view of the world surrounding us. The electromagnetic force is also an important motor in any living organism and drives molecules and cells. Computers and modern society depend strongly on electricity, the macroscopic emanation of the electromagnetic force. Stars and planets have magnetic fields, influencing their physical appearance and interaction with the world.

It is these two forces, gravity and the electromagnetic force, which keep everything running and in place and are uniquely important throughout the universe, form the smallest to the largest scales. Even on Earth their strength stretches over many magnitudes, from barely measurable, like the mass of an atom or the charge of an electron[1], to extremely powerful like the mass of Earth itself or the charge of a lightning[2]. Understanding these forces and their influence on the world in every detail is one of the major questions of physics. Many experiments are carried out to answer this question. However, even the most powerful gravitational and electromagnetic forces found on Earth are weak compared to what is present in distant stars and galaxies. These objects cannot be brought into the laboratory to be investigated in a controlled environment, but we can still learn a lot about them thanks to the means of modern astronomy. Astronomical observations allow us to apply and extend the theories of the forces found on Earth to powers many orders of magnitude stronger than producible here.

One particularly interesting example, because of their extreme gravitation and magnetic fields in a very concentrated space, are neutron stars. Neutron stars are the remaining cores of dead stars and show magnetic fields of up to 10^{15} G (Rea & Esposito, 2011) and

---

[1] an hydrogen atom, for example, has a mass of only $\sim 1.6 \times 10^{-24}$ g and is only measurable by means of mass spectroscopy (Coursey et al., 2010), and the charge of an electron is only $e = -1.602 \times 10^{-19}$ C (Demtröder, 2008).

[2] Currents in lightnings can reach up to 200 A, setting free up to 20 GW of electric power (Ebert, 2010). Earth’s mass is 5.9736×10^{27} g (Williams, 2011).

densities of $\sim 10^{15}\,\mathrm{g\,cm^{-2}}$ with a typical mass of $1.4\,\mathrm{M}_\odot$ (Bombaci, 1996). This mass and density results in a gravitational force at their surface which is typically 10^{11} times stronger than that on Earth (Haensel et al., 2007). It also means that neutron stars very suitable objects to study the laws of nature in regimes not accessible on Earth. To observe them, we measure the electromagnetic radiation they emit, mostly radio waves and X-rays. This light carries a wealth of information about their physics and by comparing the measurement to theory we can learn about what forces are at work in these systems. By using more and more sensitive detectors, more and more details about them are revealed. In the future, even gravitational waves might be detectable, opening a whole new window to the investigation of neutron stars.

In this thesis neutron stars in binary systems are investigated, which show up as strongly variable and violent X-ray sources. In these systems the neutron star is in close orbit with another star, which has not yet reached the end of its life. Due to the large gravitational pull matter from the companion star is transferred to the neutron star and thereby converted into energy, following Einstein's theory of special relativity (Einstein, 1905). These systems consequently allow us to see the influence of the strong gravitation on mass directly, for example they allow to investigate how the presence of the neutron star changes the physics of the companion star. As the matter surrounding the two stars is ionized, i.e., charged, it also interacts with the strong magnetic field of the neutron star and thereby provides insight how this interaction works. Neutron stars in binaries are therefore the ideal objects to study how gravity and the electromagnetic interaction work when pushed to extreme powers. This thesis deals with three of these objects, namely 3A 1954+319, 4U 1909+07, and GX 301−2, all very similar but still showing distinct properties.

Before presenting the analyses, Chapter 2 deals in more detail with the physics of neutron stars, how they are born, and what makes X-ray binaries so special. The Chapter concludes with an outlook on the main results of the analyses. In Chapter 3 the satellites and instruments used for the investigations are introduced. A very brief discussion of the data analysis methods applied is also given. Starting with Chapter 4 the scientific analysis begins. In this Chapter 3A 1954+319 is presented, the system with the smallest companion star. Chapter 5 deals with 4U 1909+07, a relatively unknown X-ray binary. Last but not least, Chapter 6 presents a detailed analysis of GX 301−2, a very famous source with a very massive companion star. All three of the scientific Chapters are based on publications accepted in or submitted to peer-reviewed journals. Concluding this thesis is Chapter 7, in which the results are summarized, their implications discussed, and an outlook to future investigations given.

As common in astrophysics throughout this work the *cgs* system of units will be used.

Binary pulsars. The gravitational forces between them are so intense that everything within 50 million kilometers is getting pulled in.[1]

(Capt. K. Janeway on Star Trek Voyager – "Scientific Experiments")

2 Neutron Stars in X-ray Binaries

NEUTRON stars are the remaining cores of massive stars which have exploded violently at the end of their life. They exhibit extreme physical conditions not found anywhere else in the universe. The most obvious one is their high density, which is on the order of $10^{14}\,\mathrm{g\,cm^{-3}}$. This compactness results in a very steep gravitational well in which potential energy can be very effectively transferred into radiation. Another most special feature are their strong magnetic fields, which can be on the order of 10^{12}–10^{15} G (Haensel et al., 2007). The geometry of these fields can be approximated by a dipole, resulting in two very powerful magnetic poles on the neutron star's surface which influence strongly the surrounding material. The effects of these extreme gravitational and magnetic forces are what makes the investigation of neutron stars so fascinating.

More than 1800 neutron stars are known, most of them are located in our galaxy (Manchester et al., 2005). Isolated, magnetized, and quickly rotating neutron stars can be observed as radio pulsars.[2] Through their co-rotating magnetic field, electromagnetic radiation is generated which produces a torque on the neutron star and thus slows it down. Depending on the strength of the spin-down compared to the rotational period, the neutron star's characteristic age τ_c and magnetic field B can be estimated via

$$\tau_c = \frac{P}{\dot{P}} \quad \text{and} \quad B = 3.2 \times 10^{19} \sqrt{P\dot{P}}\,\mathrm{G} \quad , \tag{2.1}$$

respectively, assuming a dipole magnetic field (Gaensler & Slane, 2006).

The main radiation is emitted at radio wavelengths, but through the interaction with the surrounding plasma, radio pulsars are also able to produce radiation in the X-ray

---

[1] Note: Assuming that the binary pulsars encountered by *Voyager* have each a canonical mass of $1.4\,\mathrm{M}_\odot$, the gravitational force on the ship (having a mass of 7×10^{11} g, Star Trek Voyager – "Phage") at a distance of $r = 5 \times 10^{12}$ cm will be $F_\mathrm{grav} \approx 10^{13}$ dyn. The warp core of *Voyager* is capable of delivering $\sim 4 \times 10^{15}$ dyn (Star Trek Voyager – "One") so that she can easily escape on a direct path, contradictory to Capt. Janeway's statement. If moving on an orbit around the system she could escape with even less effort, using the centrifugal force of its movement.

[2] often referred to only as "pulsars" but I would like to stress the difference to X-ray pulsars, which are the topic of this work.

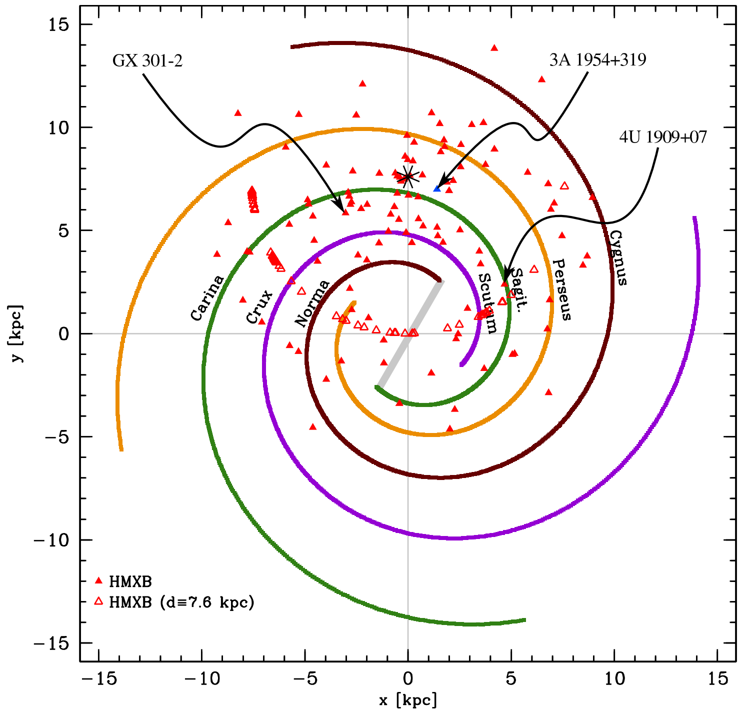

Figure 2.1.: Distribution of HMXBs in the galactic plane. Sources with unknown distances (69) are shown as open triangles and placed at 7.6 kpc from the sun, which is indicated by the star in the upper half of the figure. Sources with known distances (108) are shown as filled triangles. The spiral arms are based on the model by Vallée (2008). The sources discussed in this thesis are labeled. 3A 1954+319 is a LMXB instead of a HMXB, but anyway indicated in the plot. Plot courtesy of A. Bodaghee (2011).

regime and can even accelerate photons up to several *tera electronvolts (TeV)*. Besides these standard radio pulsars, other types of isolated neutron stars exist, such as *Soft Gamma-Ray Repeaters (SGRs)* and *Anomalous X-ray Pulsars (AXPs)*. These objects are thought to be *magnetars*, neutron stars with magnetic field strengths $B > 10^{14}\,\mathrm{G}$ and are not yet fully understood theoretically (see, e.g., Mereghetti et al., 2002; Götz et al., 2007).

Other neutron stars are found to be in orbit with a normal companion star, forming a binary system. The term “normal stars” will be used throughout this thesis for stars drawing their energy from nuclear burning. These stars are usually bright at optical wavelengths, so that they are often also referred to as “optical companion” if in orbit with a neutron star. In these binary systems the neutron star is emitting large amounts of energy because it accretes matter from its companion and transforms it into X-rays. Three examples of those X-ray binaries are discussed in this thesis. The accreted matter forms accretion columns above the neutron star surface, following the magnetic field lines. The X-ray radiation is mainly produced and up-scattered to high energies in these accretion columns (see Section 2.3).

X-ray binaries can be separated into two groups, according to the mass of their optical companions: *Low Mass X-ray Binaries (LMXBs)* and *High Mass X-ray Binaries (HMXBs)*. Around 190 LMXBs and 130 HMXBs are known, respectively (Liu et al., 2000, 2007). Bodaghee et al. (2011, priv. comm.) give an updated number of 177 HMXBs, the drastic increase mainly due to the detection of many strongly absorbed sources with *INTErnational Gamma-Ray Laboratory (INTEGRAL)* (see also Section 3.5). HMXBs are found everywhere in the galaxy, as shown in Figure 2.1. Their distribution seems not to be related with the spiral arms, but Bodaghee et al. (2011) could find a correlation with the distribution of OB-associations, clusters of active and young stars.

As the masses of their respective companions are different between LMXBs and HMXBs, mass accretion over different channels is taking place. In LMXBs *Roche lobe* overflow is the main accretion channel, while HMXBs mostly accrete from the stellar wind or from the circumstellar dis kof their companion. All systems in this thesis are wind accretors, of which the most relevant processes, i.e., stellar winds and accretion mechanisms, are described in Section 2.1.2 and in Section 2.3, respectively.

Normal stars play a crucial role in the physics of neutron stars and especially binaries. For example, the angular momentum and magnetic field strength of neutron stars is a direct consequence of their normal star progenitor. In binaries, it is only the presence of the optical companion and its material which allows us to observe the neutron star. Therefore, a basic understanding of normal stars and their mass loss rates is important for the investigation of X-ray binaries. In Section 2.1 I try to give a concise overview of their most relevant properties. Neutron stars are discussed afterwards in Section 2.2, where I describe briefly how they come into existence and what their internal structure and composition is.

Section 2.3 discusses the interaction between the optical companion and the neutron star, i.e., how the accretion process works and how X-rays are produced. Following that, Section 2.4 will discuss how the X-rays interact with the circumstellar material and how they are altered before they reach us. Finally Section 2.5 gives a short outlook on the sources investigated in the following Chapters and their peculiarities.

2.1 The Optical Companions

NORMAL stars have been the topic of investigation for many generations of astrophysicists and many good text books, introductory and otherwise, exist (e.g., Karttunen et al., 2007; Clayton, 1984; Kippenhahn & Weigert, 1994). How stars produce energy by burning hydrogen to helium and the further production of heavier elements is described in these books in detail, and I will not discuss it here. Instead, in Sect. 2.1.1 I will give a short review of stellar classification and the main observable distinctions between early and late type stars. These differences are important in order to understand the individual properties of HMXBs and LMXBs. Section 2.1.2 will give a more detailed overview about the mass loss rates of stars, a topic less extensively discussed in literature. The difference between stellar winds from early and late type stars and their structure will be the main subject of this Section.

2.1.1 Stellar classification

When admiring the night sky, it is already clear to the unaided eye that stars have different colors. There are very red stars like Beteigeuze in Orion (α Ori) and much bluer stars like Regulus in Leo (α Leo). These colors correspond to different surface temperatures of the stars, with the bluer stars being much hotter than the red ones. The connection between color and temperature comes from the fact that stellar spectra can be approximated by blackbody radiation. In a blackbody, the temperature defines the wavelength of the peak of the emission (i.e., the color), according to *Wien's Displacement Law*

$$\lambda_{\mathrm{max}} = \frac{b}{T} \quad , \tag{2.2}$$

where $b \approx 2.898\,\mathrm{mm\,K}$ denotes Wien's displacement constant. This law follows directly from *Planck's Law of blackbody radiation*, which describes the energy output of a blackbody with a given temperature, taking quantum effects into account (Planck, 1900). With increasing temperature the peak wavelength is shifted to shorter (i.e., bluer) wavelengths, while the overall energy output is increased. Thus blue stars are much more luminous than red ones of the same size. Due to different temperatures and surface gravities, different physical environments exist in the photosphere of stars. These differences give rise to characteristic temperature dependent features in the stellar spectra, like atomic absorption and emission lines, which are the main cause for the deviation of the stellar spectra from a perfect blackbody. Temperatures of stars are therefore only effective temperatures, i.e., they describe a blackbody of the same energy output as the observed star (Karttunen et al., 2007).

The spectral features are used in the *Harvard Spectral Classification* to sort the spectra into different categories according to their effective temperature, labeled with letters. Ordering them from high to low temperature the sequence reads as follows:

O – B – A – F – G – K – M – L – T – (Y)

The types L and T where added later, after the discovery of very cold brown dwarfs in the 1980s and 1990s (see Kirkpatrick, 2005, for a review). The spectral class Y was proposed by Kirkpatrick et al. (1999), if objects beyond T type stars should be discovered. Starting with spectral type O with temperatures between 15000–35000 K and shining bright blue, the sequence goes over yellow G stars, similar to the sun, with temperatures of ~5500 K to the colder and reddish M type stars with temperatures around 3000 K (Karttunen et al., 2007). The coldest stars of spectral class T have temperatures around 750 K (Kirkpatrick, 2005). The *Harvard Classification* was later enhanced to the *Yerkes Spectral Classification* (Morgan et al., 1943; Keenan, 1985), which introduced subtypes of the original spectral classes, donated by an Arabic numeral behind the spectral class letter. For example, Mirfak (α Per) is an F5 star. Additionally, the Yerkes Spectral Classification added luminosity classes, donated by roman numerals. Six luminosity classes are defined

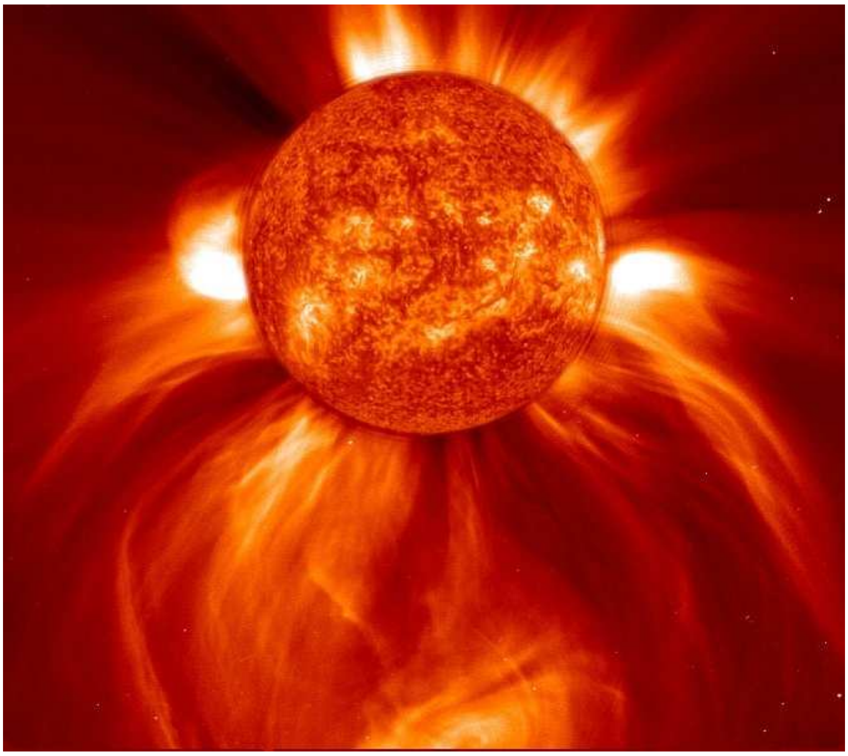

Figure 2.2.: An optical coronograph image from *SOHO* showing very large mass ejections from the sun. The center of the sun is imaged at a wavelength of 304 Å using the Extreme ultraviolet Imaging Telescope (EIT). Picture credit: NASA

from Ia being the most luminous supergiants to V describing main sequence or dwarf stars. For Mirfak the complete classification then reads F5 Ib.

O and B stars are often referred to as "early type" stars, while the colder K and M stars are known as "late type" stars. This historic description comes from the wrong assumption of the late 19th century that stars would start their life as large blue objects which contract and thereby convert gravitational energy into radiation. Stars were thus thought to get smaller and colder as they age. Nowadays it is clear that the spectral type of a star is independent of its age. Instead, its evolution and spectral type depend primarily on its initial mass (see Chiosi et al., 1992, for a review of stellar evolution models). O- and B-stars are the most massive stars, with masses $> 10\mathrm{M}_\odot$, while M stars can have masses as low as $0.1\,\mathrm{M}_\odot$ (Karttunen et al., 2007).

2.1.2 Mass loss and winds

STARS on the main sequence draw their energy from burning hydrogen to helium which provides enough energy for millions and billions of years. But even during this relatively quiet period, the outer layers of stars are very active, as observed in the sun and its flares and prominences (Figure 2.2). In hot O- and B-stars, as present in HMXBs, the outer layers of the atmosphere are pushed away by radiation pressure, resulting in a strong stellar wind. Stars of later spectral types also show strong stellar winds, probably caused by gas pressure or Alfvén waves. The two main characteristics of stellar winds are the mass-loss rate, $\dot{M}$, describing how much mass the star loses with time and the terminal velocity, v_∞, the velocity of the wind at a point far away from the star, where no forces act on it anymore. A very good review about stellar winds is given in the textbook by Lamers & Cassinelli (1999). The next paragraphs are based on this book but give only a very short summary of the most important physics of stellar winds.

Elements such as C, N, and O, as well as the Fe group have numerous resonance lines with large optical depths at UV energies. Photons at energies of these lines originating from the strong UV continuum of O- and B-stars interact with these ions. Through this absorption process momentum is transferred from the photons onto the ions. As the UV radiation is directed away from the star's surface, the momentum transfer will also be in this direction, driving the ions away from the star and producing the stellar wind. Through Coulomb coupling with the other particles in the wind, a steady outflow of matter is achieved. The wind is optically thick for photons at the resonance lines energies, such that these photons are quickly absorbed away in the lower layers of the wind. As the wind is moving, the *Doppler effect* (Doppler, 1842) shifts the wavelengths seen by the ions and with increasing wind speed photons of shorter wavelengths can be absorbed. To calculate the forces acting on the stellar wind at a given velocity, interaction probabilities for a plethora of possible resonance lines must be calculated. Some approximations can simplify these calculations. One assumption, for example, is the so-called *Sobolev approximation* (Sobolev, 1960). Here, it is assumed that the interaction for a specific line happens only at a specific point in the wind, i.e., the absorption line width is very small and the absorption coefficient can be reduced to a δ-function. Furthermore, as densities in the wind are low ($\rho \lesssim 10^{-12}\,\mathrm{g\,cm^{-3}}$, Lamers & Cassinelli, 1999) and collisional excitation is negligible, it is usually enough to regard only the contributions from the ground state lines. The model mostly used to describe radiation driven winds incorporating the above approximations, is the so-called "Castor-Abott-Klein"-model or for short "CAK"-model (Castor et al., 1975). In agreement with measurements, this model predicts terminal velocities of the wind $v_\infty \approx 1500\,\mathrm{km\,s^{-1}}$ and mass-loss rates $\dot{M} \approx 10^{-6}\,\mathrm{M_\odot\,yr^{-1}}$. The velocity profile in the wind follows the so-called β-law

$$v(r) \simeq v_0 + (v_\infty - v_0)\left(1 - \frac{R_\star}{r}\right)^\beta \quad , \tag{2.3}$$

where for line-driven winds $\beta \approx 0.7$.

In the early 1970s, while the theory of line-driven winds was still developed, Lucy & Solomon (1970) already remarked that line-driven winds are intrinsically unstable. Molecules with velocities a bit above the local wind speed see the UV continuum of the star a bit more Doppler shifted and can interact with a less absorbed part of it. Thereby they gain more momentum and their velocity increases further above the local wind speed, such that they again see a less absorbed part of the UV continuum due to the increased Doppler effect. A random velocity variation is consequently self-enhancing and leads to the formation of clumps and shocks in the stellar wind (for detailed calculations see Lamers & Cassinelli, 1999). Despite these early predictions, theorists and observers

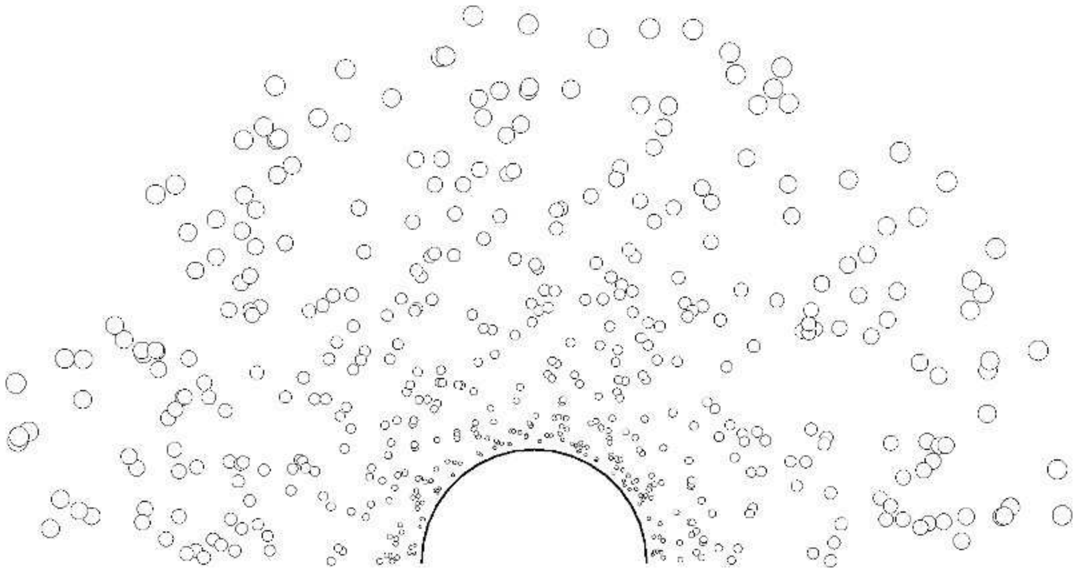

Figure 2.3.: Sketch of a very simplified clumpy wind. Clump size increases with the distance to the star. Picture taken from Oskinova et al. (2008).

are nowadays still struggling to obtain a clear picture of the amount of wind clumping and of the typical size scales of these structures. For a recent review and discussions on this topic see Puls et al. (2008) and the proceedings of the "International Workshop on clumping in Hot-Star Winds" (Hamann et al., 2008).

Simulations of the instabilities in stellar winds have been performed with 2D and 3D *Magnetohydrodynamics (MHD)* codes (Dessart, 2004; Dessart & Owocki, 2005, among others). They show that such structures appear on all length scales and travel through the stellar wind. The amount of clumping in the wind directly influences the mass loss rate and thereby stellar evolution (Puls et al., 2008). Simulations, however, do not yet allow for a unique description of the amount of clumpiness or the density of the clumps. Observational evidence for dense clumps is given by Oskinova et al. (2008) who analyzed the X-ray spectrum of isolated O-type stars.

In binary systems, especially HMXBs and *Supergiant Fast X-ray Transients (SFXTs)*, the extremely variable X-ray flux is a strong indicator for accretion from a highly structured medium (Walter & Zurita-Heras, 2007; Fürst et al., 2010). This structure is probably originating from the clumps and structure of the stellar wind. Additionally the neutron star, ploughing through this wind, will by itself disrupt it strongly. Simulations by Blondin et al. (1990, 1991) and Mauche et al. (2008) show that even a smooth wind gets disturbed quickly, especially when passing through the strong bow shock or the accretion wake of the neutron star. These disruptions are able to produce clumps and density variations compatible to the estimated momentary mass accretion rate of the neutron star (Fürst et al., 2010). In other words, neutron stars grind down the wind of the companion star into smaller clumps. They are comparable to a galactic windmill, rotating and milling.

SFXTs are binary systems which consist of an early-type mass donor and a neutron star, just like HMXBs. In contrast to these systems they have, however, a very low quiescence luminosity contrasted by large outbursts, which increase the quiescence luminosity by a factor of 1000 or more (Negueruela et al., 2008). One model to explain this behavior assumes a strongly clumped wind from the mass donor and a very wide orbit of the neutron star, such that a bright outburst happens only when a dense clump is accreted serendipitously (Sidoli, 2008). There are, however, SFXT systems known, which have relatively short orbital periods ($< 10\,\mathrm{d}$), i.e., are close to their companion (Corbet et al., 2006b). Their behavior is difficult to explain by a simple clumpy wind model.

A thorough understanding of the clumpiness of early type stellar winds is still not achieved. Especially in binaries, the interaction between the stellar wind and the neutron star makes simulations of the environment very complicated. Nonetheless, observers and theorists agree that the winds must be highly structured and that the accreted medium cannot be described by a common physical state. For example, high resolution spectroscopy of the HMXB Cyg X-1 showed that it is likely that cold clumps are embedded in a hot and highly ionized medium (Miškovičová et al., 2011; Hanke, 2011). The sources presented in this thesis are also accreting from a strongly structured medium, as seen by their large brightness variability. In the case of GX 301−2 (Chapter 6) a detailed analysis of the variability of the absorption column and the fluorescence lines is presented, which helps to understand this structure as well as the different physical conditions in the medium.

Early type stars are not the only types of stars showing wind, but the best studied ones. Outflows from cool, late type stars have also been observed and investigated. The UV continuum of these stars is, however, by far too weak to accelerate measurable amounts of matter via resonant line scattering. Therefore other mechanisms must be in place. Measurements of K- and M-type stars show winds with $v_\infty \lesssim 100\,\mathrm{km\,s^{-1}}$ and $\dot{M}$ between 10^{-5} and $10^{-11}\,\mathrm{M_\odot\ yr^{-1}}$. The large range of mass loss rates stems from uncertainties of the measurements and from the fact that different methods lead to different rates (Judge & Stencel, 1991; Espey & Crowley, 2008). The driving mechanism behind these winds has been discussed for a long time. Neither line-driven winds, nor coronal winds, nor dust driven winds seem to satisfy the measured values of $\dot{M}$ and v_∞ (Espey & Crowley, 2008). Belcher (1971) suggested that the stellar wind from the sun might partially be due to Alfvén waves, a mechanism adopted by Hartmann & MacGregor (1980) to explain the winds for cool giants and supergiants. Alfvén waves originate in oscillating magnetic flux tubes, which are strongly coupled to the stellar atmosphere and wind. Alfvén wave theory predicts, however, terminal velocities on the order of $v_\infty \approx 700\,\mathrm{km\,s^{-1}}$, i.e., much faster than observed. Recently, non-linear MHD simulations showed that a large amount of energy from the Alfvén waves can be deposited in the lower layers of the atmosphere. Furthermore, reflection of the waves has a non negligible effect on the wind speeds (Suzuki, 2007, 2011; Airapetian et al., 2010). Depending on the maximal wave period allowed for the broadband spectrum in the MHD simulations, different terminal wind velocities are predicted (see Figure 2.4). For the slowest periods ($P = 16.2\,\mathrm{d}$ and $P = 5.3\,\mathrm{d}$ in the figure) the waves are partially reflected, while for shorter periods they are effectively propagating freely. The partially reflected models reproduce observed ter-

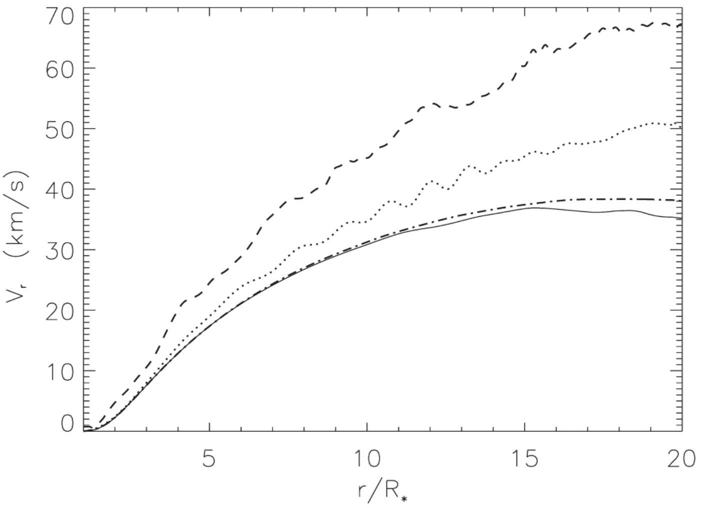

Figure 2.4.: Wind speed predictions of four Alfvén wave models with different maximal wave periods: $P = 16.2\,\mathrm{d}$ (solid), $P = 5.3\,\mathrm{d}$ (dash-dot), $P = 1.8\,\mathrm{d}$ (dot), and $P = 0.9\,\mathrm{d}$ (dash-double dot). Predictions of the first two models agree well with observations in α Tau-like stars. Plot taken from Airapetian et al. (2010).

minal velocities very well (Airapetian et al., 2010).

2.2 What are Neutron Stars?

Compared to normal stars, neutron stars are tiny dots of matter scattered throughout the galaxy. But it is just their tinyness which makes them so special, as they are extremely massive compared to their size. In this Section the birth of a neutron star is very briefly described in Section 2.2.1, introducing its most important quantities. In Section 2.2.2 it is shown that neutron stars are more than just dots of matter, but that they have a very complex inner structure. Even though it is near impossible to obtain measurements of this inner structure, it influences the mass and size of a neutron star drastically. These outer parameters are in turn responsible for the interaction of the neutron star with the surrounding space, which is what determines the observable data.

2.2.1 The Birth of a Neutron Star

Stars live by burning lighter to heavier elements via nuclear fusion. In this process the difference in binding energy between these elements is released and transferred into heat and radiation. The resulting pressure stabilizes the star against its own gravitational force. Elements heavier than iron cannot be fused together exothermically so that even the most massive star dies when iron starts to appear in its core. Details on stellar evolution, which also depends on its mass, are given in many textbooks like Kippenhahn

& Weigert (1994) and Unsöld (2005), as well in an in-depth review by Iben (1991). The death of a heavy star, with a mass $M_\star > 8\,\mathrm{M}_\odot$, can result in a supernova, the most violent release of energy in the universe. The outer layers of the star are propelled away into the surrounding medium, giving rise to beautiful *Supernova Remnants (SNRs)*, such as the Crab Nebula. The core of the star, on the other hand, is compressed gravitationally to very high densities. This collapse of the core gives the "core-collapse supernovae" their descriptive name. In the dense core, electrons and protons interact via *inverse β-decay* and are forming neutrons. If the core's mass is above the *Chandrasekhar mass* limit of $1.4\,\mathrm{M}_\odot$, the gravitational force is so strong that only the *Fermi exclusion principle* of the neutrons can provide a pressure large enough to stabilize the star. If the mass is even larger, above the *Oppenheimer-Volkov* limit, which is between 3–5 $\mathrm{M}_\odot$, the core continues to collapse to a black hole. The exact value of the Oppenheimer-Volkov mass depends on the behavior of matter under extreme densities, which is not yet fully understood (see also the following Section). Detailed studies on the formation of neutron stars can be found in the textbooks by Glendenning (2000) and Haensel et al. (2007). The newly born neutron star will have typical densities $\sim 7 \times 10^{14}\,\mathrm{g\,cm^{-3}}$, which is about 2–3 times the normal nuclear density and makes it therefore the most compact star in the universe. With a mass of $1.4\,\mathrm{M}_\odot$ the neutron star has a radius of only ∼10 km. Being so dense and massive, a neutron star has considerable influence on space and time in the context of general relativity. Any theory aiming to explain the physical properties and the composition of neutron stars has therefore to be in this context and has to take any effects from superfluidity, Fermi statistics, *Quantum-Chromo Dynamics (QCD)*, ultra-dense matter, and many more into account (Haensel et al., 2007).

2.2.2 Structure of a Neutron Star

WE have seen in the previous Section that neutron stars are complicated entities which can only be described with state-of-the-art theories in the regime of general relativity. The state of matter inside of these stars cannot be reproduced in the laboratory, so that all theories describing neutron stars have to rely on an extrapolation of formulæ used to describe the accessible regime of densities and temperatures. The only way to test these theories are detailed observations. Most theories agree on an overall structure as shown in Figure 2.5 and described below (after Haensel et al., 2007, see his book for details):

Atmosphere: a thin plasma layer surrounding the neutron star. Due to the high surface gravity it is only a few millimeters thick but responsible for the thermal emission from isolated neutron stars. It provides information about the surface temperature and the magnetic fields (see also Zavlin & Pavlov, 2002).

Outer Crust: a solid envelope consisting mainly of ^{56}Fe and dominated by the pressure from degenerated electrons. It is some hundred meters thick, extending down to a density of $\rho \approx 4 \times 10^{11}\,\mathrm{g\,cm^{-3}}$, at which the ions become so enriched with neutrons via inverse β-decay that the they start to drip out and form a free neutron liquid.

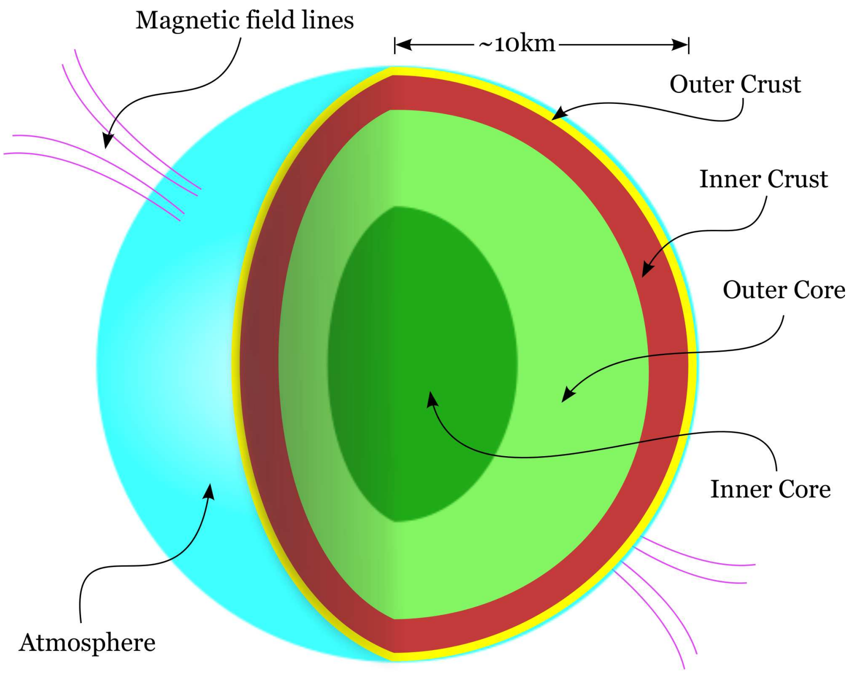

Figure 2.5.: Sketch of the interior of a neutron star after Haensel et al. (2007). See text for a description of the different constituents.

Inner Crust: in here free neutrons are mixed with neutron-rich nuclei and electrons. Densities are so high that they cannot be investigated in the laboratory any more. The inner crust is thought to be ~ 1 km thick and extends down until the density reaches values comparable to the nuclear density $\rho_0 \approx 7 \times 10^{14}\,\mathrm{g\,cm^{-3}}$, at which no nuclei exist anymore.

Outer Core: a mixture of neutrons with protons, electrons, and possibly muons, but no nuclei anymore. Densities are higher than ρ_0 and the stabilizing pressure comes from the strongly degenerate Fermi gas of the particles. The exact physical properties of the core have to be calculated with nuclear many-body theory, but most calculations give similar results.

Inner Core: the innermost part of the neutron star, where densities can reach up to 10–$15\,\rho_0$. Its properties are very model dependent as its physical conditions are far beyond the tested regime of theory. It is very likely that *hyperons* will appear, but more exotic models predict also a complete transition to quark matter composed of deconfined up, down, and strange quarks. Determining the physical properties of the inner core is a very crucial question of neutron star theory. The thickness of the inner and the outer core, which contribute the largest part of the neutron star's mass, are not known.

The relation between density and pressure $\rho(P)$, the so called *equation of state (EoS)*, is the most important relation to determine properties and structure of neutron stars. Today no tested and wildly accepted physical model exists which describes the physics at the densities inside a neutron star. Different assumptions on the behavior of matter under

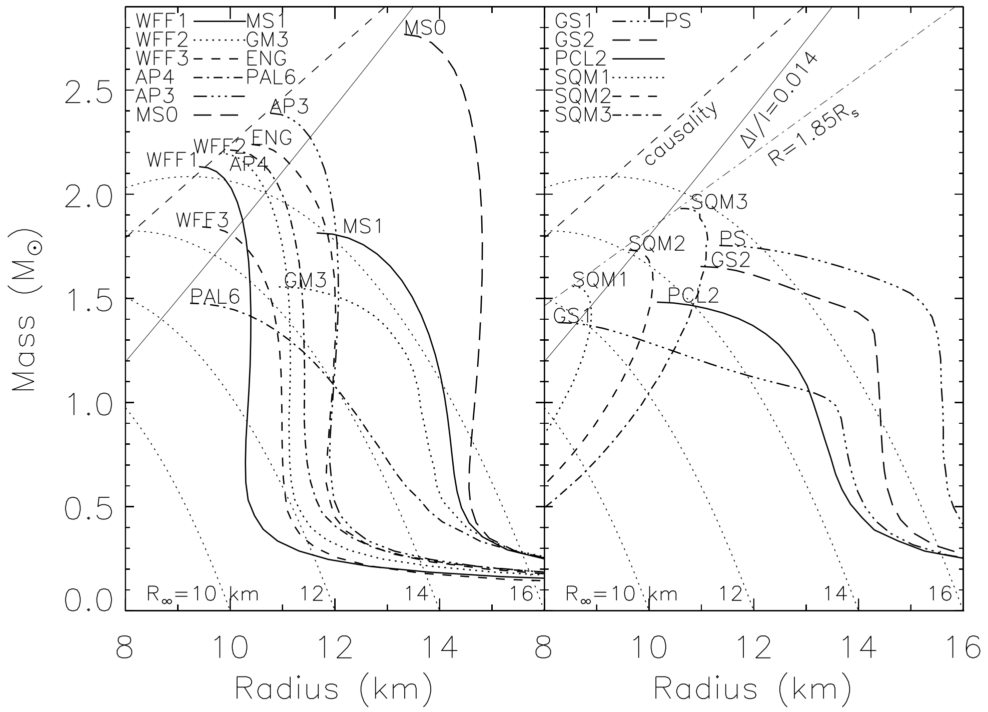

Figure 2.6.: Mass to radius diagram showing the predictions of different EoSs. The different models are labeled according to Lattimer & Prakash (2001), who state in their original caption: "The left panel is for stars containing nucleons and, in some cases, hyperons. The right panel is for stars containing more exotic components, such as mixed phases with kaon condensates or strange quark matter, or pure strange quark matter stars. [...] Contours of constant $R_\infty = R\sqrt{1-2GM/Rc^2}$ are shown as dotted curve." To differentiate between different models exact measurements of mass and radius are necessary. Plot taken from Lattimer & Prakash (2001).

these extreme conditions have been put forward, resulting in different EoSs. The models can be divided roughly in two classes, more classic ones where only hyperons exist in the core, and more exotic ones which assume that quark matter or similar new states of matter are produced (Lattimer & Prakash, 2001). Observations can help to distinguish between different models, but neither density nor pressure can be measured directly. Therefore, any EoS has to be put into the *Oppenheimer-Volkoff* equation of hydrostatic equilibrium to obtain the mass $M(\rho)$ and the radius $R(\rho)$ as a function of density, two parameters which are accessible by observation. By plotting the mass-radius-relation $M(R)$ observations can be compared to theory. The predictions of different EoS models in the mass-radius space are shown in Figure 2.6.

Even though masses and radii of neutron stars are in principle measurable, the precise determination of both quantities is a formidable task for the observer. For example, the mass can be inferred by solving the equations of motion of a binary system, i.e. by finding the exact orbital parameters (see, e.g., Kühnel, 2011). But this approach leads only to

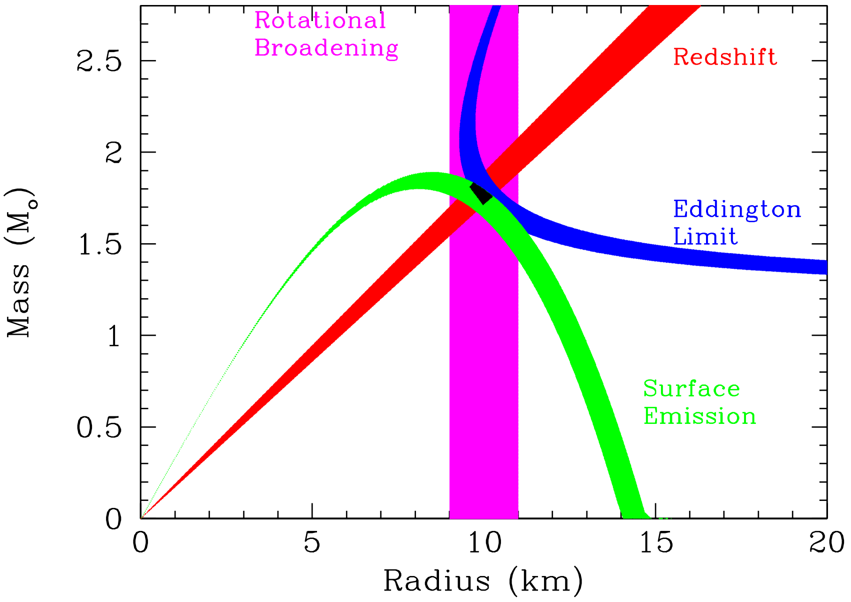

Figure 2.7.: Allowed mass to radius regions as determined by different methods. In green the relation from the surface brightness is shown, in blue the one from the Eddington limit. Red indicates the region of possible values for a given redshift of spectral lines, while magenta shows the allowed region as determined by the broadening of these lines when assuming the common values of $M = 1.4\,\mathrm{M}_\odot$ and $R = 10\,\mathrm{km}$. The width of the regions corresponds to a hypothetical 10% uncertainty but does not include systematic uncertainties as discussed in the text. Plot taken from Özel (2006).

the *mass-function* $f(m_1, m_2)$ by using Kepler's third law:

$$f(m_1, m_2) = \frac{4\pi^2}{G}\frac{(a_1 \sin i)^3}{P^2} = \frac{(m_2 \sin i)^3}{(m_1 + m_2)^2} \quad , \tag{2.4}$$

with m_1 being the mass of the pulsar, m_2 the mass of the companion, and a_1 and P the semi-major axis of the pulsar and the orbital period, respectively (Hilditch, 2001). This formula implies that for an accurate mass measurement of the neutron star the mass of the companion and the inclination must be known. The companion's mass on the other hand can also only be inferred from stellar models and thereby brings in a systematic uncertainty. The radius can be estimated from thermal radiation from the neutron star atmosphere, but thermal luminosity of neutron stars is usually very weak. It might also not be uniformly distributed over the surface, especially in young neutron stars, where the strong magnetic field and the strong gravity induce inhomogeneities. In binary systems radiation produced through accretion is responsible for the major part of the luminosity. This radiation is usually produced above the neutron star surface, so that only upper limits for the neutron star radius can be given (see also Section 2.3). Most ways to measure either radius or mass depend on many different assumptions and rarely both quantities are accessible at the same time. For an overview of different methods to determine mass and radius see Lattimer & Prakash (2001).

Recently some success was made in determining the mass and the radius of a neutron star in X-ray bursters by Özel (2006). She could measure the surface brightness of the blackbody spectrum in large thermonuclear bursts of EXO 0748−676, a LMXB. These bursts occur when the matter accreted onto the neutron star surface gets hot and dense enough to ignite nuclear fusion of heavy elements, which increases the temperature of the surface burning layer dramatically and heats up the photosphere to $\sim 3\,\mathrm{keV}$ (Lewin et al., 1993). The blackbody luminosity increases as well and can reach the *Eddington luminosity*, at which the radiation pressure equals the gravitational pressure (see Section 2.3, Equation 2.6). Both, the Eddington luminosity and the persistent surface brightness depend on the mass and the radius of the neutron star. A measurement of both quantities therefore limits the possible combinations of R and M and thereby the number of applicable EoSs, assuming that the surface of the neutron star emits isotropically (see also Lewin et al., 1993). Özel (2006) claim that she could additionally measure the gravitational redshift independently, using absorption lines in the X-ray spectrum of the LMXB and thereby narrowing down the possible models even further. Figure 2.7 shows the relation between mass and radius for each of these measurands. Additionally, as a consistency check, the allowed area as determined by the rotational broadening of the lines is shown, when assuming a $M = 1.4\,\mathrm{M}_\odot$ and $R = 10\,\mathrm{km}$ neutron star. The results of Özel (2006) indicate that very soft EoSs do not describe the physics of the neutron star in EXO 0748−676. Similar investigations with comparable results have been carried out for other LMXBs as well, see, e.g., Özel et al. (2009) and Güver et al. (2010). For this method, however, the distance to the system has to be known accurately as well as assumptions on the neutron star atmosphere have to be made, inducing large systematic uncertainties (Steiner et al., 2010). Nonetheless, detailed investigations of these bursts provide very interesting insight in the composition of neutron stars by limiting the number of applicable theoretically models (see also Kuśmierek et al., 2011).

2.3 Accretion & X-ray Production

ISOLATED neutron stars, which do not show up as radio pulsars or SGRs/AXPs, are only very faint throughout the electromagnetic spectrum. Even though they are hot ($\sim 10^6\,\mathrm{K}$) , they are so small that they are not bright enough to be visible to an observer far away. The case is completely different if the neutron star is in close orbit with a normal companion star. By transforming the potential energy of matter from the companion falling down the deep gravitational well of the neutron star, i.e., by accreting matter, it can get very bright, especially in X-rays. The amount of released gravitational energy E_grav, which is transferred into kinetic energy and, in the accretion column and finally on the solid surface of the neutron star, into radiation, can be easily calculated to be

$$E_\mathrm{grav} = \frac{GM}{R} \approx 1.8 \times 10^{20}\,\mathrm{erg\,g^{-1}} \tag{2.5}$$

using typical values for a neutron star of $M = 1.4\,\mathrm{M}_\odot$ and $R = 10\,\mathrm{km}$. For typical X-ray luminosities of 10^{36}–$10^{37}\,\mathrm{erg\,s^{-1}}$ in HMXBs, this means that $\sim 10^{-8}\,\mathrm{M}_\odot\ \mathrm{yr}^{-1}$ need to be accreted, if we assume that 10% of the gravitational energy is radiated away as X-rays. These mass accretion rates can be easily realized in the dense winds of early type stars.

If infinite amounts of material were present, there would still be a limit to the accretion rate, as soon as the radiative pressure on the material exceeds the gravitational force. Assuming spherical symmetric accretion of a fully ionized hydrogen plasma, this maximal luminosity is called the Eddington luminosity. The main radiative pressure will be exerted on the material via *Thomson scattering* of the photons with the electrons, whose scattering cross-section σ_T is a factor $\sim 10^8$ larger than for protons (Frank et al., 2000). The main gravitational force is exerted on the more massive protons with mass m_p. Through electromagnetic coupling, electrons and protons appear as closely connected pairs, so that the Eddington luminosity is reached at equilibrium between the radiative pressure on the electrons and the gravitational force on the protons. It can then be written as (Frank et al., 2000):

$$L_\mathrm{edd} = \frac{4\pi G M m_p c}{\sigma_\mathrm{T}} \approx 1.3\times 10^{38}\,(M/\mathrm{M}_\odot)\,\mathrm{erg\,sec^{-1}} \quad , \tag{2.6}$$

which is about an order of magnitude higher than observed in flares from HMXBs. However, as neutron stars are highly magnetized and the accreted material is ionized, accretion does not happen spherically symmetric[3] but is collimated onto the magnetic poles of the neutron star. The resulting accretion columns and the hot spots have a typical radius on the order of 1 km (Becker & Wolff, 2005b), reducing the local Eddington luminosity by a factor of ~ 200. It is therefore possible that the Eddington luminosity is exceeded locally, changing the behavior of the material in the accretion column drastically and leading to the formation of a shock front in the column (see Becker & Wolff, 2005a, and Section 2.3.1). This luminosity is called the critical luminosity L_crit. It is not a hard limit like the Eddington luminosity is for spherical symmetric accretion, as radiation can also escape to the sides of the accretion column (Harding, 1994).

In order to sustain the observed luminosity $\sim 10^{11}\,\mathrm{g\,sec^{-1}}$ need to rain down the accretion columns.[4] It is immediately clear that enormous amounts of energy are released in there and physical processes in the high energy regime can be studied, which are not easily accessible in the laboratory.[5] The energy is emitted over a broad range of the electromagnetic spectrum, with the most flux typically between 2–20 keV. The time dependence of the flux (i.e., lightcurves) and its energy distribution (i.e., spectra) are unique tracers of the object and its underlying physics.

Since the discovery of neutron star binaries, theorists have tried to provide physical models which can describe the observed spectra and lightcurves. Most famous is the classic series by Ghosh et al. (1977), Ghosh & Lamb (1979a), and Ghosh & Lamb (1979b) which, for the first time, gave a concise picture over the formation of accretion disks and the influence of the strong magnetic fields on the accretion geometry. Basko & Sunyaev (1976) calculate the maximal luminosity L_crit before the radiation pressure stops the infalling

---

[3] even without magnetic fields the conservation of angular momentum would prevent that

[4] this is roughly equivalent to the mass of 2 giant ocean liners per second

[5] the total annual energy consumption on Earth is only $\sim 5\times 10^{27}$ erg (Gruenspecht, 2010)

material. This critical luminosity has a major influence in determining the possible structures in the accretion column. In the last years a series of papers by Becker & Wolff (2005a,b, 2007) dealed in detail with these structures and the production of X-rays in the column. I will very briefly summarize the main concepts presented in these papers in the following paragraphs. For more details the interested reader is referred to the textbook by Frank et al. (2000).

2.3.1 The continuum spectrum

MATERIAL falling down the gravitational potential bears angular momentum with respect to the neutron star and is strongly ionized, i.e., it is a plasma. The angular momentum will be dissipated through viscous friction in an accretion disk, which is forming around the neutron star. This disk will not reach down to the surface of the neutron star, but is disrupted at the so-called *Alfvén radius*. Inside the Alfvén radius the plasma follows the magnetic field lines closely. This tight connection between material and field lines leads to the formation of accretion columns above the poles of the neutron star[6]. The most simple geometry of these accretion columns would be a filled cylinder, but whether this corresponds to reality is uncertain. The geometry depends strongly on the way the material couples to the magnetic field lines and other geometries like hollow cylinders or even multiple small cylinders ("spaghetti geometry") are thinkable (Mészáros, 1984). The geometry is also influenced by the accretion rate and the luminosity. If the luminosity increases above a critical luminosity L_crit, the radiation pressure of the photons on the infalling electrons will effectively slow down the plasma to subsonic velocities above the neutron star surface. L_crit can be regarded as a local Eddington luminosity, scaled with the size of the column. The shock will move farther away from the neutron star surface with a higher accretion rate, as the radiative pressure increases. In this geometry, X-rays can only escape through the walls of the accretion column, in a so-called "fan beam". If the luminosity is below L_crit, no radiation dominated shock forms, and X-rays escape the column primarily parallel to the magnetic field lines, forming a "pencil beam" (Becker, 1998). The exact determination of L_crit is still under debate and different theoretical models are investigated (Harding et al., 1984, and Becker, 2011, priv. comm). The geometry as depicted by Becker & Wolff (2007) is shown in Figure 2.8. Here a filled cylinder is assumed and a luminosity above L_crit, so that a sonic shock is formed. The model developed by Becker & Wolff (2005a,b, 2007) is based on this geometry of which the main aspects are briefly outlined in the following paragraphs.

Inside the accretion column, the material will be heated up to temperatures on the order of 10^7 K. It will be stopped completely at the bottom of the accretion column by the solid surface of the outer crust of the neutron star. There a hot-spot is formed which emits photons as a blackbody, resulting in typical photon energies $\sim$1 keV. Additionally the plasma in the accretion column will produce photons via *bremsstrahlung*, i.e., through the interaction of its electrons with its ions. These photons carry away some of the energy of the electrons and thereby cool the plasma. The bremsstrahlung energy spectrum has

---

[6] assuming that the magnetic fields of neutron stars can be approximated by dipole fields

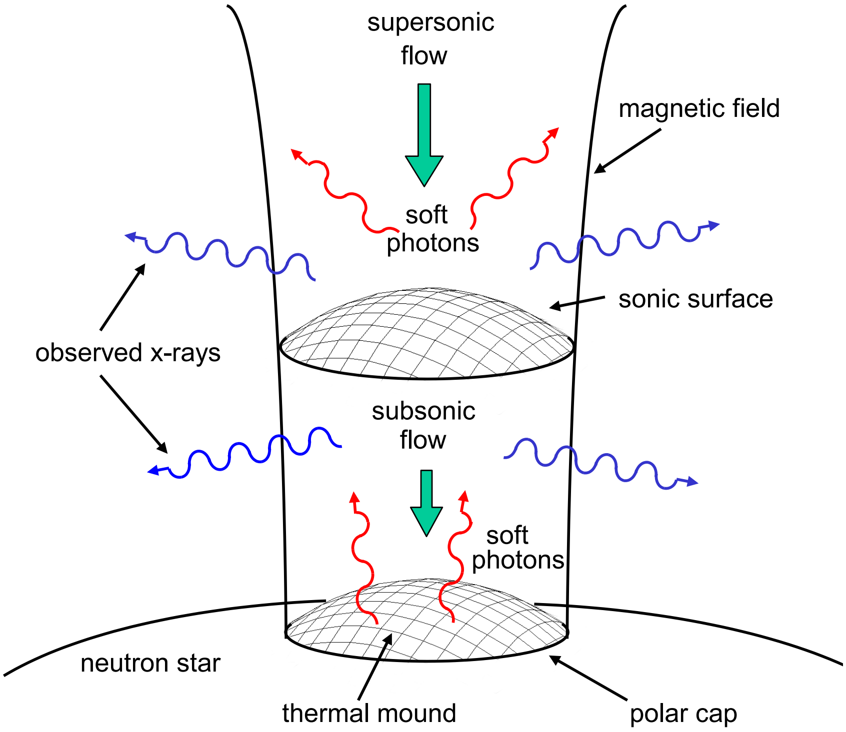

Figure 2.8.: Sketch of the accretion column in a fan-beam geometry. Figure taken from Becker & Wolff (2007).

an exponential cutoff characterized by the temperature of the plasma. That means that the plasma emits many soft photons, but almost no X-ray photons with energies $> 3\,\mathrm{keV}$.

The photons interact with the hot electrons in the plasma, but the interaction cross section is influenced by the strong magnetic field, which leads to a quantization of the electron energy perpendicular to its field lines. The electron momentum distribution is thus only continuously in the direction parallel to the magnetic field but constrained to specific energy levels, the so-called *Landau levels*, in the perpendicular direction. This quantization influences the cyclotron radiation[7] produced by the movement of the electrons in the magnetic field (see also Section 2.3.2). Cyclotron radiation is only emitted when the electrons undergo a transition from one Landau level to the next, similar to atomic shell transitions. This effect gives rise to a line spectrum of resonant cyclotron lines, which is smeared out thermally by the electron movement in the direction of the magnetic field.

There are thus three sources of mostly soft X-ray photons in the accretion column: blackbody radiation from the hot spot, strong bremsstrahlung in the column, and cyclotron radiation also in the column. To produce the observed hard X-ray continuum, these photons need to be accelerated to higher energies, which can be achieved by Comptonization. That means that photons are accelerated by scattering on relativistic electrons via the *inverse Compton effect* (Compton, 1923). Two different kinds of Comptonization need to

---

[7] the term cyclotron radiation is used here in a general way as common in the literature, i.e., it is not used explicitly for non-relativistic electrons only

be considered (Becker & Wolff, 2007): “bulk” or “dynamical” and “thermal” Comptonization. The first dominates over the latter if the kinetic energy of the infalling electrons is higher than their thermal energy (Becker & Wolff, 2005b). In that case, where “bulk” Comptonization is most important, the kinetic energy of the electrons is transfered to the photons by scatterings across the shock in the accretion column, as described by first-order Fermi acceleration (Fermi, 1949). The resulting spectrum follows a power law $E^{-\Gamma}$ with $\Gamma \geq 2$ and no cutoff at high energies. In very bright sources, the temperature of the accretion column increases above 10^7 K and thermal Comptonization is no longer negligible. Here photons are accelerated through a second-order Fermi process, i.e., by drawing energy from the thermal motion of the electrons. Their spectrum is overall flatter than for bulk Comptonization, but shows a characteristic high energy cut-off (Becker & Wolff, 2007). Becker & Wolff (2007) could explain the broadband spectra of Her X-1, LMC X-4, and Cen X-3 with this model, and Ferrigno et al. (2009) successfully applied it to 4U 0115+63. For these sources a good description was obtained when the bremsstrahlung component dominated as source of soft photons. The model requires, however, still some manual fine-tuning, as it incooperates many free parameters. It also does not include a self-consistent model for *Cyclotron Resonance Scattering Features (CRSFs)* (see Section 2.3.2) and is only applicable for sources in which a shock is formed in the accretion column.

2.3.2 Cyclotron lines

As described in the previous Section the strong magnetic field in the accretion column leads to a quantization of the electron movement perpendicular to the B-field on quantized Landau levels. Besides the production of cyclotron radiation these levels lead also to a strongly increased cross-section for photons with energies equal to the energy difference between them, in the electron’s rest-frame (Figure 2.9). The opacity at these resonant energies is so large that photons can only escape the line forming region when they are inelastically scattered and thereby change their energy.

The quantization of the electron movements gives consequently rise to absorption line like features in the X-ray spectrum. These components are called Cyclotron Resonance Scattering Features (CRSFs)[8], or more colloquial “cyclotron lines”. Their energy is a direct measurement of the magnetic field in the accretion column, as the energy of the Landau levels depends directly on the magnetic field strength. Solving the *Dirac equation* of electrons in a strong magnetic field, one obtains the following relation (Schönherr et al., 2007):

$$E_\mathrm{n} = m_e c^2 \frac{\sqrt{1 + 2nB/B_\mathrm{crit}\sin^2\theta} - 1}{\sin^2\theta}\frac{1}{1+z} \tag{2.7}$$

where B_crit is the critical magnetic field, at which the cyclotron energy and the electron

---

[8] I am using the term “cyclotron *resonance* scattering feature” as used by Schönherr et al. (2007), however, there are other authors who use “cyclotron *resonant* scattering feature” to describe the same phenomenon (e.g., Harding & Lai, 2006).

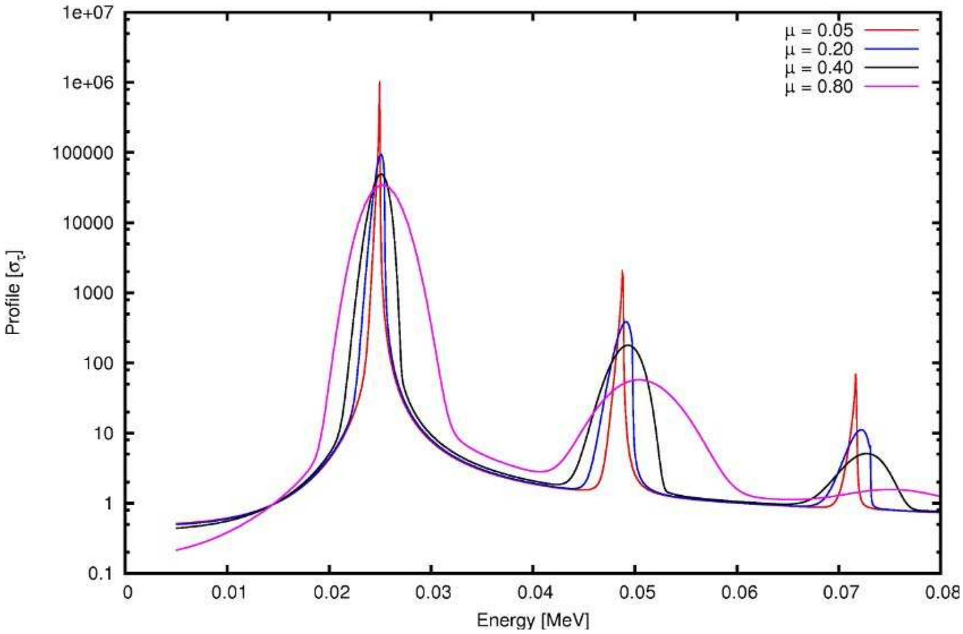

Figure 2.9.: Thermally averaged scattering cross-sections as a function of energy for different value $\mu = \cos\theta$, the cosine of the angle between the photon path and the magnetic field lines. For photons almost parallel to the magnetic field the cross-section is very sharply peaked at the Landau levels, while at shallower angles the peaks are broadened due to the thermal motion of the electrons and are additionally shifted to higher values. Cross sections are given in units of the Thomson scattering cross section σ_T. Plot courtesy of F. Schwarm (2011).

rest energy are equal (Schwarm, 2010):

$$B_\mathrm{crit} = \frac{m_e^2 c^3}{e\hbar} \approx 4.4 \times 10^{13}\,\mathrm{G} \tag{2.8}$$

Here, θ is the angle between the photon path and the magnetic field lines and n is the number of the line, starting with $n = 1$, the fundamental line. In most HMXBs systems, B is much smaller then B_crit, such that Equation 2.7 can be simplified via a Taylor expansion. For the fundamental line ($n = 1$) with photons moving parallel to the magnetic field lines ($\theta = 0$) it can then be written as

$$E_1 = \frac{\hbar e B}{m_e c}\frac{1}{1+z} \approx 12\,\mathrm{keV} \cdot B_{12} \quad , \tag{2.9}$$

the so-called "12-B-12" rule in which B_{12} describes the magnetic field strength in units of 10^{12} G. As often only this fundamental line is detected in the spectra of HMXBs and as it plays the most important role in measuring the magnetic field strength, I will refer to it as E_CRSF in the rest of this thesis. The gravitational redshift z, used in Equations 2.7 and 2.9, is defined as

$$z = \frac{1}{\sqrt{1 - R_G/R}} - 1 \quad , \tag{2.10}$$

with gravitational radius $R_G = 2GM/c^2$, leading to redshifts typically around $z \approx 0.3$ for neutron stars.

The close connection between the magnetic field strength of the neutron star and the energy of the CRSFs makes these features the only available method to directly measure the magnetic field strength close to the neutron star. Their exact energy depends on the local magnetic field at their production region, which changes with distance from the neutron star. It is expected that the altitude of the X-ray production region changes with different accretion rates, and therefore relative changes in E_{CRSF} allow to trace these changes. Depending on the luminosity being above or below L_{crit}, i.e., depending on if a shock is formed or not a negative or a positive correlation is expected. If the luminosity is above L_{crit} most X-rays will be produced close to the shock front. With increased accretion rate, the altitude of the shock increases into regions with a lower magnetic field. That means that when the source gets brighter, E_{CRSF} is decreased, i.e., a negative correlation is observed. Negative correlations have been observed in a number of sources, e.g., 4U 0115+64 or V 0332+53 (Müller et al., 2011b; Mihara et al., 2007)[9]. For energies below L_{crit} a positive correlation is predicted, as observed in Her X-1 (Staubert et al., 2007). Not all sources, however, show a change in E_{CRSF} with luminosity (e.g., A 0535+26, Caballero et al., 2007). The reasons for this behavior are not understood yet. For a more detailed discussion on the correlation between E_{CRSF} and luminosity see Caballero (2009), and references therein.

The different Landau levels are spaced almost equidistantly, except for some relativistic shifts, so that harmonics of the fundamental cyclotron line should show up at n times the fundamental energy E_{CRSF}. The source with the most known CRSFs to date is 4U 0115+63, where up to five lines have been observed (Santangelo et al., 1999; Heindl et al., 2000). In other sources only two or rarely three lines are known. For sources with multiple lines the magnetic field can be measured with much higher accuracy, as the distance between the lines can be used to constrain the fundamental energy.

2.3.3 Pulse profiles

RESULTING from the rotation of the neutron star, we see varying regions of the narrowly confined accretion column and of the X-ray production region. X-rays are usually emitted in a preferred direction, e.g., along the magnetic field lines or perpendicular to them, depending on the accretion geometry as described above. As most often the magnetic field axis is not co-aligned with the rotational axis of the neutron star X-rays reach us only at specific phases, due to the so-called “lighthouse” effect. We consequently observe pulsed emission with the pulse period corresponding to the rotation period of the neutron star. From the analysis of the evolution of the pulse period we can infer on the amount of angular momentum transferred onto the neutron star. In most cases, accretion happens on both poles of the neutron star’s magnetic field, so that X-rays can reach us twice per rotation and the pulse profile has a characteristic two peaked profile (see the

---

[9] The results of Müller et al. (2011b), however, indicate that this correlation depends on the applied continuum model.

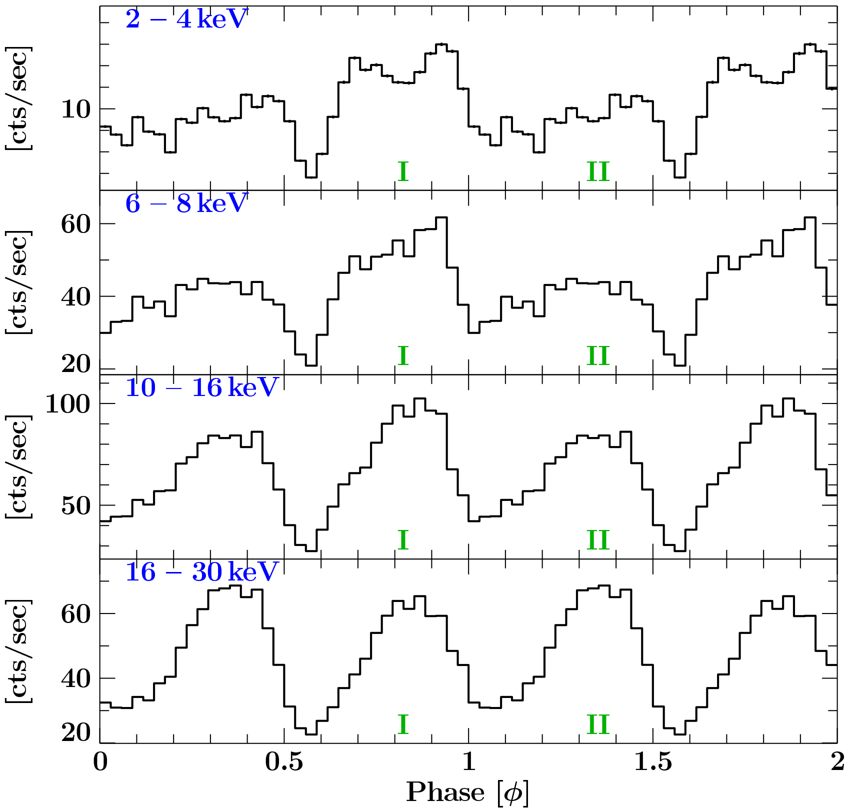

Figure 2.10.: Energy resolved pulse profiles from *RXTE*/PCA of Vela X-1, taken in December 2008. An evolution from a multi-peaked profile to a simpler two peaked profile with energy is visible. The primary and secondary peak are labeled with I and II, respectively. The y-axis shows the average countrate in the respective energy band.

bottom panel of Figure 2.10).

Care has to be taken, however, as gravitational lightbending can immensely influence the shape of the pulse profile, especially when X-rays are emitted very close to the neutron star surface. Through the lightbending effect, more than 80% of the neutron star's surface are visible at any time and in extreme cases X-rays emitted just opposite of the observer can anyway reach us and be brighter than at any other phase (Kraus et al., 1995)[10].

The spectral shape usually changes continuously with pulse phase. This effect is directly visible in the energy dependence of the pulse profile, which on average gets simpler, i.e., has less substructure, at higher energies. This effect is seen for example in the pulse profile of Vela X-1, a HMXB with a ~280 sec pulse period (Kreykenbohm et al., 1999). In Figure 2.10 the evolution of its profile is shown, as measured with *RXTE*/PCA (see Section 3.3 for a description of the satellite). The primary peak (labeled I) shows two subpeaks at low energies, while the secondary peak (labeled II) is much weaker and has also some sub-structure. With increasing energy the substructure vanishes and both peaks

---

[10] see `http://www.spacetimetravel.org/xpulsar06/xpulsar06.html` for very nice animations (in German only)

are of almost equal strength. The behavior can be understood, when keeping in mind that through the rotation of the neutron star we see different regions of the accretion columns showing different physical properties. Assuming that the two peaks of the pulse profile originate from the two different accretion columns of the north and south magnetic pole, a strong variance between the peaks indicates that the columns have different physical properties, e.g., different temperatures or sizes. Most notably is the variation of E_{CRSF} with pulse phase. From this variation, a reconstruction of the dipole magnetic field and its orientation with respect to the neutron star can be inferred (Suchy et al., 2011a, see also Chapter 6).

From a decomposition of the energy dependent pulse profile we can theoretically infer on the physical structure of the accretion columns and investigate how and where X-rays are produced and where they escape the column. However, different geometries can lead to very similar observed pulse profiles so that some assumptions on the structure have to be made a priori. Some success has recently been made by Sasaki et al. (2010) and Caballero et al. (2011) for EXO 2030+375 and for A 0535+26, respectively, based on models by Kraus et al. (1995). The model, however, still uses some simplifications and needs a lot of manual work to select the physically most sensible parameters.

2.4 Absorption & Fluorescence

PHOTONS from the neutron star's surface and from the accretion column have to travel a long way before we can detect them. Most of the way they move through empty space, but in the first few thousand light-seconds they have to pass through dense material such as the stellar wind or the accretion wake of their host system. While passing through this material, they react in several ways with it, e.g., via absorption and scattering. Their energy distribution is strongly influenced by this interaction and the material imprints its fingerprint on the measured spectrum. By measuring the X-ray spectrum we can therefore not only learn something about the X-ray producing region, but also about the surrounding material, its composition, and its physical state. In other words, the radiation from the neutron star allows us to X-ray the stellar wind.

When a photon encounters a not-fully ionized atom, it can get absorbed by this atom via *photo-electric absorption*, i.e., the photon is destroyed and transfers its energy to an electron which either is transfered to a higher bound state (excitation) or leaves the atom entirely (ionization). The probability for this interaction to happen depends on the cross-section σ, which is depending on the atom, its ionization state, and the energy of the photon. Calculation of σ is a difficult quantum-mechanical and quantum field theoretical process, and can only be done semi-empirically and iteratively using approaches like the famous *Hartree-Fock* method (see, e.g., Pradhan & Nahar, 2011, and references therein). In a first general approximation σ is proportional to E^{-3}, that is, for a photon of higher energy material is more transparent. But as the energy levels of the electrons in an atom are quantized and organized in so-called *shells*, σ has distinct jumps at energies where the X-ray photons can liberate electrons from lower shells (Als-Nielsen & McMorrow,

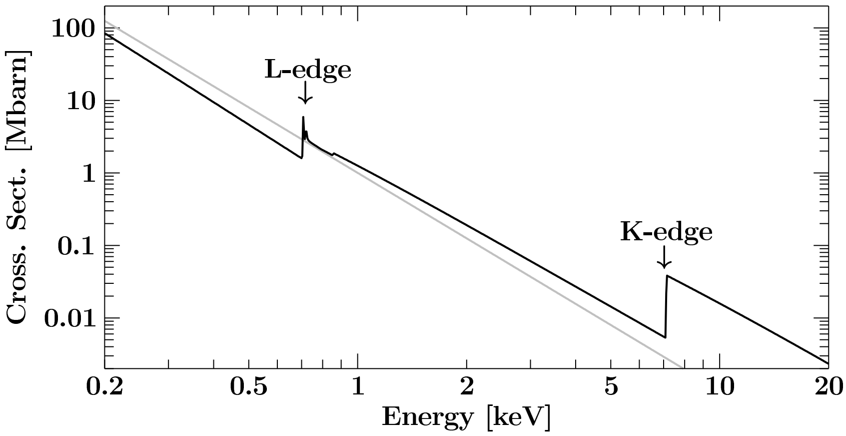

Figure 2.11.: Photoionization cross section of Fe according to Verner et al. (1996). One Mbarn is equal to $10^{-18}\,\mathrm{cm}^{-2}$. The light-gray line shows an E^{-3} dependence.

2011). These jumps are responsible for the *absorption edges* observed in X-ray spectra. Most important for X-ray astrophysics is the K-edge of iron, which occurs at 7.1 keV, see Figure 2.11. Between the edges the cross-section is not smooth, but has very narrow peaks for photons having just the right energy to lift one electron from one level to the next.

After an ionizing absorption process, the atom has lost an electron. If the electron was expelled from a strongly bound lower shell (e.g., the K-shell), the atom is in an unstable excited state which decays to a stable state by filling the gap in the lower shell with an electron from a higher shell. As the lower shell is more strongly bound, energy is released in the process which can be emitted as a photon. This photon is called the *fluorescence* photon and gives rise to characteristic fluorescent emission lines in the energy spectrum. For high-Z elements and processes involving the lowest electron shells K, L, and M these photons can have energies in the X-ray regime. In *Siegbahn notation*, the observed lines are named after the shell in which the initial hole was produced, plus a Greek subscript indicating the shell from which the electron filling the gap came. The photon emitted when an L-shell electron falls down to the K-shell is called K_α, and K_β if the electron originated in the M-shell (Figure 2.12). This description of the fluorescence lines has been invented by Siegbahn (1918) before a full quantum-mechanical understanding of the atomic structure was established. It is still widely used in X-ray spectroscopy.

The above described model of electrons sitting quietly in different shells and falling down to lower shells is of course only a very simple toy model of the atomic structure. Quantum mechanics has shown that the electron shells must be interpreted as probability density functions, characterized by different quantum numbers, of which an explanation can be found in any introductory textbook to quantum mechanics (e.g., Cohen-Tannoudji et al., 1978). One of these quantum numbers is the spin s of a particle, which cannot be understood in classical physics. Electrons have a spin $s = \pm\frac{1}{2}$. According to the *Pauli exclusion principle* no two electrons can occupy exactly the same quantum state, so that for electrons in the same shell with the same angular and magnetic quantum number

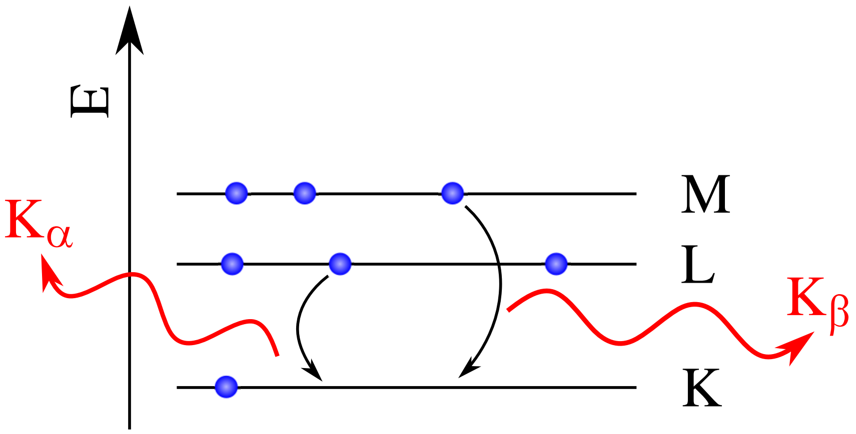

Figure 2.12.: Sketch of the basic principle of fluorescence. The electrons are shown in blue, the red lines indicate emerging photons. Note that the K-shell can hold only two electrons, so that in this case either K_α or K_β emission is possible, but not both. Plot after Als-Nielsen & McMorrow (2011).

at least the sign of the spin must be opposite. Through the coupling between orbital and spin quantum number, the energy niveaus of electrons in the same shell differ a little. These differences lead for example to the sub-structure of the L-edge as seen in Figure 2.11. In the case of K_α fluorescence the different energies give rise to slightly different fluorescence lines, denoted $K_{\alpha 1}$ and $K_{\alpha 2}$, depending on the spin orientation of the electron. These lines are very close together and can usually not be separated in astronomical X-ray sources.[11]

The energy levels of the different shells depend on the ionization state and the configuration of the atom, as the interaction between electrons cannot be neglected when calculating these levels. This interaction means that line and edge energies can be used as a tracer for the ionization state of the medium. For example, the iron K-edge can vary by up to 2 keV for the highest ionized species (Kaastra & Mewe, 1993). For lower ionization states the energy shift is much less, usually on the order of a few 10 to 100 eV. To measure these differences very good calibrated and high resolution spectra are necessary. Figure 2.13 shows examplorary laboratory measurements of silicon, in which the energy shift of the $K\alpha$ line with ionization state is clearly visible.

Exact measurements of the ionization state are made even more difficult by the fact that in real sources, it is unusual to probe only material with exactly one ionization state. Instead, the observed lines will be a superposition of lines from differently ionized atoms and therefore be intrinsically broadened. Additionally, the fluorescent material is often moving with several 100–1000 $\mathrm{km\,s^{-1}}$, be it in the stellar wind or in an accretion disk. This movement gives rise to a shift and a broadening of the lines due to the Doppler effect. These effects contribute systematic uncertainties to the measured energies of the lines and allow only for a reliable measurement of the ionization state for very strongly

---

[11] the transition from the L-shell with an orbital angular momentum of 0 is dipole-suppressed, as in a dipole transition the angular momentum must change by ±1. Hence only two K_α lines are observed.

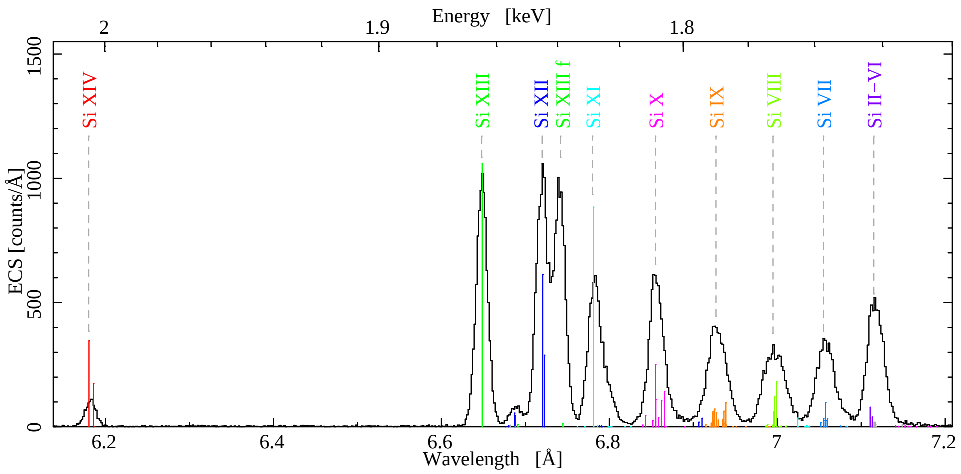

Figure 2.13.: Measurements of silicon Kα lines for different ionization states using the EBIT Calorimeter Spectrometer (ECS, Porter et al., 2009) at the Lawrence Livermore National Laboratories. The colored and labeled lines are predicted by theory for the corresponding ionization state. Plot courtesy of N. Hell (2011).

ionized elements.

Besides emission features, absorption lines resulting from photo excitation can also provide a signature of the absorber. Photons with energies corresponding to a transition in the atom are removed from the continuum. The excited atom will eventually deexcite and emit a photon of equal energy as the absorbed one, but this photon will be emitted unidirectional. For an absorbing medium directly in the line of sight to the X-ray source, less photons at the energies of the atomic lines will arrive at the observer, and an absorption line is formed. These lines are very narrow and can only be investigated with very high spectral resolution, like provided by the gratings on board *Chandra* and *XMM-Newton*. At lower spectral resolution they are blended into the continuum. A wealth of these absorption lines has for example been observed in Cygnus X-1 and provided deep insight in the ionization state and structure of the absorbing stellar wind (Hanke et al., 2009).

2.5 Outlook

Much more could be said and explained about neutron stars and X-ray binaries and how we can obtain information about them. These explanations would, however, lead us far beyond the scope of this thesis and the interested reader is referred to textbooks like Frank et al. (2000) or invited to visit an university lecture about X-ray astronomy. Instead I would like to conclude this Chapter with a short summary and an outlook on the main topic of this thesis, the analysis of real galactic sources.

We have seen that neutron stars are objects in which we can find matter in one of its most extreme states. In the inner cores of neutron stars, densities far beyond the density of nuclei are present. These densities lead to a complete neutralization of matter, where atoms no longer exist. Elementary particles are pressed together and new states of matter, like hyperons or even quark-matter, might be produced. Isolated neutron stars are only seldom observable, but they become very bright in X-rays when they are in close orbit with an optical companion. Due to their enormous gravitational pull they accrete parts of the stellar wind from the companion and transfer it into energy. This energy is radiated away as photons, which have been accelerated to X-ray energies through the inverse Compton effect. The spectrum of these photons carries information about the temperature of the accretion column as well as about the magnetic field strength close to the neutron star by means of CRSFs. The medium surrounding the neutron star is illuminated by the X-rays from the neutron star and the photons we measure also carry information about this medium in the shape of absorption and fluorescence lines. As the neutron star rotates, we can get a look at different regions of the accretion column and by studying the variability of the spectrum over the pulse we can infer the accretion and magnetic geometry.

For three different sources analyses of this kind were performed for this thesis. All of them are X-ray binaries, but each source has its own peculiarities. Their timing and spectral features were compared to and checked against the theoretical picture in order to understand their physics. The first source is 3A 1954+319 (Chapter 4), a very peculiar source as the mass donor is an M-type giant with a mass of only $\sim 1\,\mathrm{M}_\odot$. Less then 10 sources with similar companions are known. It was observed during an outburst which strongly influenced its very long pulse period of $\sim 5\,\mathrm{h}$. In 3A 1954+319 the distance between the mass donor and the neutron star is thought to be very large, so that the structure of the wind far away from the star can be probed. The accreted matter from the wind seems to transfer large amounts of angular momentum onto the source. For the first time the pulsating flux of this source could be observed directly in the lightcurve, showing a relatively stable pulse profile, indicating that the accretion columns do not change much over the outburst. In the spectrum no evidence for a CRSF was found so that the magnetic field strength can not be measured directly.

The next source, called 4U 1909+07, is a HMXB with a more massive companion than 3A 1954+319, having at least $10\,\mathrm{M}_\odot$. Through pulse phase resolved spectral analysis, I found that the flux of the blackbody component is varying sinusoidal with phase. This variation shows that the hot spot from where the blackbody originates is only visible at certain phases and is hidden either behind the neutron star or behind some dense absorbing matter at all other times. I also present evidence that the spectrum of 4U 1909+07 is changing on long timescales, by comparing data from 2003 and 2010. Besides the spectral analysis the long term timing behavior was investigated. When comparing it to the behavior of 3A 1954+319, we see that it behaves completely different and that it follows a random walk like behavior. This difference directly shows the contrast between the two companion stars and the diversity in transfer of angular momentum during accretion. In Chapter 5 on page 77 the results are presented in detail.

The most massive companion star with more than $40\,\mathrm{M}_\odot$ is the optical companion of GX 301−2. GX 301−2 is a very famous X-ray binary and has been studied in great detail since many years. In my analysis it shows different states of activity, with one outstanding phase where the regular pulsations disappear. An unpulsed flux from the source is still measured which most likely comes from a reflected and time-delayed component. Studies of the fluorescence lines and the variability of the absorption column are made and thereby the state of the accreted medium is probed. Different fluorescence lines from different elements are found. In harder X-rays the behavior of the CRSF is investigated. This analysis is laid out in Chapter 6.

A comprehensive model taking into account all physical effects and properties of the accretion column with its extreme magnetic and gravitational fields does not yet exist. Theoretical astrophysicists are still working on such a model, but to give them a guideline what the model should describe, observational evidence is necessary. The data and analyses here are only a very small part of this observational evidence. Still I hope that the results can help to arrive one day at a thorough understanding of neutron stars, their radiation, and their companions.

Take a look beyond the moon, you see the stars.

(Caro Emerald - "A Night Like This")

3

Satellites & Data Analysis

X-RAYS can only be observed from space as Earth's atmosphere is opaque to photons in this energy range. First X-ray detectors were brought above the densest parts of the atmosphere by means of weather balloons and small rockets, allowing only for a very limited observation time and typically carrying only simple detectors (see, e.g., Seward & Charles, 2010). The first cosmic X-ray source detected outside of the solar system was Sco X-1, during a 5 min rocket based observation (Giacconi et al., 1962). Nowadays almost all X-ray astronomy is done using X-ray satellites in orbit. The satellites cover an energy range from $\sim$0.1 keV up to $\sim$100 MeV, i.e., more than 5 decades of the electro-magnetic spectrum. Photons between 0.1 keV to 10 keV are usually referred to as soft X-rays, between 10 keV–100 keV as hard X-rays, and above 100 keV as soft γ-rays. This definition, however, varies depending on the satellite in question and the available data set. Each satellite is built to achieve specific scientific goals and has therefore different strengths concerning spectral resolution, sensitivity, and timing capabilities. These different objectives result in a large variety of designs and orbital parameters, depending also on the budget the satellite was built on and on the technology available at the time.

To detect X-rays from a source they need to be somehow focused or collimated onto a detector by means of an optical device which is able to influence light at these energies. The different possibilities of building X-ray optics are explained in Section 3.1. In the following Sections, the five satellites from which data were used in this thesis are presented. In Section 3.2 the *X-ray Multi Mirror Mission (XMM-Newton)* is described, a satellite built to measure soft X-rays with a very high spectral resolution. In Section 3.3 the *Rossi X-ray Timing Explorer (RXTE)* is introduced, which has no imaging capabilities but outstanding timing capabilities and is covering the X-ray energy range. Section 3.4 is dedicated to the Japanese-American satellite *Suzaku* which provides broad band coverage from soft X-rays to γ-rays. The *INTErnational Gamma-Ray Laboratory* (*INTEGRAL*), the only instrument capable of taking images of the hard X-ray and soft γ-ray sky, is presented in Section 3.5. The imaging capabilities of this satellite alone allowed to obtain the data used in Chapter 4. For the analysis of 3A 1954+319 also data from the *Burst Alert Telescope (BAT)* on board *Swift* were used. This satellite is described in Chapter 3.6.

Table 3.1.: The most important properties of the X-ray detectors of all satellites presented in this work. Note that most values depend on the observational conditions, like background and source flux, and thus should be taken as guiding values only.

Satellite Instrument	Pixel size (ang. resolution)	FoV [arcmin]	E range [keV]	$[E/\Delta E]$	T-res
XMM-Newton					
EPIC-pn	$150\,\mu$m ($4''.1$)	30	0.15–15	$\sim$40	0.03 ms
EPIC-MOS	$40\,\mu$m ($1''.1$)	30	0.2–10	$\sim$45	1.75 ms
RGS	$27\,\mu$m (N/A)	N/A	0.33 – 2.5	$\sim$500	5.7 s
RXTE					
PCA	N/A	60	3–50	5.5	$1\,\mu$s
HEXTE	N/A	60	15–250	6.7	$7.6\,\mu$s
ASM	N/A ($3'\times15'$)	360×5400	1.5–12	$\sim$2.5	90 s
INTEGRAL					
IBIS	4 mm ($12'$)	1746	15–10000	$\sim$10	$61\,\mu$s
SPI	3.2×6.9 cm ($1^\circ.5$)	1920	18–8000	450	$129\,\mu$s
JEM-X	6.6 mm ($3'$)	450	3–35	7.7	$122\,\mu$s
Swift					
BAT	4 mm($17'$)	1500×900	15–150	20	$200\,\mu$s
XRT	$40\,\mu$m ($2''.4$)	23.5	0.2–10	50	$140\,\mu$s
Suzaku					
XRS†	$625\,\mu$m ($1'.8$)	$2'.9$	0.3–12	$\sim$1000	$\sim$100 ms
XIS	$24\,\mu$m ($1'.8$)	$18'$	0.2–10	50	7.8 ms
HXD/PIN	21 mm (N/A)	$34'$	10–70	11	$61\,\mu$s
HXD/GSO	24 mm (N/A)	$4^\circ.5$	40–600	7	$61\,\mu$s
SRG‡					
eROSITA	$75\,\mu$m ($15''$)	60	0.5–10	43	50 ms
Athena‡					
WFI	$130\,\mu$m ($2''.3$)	25	0.3–20	40	$20\,\mu$s
XMS	$250\,\mu$m ($4''.5$)	2.4	0.3–12	2000	$50\,\mu$s

† instrument failed shortly after launch ‡ future mission

In Section 3.7 a very brief outlook to two future projects, in which the Dr. Karl Remeis-Observatory and the *Erlangen Centre for Astroparticle Physics (ECAP)* play an important part, is given, namely the *extended ROentgen Survey with an Imaging Telescope Array (eROSITA)* on board the Russian *Spectrum-X-Gamma (SRG)* and the *Advanced Telescope for High ENergy Astrophysics (Athena)*. Last but not least in Section 3.8 the most important data analysis methods used in X-ray astronomy are explained briefly, as far as they are relevant for this thesis.

Table 3.1 gives a concise overview of the most important properties of the different satellites and their respective instruments. Figure 3.1 shows the corresponding effective areas as a function of energy.

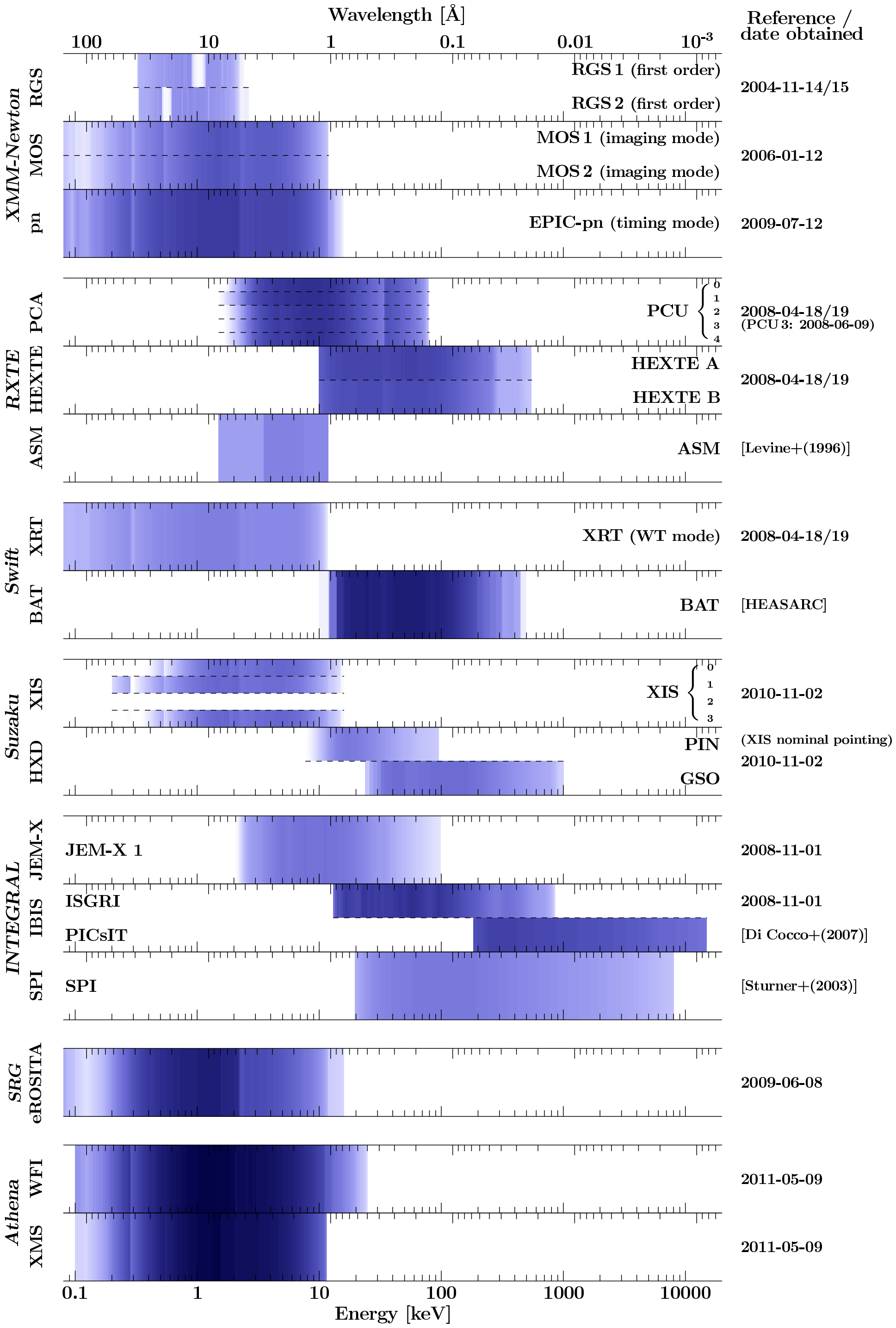

Figure 3.1.: Graphical representation of the effective areas A_{eff} of all instruments presented here, after Hanke (2011). The color scale shows the effective area A_{eff} according to the logarithmic scale on the right. The *XMM-Newton*/RGS, *RXTE*/PCA, *RXTE*/HEXTE, and *Swift*/XRT values are from Cyg X-1 observations and courtesy of M. Hanke. A_{eff}(*XMM-Newton* MOS) is from an observation of NGC 1052 and courtesy of M. Böck. A_{eff}(*XMM-Newton* EPIC-pn) is from the GX 301−2 observation (Chapter 6). A_{eff}(*RXTE* ASM) is according to Levine et al. (1996). A_{eff} (*Swift* BAT) is from the HEASARC websites. The *Suzaku* values are from the 4U 1909+07 observation (Chapter 5). A_{eff}(*INTEGRAL*/JEM-X1) and A_{eff}(*INTEGRAL*/ISGRI) are from the 3A 1954+319 observation (Chapter 4), A_{eff}(*INTEGRAL* PICsIT) and A_{eff}(*INTEGRAL* SPI) are taken as distributed with OSA 9.0 (Di Cocco et al., 2007; Sturner et al., 2003). A_{eff} for eROSITA and *Athena* are taken from the respective MPE webpages (see text).

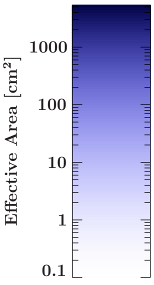

3.1 X-ray optics

Influencing X-ray light is not as easy as optical light because X-rays penetrate most materials without being strongly affected by them. Lenses and mirrors, necessary to built focusing optics, i.e, telescopes, only work if the material can bend or reflect the light. In X-rays other approaches are required to obtain images of the sky, making use of several physical or mathematical tricks. The most commonly used methods are simple collimators (Section 3.1.1), grazing incidence Wolter mirrors (Section 3.1.2 on the facing page), and mathematically complicated coded masks (Section 3.1.3). Other methods, like Bragg-reflection crystals have not yet been used in X-ray astronomy, as it is difficult to built them in such a way that they reflect a broad X-ray spectrum. They have been, however, used for solar soft X-ray spectroscopy (Mariska, 2006) and a focal plane spectrometer was installed onboard the *Einstein* satellite (Lum et al., 1992). Considerations also existed at one time to mount a Bragg spectrometer on board of SRG (Halm et al., 1998).

3.1.1 Collimators

By just looking through a long, opaque tube the region visible to a detector can be limited, as only photons entering parallel to the tube will reach it. In this way, single areas and sources in the sky can be picked out for investigation, without the need to focus the X-rays. However, imaging is not directly possible as the direction of the measured photons within the *Field of View (FoV)* cannot be reconstructed.

Collimators usually consist of many narrow tubes made out of material with high opacities for X-rays, often dense metals like copper or lead, and put together in a honey-comb structure (Figure 3.2). Due to their high opacity a single collimator tube can have thin walls, which do not obstruct much of the FoV but still absorb X-rays effectively. The FoV θ is determined by the ratio between the radius of the single tubes and their length and is usually on the order of 1°.

Collimators provide a very good way to build relatively cheap telescopes with large effec-

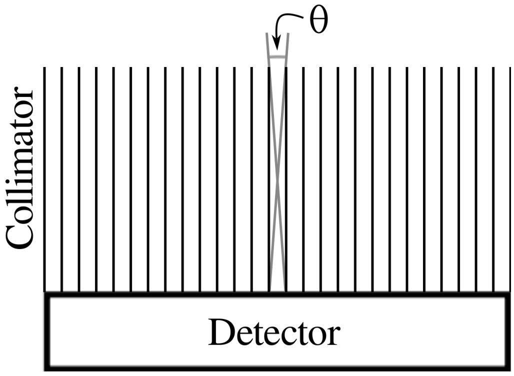

Figure 3.2.: Schematic view of a collimator, θ shows the FoV.

tive areas but with the caveat that investigations in crowded fields are difficult, as sources can hardly be discriminated. In order to get images of extended sources or sky regions, many observations with slightly different pointings need to be performed. Collimators are primarily used in the hard X-rays above 10 keV, an energy range for which focusing optics are not so easily built (see Section 3.1.2). The large instruments aboard the *RXTE* satellite (Section 3.3) and the hard X-ray detector of *Suzaku* (Section 3.4) are famous examples for collimated instruments. The upcoming European mission *Large Observatory For x-ray Timing (LOFT)* will also host a very large collimating detector (Feroci et al., 2011).

3.1.2 Mirrors

EVEN though X-rays can not be focused by mirrors in the same way as optical light, telescopes which use grazing incidence mirrors are very common in X-ray astronomy. To understand their basic physical principles, it is helpful to take a look at the refractive index $n(\omega)$ of matter. The refractive index of vacuum n_{vac} is 1 and the stronger the difference to $n(\omega)$, the stronger the light is bent in the matter. This fact is described by *Snell's law*

$$\frac{\sin\alpha_1}{\sin\alpha_2}=\frac{n_2}{n_1}=n \tag{3.1}$$

where α_i is measured from the normal of the surface. In optical light, glass has a refractive index $n(\omega)\sim 1.6$, allowing to build effective lenses. The refractive index depends, however, on the frequency[1] of the incident light and is lower for X-rays. To quantize this dependency and to calculate value of $n(\omega)$ at high energies we follow the arguments from Wilms (2008) and Aschenbach (2009). The refractive index $n(\omega)$ is given by

$$n(\omega)=\sqrt{\epsilon(\omega)\mu} \tag{3.2}$$

using the dielectric constant ϵ and the permeability μ. We can assume $\mu\approx 1$ and according to *Drude's Formula* (Drude, 1900; Jackson, 2006),

$$\epsilon(\omega)=1+\frac{4\pi n_a e^2}{m_e}\sum_j f_j\left(\omega_j-\omega^2-\imath\omega\gamma_j\right)^{-1} \tag{3.3}$$

where f_j electrons have the same bonding frequency ω_j and dampening constant γ_j in a given volume element, and

$$\sum_j f_j = Z \quad . \tag{3.4}$$

Here Z is the nuclear charge (i.e., the numbers of electrons), n_a the number density of atoms, e the charge of an electron and m_e the mass of an electron. As X-rays have frequencies much higher than the highest resonant frequency, we can simplify Equation 3.3 to (Jackson, 2006):

$$\epsilon(\omega)=1-\left(\frac{\omega_p}{\omega}\right)^2 \tag{3.5}$$

---

[1] remember that $E=\hbar\omega=hc/\lambda$ and $\omega=2\pi\nu$ with the energy, E, wavelength, λ, and frequency, ν, respectively angular frequency, ω.

where ω_p is the plasma frequency of the material defined as

$$\omega_p^2 = \frac{4\pi n_a Z e^2}{m_e} \quad . \tag{3.6}$$

This simplification implies that the dampening constant is negligible, i.e., $\epsilon(\omega)$ has only a real contribution. We can also see that $\epsilon(\omega)$ in a medium is reduced from the vacuum value $\epsilon_{\mathrm{vac}} = 1$ at the frequencies of X-rays.

Substituting $\omega = 2\pi c/\lambda$ in Equation 3.5 we obtain

$$\epsilon(\lambda) = 1 - \frac{n_a Z r_e}{\pi} \lambda^2 \tag{3.7}$$

where $r_e = e^2/m_e c^2 = 2.8 \times 10^{-13}$ cm is the classical electron radius. We define

$$\delta := \frac{n_a Z r_e}{2\pi} \lambda^2 = \frac{\rho Z r_e}{2\pi A m_u} \lambda^2 \tag{3.8}$$

Using the atomic weight A and $m_u = 1.661 \times 10^{-24}$ g the atomic mass unit to replace n_a with the more easily measurable density ρ. This substitution gives us

$$\epsilon(\lambda) = 1 - 2\delta \quad . \tag{3.9}$$

Using Equation (3.2) on the preceding page and $\delta \ll 1$ we find

$$n(\lambda) = \sqrt{1 - 2\delta} \approx 1 - \delta \tag{3.10}$$

Putting in realistic numbers for X-rays ($\lambda \approx 1\,\text{Å}$) and gold ($Z = 79$, $A = 197$, $\rho = 19.3\,\mathrm{g\,cm^{-3}}$) we find $\delta \approx 5 \times 10^{-4}$, so that $n(\lambda) \approx 1$, very similar to the refractive index of vacuum. This means that neither lenses nor normal mirrors, in which the light rays hit the mirror surface almost perpendicular, can be used to focus X-rays. Since δ is positive and is thereby reducing $n(\omega)$ below one, lenses in X-rays are dispersing light instead of focusing it, i.e., the material is optically thinner than vacuum.

Still, $n(\omega)$ is not exactly 1 so X-ray light is still slightly influenced. According to Snell's law (Equation 3.1) total reflection is possible when going from the optical denser to the optical thinner medium, when defining total reflection as the case, where the refracted ray has $\alpha \geq 90°$. The critical condition for total reflection is thus $\sin\alpha_c = n$ or $\cos\theta_c = n$ with $\theta_c = \pi/2 - \alpha_c$. Inserting this condition into Equation (3.10) gives

$$\cos\theta_c \approx 1 - \delta \quad . \tag{3.11}$$

Expanding $\cos(x) \approx 1 - x^2/2$ we find

$$\theta_c = \sqrt{2\delta} \quad . \tag{3.12}$$

Using the numbers for X-rays and gold from above we obtain $\theta_c \approx 1°$.

This very shallow angle means that the mirrors must be aligned almost parallel to the incident rays, i.e., a hollow mirror shell with a diameter much larger than the effective

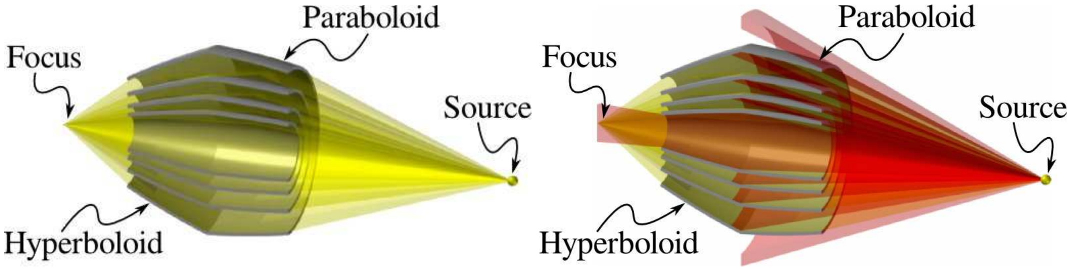

(a) Focused X-rays **(b)** Lost X-rays

Figure 3.3.: (a) Schematic of the mirrors and light path in Wolter optics. Note that in astronomy the source would be at infinite distance and that the incident light rays would be parallel. Note also that the reflecting angle is exaggerated to better show the principle. **(b)** Shown in red are light rays not focused by the mirrors and therefore lost. Clearly the effective area of the telescope is much smaller than the geometric aperture. Picture credit: `http://www.x-ray-optics.de/`.

reflecting area is used. Compared to the size of the mirror, only very few light rays will be reflected (Figure 3.3b). These light rays are only slightly deviated from their original path, resulting in a long focal length. Wolter (1952) proposed to use a combination of parabolic and hyperboloidal mirrors to obtain two reflections and thereby improving the imaging quality and reducing the focal length (Figure 3.3a). Wolter (1952) had only X-ray microscopes in mind, and it were Giacconi & Rossi (1960) who transferred this idea to X-ray telescopes. Today, Wolter Type I telescopes, as this kind of optics is called, are the most common imaging telescopes for soft X-rays (for a review see Aschenbach, 2009). To increase the effective area of the telescopes several concentric nested shells of mirrors with the same focal point are used (see Figures 3.3 and 3.4).

3.1.3 Coded Masks

HARDER X-rays above $\sim 20\,\mathrm{keV}$ are only very difficult to focus with grazing incidence optics, as θ_c gets very small. To obtain pictures of the hard X-ray sky a different technology has to be applied. The mostly used one nowadays is the so-called “coded mask”, an example of which is shown in Figure 3.5a.

This mask is a grid of opaque and transparent pixels forming a mathematically defined pattern, and placed in the light-path above the detector. All X-rays within the FoV have to pass through that mask, casting a shadow on the detector. Each source in the sky will cast a slightly different shadow, as it shines on the mask from a slightly different angle. A sketch for two sources is shown in Figure 3.5b. If the pattern of the mask is defined in such a way that it has a correlation inverse, the position of the X-ray’s origin encoded in the shadow can be reconstructed with an accuracy depending only on the pixel size of the mask and the detector. This reconstruction is often referred to as “deconvolution” of the image, as the mask’s pattern has to be deconvolved out of the measured shadowgram. It has been found that so-called *Modified Uniformly Redundant Array (MURA)* patterns

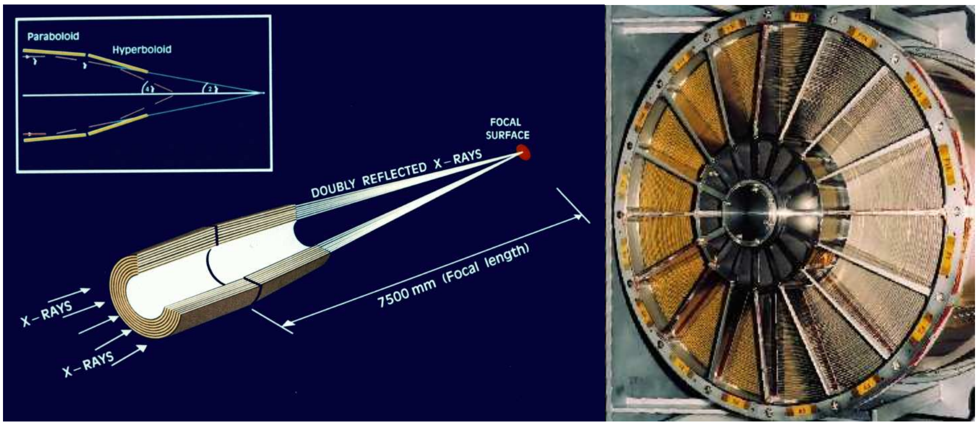

(a) Schematic **(b)** Photograph

Figure 3.4.: Schematic **(a)** and photograph **(b)** of one of the Wolter Type I telescopes of *XMM-Newton*. X-rays are first totally reflected at a grazing incidence by paraboloid mirrors and than by hyperboloid mirrors and focused 7.5 m behind the optics. Picture credit: ESA/ESTEC.

(a) BAT mask **(b)** IBIS Imaging

Figure 3.5.: **(a)** Photograph of *Swift*/BAT's coded mask during assembly. Picture credit: NASA **(b)** Sketch showing the different shadows cast by two different sources (red and blue star) through the mask of *INTEGRAL*/IBIS. Through the well-chosen pattern, the red and blue shadows are almost unique and the flux of each source can be reconstructed. Picture credit: ESA

provide all the prerequisites to perform optimal imaging with around half of the pixels being opaque to X-rays (in 't Zand et al., 1994; Skinner & Ponman, 1994; Goldwurm et al., 2003, among others). This kind of imaging technique is of course far worse than direct imaging like done with Wolter telescopes (Skinner, 2004). Its major drawbacks are the lower spatial resolution and the difficulty in deconvolving the image, especially for crowded fields and for weak sources in the vicinity to very bright sources, where the shadow cast by the bright source dominates the rest of the sky. Coded mask detectors are usually very large to be able to stop and detect the high energetic photons they were designed to measure. They also need to cover a large area to detect enough photons for a usuable *signal-to-noise ratio (S/N)*. Due to their large volumina, however, they are hit by many background X-rays and cosmic rays. These need to be filtered out in the detector electronics and software, increasing the uncertainties and the intrinsic background.

3.2 *XMM-Newton*

THE European satellite *XMM-Newton* consists of three grazing-incidence Wolter telescopes, which focus soft X-rays on *Charge Coupled Device (CCD)* detectors 7.5 m behind the mirrors. Each telescope is made of 58 nested gold-coated mirror shells, adding up to almost 1500 cm^2 of effective area at 1 keV, making it one of the largest X-ray telescopes ever flown (Jansen et al., 2001). The telescopes allow for very detailed spectral and timing analysis of faint objects. A schematic view and a picture of one of the telescopes are shown in Figure 3.4. The effective area falls rapidly off above 7 keV (10^{-2} Å) and is effectively zero at 11 keV (10^{-3} Å), due to the strong dependence of n on the wavelength. The telescopes provide a spatial resolution of up to 5” in the center of the FoV (Jansen et al., 2001). *XMM-Newton* uses different kinds of CCD detectors to measure the focused X-rays. The *European Photon Imaging Cameras (EPICs)*, consisting of the *EPIC-pn* and the two *Metal Oxide Semi-conductor (MOS)* instruments (described in detail in Section 3.2.1) are used to obtain images with average time and spectral resolution (Strüder et al., 2001; Turner et al., 2001). They can also be operated in a fast read-out mode, sacrificing imaging capabilities, but increasing the time resolution to high values. The *Reflection Grating Spectrometers (RGS)* use, as the name suggests, gratings to separate the X-rays by wavelength, allowing for very high spectral resolution, but sacrificing imaging capabilities (see den Herder et al., 2001, and also Section 3.2.2). *XMM-Newton* was launched on December 10, 1999 and has produced outstanding results since then (see, e.g., Santos-Lleo et al., 2009; Schartel et al., 2010). An artistic view of the satellite is shown in Figure 3.6.

3.2.1 EPIC

AT the focal point of each of the three telescopes of *XMM-Newton* a part of the EPIC CCD system is installed. The EPIC-pn camera, with a CCD area of 36 cm^2, is the largest one, installed solitary behind one of the Wolter telescopes. Behind the other two telescopes, the MOS1 and MOS2 cameras, as well as the RGS system, are installed. The RGS divert roughly half of the X-rays to their own detectors, so that the MOSs receive less photons than the EPIC-pn, making EPIC-pn the most sensitive camera of the system.

The usage of CCDs to measure X-rays brings the advantage of having a detector which is able to resolve the position as well as the energy of an incoming X-ray photon. The position can be measured because CCDs are pixelized. In the case of the EPIC-pn the

Figure 3.6.: Artistic view of *XMM-Newton* in orbit. Clearly visible are the three big X-ray telescopes to the right. The small telescope is the optical monitor. X-rays are focused and measured in the focal plane platform on the left. Picture credit: ESA.

pixels have a size of $150 \times 150\,\mu$m on a chip with an imaging area of 6×6 cm, allowing for an angular resolution on the sky of $3''.3$ and a FoV of $30'$ (Strüder et al., 2001). The energy can be measured by registering the number of electrons (i.e., their charge cloud) per pixel produced by the incoming X-ray photon. In EPIC-pn this can be done with an accuracy of $\sim$150 eV at 6.4 keV or $E/\Delta E = 40$. The pixels of the MOSs are a little bit smaller, resulting in a higher angular resolution of $1''.1$. The energy range covered and the energy resolution are comparable to EPIC-pn.

Like all other detectors, CCDs are not free of background, even though it is typically weaker than in other detectors, thanks to their comparable smaller detector volume. The background is mainly induced through detector intrinsic noise and through radiation or particles hitting the detector from outside. Some of these particles, like high energetic protons, are channeled through the mirrors just like the source X-rays and are registered in the detector. Their signal is, however, clearly different from an X-ray photon so that they can be easily filtered out. Thermally induced "dark current" is a negligible source of background in the *XMM-Newton* detectors at their nominal working conditions, i.e., when the chips are cooled to $-90°$C. The background rate can be estimated by measuring the count rate in off-source regions of the image. Compared to the count rates of the sources investigated in this thesis only 1% or less of the overall events are from the background. A detailed discussion of the background and its components is therefore not given here, but the interested reader is referred to Carter & Read (2007) and references therein.

The main disadvantage of CCDs is that the electrons collected in each pixel need to be read-out by the read-out node electronics. These electronics are situated on the border of the chip, which means that the electrons have to be moved and shifted through the chip to the read-out node. The position on the chip is then reconstructed by counting the numbers of shifts, or cycles, until a specific row has reached the chip's border. The imaging process of a CCD has thus two steps: first, electrons are collected on the chip in each pixel for a fixed period of time, the so-called exposure time. Second, the produced electrons are shifted and read out, during the so-called read-out time. During this read-out time, further X-rays hitting the detector will not be registered correctly. For bright sources this can be a severe problem, leading to out-of-time events which bias the following measurements.

Another problem when observing bright sources with CCDs is pile-up, where two or more source photons hit the same or neighboring pixels during one exposure (Davis, 2001). As the energy of the incoming photons is reconstructed by the amount of charge they produce, the charges of two soft photons next to each other can not be distinguished from the charge of one hard photon. The shorter the exposure time, the less likely it is, that pile-up will pose a problem. The exposure time, however, has to be fixed a priori and is depending on the instrument, so that unexpected large luminosities can easily cause problematic amounts of pile-up in an observation.

To circumvent the problems of pile-up and out-of-time events and to increase the temporal resolution, the EPICs allow to change the size of the measured image, which means that events outside this region are not read-out. This operational mode is called "Window Mode". The trade-off is a smaller imaging region, which is not an issue if no other X-ray sources are close by or if the investigated source is not strongly spatially extended. To enhance the temporal resolution further, the cameras can also be operated in a "Timing Mode", in which the chip is continuously read out, loosing all spatially information in the read-out direction, but obtaining very high time resolution. In this mode the time resolution is more than 2000 times higher compared to the full frame mode and count rates up to 800 cts $\sec^{-1}$ can be measured without severe pile-up.

3.2.2 RGS

PILE-UP is much less of a problem for the other two detectors aboard *XMM-Newton*, the RGSs, as they do not image the photons from the telescopes directly. Instead, the photons are dispersed by a grating array according to their energy (den Herder et al., 2001). In the image on the CCD chip behind the gratings the energy of the photons is thus coded in their position. The RGSs are constructed to measure the first two diffraction orders, which are overlapping on the CCD but are seperable due to the intrinsic energy resolution of the chip. With such gratings much higher energy resolution is achievable than with CCDs alone, up to $E/\Delta E = 500$ at the softest energies (den Herder et al., 2001). However, the dispersion inhibits the possibility to take images of the X-ray sky, and thus the MOS and the RGS supplement each other. The RGS is sensitive in the energy range from 0.33 – 2.5 keV (5–38Å). The source for which *XMM-Newton* was used in this thesis is strongly absorbed so that no flux could be measured below 2 keV, rendering the RGS useless for this kind of observation. As the RGS is not used in this work the reader is referred to den Herder et al. (2001, and references therein) for more details on the grating system.

3.2.3 Optical Monitor

Next to the three X-ray telescopes of *XMM-Newton* there is an optical telescope mounted on the satellite and co-aligned with the X-ray instruments. It extends the energy range of *XMM-Newton* down to optical and UV energies and thereby provides broadband coverage of the observed source. The *Optical Monitor (OM)* is a 30 cm Ritchey-Chrétien telescope with a focal length of 3.8 m ($f/12.7$) (Mason et al., 2001). The detector, a microchannelplate-intensified CCD is sensitive between 170 nm and 650 nm (1.9–7.3 eV) and has a FoV of $17''$. Directly in front of the CCD a filter wheel is installed, which harbors filters allowing for photometry in different wavelength bands, from optical to UV. Additionally two grisms can be brought into the optical path, dispersing the photons on the detector and allowing for spectroscopy. The OM is not only used for simultaneous optical observations but allows also to improve the satellite's pointing by star tracking. For more information see Mason et al. (2001).

3.3 *RXTE*

Unlike *XMM-Newton* the main instruments of the *Rossi X-ray Timing Explorer* (*RXTE*) are not able to take pictures of the X-ray sky, but just measure photons from one particular region using collimators. *RXTE* carries three independent detectors: the *Proportional Counter Array (PCA)*, the *High Energy X-ray Timing Experiment (HEXTE)*, and the *All Sky Monitor (ASM)*, where the first two are the large and main scientific instruments and the latter is a small monitoring device, as the name suggests. Figure 3.7 shows a sketch and a photograph of the satellite and its instruments.

RXTE was launched on 1995 December 30th, and started orbiting Earth in an almost circular *Low Earth Orbit (LEO)* with an altitude of about 592 km. The satellite is still in operation today and the current status and location of the satellite can be checked online[2]. It is very likely, however, that it will be decommissioned by the end of 2011. Through its over 16 years of operation *RXTE* has provided very useful data to understand the quickly variable X-ray sky. For example it investigated variations in the disks around black holes or the spin evolution of micro-second pulsars (see, e.g., Strohmayer et al., 1996; Roy et al., 2011, and many more).

3.3.1 Proportional Counter Array (PCA)

Obtaining data with medium spectral resolution but with a very high time resolution is the main goal of all instruments aboard *RXTE*. The PCA fulfills this task

---

[2] `http://heasarc.gsfc.nasa.gov/docs/xte/SOF/CurrentLocation3.html`

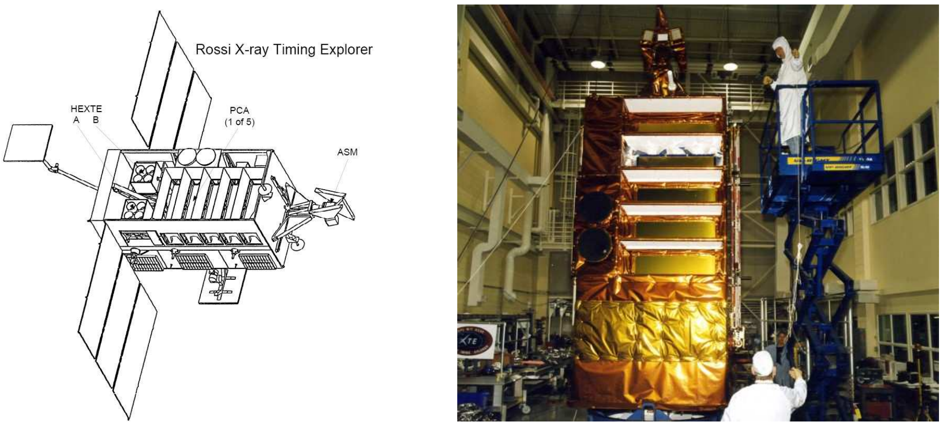

(a) Sketch

(b) Photograph

Figure 3.7.: (a) Sketch and **(b)** photograph of *RXTE*. The picture was taken at pre-launch tests in 1995. PCA is the large structure in the middle, HEXTE is hidden in the lower part of the satellite behind the golden beryllium foil. ASM is situated on top of the satellite. Solar panels were not yet attached. Picture credit: NASA/GSFC.

splendidly with a timing resolution of 1 μs and an energy resolution of $E/\Delta E = 5.5$ at 6 keV. It combines five identical gas-filled chambers, each with a maximal effective area of ~1300 cm^2, sensitive between 3–50 keV (Glasser et al., 1994, and see also Figure 3.1). These chambers are called *Proportional Counter Units (PCUs)*. The scientific gas volume of the PCUs is filled with a 90/10 xenon/methane mixture and is surrounded by anti-coincidence gas layers, of which the top-most layer is a propane filled chamber (Jahoda et al., 1996). The propane layer is separated from the xenon/methane gas by a thin Mylar foil. The xenon/methane gas volume is split into three layers of independent anode wires which operate at ~1970 V (Jahoda et al., 2006). An X-ray photon hitting the detector is detected because it ionizes many xenon molecules when interacting with the xenon gas. The number of ionized molecules is proportional to the energy of the absorbed X-ray photon. The liberated electrons are accelerated to the anode wires and on their way free more electrons by ionizing more gas molecules. If the electric field is calibrated correctly, each electron ionizes almost the same amount of gas molecules, so that the number of ions close to the anode is still proportional to the energy of the X-ray photon. Their number, however, is increased by a factor of 10^3–10^6 compared to the ions produced directly by the X-ray photon (Knoll, 2010). That means, by measuring the anode voltage pulse, the energy of the X-ray photon can be calculated. Not all electrons interacting with another gas molecule ionize it, but the molecule is sometimes only excited and emits an UV photon when decaying to its ground state. This UV photon can ionize more molecules and may produce another cascade, increasing the duration of the event. To prevent these secondary cascades, the detector gas is mixed with another gas, the so-called “quenching gas” (methane in the case of the PCA), which absorbs UV photons without getting ionized (Knoll, 2010). The signals in proportional chambers are very short, on the order of μs and, unlike in CCDs, no complicated shifting of charges to the read-out nodes is necessary.

This effect allows for very high time resolution in this kind of detectors.

Above the PCA detectors a Beryllium-Copper (BeCu) collimator is installed, consisting of hexagonal tubes with an edge length of 0.32 cm (Glasser et al., 1994). This collimator limits the FoV of the PCA to about 1°. Apart from spurious sources in the FoV, activation of heavy elements in the collimator and the detector housing are the largest source of background in the PCA. As the orbit of *RXTE* can pass through the *South Atlantic Anomaly (SAA)* (Fürst et al., 2009), activation can be quite strong, resulting in an average background rate of 18–24 $\mathrm{cts\,s^{-1}\,PCU^{-1}}$. The background of the PCA cannot be measured simultaneously, but is estimated by a background model. Separate background observations are performed regularly and show that the model is accurate within a few percent (Jahoda et al., 1996).

The PCA detector gas is only shielded by a small mylar foil (and partly by the collimator) from dangerous particles from space, e.g., micro-meteorites. In May 2000 PCU 0 was hit by such a meteorite, resulting in a drop of pressure in the propane layer (Jahoda et al., 2006). A very similar incidence happened to PCU 1 in December 2006. As the foil covering the xenon layer stayed intact, both detectors can still be used for observations of bright galactic sources but show an increased background rate.

3.3.2 High Energy X-ray Timing Experiment (HEXTE)

SMALLER in effective area but equally important for science is the second main instrument of *RXTE*, the High Energy X-ray Timing Experiment (HEXTE). It was built at the *Center for Astrophysics & Space Sciences (CASS)* at the *University of California, San Diego (UCSD)* and the following description is based on information contained in Swank et al. (1995, Chap. 5) and Rothschild et al. (1998). HEXTE is sensitive for the harder X-rays between 15 and 250 keV and consists of two independent clusters, A and B, each containing four phoswich detectors. Phoswich detectors are solid state instruments, and measure X-rays using scintillation in a crystal. A sketch of one HEXTE detector is shown in Figure 3.8a. The main scintillation crystals of HEXTE are sodium-iodine crystals, doped with thallium (NaI(Tl)) which are only 0.3175 cm thick. X-rays striking the detector interact primarily with the iodine and can ionize one atom in the crystal. The freed electron induces light-generating modes in the detector, the so-called “scintillation”. The intensity of this pulse of light is proportional to the energy of the X-ray photon and allows for an energy resolution comparable to that of the PCA. The NaI(Tl) crystals are glued to secondary sodium-doped caesium-iodine (CsI(Na)) scintillation crystals, which are 12.715 cm thick and act as an anti-coincidence shielding as well as a guide for the scintillation from the NaI crystals to the photomultiplier tubes. The two crystals glued together make up kind of a sandwich, hence the name “phoswich” detector. In the photomultiplier tube, the scintillation is converted into electrons and thereby amplified.

The scintillations happen very fast, so that a time resolution of up to 7.6 μs is achievable. Processing in the electronics, however, takes longer, typically around 20 μs, but even longer for events caused by high-energetic charged particles. During processing no other events can be registered correctly, so that this time is “dead-time”. In HEXTE the dead-

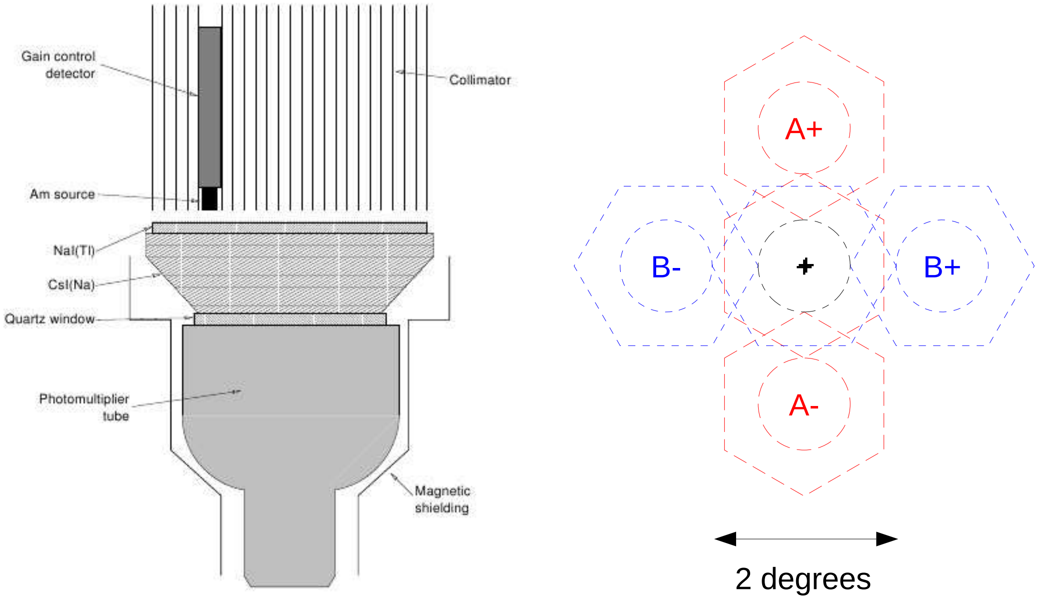

(a) Sketch **(b)** Rocking pattern

Figure 3.8.: (a) Sketch of one detector of HEXTE. Picture credit: Wilms (1998) **(b)** Field of views of HEXTE at different positions due to the rocking. Cluster A is moving perpendicular to Cluster B and thereby covering a different background region, while the on-source position is nearly identical. Picture credit: Swank et al. (1995)

time can be as high as 40%, due to the large flux of high energtic particles of up to 150 cts s^{-1}.

Similar to the PCA, HEXTE is also not an imaging instrument and uses collimators providing a FoV of 1°. They consist mainly of lead and are mounted in a hexagonal honeycomb structure.

The most distinctive feature of HEXTE is its “rocking mechanism”. The two clusters are mounted on separate axes, allowing each cluster to move up to 3° away from its nominal pointing position in both directions. While the zero positions of both clusters are co-aligned (and co-aligned with the PCA), the off-center positions are perpendicular to each other, allowing for four independent off-source measurements (Figure 3.8b). These measurements are made to provide an almost real-time background estimate. Usually HEXTE rocks every 16 s, with the clusters alternately pointing at the source. The near real-time measurement of the background is necessary, as HEXTE is a background dominated instrument.

The constant rocking of the clusters brings a huge strain on the mechanics and electronics of the instrument. Nonetheless, HEXTE rocked back and forth almost without problems for more than 10 years. In 2006 October cluster A showed glitches in its rocking mechanism and was therefore fixed in the on-source position since then. Cluster B continued rocking until 2010 April when it was frozen in the off-source position due to similar issues. In this configuration HEXTE is still taking valuable data from Clus-

Figure 3.9.: Picture of the three SSCs of ASM, standing on their mutual rotation axis. The camera in the middle looks to the top and parallel to the rotation axis, while the cameras on the side look to the left of the picture.

ter A but the background of these measurements has to be extrapolated from Cluster B data. Even though both clusters are very similar this estimate can up-to-date only be done within 10% accuracy (Pottschmidt et al., 2006). Work is ongoing to improve this estimate (R. E. Rothschild, 2011, priv. comm.).

3.3.3 All Sky Monitor (ASM)

WHAT is happening in the highly variable X-ray sky and where is it happening? This question is what the ASM tries to answer. As a monitoring instrument its goal is to cover the whole sky regularly and alert observers on outbursts of transient sources or other quickly variable events. It was built at the Kavli Institute for Astrophysics and Space Research at the *Massachusetts Institute of Technology (MIT)*. The following description is mainly taken from Levine et al. (1996). To achieve its monitoring goals ASM boasts a very large FoV of $6^\circ \times 90^\circ$ for each of its three cameras. These cameras are mounted askew to each other on one rotation axis, around which they move every 90 s to cover a different region of the sky. A photograph of the ASM is shown in Figure 3.9. The rotations are pre-planned in such a way as to minimize Earth and Sun occultation. The cameras are so-called *Scanning Shadow Cameras (SSCs)*, that means, they take pictures of the X-ray sky by viewing the sky with a position sensitive detector through an one dimensional coded-mask (see Section 3.1.3). The detectors of the ASM are position-sensitive proportional counters, which, like the PCA, use xenon as the main detector gas. The ASM cameras are sensitive for soft X-rays between 1.5–12 keV and provide a rough energy resolution by dividing the events into three channels, $A \approx 1.5$–3 keV, $B \approx 3$–5 keV, and $C \approx 5$–12 keV. With a relatively small maximal effective area of $\sim 90\,\mathrm{cm}^{-2}$ at 5 keV ASM detects only the brightest events, but as many transient sources can have outbursts of several hundreds of *mCrab* this is still enough to fulfill its purpose. A given source on the sky is on average monitored every 90 min, if not occulted or to close to the sun, leading to a good long-time coverage. With the long live-span of *RXTE* and the almost flawless functionality of ASM it now provides a huge data base of lightcurves of >15 years length, enabling long-term studies of many sources and thus providing important scientific output. Up to date lightcurves can be found on the ASM websites at MIT.[3]

3.4 *Suzaku*

PLANNED as a mission which would extremely enhance our view of the X-ray universe by allowing broad band coverage and very high spectral resolution, ASTRO-E was launched in February 2000 by the *Japan Aerospace eXploration Agency (JAXA)*. Unfortunately the launching rocket failed and the satellite never achieved the inteded orbit (Inoue, 2003). A recovery mission, called ASTRO-E2, using slightly enhanced versions of the same instruments was then successfully launched in July 2005. It was renamed to *Suzaku* after it started to operate within specifications. *Suzaku* was not spared from problems, however, and the main instrument, the *X-ray Spectrometer (XRS)* lost its essential cooling gas in only a few weeks (Mitsuda et al., 2007). The XRS was a micro-strip calorimeter which would have been able to measure spectra with unprecedented resolution and throughput between 0.2 –10 keV[4]. Complementary to *Chandra* with its very good imaging capabilities and to *XMM-Newton* with its huge collection area, *Suzaku* still provides a valuable addition to the X-ray satellite family. The two remaining instruments are the *X-ray Imaging Spectrometer (XIS)*, which provides CCD-resolution spectra and images in the soft X-rays and the *Hard X-ray Detector (HXD)*, an collimated, non-imaging detector for X-rays above 10 keV (Mitsuda et al., 2007). These instruments are described in more detail in the following Sections. Figure 3.10 shows an artistic view of *Suzaku* in space.

3.4.1 X-ray Imaging Spectrometer (XIS)

AFTER the failure of XRS the XIS is the only instrument sensitive between 0.2–10 keV aboard *Suzaku* (Koyama et al., 2007). The XIS consists of four independent CCDs installed behind separate Wolter telescopes. Three of the CCDs are front-illuminated, the last one is back-illuminated in order to have higher sensitivity at the very low energies. All four XIS chips have 1024×1024 pixels with a pixel size of $24\,\mu$m squared. Together with the Wolter telescope this allows for a FoV of $18'$ and an angular resolution of $\sim 1.8'$. Similar to the EPICs of *XMM-Newton* the XISs can be operated in different modes, allowing for higher time resolutions at the cost of smaller FoVs. XIS filters the CCD data on board, sending only the information of 5×5 or 3×3 pixels centered around the event center to the ground. These editing modes depend on source flux and available telemetry and show identical spectra, according to the *Suzaku* technical description[5]. The energy resolution at 6 keV is with $E/\Delta E = 50$ typical for CCDs. The background of the XIS is very low, thanks to the LEO of *Suzaku* and the instrumental design. Therefore XIS is able

---

[3] `http://xte.mit.edu/asmlc/ASM.html`

[4] as the XRS ceased operation so quickly, no refereed publication on the instrument exists. The information concerning the instrument was obtained from `http://heasarc.nasa.gov/docs/suzaku/about/xrs_inst.html` on May 30, 2011

[5] `ftp://legacy.gsfc.nasa.gov/suzaku/nra_info/suzaku_td.pdf` (Version October 2010)

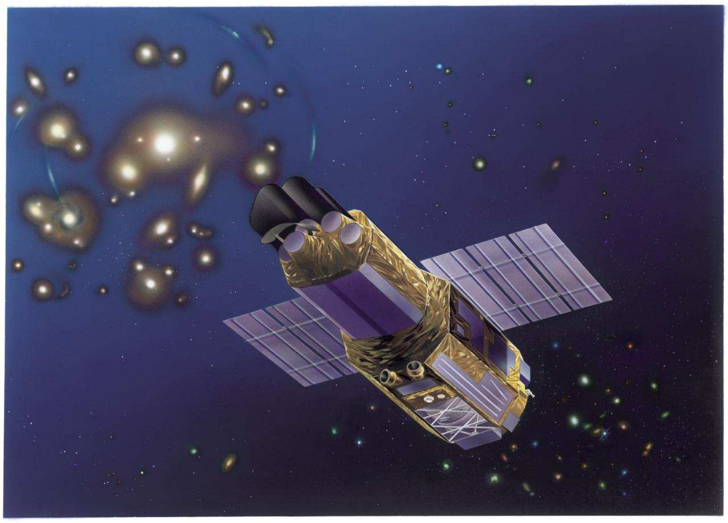

Figure 3.10.: Artistic view of *Suzaku* in space. On the top left the Wolter telescopes for the XRT and the XISs are visible. HXD is located on the back-side of the satellite and not visible in this view. Picture credit: JAXA

to investigate very faint sources and weak spectral features which vanish in the noise of other detectors. In November 2006 one of the XIS detectors showed a large increase of counts, probably due to some charge leakage. Since then, this detector is unusable, and the XIS is reduced to only 3 CCDs.[6]

3.4.2 Hard X-ray Detector (HXD)

BUILT in a similar way as the HEXTE of *RXTE*, the HXD is a collimated detector sensitive between 10–600 keV. It is described in detail in Takahashi et al. (2007) and the following Section gives only a brief summary of the most important aspects of the instrument. To cover this broad energy band it consists of two detectors: photons with energies between 10–70 keV are detected in the *PIN* diodes, while the harder X-rays are measured with the *Gadolinium Silicate (GSO)* phoswich scintillators. PIN consists of 16 2 mm thick silicon diodes with an edge length of 21.5 mm, which register X-rays by separating the produced charge cloud in the crystal. Unlike to CCDs each pixel is separately connected to a read-out node, so that it is not necessary to shift charges through the crystal. The energy of the detected photon is measured by the amount of charge produced by the event, which leads to an energy resolution of $E/\Delta E \approx 11$.

Each PIN diode is placed onto one scintillation crystal of GSO, which are each 5 mm thick. These scintillators measure all X-ray events which pass through the PIN diodes, up to an energy of ~600 keV. The diodes and scintillators are grouped together into arrays of 2×2 pixels, which are each connected to one *Bismuth Germanate (BGO)* scintillator crystal, as anti-coincidence shielding. As in HEXTE the BGO additionally guides the scintillation

---

[6] see `http://heasarc.nasa.gov/docs/suzaku/news/xis2.html`

light to the *Photo-Multiplier Tubes (PMTs)*, in which the events are registered. HXD uses 16 separate PMTs. The collimator of HXD also consists of BGO scintillators with separate PMTs, to provide an 5-sided anti-coincidence shielding for the GSO. The scintillation signals for BGO and GSO have different characteristic rise times, so that they can be easily discriminated in the PMT signal. The BGO collimator restricts the FoV of HXD to $4.5^\circ \times 4.5^\circ$. This relatively large FoV, is still mostly sufficient for hard X-rays above 100 keV, as bright sources in this energy range are sparsely scattered in the sky. To reduce the FoV at lower energies, the pixels of the 2×2 arrays are separated by passive bronze collimators, which are opaque for X-rays below $\sim$100 keV. These collimators provide a FoV of only $34'$ square for the PIN detector, much smaller than comparable detectors like *RXTE*/HEXTE. GSO has an energy resolution of $E/\Delta E \approx 7$ at 300 keV but this resolution is strongly depending on the energy and is better for higher energies.

Thanks to the quick read-out possibilities of the PIN diodes and the GSO scintillations, HXD can take data with up to 61 μs time resolution.

3.5 *INTEGRAL*

IMAGING the hard X-ray sky is a difficult, yet important task. Images allow the analysis of extended sources and regions with closely clustered sources, tasks which cannot be adequately done with collimator instruments like *RXTE*. We have seen in Section 3.1.2 that soft X-rays can be focused using the grazing incidence technique, but that the grazing incidence angle depends strongly on the energy of the X-ray photon. With increasing energy this angle gets more and more shallow and for X-rays above 20 keV Wolter telescopes are not easily workable any more. *INTEGRAL* was built to investigate and image the hard X-rays and soft γ-ray sky at energies much higher than 20 keV, necessitating the use of a different imaging technology (Winkler et al., 2003). For *INTEGRAL* the coded-mask technique was chosen, which is explained in detail in Section 3.1.3. Due to the coded mask, *INTEGRAL* observations are usually split into many short pointings, each pointing a few degrees differently. In this way a more robust image reconstruction can be achieved. For telemetry the data are split into packages called *Science Windows (ScWs)*, often coinciding with the pointings. On average, one ScW has an exposure time around 2 ksec (Jensen et al., 2003).

Figure 3.11 shows an artist impression of the satellite, where the two main instruments and the two monitoring instruments can be clearly seen: the square mask of the *Imager on Board the INTEGRAL Satellite (IBIS)*, the large round mask of the *Spectrometer on INTEGRAL (SPI)*, the two smaller round masks of the *Joint European X-ray Monitor (JEM-X)* and to the left the baffle of the *Optical Monitoring Camera (OMC)*. Figure 3.12 shows a photograph of *INTEGRAL* before launch.

INTEGRAL was launched on 2002 October 17 into an highly eccentric orbit, reaching out as far as 153 000 km at apogee. The long orbital period of 3 days allows for long, almost uninterrupted monitoring observations.

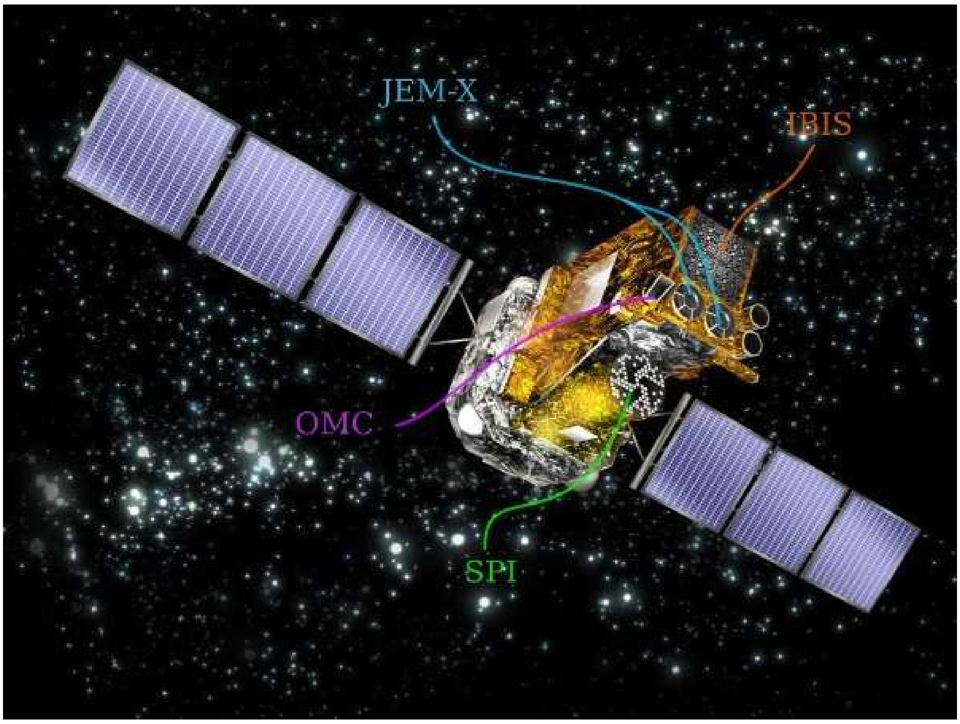

Figure 3.11.: Artist impression of *INTEGRAL* in orbit. The four scientific instruments are labeled. Picture modified after ESA.

3.5.1 Imager on Board the *INTEGRAL* Satellite (IBIS)

While all instruments of *INTEGRAL* are imaging instruments, the Imager on Board the *INTEGRAL* Satellite (IBIS) is the only one dedicated to high spatial resolution in hard X-rays. With an angular resolution of up to $12'$ it can separate sources even in regions as crowded as the Galactic Center (Ubertini et al., 2003). The point source location accuracy can even be as high as $20''$ for a source detected with very high significance ($\sigma \approx 100$, Bélanger, 2011).

IBIS has two detectors below its mask, the *INTEGRAL Soft Gamma-Ray Imager (ISGRI)* for the softer radiation between 15 keV – 1 MeV (Lebrun et al., 2003) and the *PIxelated Caesium Iodide (CsI) Telescope (PICsIT)* (Labanti et al., 2003) for the harder radiation between 170 keV –10 MeV. ISGRI consist of 128 × 128 Cadmium Telluride (CdTe) semiconductor pixels, each 4 mm edge-to-edge, adding up to a total detector area of $2600\,\mathrm{cm}^2$. Unlike in a CCD all pixels are connected individually to the read-out electronics, rendering shifting of charges through the crystal unnecessary. This kind of wiring makes the read-out also very fast, allowing for a high time resolution. However, the time resolution is somewhat reduced due to dead time in the pixels and telemetry limits so that the maximal achievable timing accuracy is around $90\,\mu$s (Lebrun et al., 2003). Of course obtaining lightcurves with this time resolution is only possible in very special cases like bright *Gamma-Ray Bursts (GRBs)*, because for every time bin a separate deconvolution of the shadowgram is necessary, which can only be done with enough photons.

Figure 3.12.: Picture of *INTEGRAL* during testing at ESTEC. The coded masks are hidden behind golden foils. Note the persons in the back for size comparison. Picture credit: ESA

Below ISGRI PICsIT, a pixelated detector consisting of 4096 scintillator Caesium Iodide (CsI) crystals is located. PICsIT is sensitive to high energy photons, which did not deposit their energy in the thin ISGRI layer, but passed right through it. Similar to HEXTE it uses scintillation, i.e., the production of short flashes of light in the crystal, to measure time and energy of the incident photon. The background due to cosmic ray induced events is very high in PICsIT, so that telemetry limits do not allow to transfer every event to the ground, contrary to ISGRI (Stephen et al., 2003). The detector is therefore usually operated in the “histogram” mode, where events are binned into 8 energy channels with a 16 ms time resolution before being transfered to the ground (Bélanger, 2011). The usable spectral resolution is thereby reduced from intrinsic an $E/\Delta E \approx 10$ to $E/\Delta E \approx 2.4$ at 1 MeV.

3.5.2 Spectrometer on *INTEGRAL* (SPI)

As the name suggests the main focus of the Spectrometer on *INTEGRAL* (SPI) is not high resolution imaging, but high resolution spectrometry in the hard X-rays and soft γ-rays. At these energies gratings, which provide the best spectral resolution at soft X-rays, are not usable anymore. SPI therefore needs a detector with an intrinsic very high energy resolution. A suitable detector was found by using a camera built from 19 very pure *Germanium detectors (GeD)* (Vedrenne et al., 2003). Germanium is a semi-conductor, detecting photons by their ionization power and the subsequent separation of electrons and holes, just like in each pixel in a CCD or in ISGRI. With this detector a spectral resolution of up to $E/\Delta E = 450$ at 1.33 MeV is possible (Roques et al., 2003). Photons of these energies have a very high penetrating power of matter, so that each pixel of SPI is 3.2×6.9 cm large (accounting for a mass per pixel of almost 1 kg!) in order to effectively stop γ-rays. The germanium detectors are cooled to 85 K by four Stirling cycle radiators to provide optimal working conditions (Vedrenne et al., 2003). Imaging capabilities of SPI are obtained through a coded mask of 3 cm thick tungsten pixels. These provide an opacity of only 90% in the energy range of SPI, but thicker and heavier pixels were discarded due to cost and pay-load reasons. The pixels have a similar size as the detector pixels and the complete mask allows for a 46° FoV with 2.5° angular resolution (Attié et al., 2003). SPI's scientific goals are, among others, the investigation of nucleosynthesis by finding evidence for and mapping radioactive γ-ray lines and the 511 keV positron annihilation line. At 511 keV the effective area of SPI is only $\sim$150 cm^2 (Attié et al., 2003), so that long observations are necessary to perform the scientific goals. In order to measure the spectra from neutron stars in X-ray binaries unrealistic long observations are necessary, as most of these sources are very weak at energies above 200 keV. Therefore no SPI data are used in this thesis.

3.5.3 JEM-X and OMC

FORMALLY only monitoring instruments, the Joint European X-ray Monitor (JEM-X) and the Optical Monitoring Camera (OMC) are valuable scientific instruments on their own. They complement IBIS and SPI to softer energies and thereby help to provide a more complete picture of a given astronomical object. JEM-X consists of two almost identical telescopes, as shown in Figure 3.11. It detects X-rays between 3–35 keV using a micro-strip gas chamber in each telescope (Lund et al., 2003). Micro-strip gas chambers are similar to proportional counters like the PCA (see Section 3.3.1), but contain much finer anode strips, lithographed on a base material (see also Knoll, 2010). This way, they have higher spatial and temporal resolution, but usually a smaller detector volume. The detector volume of JEM-X is filled with a mixture of 90% xenon as detector gas and 10% methane as quenching gas and amounts to an effective area of 500 cm^2 (Lund et al., 2003). The time resolution of JEM-X is 122 μs and its energy resolution is $E/\Delta E \approx 7.6$ at 10 keV. To obtain images, JEM-X uses a coded mask, just like its big siblings IBIS and SPI. Only 25% of the mask of JEM-X is transparent, the rest is covered by 0.5 mm thick tungsten pixels. The small open fraction was chosen to increase image resolution in crowded fields and also to save telemetry. The masks of the two JEM-X telescopes use the same pattern, but are rotated by 180° with respect to each other, to improve image reconstruction. Overall an angular resolution of $3'$ is achieved, over a FoV of only 7.5° (Lund et al., 2003). This comparatively small FoV is the biggest drawback of JEM-X, as it means that a given source might not be seen by JEM-X even though it can be perfectly observed with IBIS and SPI.

The OMC is the only non X-ray scientific telescope aboard *INTEGRAL* and the only one using lenses as optics for imaging. It provides photometry between 500–600 nm over a $\sim$5° FoV (Mas-Hesse et al., 2003). The detector is a CCD chip with 1024×1024 pixels. The OMC is only a very small supporting instrument. Nonetheless in recent years there have been a number of publications using explicitly OMC data, mainly thanks to the large data archive and source monitoring since the launch of *INTEGRAL* (see, e.g., Caballero-García et al., 2006; Zasche, 2011).

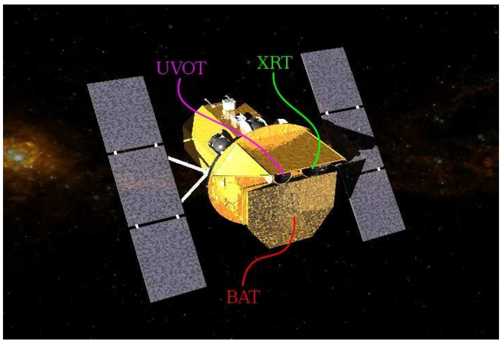

Figure 3.13.: Artist's impression of *Swift* in space. The instruments are labeled and the coded mask of BAT is seen clearly. The optical and X-ray telescope are half hidden below the sun screen. Picture modified after NASA.

3.6 *Swift*

EVER since the discovery of GRBs in the late 1960s and early 1970s (Klebesadel et al., 1973) astronomers were puzzled by their origin. Being the most luminous events in the universe and sometimes being extremely far away[7], understanding their behavior better will give insight in the early universe and the physics at extreme regimes of relativity. GRBs are transient events, typically lasting only a few seconds in γ-rays and showing a quickly fainting afterglow in X-rays, which can be visible for some 1000 sec. GRBs seem to be distributed over the whole sky with a rate of only a few hundred per year. To detect and observe GRBs the sky needs to be monitored continuously and a quick response time to observe the afterglow is necessary. *Swift* was built as a medium explorer mission by the *National Aeronautics and Space Administration (NASA)* in order to fulfill this task, i.e., to find GRBs and to be able to quickly observe them in X-rays and optical (Gehrels et al., 2004). In order to find GRBs *Swift* is a equipped with a large monitoring instrument, the Burst Alert Telescope (BAT). BAT data is analyzed on board the satellite, and if a GRB is detected, the satellite slews automatically to its position in order to obtain detailed spectral information using the X-ray Telescope (XRT) and the UV/Optical Telescope (UVOT). With up to 0.7°/s *Swift* slews very quickly, allowing to catch a larger part of the X-ray afterglow (Gehrels et al., 2004). An artistic view of the satellite and its instruments is shown in Figure 3.13. *Swift* was launched on November 20, 2004 into a LEO, comparable to the orbit of *RXTE*.[8]

3.6.1 Burst Alert Telescope (BAT)

JUST like the ASM aboard *RXTE* the Burst Alert Telescope (BAT) monitors large portions of the sky and can quickly alert scientists about any flares or bursts. It is a coded mask instrument, comparable to *INTEGRAL*/ISGRI with 32768 semi-conductor pixels as detector. Each pixel is connected individually to the read-out electronics, so that the loss of individual pixels does not greatly hamper the instrument's performance. The detector is sensitive between 15–150 keV with a maximal energy resolution of $E/\Delta E = 20$ (Barthelmy et al., 2005). The coded-mask is 50% opaque and uses a completely random

---

[7] the most distant GRB measured up to date was at a redshift of $z \approx 8.1$ (Salvaterra et al., 2009)

[8] see the NASA/GSFC *Swift* website: `http://swift.gsfc.nasa.gov/docs/swift/about_swift/`

pattern of pixels. With 2.7 m^2 it is much larger than the detector, increasing the FoV overall to $100° \times 60°$ (Barthelmy et al., 2005). A picture of the mask before it was installed on the satellite is shown in Figure 3.5a. The BAT team maintains a website[9] providing an overview over the X-ray flux of many known sources, which are of course also monitored by the instrument. The lightcurves on this website are a major source for astronomers working on galactic sources like transient HMXBs to monitor the source behavior and schedule observations accordingly. The time resolution for these survey lightcurves is $\sim$5 min. If BAT detects a GRB it leaves the survey mode and switches into a photon-by-photon mode, in which events are tagged with 200 μs time resolution (Barthelmy et al., 2005).

3.6.2 XRT and UVOT

Not only for GRBs but also for many other transient events, like outbursts of known galactic sources, the fast response time of *Swift* is very useful to obtain almost real-time spectra and fluxes. These outbursts are very bright in X-rays, so that the *X-ray Telescope (XRT)* is the instrument of choice for quick observations. XRT is a Wolter type I telescope with a MOS-CCD chip as detector. The Wolter optics provide an effective area of only 110 cm^2 and a FoV of $23.5'$ with $\sim 15''$ resolution (Burrows et al., 2000). Sky positions can be measured with an accuracy of $5''$, important for the identification of GRBs in the optical. Sensitive between 0.2–10 keV the detector of XRT has an energy resolution of $E/\Delta E \approx 50$. In one word, XRT is a close copy of *XMM-Newton*/MOS with an optics just a little worse. The *UV/Optical Telescope (UVOT)* is also an almost exact copy of the *XMM-Newton*/OM. The reader is therefore referred to Section 3.2.3 and Roming et al. (2004) or Boyd et al. (2005) for information about UVOT.

3.7 Future Missions

Most X-ray observatories are designed to operate in the hostile space environment for 3–5 years. The last addition to the X-ray satellite family, *Suzaku*, was launched in 2005, already 6 years ago. Obviously the currently available instruments have already outlived their expected lifetime. Even though it is true that most of them are still perfectly functional, there is no guarantee that this will stay so for much longer. Missions like *RXTE*, which is operating now for almost 16 years are the rare exception. While we might live in the “golden age” of X-ray astronomy at the moment, new missions and instruments are necessary to provide X-ray observations in the future and to increase our knowledge of the X-ray sky. The Dr. Karl Remeis-Observatory and ECAP are playing a major role in the development of two such future missions, the eROSITA detector aboard SRG and *Athena*. They will be described briefly in the next Sections.

---

[9] `http://swift.gsfc.nasa.gov/docs/swift/results/transients/`

3.7.1 eROSITA

All-Sky-Monitors, like ASM and BAT, regularly observe the whole X-ray sky and monitor the behavior of many sources. They are, however, limited in sensitivity, as they aim to cover the whole sky more or less simultaneously to provide quick alerts on transient events. eROSITA will use a different observation strategy, scanning the sky in slices piece by piece, so that after roughly half a year the whole sky has been observed. These observations will add up to an average of 2–3 ksec exposure of every part of the sky in ~4 years. The scientific goal are not variable sources, but millions of faint and almost constant background sources, mainly *Active Galactic Nuclei (AGN)*. Observations of clusters of these galaxies and the hot gas in between will allow to refine cosmology models and help in the search for Dark Energy. To that end eROSITA will use seven identical Wolter telescopes, which provide the necessary sensitivity and angular resolution between 0.5–10 keV to accomplish the goals in roughly 4 years (Cappelluti et al., 2010). A sketch of the layout of the instrument is shown in Figure 3.14a. Behind each telescope an enhanced version of the EPIC-pn CCD camera is installed, using smaller pixels and faster readout (Meidinger et al., 2010). The seven instruments are completely independent from each other, providing a high redundancy. The data from the whole X-ray sky gathered during that time will also contain information on many galactic sources, like X-ray binaries. The long time behavior of these sources in the soft X-rays can thereby be studied in a detail not possible with the monitoring instruments available to date. eROSITA is scheduled for launch in 2013 on board the Russian satellite Spectrum-X-Gamma (SRG) (Cappelluti et al., 2010). More and up-to-date information can be found on the eROSITA websites of *Max-Planck-Institut für extraterrestrische Physik (MPE)*.[10]

3.7.2 *Athena*

After a long political discussion and monetary cuts, *Athena* is the most recent project to push X-ray astronomy to new limits. It is the successor of the European project *X-Ray Evolving Universe Spectrometer Mission (XEUS)* and the worldwide *International X-ray Observatory (IXO)*, which both had to be stopped for financial reasons. *Athena* is a European led project, and scheduled for launch in the mid 2020s. It is still in a planning phase, but in the most probable scenario it will use two separate Wolter telescopes, each with ~$0.5\,\mathrm{m}^{-2}$ effective area at 1 keV. To increase the effective area the telescopes will be not only made out of concentring, circular shells, but additional shell segments will be placed around the main mirrors to better fill the circular satellite base (see Figure 3.14b on the following page). Because of the visual similarity this layout is called “Owl”-layout. Behind one telescope the *Wide-Field Imager (WFI)* will be installed, behind the other the *X-ray Microcalorimeter Spectrometer (XMS)*.

The XMS will be the first of its kind to be installed on a satellite and used for X-ray astronomy. It will allow for unprecedented imaging spectral resolution, i.e., it is a pixelized sensor in which each pixel has very good spectral resolution. A detailed description of this kind of detector is presented in Knoll (2010) and de Korte et al. (2004), of which

---

[10] `http://www.mpe.mpg.de/erosita/`

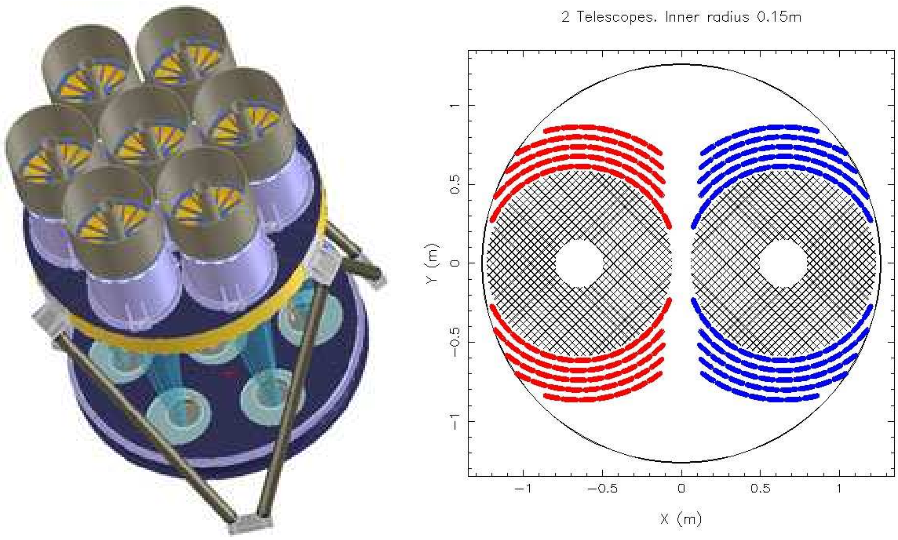

(a) eROSITA sketch **(b)** The mirror configuration of *Athena*

Figure 3.14.: **(a)** Sketch of the eROSITA instrument. **(b)** Mirror layout of the two X-ray telescopes of *Athena*. The cross-hatched areas represent concentric, circular mirror shells. Picture credit: MPE

only a short summary will be given here. A microcalorimeter was installed on *Suzaku* and is planned to be launched with *ASTRO-H* (Mitsuda et al., 2010), however, the XMS will be the first one to use a superconducting detector, as described below.

In XMS the spectral information of the absorbed photon is obtained by measuring a small temperature change in the absorber due to the energy deployed by the X-ray photon. The temperature change is directly proportional to the X-ray energy, so that a very good spectral resolution can be obtained if the temperature change can be measured accurately. The most sensitive device to measure temperature changes are superconductors close to their transition temperature between superconducting and normally conducting state. These devices are called *Transition Edge Sensors (TESs)*, as they are operating on the transition edge of the superconductor. To measure a temperature change in the absorber due to a single X-ray photon, the absorber must be kept at temperatures close to 0 K to reduce its heat capacity. For XMS temperatures between 70–90 mK are devised, which is in the transition region of a Ti/Au bilayer superconductor (den Herder et al., 2010). It becomes clear that operating such a detector is a formidable task on the ground, yet alone in the hostile space environment, as extreme temperature stability is required. The developer team of XMS at *Netherlands Institute for Space Research (SRON)* is nonetheless confident that the detector will work within the specified goals for *Athena*. The absorber and superconductor of the detector are only weakly coupled to a thermal reservoir providing the low temperatures, so that the temperature change induced by the absorbed X-ray photon can be registered in the TES. Through this weak thermal link it takes a few milliseconds to restore the temperature in the detector, during which time no further photons can be accurately registered. The restore time can be improved in TES systems, when the superconductor is biased with a constant voltage, heating the detector to be exactly on its transition edge. The temperature change induced by the photon will immediately increase the resistance in the TES, thereby reducing the heating current and effectively cooling the chip again. Through this method the achievable time resolution can be reduced to $\gtrsim 50\mu$s.

The energy resolution of the XMS will be around 3 eV at 6 keV ($E/\Delta E = 2000$), determined by the internal energy resolution of the sensor of ~1.7 eV and the additional readout noise (den Herder et al., 2010). The FoV is planned ot be $2.4'$ with 32 by 32 pixels, each viewing $4.5''$ of the sky. Please note that these numbers are still subject to change, depending on technical feasibility and scientific requirements. For the latest news see the MPE webpages.[11]

3.8 Data analysis methods

In the above Sections different satellites with many different detectors and technologies were described. But they all have something in common: they all detect photons which traveled a long way from a cosmic source, passed through some kind of optics and produced a physical reaction in the detector. The results of this reaction (mostly electrons or ions) are measured and digitized, before they are transferred back to Earth. The observer is provided with the digitized data, usually in a format called *Flexible Image Transfer System (FITS)* and tries to reconstruct the real, incident source flux as a function of photon energy. This description of the source is called its "spectrum" (Section 3.8.1). The measured events are also tagged with a time stamp, so that the observer knows when which photon was measured. The available time resolution depends on the satellite and its operational mode (see Table 3.1). This time dependent description of the source flux is called a "lightcurve". The variability in the lightcurve from, e.g., shot noise or the rotation of a neutron star, holds a wealth of information about the source. Only through the combination of a good description of the spectrum as well as a thorough understanding of the lightcurve the whole picture of the X-ray source can become visible.

Most data presented in this thesis were analyzed using the *Interactive Spectral Interpretation System (ISIS)*[12], a powerful, extensible, and free software package made for the analysis of high-resolution X-ray data (Noble & Nowak, 2008, and references therein). ISIS tasks can be automated and scripted, so that large amounts of data can be easily handled. The software package can also be enhanced by functions and packages, based on the interpreter language *S-Lang*[13] (see, e.g., Ayers, 1996). Most notably an interface, created by John E. Davis, between ISIS and *xfig* exists[14], which allows to easily make complex and informative vector graphics. Most plots in this thesis are produced through this package.

---

[11] `http://www.mpe.mpg.de/athena/resources.php?lang=en`

[12] `http://space.mit.edu/cxc/isis/`

[13] `http://www.jedsoft.org/slang/`

[14] `http://www.jedsoft.org/fun/slxfig/`

3.8.1 Spectral analysis

DESCRIBING the real spectrum cannot be a straightforward process, as so many things happened to the information stored in the photons before the observer can start working with the data. Most importantly the measured events cannot be uniquely returned to the original photon flux. Instead he or she has to find a model, which describes the measured data best (and which also should have some physical relevance). To do so, the observer assumes that the source emits photons exactly following his or her model and then simulates the way the incident photons have to take before they are measured. By changing model parameters the observer tries to minimize the difference between the simulation and the measured values. Usually the difference is given in the form of a χ^2 value, but other fit statics are also possible, especially when dealing with low count rates. A thorough mathematical description of this process can be found in Davis (2001), but here I will try to be more descriptive, following Nowak (2010), Wilms (2008), and Hanke (2007).

The process of model fitting can be put into one formula, the foundation of all X-ray spectroscopy:

$$C(h) = \mathrm{d}t \int_0^\infty R(h,E)A(E)S(E)\,\mathrm{d}E + B(h) \tag{3.13}$$

Here we assume that the source flux $S(E)$ is time invariant over the exposure time $\mathrm{d}t$. It is given in photons $\mathrm{s}^{-1}\,\mathrm{cm}^{-2}\,\mathrm{keV}^{-1}$. $R(h,E)$ is the unit-less *Redistribution Matrix Function (RMF)*, describing with which probability an incoming photon with energy E is measured in the data channel h. The channels h are bins on an energy grid H, describing which channel corresponds roughly to which energy range. Ideally there is a linear correlation between E and h, but most often physics prevents that. As one example the escape peaks in the detector material shall be named. Here, an incoming photon might hit an L-shell electron of the detector material and thereby stimulating a Kα fluorescence line. The energy of this line is lost to the original event, and the event will be registered with its original energy lowered by the energy of the fluorescence line. The response of *XMM-Newton*/EPIC-pn and *RXTE*/PCA to a bright but narrow Gaussian at 6.4 keV are shown in Figure 3.15.

With careful calibration the probability of this effect as well as of many other effects can be put in numbers and transfered into the RMF. Still only a probability can be given which means that the function $E \to h$ is not injective and that $R(h,E)$ is not analytically reversible. The *Ancillary Response Function (ARF)* $A(E)$ describes the effective area of the instrument as function of energy in units of $\mathrm{cm}^2\,\mathrm{photon}^{-1}$. X-rays with different energies are focused differently or react with the detector material in different ways. These differences are stored in the ARF. The effective area depends also on the off-axis angle, so that for each source it has to be calculated again, taking the exact optical path for the X-rays from the source location into account. For Wolter telescopes this is usually a relative smooth function of off-axis angle, but in coded mask telescopes the ARF can also change strongly for small differences of the source position. The last factor influencing the measured counts $C(h)$ are the background counts $B(h)$. $B(h)$ describes

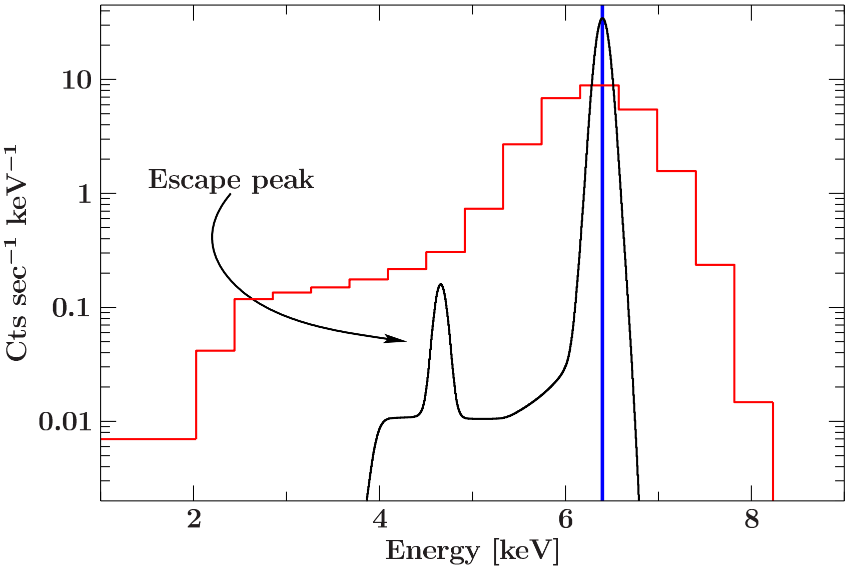

Figure 3.15.: Theoretically measured counts in *XMM-Newton*/EPIC-pn (black) and *RXTE*/PCA (red), if the incident spectrum is a very narrow Gauss centered at 6.4 keV (blue). Clearly visible is the escape peak in the *XMM-Newton* data as well as the broadening of the narrow Gauss in both detectors. The energy binning shown originates from the binning of the RMF and, in the case of EPIC-pn, overestimates the real energy resolution.

only the instrumental background and non X-ray background, like noise, cosmic rays, etc. The X-ray background is measured together with the source flux, and therefore part of $S(E)$.

The response of a detector is not fixed forever, but will change over time. In space the detector will be constantly bombarded by high energetic particles, influencing and degrading its capabilities to measure X-rays. Also micro-meteorites can irreversibly damage the detector. The instrument teams of the satellites are therefore updating the RMF and ARF once in a while, depending on the rate of change and distribute the new versions through the *Guest Observer Facilities (GOFs)*. To measure the changes in the detector observations of sources which are believed to be constant (so-called standard candles), most notably the *Crab nebula*, are preformed. Finding standard candles is complicated in the highly variable X-ray sky, for example, Wilson-Hodge et al. (2011) have shown recently that the Crab nebula might not be as stable as commonly believed. *XMM-Newton* therefore uses a whole set of calibration sources with different luminosities, among them many SNRs and AGN which are among the most steady X-ray sources known (Kirsch et al., 2005). Energy and flux calibration of the operational X-ray telescopes is still a somewhat tricky task, which needs thorough understanding of the detector and the influence of the environment.

Besides the long-term changes in RMF and ARF the response of the detector can change on timescales as short as several seconds. In CCD detectors for example, the *Charge Transfer Inefficency (CTI)* can change as a function of incident X-ray flux. When shifting the electrons through the chip to the read-out node, some of them can be lost to impurities in the detector, decreasing the measured charge and thereby directly decreasing the measured energy of the X-ray photon. The farther away from the read-out node the photon was registered, the stronger this effect is. This effect can be taken care of in the calibration. If a bright source is observed, many charge clouds need to be shifted through the chip in quick order. In this case it is possible that some of the impurities are still filled with electrons when the next shift occurs, so that much less electrons get lost on the way. This effect means that the CTI is decreasing as a function of X-ray flux, and that a higher charge as expected is measured. If the standard CTI correction is applied, the measured photon energies will be systematically shifted to higher values. This effect is very complicated to be put into the calibration, as it depends on the operation mode of the chip, the X-ray flux, and the X-ray spectrum. It is also mostly negligible, but for bright sources with prominent lines like GX 301−2 (Chapter 6) this effect can play an important role. The spectral analysis software package ISIS allows to correct for these energy shifts by allowing for a "gainshift" kernel. This kernel rebins the model counts after folding it through the response to an shifted energy grid H_shift, according to

$$H_\text{shift} = H_\text{orig}/a - b \tag{3.14}$$

This shift in the energy grid means that for the slope $a > 1$ the model components appear at a higher energy as without the gainshift (see also Hanke, 2011). Applying the kernel to the energy grid of the evaluated model and not before is important, as the RMF and ARF can change strongly around absorption edges in the mirrors or the detector. Changing the model energies before folding through the response would therefore result in incorrect fluxes. For CTI correction only the slope a is relevant, changing the energy grid usually on the order of below 2%.

Only when the RMF and ARF, as well as the background and the gainshift, are accurately known and correctly calibrated can the incident source spectrum $S(E)$ reconstructed from the measured data $C(h)$ by comparing the model folded through the response $M(h)$ to it. But even then, $C(h)$ will only be a coarse representation of $S(E)$ and different physical models $M(E)$ might describe the data equally well. It is then the task of the observer to find the physically most sensible and most robust model.

3.8.2 Timing analysis

Light curves, showing the source flux as a function of time, are usually highly variable. In neutron star X-ray binaries the two most important periodic variations are the movement of the neutron star around its companion and the rotation of the neutron star itself.[15] As described in Section 2.3 X-rays are produced and emitted only in a very small region close to the neutron star surface, so that the rotation of the compact objects gives rise to a periodically pulsating X-ray flux. By measuring this "pulse period" and following

---

[15] other periodicities, like the precession period of an accretion disk (as seen, e.g., in Her X-1, Staubert et al., 2009) or quasi-periodic oscillations seen in black hole binaries (see, e.g., Uttley et al., 2011) will not be discussed here, as they do not play a major role for the systems under investigation.

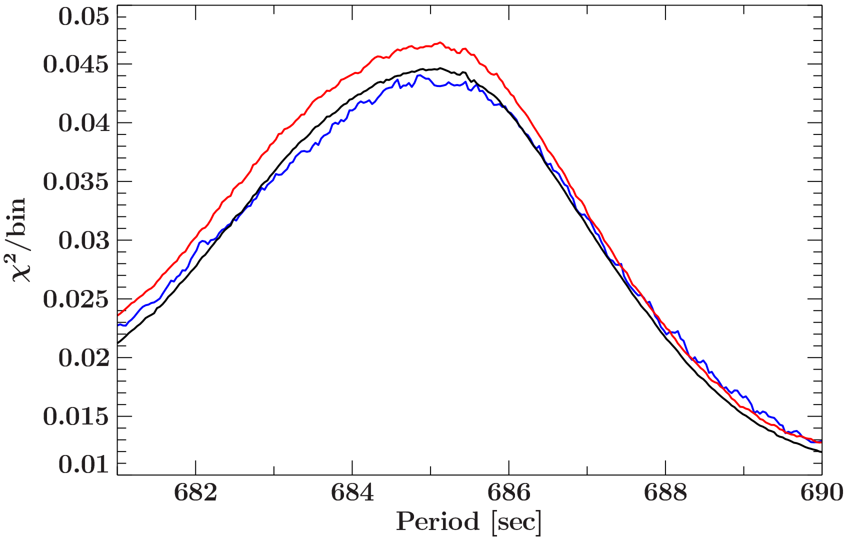

Figure 3.16.: Epochfolding result of *XMM-Newton* GX 301−2 data, as presented in Chapter 6. The black curve shows the result from the complete data set, the red one with 30% and the blue one with 60% of the data removed at random. Units on the y-axis are given in χ^2 per time bin of the lightcurve, as the three lightcurves had different lengths.

its evolution with time the transfer of angular momentum on the neutron star can be investigated. To measure it, a *Fast Fourier Transformation (FFT)* of the light curve from the time to the frequency domain can be made. The resulting *Power Spectral Density (PSD)* will show peaks at the pulse period and its harmonics. Fourier transformation is ideally suited for sinusoidal pulse shapes, but requires equally sampled data and can be computationally intensive. A simpler method to search for arbitrarily shaped pulses and the corresponding periods directly in the time domain is the so-called "epoch-folding method" (Leahy et al., 1983; Schwarzenberg-Czerny, 1989). A description of this method and its complications can be found in Kühnel (2011). In brief, the method is based on dividing the light curve by time into parts of equal length P_{test} and then summing up all these parts and binning them by phase. This results in a "pulse profile". If the test period P_{test} represents a prominent period in the data, the pulse profile will show clear variation with phase. If P_{test} is not found in the data, the pulse profile will be rather flat. By performing this calculation for many test periods around the expected period P and measuring the variance with a suitable estimator, e.g., the χ^2 value, the correct period can be found. Obviously the method can only be applied on lightcurves of sufficient length ($T \gtrsim 20P$) and of sufficient fine binning ($t_{\text{res}} \lesssim P/10$). It does depend only weakly on the sampling of the lightcurve and periods can be found even if long gaps in the lightcurve are present, as long as the period did not change significantly during that time (see Figure 3.16).

The orbital period of the binary system will induce a shift on the measured pulse period, caused by the Doppler effect. The period will appear shorter while the neutron star is moving towards us, and longer when it is receding. This shift will have the same periodicity as the orbit of the neutron star. The period shifts will appear as a skewed sinusoidal, depending on the eccentricity and the viewing angle of the system. Consequently, measuring the period shifts is a direct way to obtain the orbital parameters of the system. These parameters can then be used to infer on the distance between the neutron star and its optical companion, as well as its mass by solving the *Kepler equations*.

These regular period changes are in accreting sources superimposed by more random changes, which can have significant contributions up to the second ($\partial^2 t$) or third order ($\partial^3 t$). They result from the transfer of angular momentum from the accreted material. In wind accreting sources the pulse period evolution is expected to show a random walk like behavior, as the wind randomly transfers angular momentum onto the source (Ghosh & Lamb, 1979b). In sources with a stable accretion disk a long-term spin-up or spin-down trend is predicted, as the disk can continuously transfer angular momentum onto the compact object. Bright X-ray flares are often accompanied by very strong changes in the pulse period, clearly because the matter responsible for the flare carries angular momentum. From monitoring the pulse period evolution of HMXBs we can thereby infer on the accretion mode and compare the findings with theoretical models. Only through a precise measurement of the pulse period the correct pulse profile can be calculated and the correct physical interpretations be drawn (see also Section 2.3.3).

Nun sieh mal an! Ei ei!
Am Himmel stehn drei Sterne;
Vor Kurzem standen da nur zwei.
Nun wüßt ich gar zu gerne
Was Näheres über die Ferne,
Denn etwas stimmt mir nicht dabei.

(Joachim Ringelnatz)

4

The symbiosis of 3A 1954+319

During observations of Cyg X-1 in 2008 November another bright source appeared in the FoV of *INTEGRAL*/ISGRI. It was quickly identified as the binary system 3A 1954+319, which had not been observed with *INTEGRAL* at such luminosities before. The discovery triggered detailed investigation due to two very specific qualities: first, it belongs to a very small group of LMXBs, the so-called *Symbiotic X-ray Binaries (SyXBs)*, in which a neutron star orbits an M-giant. Second, it shows a very long pulse period of ∼5.3 h, longer than any other binary known.[1] The source shows strong flaring activity with irregular large outbursts. During these outbursts the spin period decreases dramatically as shown in the following Sections. How these outbursts are triggered and why the spin period is changing so quickly are two of the most crucial questions in the investigation of SyXBs. If these questions can be answered through theoretical calculations and observational evidence, the evolution of these rare objects can be uncovered.

In the following analysis data from *INTEGRAL* are presented and the evolution of the pulse period between 2005 and 2010 is tracked. As the theoretical understanding of SyXBs is still under development different models which could explain the observed behavior are briefly discussed. This Chapter is taken, partly verbatim, from a conference proceeding for the 8th *INTEGRAL* Workshop "The Restless Gamma-ray Universe" held in Dublin, Ireland from September 27 to 30, 2010 (Fürst et al., 2011b) and from an article accepted in the "Astrophysical Journal" (Marcu et al., 2011). The spectral analysis of the source was mainly done by D. Marcu at the *Goddard Space Flight Center (GSFC)*, while the timing analysis was done by myself. The physical interpretation was done jointly and in large parts performed during my stay at GSFC. I will use the "we"-style, common to scientific publications, throughout this Chapter. The Chapter is structured in a way often found in journal articles and starts with an introduction to the source in Section 4.1. In Section 4.2 the timing analysis is presented, followed by the spectral analysis in Section 4.3. Finally in Section 4.4 the results are discussed and a short outlook is given.

---

[1] There is only one slower neutron star known, the pulsar in the SNR RCW 103 with a period of ∼6.67 h (De Luca et al., 2006).

4.1 Introduction

While most LMXBs have close orbits and accretion takes place via Roche lobe overflow, SyXBs usually have wide orbits, comparable to HMXBs. And just like HMXBs they are wind accretors (Masetti et al., 2006). The wind and accretion mechanism of HMXBs and their early type companions are well studied (see, e.g., Nagase et al., 1986; Mauche et al., 2008), but much less is known about systems with late type companions. Only seven SyXBs are clearly identified today (Nespoli et al., 2009) and only a few of them, such as GX 1+4 or 4U 1700+24, have already been studied in detail in X-rays.[2] GX 1+4 is a very bright, persistent but variable source and has become the prototype SyXB. Since the mid 1980s, it has shown a strong spin-down trend, the strength of which seems to be related to its luminosity (Ferrigno et al., 2007; González-Galán et al., 2011). To explain this spin-down trend within the framework of standard accretion theory, magnetic fields in the excess of 10^{13} G are necessary (Cui & Smith, 2004). Similar properties have also been observed in 3A 1954+319, namely a highly variable flux and a strongly changing pulse period. 3A 1954+319 is overall dimmer than GX 1+4 and has as of today been studied much less. Much is still to be learned about these systems and the properties of the wind and the accretion mechanism. Being easily observable in X-rays SyXBs provide an unique opportunity for studying the wind properties of late type stars, via X-ray variations of the emission lines and absorption column (see, e.g., Tiengo et al., 2005).

The name "symbiotic X-ray binary" is drawn from an analogy to "symbiotic stars" consisting of a white dwarf and a late-type companion. These systems were named after their optical spectra in which both components, the hot white dwarf and the cold companion, are seen. Such features are not seen in SyXBs, as the neutron star is invisible in the optical. Only investigations in X-rays can therefore reveal the behavior of the neutron star.

3A 1954+319 was detected in the late 1970s with *Uhuru* and *Ariel V* (Forman et al., 1978; Warwick et al., 1981). Tweedy et al. (1989) analyzed *Ginga* data and found a hard X-ray spectrum as well as strong intensity variations on short timescales. They proposed that the system could be a HMXB. No more detailed studies were performed until Masetti et al. (2006) identified the companion as the M4-5 III star USNO-A2.0 1200-13816030 using an accurate *Chandra* position. Figure 4.1 shows an optical image of the region, in which the companion is clearly visible with a magnitude of ~10.7 mag. This identification placed the system in the group of SyXBs.

After 3A 1954+319 was established as a member of the very small class of SyXBs, more investigations were carried out. Mattana et al. (2006) presented the first broad-band spectrum of the source, using *INTEGRAL* and the Italian *"Beppo" Satellite per Astronomia X (BeppoSAX)*. These authors found that an absorbed cutoff powerlaw, with a pho-

---

[2] Most recently Smith et al. (2011) have discovered another neutron star with an M-class companion, namely XTE J1743−363, increasing the number of SyXBs to 8. For IGR J16393−4643, listed as another SyXB by Nespoli et al. (2009), Pearlman et al. (2011) show that the X-ray mass function argues against this classification.

Figure 4.1.: L-UVB composite optical image of the counterpart of 3A 1954+319, taken with the 40 cm telescope of the Dr. Karl Remeis-Sternwarte, Bamberg on 2011, May 30 using an SBIG STL-11000M CCD camera.

ton index $\Gamma \approx 1.1$, a folding energy $E_{\mathrm{fold}} \approx 17\,\mathrm{keV}$, and an equivalent hydrogen column $N_{\mathrm{H}} \approx 2.8 \times 10^{23}\,\mathrm{cm}^{-2}$ could describe the data well. These values are in agreement with values expected for an accreting neutron star. Further spectra were presented by Masetti et al. (2007), who showed that the spectrum can also be described with a thermal Comptonization model, when allowing for complex absorption to explain the data below 2 keV.

The rather featureless spectrum is contrasted by the very interesting timing behavior of 3A 1954+319. Corbet et al. (2006a) discovered a ~5 h period in *Swift*/BAT data. The period is much too short for the expected wide orbit of the system and is therefore most likely the spin period of the neutron star. No other significant periods have been found between 5×10^{-3} s and 3.5×10^{8} s (Corbet et al., 2006a; Corbet et al., 2008; Masetti et al., 2007). During an outburst in 2004/2005, Corbet et al. (2008) measured a strong decrease of the pulse period from 5.17 h to 5.09 h, resulting in a $\dot{P} = (2.6 \pm 0.2) \times 10^{-5}\,\mathrm{h\,h^{-1}}$. It is unlikely that this decrease in the period is due to a Doppler shift from the orbit of the binary system, as the mass function would then lead to unrealistically large values for the mass of the companion ($M_\star > 10^{6}\,\mathrm{M}_\odot$), assuming a canonical mass of $1.4\,\mathrm{M}_\odot$ for the neutron star.

According to standard disk accretion theory, strong changes in the rotational period of a neutron star are only possible if the neutron star is rotating close to its equilibrium pulse period (Ghosh & Lamb, 1979a; Ferrigno et al., 2007). An hour-long equilibrium period is only possible, if the magnetic field of the neutron star is on the order of $\sim 10^{15}$ G (Corbet et al., 2008). Magnetic fields of this strength are only known to exist in magnetars, a very young ($\sim 10^3$ yr) and rare type of neutron stars (see also Chapter 2). Due to the low mass nature of the system, the neutron star is likely rather old ($\sim 10^9$ yr) and even if the magnetic field was that strong originally it would now have decayed away (Haensel et al., 2007).

In 2008 November a strong outburst of 3A 1954+319 was serendipitously observed with *INTEGRAL*, obtaining high quality lightcurves and spectra, which are presented here. This was the first outburst after the one observed by *Swift*/BAT in 2004/2005 for which accurate pulse periods could be measured, thereby extending the pulse period monitoring of this source considerably.

4.2 Lightcurves and Timing

In the upper part of Figure 4.2 the long-term *Swift*/BAT lightcurve between 15–50 keV is shown. It is clearly seen that 3A 1954+319 shows irregular flaring with some flares being as bright as almost 100 mCrab and other phases where it falls below the detection limit of *Swift*/BAT. Most notable are the flaring episodes in 2005 and 2008. *Swift*/BAT data taken during the 2005 episode have been presented in Corbet et al. (2008). The short tickmarks above the lightcurve in Figure 4.2 mark times when 3A 1954+319 was in the FoV of *INTEGRAL*/ISGRI, with a pointing offset angle $\leq 10°$. Longer tickmarks mark observations where 3A 1954+319 was detected in ISGRI, with the standard significance criterion of the *Offline Scientific Analysis (OSA)*, `DETSIG` ≥ 6.

A dense sampling of *INTEGRAL* observations was obtained serendipitously during the flare in 2008 November when Key Programme observations of Cyg X-1 (PI J. Wilms) were performed. As seen in Figure 4.2 this flare was one of the brightest since the monitoring of *Swift*/BAT began, and had an average flux over the outburst of $\sim 8.6 \times 10^{-10}\,\mathrm{erg\,cm^{-2}\,s^{-1}}$ between 20–100 keV, i.e., $\sim$ 40 mCrab and a peak flux of more than 160 mCrab. In the following we concentrate on data from this outburst. We extracted ISGRI data using `ii_light`, as distributed with OSA 7.0, to obtain lightcurves with a time resolution of 100 s, in the energy bands 20–40 keV, 40–100 keV, and 20–100 keV. The resulting 20–100 keV lightcurve is shown in Figure 4.4. Even though 3A 1954+319 was in an overall bright state during that time the data show that the X-ray flux is still variable by a factor of $\sim$20. Using the epoch-folding technique (Leahy et al., 1983, see also Section 3.8.2), a period of $\sim$5.3 h is clearly detected in the data. Compared to the results by Corbet et al. (2008), the pulse period is significantly longer, i.e., the neutron star has spun down between 2005 and 2008 (see Figure 4.3a).

As Corbet et al. (2008) found a strong spin-up trend in the 2005 flare, we split the lightcurve into three equally long parts and searched in each one for the pulse period separately. We also found a clear spin-up trend in the data, with the pulse period decreasing from 5.34 h in the beginning of the outburst to 5.26 h in the end (Figure 4.3a and bottom panel of Figure 4.4). From this analysis we determined the pulse ephemeris

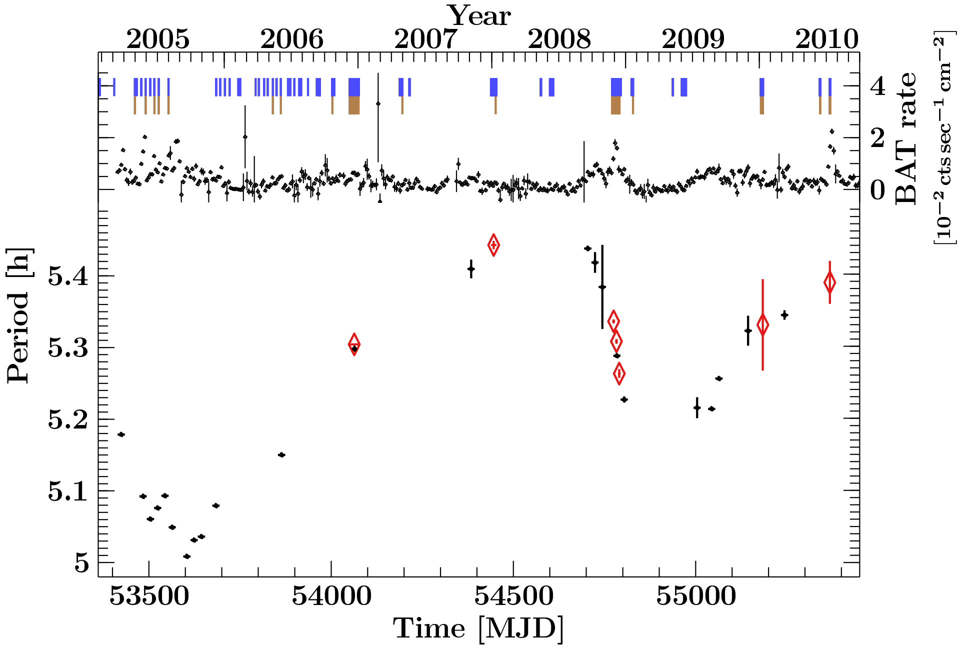

Figure 4.2.: The blue tickmarks on the top indicate times of *INTEGRAL* observations, the long brown ones indicate observations where 3A 1954+319 was detected. The data points below show the *Swift*/BAT lightcurve between 15–50 keV with 5 d resolution, using the righthand y-axis. The lower part of the figure shows the pulse period evolution, where black data points are obtained with BAT, and the red diamonds with *INTEGRAL*/ISGRI.

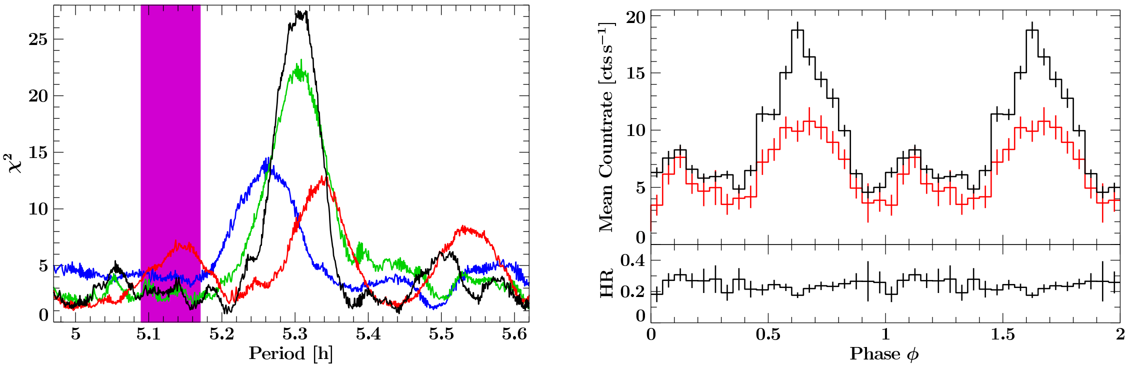

(a) Epoch folding results **(b)** Pulse profiles

Figure 4.3.: **(a)** Results of the epoch folding analysis, with the lightcurve split into three equally long parts, part 1 is shown in red, part 2 in green, and part 3 in blue. Additionally the overall result is shown in black and the range of the 2005 pulse period is marked in magenta. **(b)** *Top:* Pulse profile over the flare of 2008 in 20–40 keV (black) and 40–100 keV (red, multiplied by 3 for better visibility). *Bottom:* Hardness ratio between the two pulse profiles.

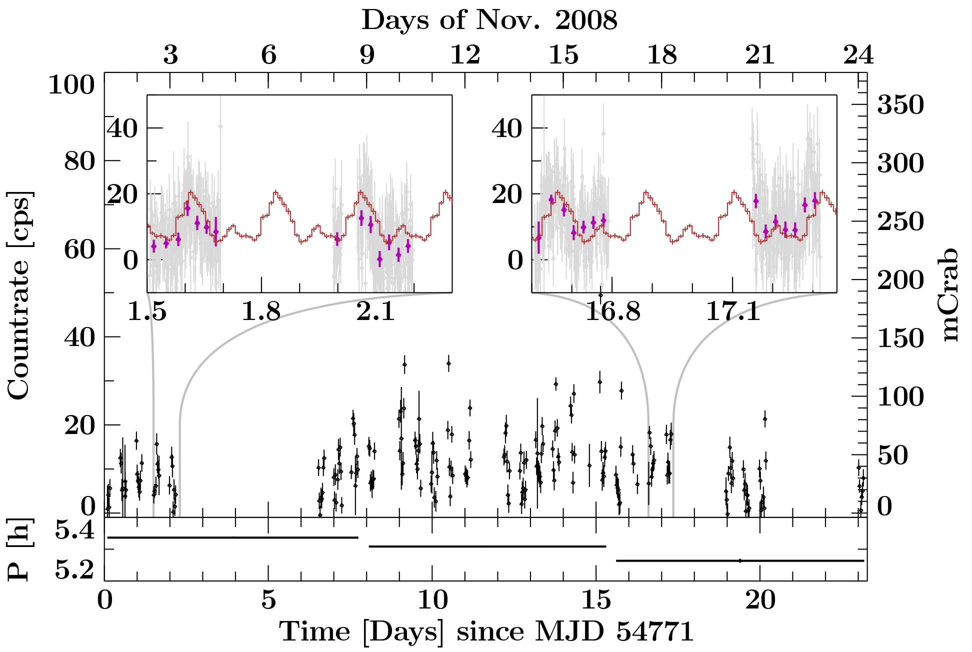

Figure 4.4.: *Top: INTEGRAL*/ISGRI 20–100 keV lightcurve in November 2008. The data were binned to ScW resolution (∼2 ksec). The insets show zooms and a more detailed lightcurve with 100 s resolution in gray. Overplotted in purple is the same data as in the ScW lightcurve and in red the average pulse profile. *Bottom:* Pulse periods obtained from the *INTEGRAL* data (see Figure 4.3a).

during the 2008 outburst to be: T_0 = MJD 54782.6897 (mean of observation), $P(T_0) = 5.3060 \pm 0.0007\,\mathrm{h}$, and $\dot{P}(T_0) = (-1.81 \pm 0.17) \times 10^{-4}\,\mathrm{h\,h^{-1}}$. Note that the spin-up trend is an order of magnitude larger than the one found by Corbet et al. (2008) in the 2005 outburst. We folded the lightcurve using that ephemeris and obtained the best quality pulse profile available for 3A 1954+319 to date. The profiles for the soft (S, 20–40 keV) and the hard (H, 40–100 keV) energy band are shown as a function of phase ϕ in Figure 4.3b. A comparison between the pulse profiles did show no significant change of the shape with energy, as can be seen in the hardness ratio H/S plotted in the lower panel of Figure 4.3b. Only around $\phi = 0.6$, the hardness ratio drops significantly compared to the average ratio, indicating a slightly different spectrum. Nonetheless, both profiles have a clear double peaked structure, with the peak between $0.4 \leq \phi \leq 0.9$ being clearly stronger than the one between $0.0 \leq \phi \leq 0.3$. Indications for this secondary peak have already been found by Corbet et al. (2008) in the *Swift*/BAT data below 50 keV, but its presence in the hard X-rays was not known before.

To check for consistency, we compared the pulse profile to the measured lightcurve. As seen in the insets of Figure 4.4 the pulse profile describes the lightcurve very well, in the beginning of the outburst as well as close to the end. This is the first time that the pulsed flux of 3A 1954+319 is directly visible in a lightcurve, revealing that it does not show large pulse-to-pulse variations.

In order to put our *INTEGRAL* results into perspective, we updated the *Swift*/BAT period analysis of 3A 1954+319, again using the epoch-folding technique. Using all publicly available *Swift*/BAT lightcurve data, local period determinations were performed for segments with 20 d duration each. Figure 4.2 shows all successful measurements, i.e., where a clear period could be found. As the *Swift*/BAT data are impaired by a low S/N, we also performed a period search in the other *INTEGRAL* ScWs in which 3A 1954+319 was detected. This search resulted in the addition of four more data points. Successful measurements were mainly obtained during times of extensive *INTEGRAL* coverage of the region. All data points, *Swift*/BAT and *INTEGRAL*/ISGRI, are shown in Figure 4.2. As can be clearly seen the measurements for both satellites agree very well. The pulse period is slowly decreasing during quiescence but increases strongly during prominent outbursts. This behavior had been proposed by Corbet et al. (2008), but our data clearly show it for the first time. Standard disk accretion theory predicts a similar behavior. The absolute values of the predicted spin change are, however, smaller than what we measure in 3A 1954+319 (Ghosh & Lamb, 1979a, see also Section 4.4).

4.3 Spectral analysis

Gaining knowledge about the accretion physics of a SyXB during a strong flare, which was additionally accompanied by a strong spin-up, has been made uniquely possible by the *INTEGRAL* observations. Due to the fact that the source is close to *INTEGRAL*/ISGRI's detection limit during pulse minimum, even in the bright flare, we created a spectrum of only the peak phase, i.e., $0.45 \leq \phi \leq 0.85$, in order to improve the S/N. As the hardness ratio did not show a significant phase dependence, we can assume that the spectrum is not strongly sensitive to the selected pulse phase and that the obtained spectrum is very similar to an overall phase averaged spectrum. The data were extracted for an offset angle $\leq 10°$ for ISGRI and $\leq 3°$ for JEM-X using OSA 9.0. The resulting ISGRI spectrum had an exposure of 85 ks and was modeled in the 20–80 keV range, while the JEM-X spectrum had an exposure of 9.8 ks, was extracted from mosaic images using `mosaic_spec`, and was modeled in the 3–30 keV range. Response and auxiliary response files were selected or created following the respective analysis documentation (Marcu et al., 2011).[3]

The spectrum could be well described by the thermal Comptonization model `compTT`, resulting in $\chi^2_{\text{red}} = 1.3$. The `compTT` model is based on theoretical calculations of Comptonization of soft photons in a plasma with a Maxwellian electron distribution, using a spherical geometry (Hua & Titarchuk, 1995; Titarchuk & Lyubarskij, 1995). The parameters of the best description were overall in agreement with the parameters found by Masetti et al. (2007) and are listed in Table 4.1. Furthermore, a cross-calibration factor of $0.84^{+0.12}_{-0.11}$ was applied to the JEM-X data. The remaining residuals are mainly due to known calibration issues of ISGRI (Grinberg et al., 2011). A slightly better description, with $\chi^2_{\text{red}} = 1.2$, was obtained when using a broken power law model. This phenomenological model consists of two power-laws with different photon indices Γ_1 and Γ_2, with

---

[3] See `http://www.isdc.unige.ch/integral/analysis#Documentation`

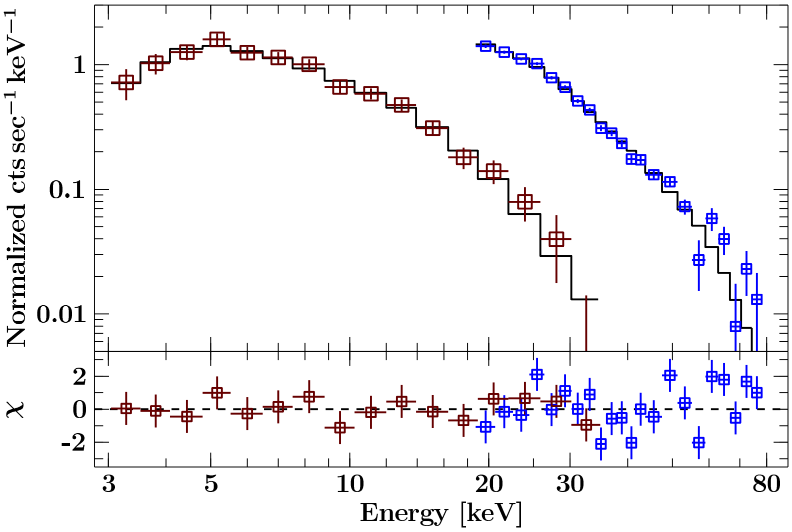

Figure 4.5.: *Top:* Spectrum taken with JEM-X (red) and ISGRI (blue), together with the best fit `compTT` model. *Bottom:* Residuals of the best fit. Uncertainties are given at the 90% confidence limit.

Table 4.1.: Best fit parameters of the `compTT` and the broken power law model. A_{bknpower} is given in ph keV^{-1} cm^{-2} s^{-1}.

`compTT`	N_{H} [cm^{-2}]	kT_0 [keV]	τ	kT_e [keV]	
	$(3.9^{+6.7}_{-2.2})\times10^{22}$	$0.9^{+0.4}_{-0.9}$	4.2 ± 0.7	$7.5^{+0.5}_{-0.4}$	
broken	N_{H} [cm^{-2}]	A_{bknpower}	Γ_1	Γ_2	E_{break} [keV]
powerlaw	$(7^{+6}_{-5})\times10^{22}$	$0.23^{+0.12}_{-0.08}$	$1.67^{+0.14}_{-0.13}$	$3.86^{+0.20}_{-0.18}$	27.4 ± 1.2

the change from one photon index to the other taking place at a specific break energy E_{break}. The best fit value of E_{break} is exactly at the energy range in which the ISGRI data start and the JEM-X data end. As the transfer between the two powerlaws is very abrupt at this energy, the model can be interpreted as Γ_1 describing only the JEM-X data, while Γ_2 describes only the ISGRI data. No cross-calibration constant was needed in that model. This means that the two very different indices mainly describe the different calibrations of the instruments, but do not add physical meaningful information. We note, however, that Γ_1 is very close to the powerlaw index found by Mattana et al. (2006) for the 0.6–300 keV spectrum. The best fit values of this model are also given in Table 4.1. Using a power-law with an exponential cutoff at high energies (`cutoffpl`) to describe the data, resulted in a clearly worse fit, contrary to the results by Mattana et al. (2006) for older data. We therefore base the discussion only on the `compTT` model.

We measured the absorbed flux of the spectrum to be 6.1×10^{-10} erg cm^{-2} s^{-1} and 12.1×10^{-10} erg cm^{-2} s^{-1}, between 2–10 keV and 10–100 keV, respectively. The unabsorbed flux was 7.6×10^{-10} erg cm^{-2} s^{-1} and 12.2×10^{-10} erg cm^{-2} s^{-1} for the same energy ranges. These fluxes are comparable to the brightest observation reported by Masetti et al. (2007).

4.4 Outlook & Conclusions

We have presented a timing and spectral analysis of *INTEGRAL* data of the large outburst of 3A 1954+319 in 2008 November. We confirm the unusually long spin period and measure a value of $\sim$5.3 h. In a model proposed by Ikhsanov (2007) for slowly rotating HMXBs these long periods can be explained without the need to invoke a very strong magnetic field. Instead the pulsar spins rapidly down in an early phase after its creation, in the so-called subsonic propeller regime. The resulting period is close to the equilibrium period of spherical accretion. For LMXBs, which have a longer life time, these slow periods are also explainable in standard accretion theory, as the neutron star will spin down as if isolated, as long as its companion has not yet evolved to a red giant (Mattana et al., 2006). This evolution is taking $\sim 10^9$ yr, enough time for the neutron star to reach periods of a few hours.

During the outburst we found that the pulse period is drastically increasing, with a spin-up rate as high as $\dot{P} = -1.8 \times 10^{-4}\,\mathrm{h\,h^{-1}}$. This rate is an order of magnitude higher than the one found by Corbet et al. (2008) for the 2005 outburst. As these authors already stated, a change of this magnitude cannot be due to the orbital motion, as it would lead to a mass-function for the companion of $> 5 \times 10^6 \mathrm{M}_\odot$. Different accretion models and geometries have been proposed to explain similar changes in other sources, including retrograde spinning accretion disks (Nelson et al., 1997) and a fall-back of matter during the propeller phase (Perna et al., 2006). A model which can very well explain both, the long pulse period and the magnitude of its changes, has been put forward by Shakura et al. (2011), providing a mechanism allowing for quasi-spherical accretion. In this model a subsonic settling regime occurs for X-ray luminosities below $\sim 3 \times 10^{36}\,\mathrm{erg\,s^{-1}}$, i.e., for luminosities consistent with those observed for 3A 1954+319. A shell of hot material forms around the magnetosphere which mediates the transfer of angular momentum to/from the neutron star by advection and viscous stress. The accretion rate is determined by the ability of the plasma to enter the magnetosphere. The equilibrium pulse period in this case is:

$$\frac{P_\mathrm{eq}}{10^3\,\mathrm{s}} \sim \left(\frac{B}{10^{12}\,\mathrm{G}}\right)^{12/11} \left(\frac{P_\mathrm{orbit}}{10\,\mathrm{d}}\right) \left(\frac{L_\mathrm{X}}{10^{36}\,\mathrm{erg\,s^{-1}}}\right)^{4/11} \left(\frac{v_\mathrm{wind}}{10^3\,\mathrm{km\,s^{-1}}}\right)^{4} \tag{4.1}$$

where P_orbit is the binary period and v_wind is the stellar wind velocity with respect to the neutron star. Reporting on population synthesis simulations for SyXBs based on this model, Postnov et al. (2011) showed that the 5.3 h pulse period of 3A 1954+319 can be well reproduced.

3A 1954+319 seems to show long spin-down episodes between major flares ($\dot{P} \sim 2.1 \times 10^{-5}\,\mathrm{h\,h^{-1}}$) which are reminiscent of the spin-down displayed by GX 1+4 since the early 1980s ($\dot{P} \sim 10^{-7}\,\mathrm{h\,h^{-1}}$, González-Galán et al., 2011). These authors showed that the quasi-spherical accretion model reproduces the correct sign and magnitude of the negative correlation between spin frequency change $\dot{\nu}$ and X-ray flux F_X observed during spin-down in this source ($-\dot{\nu} \propto F_\mathrm{X}^{3/7}$, González-Galán et al., 2011). For 3A 1954+319 such a detailed study of the $\dot{\nu}$-F_X-relationship is difficult, especially during spin-down since the low flux allowed for only a few $\dot{\nu}$ measurements (Figure 4.2).

On longer time scales we observe torque reversals and a positive $\dot{\nu}$-F_{X}-correlation exists comparing low (spin-down) and high flux (spin-up) episodes (Figure 4.2). This behavior is consistent with the behavior predicted by the quasi-spherical accretion model for higher accretion rates within the settling regime (see Figure 1 of Shakura et al., 2011).

The strong spin-up in 2008 translates to $\dot{P}/P = -0.9 \times 10^{-8}\,\mathrm{s}^{-1}$. While still high, the absolute value is of the same order of magnitude as the spin-down related $\dot{P}/P$ of $3.1 \times 10^{-8}\,\mathrm{s}^{-1}$ observed for the SyXB IGR J16358−4724 (Patel et al., 2007). The X-ray luminosity required to sustain such a spin-up in 3A 1954+319 in the equilibrium disk accretion case would be $\sim 5 \times 10^{36}\,\mathrm{erg\,s^{-1}}$ (Joss & Rappaport, 1984), whereas we measured a pulse peak value of $\sim 5.7 \times 10^{35}\,\mathrm{erg\,s^{-1}}$, again arguing against disk accretion.

The quasi-spherical model seems to be the most successful one in explaining the observed properties of 3A 1954+319. Still continued monitoring of the source is necessary to clarify possible models and check if the source continues to spin down during quiet phases, while strongly spinning up during flares.

The *INTEGRAL* pulse peak spectrum of 3A 1954+319 can be modelled with an optically thick Compton plasma, which is overall in agreement with the spectral parameters found by Masetti et al. (2007). It is also similar to the spectra found for other SyXBs, especially the one of GX 1+4 which can be described with $\tau = 6.80 \pm 0.15$ and $kT_e = 13.1 \pm 0.2\,\mathrm{keV}$ (Ferrigno et al., 2007). It is furthermore similar to spectra observed in some HMXBs, which can also be described by an optically thick Compton plasma (e.g., 1A 1118−61 Suchy et al., 2011b). In these sources the material is channeled along an accretion column following the strong magnetic field lines, in which the thick plasma produces the observed hard X-ray radiation. The similarity of the spectral shape is indicative for a similar configuration in 3A 1954+319. Many of the HMXBs also show CRSFs, due to their strong magnetic field on the order of $10^{12}\,\mathrm{G}$ (see Section 2.3.2). In the *INTEGRAL* spectrum we find no indication for other features besides the absorption and the continuum, especially no indication for a CRSF. If 3A 1954+319 would posses a magnetic field on the order of $10^{15}\,\mathrm{G}$, as necessary in the context of standard disk accretion theory, it is not surprising that we do not see a CRSF. Even the fundamental line energy would be at energies above 10 MeV, i.e., at energies where 3A 1954+319 is not detected by *INTEGRAL* anymore. For a more realistic magnetic field of $10^{12}\,\mathrm{G}$ the CRSF would be at more easily observable energies, but its non-detection does not rule out a magnetic field of this order. Theoretical calculations show that CRSFs can be filled or smeared out below the detection limit, depending on the geometry of the accretion column (Schönherr et al., 2007; Schwarm, 2010).

In order to explain the soft X-ray spectrum below 2 keV, an energy range not accessible to *INTEGRAL*, Masetti et al. (2007) needed a complex absorption column, including an ionized absorber. Additionally they included a thermal component from a hot, optically thin gas. Such a complex low energy spectrum has not been seen before in a SyXB. To get a better understanding of the behavior and physical state of the hot plasma, we obtained a 40 ksec *Chandra* observation (PI K. Pottschmidt). The data are being currently analyzed, but seem to indicate that the absorption is less complex than anticipated.

Furthermore a *Target of Opportunity (ToO)* observation of 3A 1954+319 was performed on October 7th, 2011 (PI S. Müller) with *XMM-Newton*. The expectation was to catch the source during a flare and so to get fruitful insight in the difference between phases of low and high accretion by comparing the data to the *Chandra* observation. However, the luminosity of 3A 1954+319 declined quickly after the *XMM-Newton* trigger and it was supposably not significantly brighter than during the *Chandra* observation. The *XMM-Newton* data were not yet available at the time of writing, but they will be very likely of equal or better quality as the *Chandra* data and also allow for a detailed study of the absorber and its ionization state.

> Watch the stars, and from them learn
> To the Master's honor all must turn,
> each in it's track, without a sound,
> forever tracing Newton's ground.
>
> *(Albert Einstein)*

5

4U 1909+07: an overlooked source

SINCE the early 1960s HMXBs have been studied in X-rays and for some famous sources, such as Vela X-1 or Cyg X-1, a lot of data exist, presented in numerous publications. However, among the ~170 known HMXBs (Bodaghee et al., 2011), the one or the other source has been overlooked by the community and only very few observations have been performed. The main reasons for this negligence are usually that the source is very dim or that it does not show any peculiar behavior, which would trigger further interest. The newly discovered IGR sources are strongly absorbed and have therefore not been detected in softer X-rays before (see Section 2). Contrary to these sources, 4U 1909+07 has already been discovered in the early 1970s with the *Uhuru* satellite (Giacconi et al., 1974). It has still been largely ignored and only two publications exist so far which deal exclusively with it (Wen et al., 2000; Levine et al., 2004). 4U 1909+07 is a persistent, yet highly variable source, located not far from the more famous 4U 1907+09. In states of high flux it can even outshine its neighbor, allowing for high quality observational data.

Through an extensive serendipitous coverage with *INTEGRAL*/ISGRI between 2003–2010, it is now possible to study the source in more detail. The main focus lies here on the evolution of the pulse period, allowing to distinguish between disk and wind accretion (Section 5.3). In contrast to 3A 1954+319, the pulse period evolution of 4U 1909+07 is more random and does not show a clear correlation with flux. Additionally I reanalyzed the 2003 *RXTE* data presented by Levine et al. (2004) thoroughly and performed phase resolved spectral analysis (Section 5.4). Through phase resolved analysis the contributions of the two accretion columns can be separated and analysed. The results of the spectral analysis were then compared to more recent *Suzaku* data.

This Chapter starts with an introduction to the source (Section 5.1), followed by details of the utilized data (Section 5.2). The scientific analysis is expounded in Sections 5.3 and 5.4. The Chapter is concluded by Section 5.5 in which the results are summarized and discussed. It is largely based on a publication in "Astronomy & Astrophysics" (Fürst et al., 2011a) and parts of this Chapter are taken almost verbatim from there. I therefore adopt the "we" style used in the paper.

5.1 Introduction

THE accreting neutron star X-ray binary 4U 1909+07 was first mentioned in the 3rd *Uhuru* catalog as 3U 1912+07 (Giacconi et al., 1974). The position and name of the source were later refined to 4U 1909+07 in the 4th *Uhuru* catalog (Forman et al., 1978). Many other X-ray missions, such as *OSO 7*, *Ariel 5*, and *EXOSAT*, among others, also detected a source close to these coordinates. Wen et al. (2000) showed that these detections are likely all originating from the same source and refer to it as X1908+075. We will use the name 4U 1909+07 to honor the original discovery.

Despite the regular detections, the first dedicated paper to discuss 4U 1909+07 was published in 2000 when Wen et al. (2000) analyzed *RXTE*/ASM data and found a stable period of 4.4 days. This period is interpreted as the orbital period of a binary system. Due to the high column density, however, no optical counterpart could be identified. In *RXTE*/PCA data, Levine et al. (2004) found a second, shorter period of ~605 s in the X-ray flux, explained as the pulse period of a slowly rotating neutron star. Using Doppler delay curves, they could also refine the binary orbit parameters and estimated the mass of the companion star to be $M_\star = 9\text{–}31\,\mathrm{M}_\odot$ and the radius of the companion star to be $R_\star \leq 22 R_\odot$, adopting a canonical mass of $1.4\,\mathrm{M}_\odot$ for the neutron star. One year later, Morel & Grosdidier (2005) detected an OB star in the near infrared at the location of the X-ray source, thus confirming that the system is a HMXB. The distance of the system was estimated to be 7 kpc (Morel & Grosdidier, 2005). Prior to this discovery, Levine et al. (2004) argued that the companion star could be a Wolf-Rayet star, which would make this system a possible progenitor system to a neutron star-black hole binary. With the identification of the companion, however, this intriguing possibility must be ruled out. The X-ray luminosity L of 4U 1909+07 is around $2.8 \times 10^{36}\,\mathrm{erg\,s^{-1}}$ for 4.5–200 keV. Although the system shows no eclipse, the X-ray flux is still strongly orbital phase dependent as shown by Levine et al. (2004). These authors analyzed orbital phase resolved PCA spectra and found that around orbital phase $\phi_\mathrm{orb} = 1$ the photoabsorption increases by a factor of 2 or more to $N_\mathrm{H} \geq 30 \times 10^{22}\,\mathrm{cm^{-2}}$, explaining the decreased ASM flux. This increase in absorption can be very well described by a spherical wind model and an inclination of $54° \leq i \leq 70°$, depending on the parameters of the wind model.

In archival *Chandra* data, Torrejón et al. (2010) found that the soft energy spectrum of 4U 1909+07 shows evidence for a Compton shoulder on the soft energy edge of the iron Kα line. This feature has so far only been seen in GX 301−2 but in no other HMXB with *Chandra* (see also Chapter 6). Torrejón et al. (2010) showed that the Compton shoulder is consistent with the X-ray source being embedded in a Compton thick medium, which is also responsible for the observed photo absorption. Additionally these authors have shown that 4U 1909+07 is an exception from the correlation between N_H and the equivalent width of the iron line found in most other HXMB (Inoue, 1985). The origin of this exception is still a mystery and can only be investigated with more high-resolution spectra.

Although there was renewed interest in 4U 1909+07 in recent years, many basic parameters are still unknown. For example, despite the detection of the pulse period, its evolu-

Table 5.1.: Observation log of the *RXTE*, *INTEGRAL*, and *Suzaku* data used. The dates given are the start dates of the respective observation.

Obs-ID / ScW	Start date	Exposure [ksec]
RXTE		
70083-01-01-00 – 70083-01-28-00	2002-12-23	105
70083-02-01-00 – 70083-02-19-00	2003-01-30	75
INTEGRAL		
004800030010 – 007000670010	2003-03-06	1352
017200250010 – 020200020010	2004-03-11	1192
022600370010 – 025900180010	2004-08-20	966
029100170010 – 032300140010	2005-03-02	340
036100020010 – 038300520010	2005-09-27	880
047600030010 – 050600200010	2006-09-06	397
053700090010 – 055600710010	2007-03-07	608
060100090010 – 062300080010	2007-09-15	967
072200090010 – 074300080010	2008-09-11	1072
078200500010 – 080400080010	2009-03-10	690
085200680010 – 086500270010	2009-10-03	236
Suzaku		
405073010	2010-11-02	22

tion with time was not yet studied. Additionally, no detailed analysis of the high energy spectrum above 30 keV has been carried out so far. *RXTE* data provide enough statistics to even perform pulse phase resolved spectroscopy, allowing us to obtain a better understanding of the accretion region and mechanism together with the energy dependence of the pulse profile.

5.2 Observations and data reduction

For our study of the 4U 1909+07 system we used all publicly available data from the X-ray missions *INTEGRAL* (Winkler et al., 2003, see also Section 3.5) and *RXTE* (Bradt et al., 1993, see also Section 3.3) as well as a pointed observation of *Suzaku* (Mitsuda et al., 2007, see also Section 3.4). Even though no pointed observations on 4U 1909+07 were performed with *INTEGRAL*, thanks to IBIS/ISGRI's large FoV of almost 30° × 30°, there are more than 9 Msec of off-axis data available. A huge part of these data were obtained in the core program on the Galactic Center performed in the early *Announcements of Opportunity (AOs)* (Winkler, 2001). Data from later AOs were mainly taken from the extended monitoring campaigns of the microquasars GRS 1915+105 (Rodriguez et al., 2008) and SS 433 (Krivosheyev et al., 2009). See Table 5.1 for a detailed

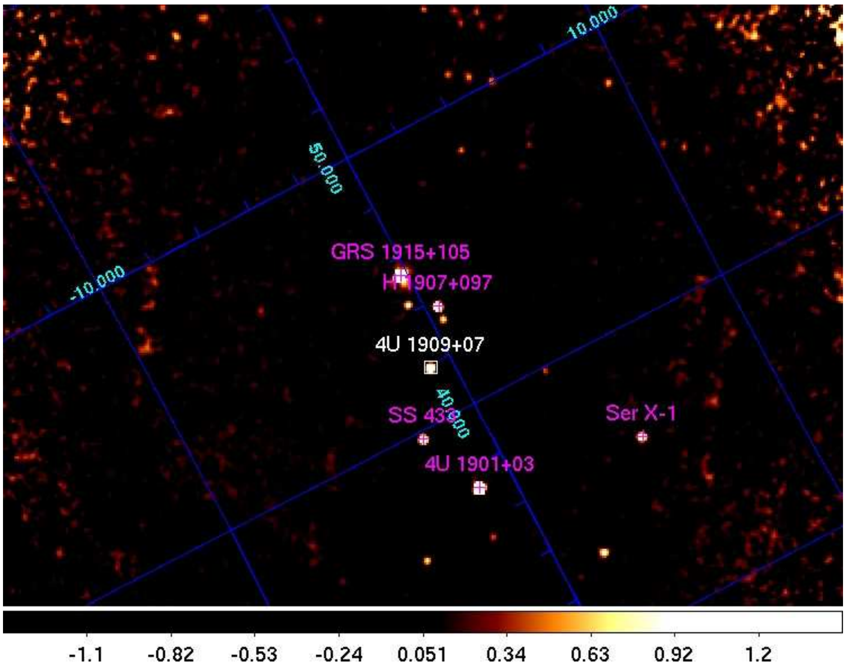

Figure 5.1.: ISGRI image of the X-ray sky in the 20–40 keV energy band, averaged over 353 ScWs from Revs. 51–68. Coordinates are in galactic longitude and latitude. To avoid confusion only the 6 brightest of overall 12 detected sources are labeled. In this image 4U 1909+07 is the fourth brightest source in the FoV after GRS 1915+105, the transient 4U 1901+03, and H 1907+097.

list of the data used. As the monitoring programs continued in 2010 and 2011 there are more data available, however, the coverage of 4U 1909+07 was either to sparse or the source to dim to be significantly detected.

An IBIS/ISGRI mosaic showing the hard X-ray sky in spring 2003 for the region around 4U 1909+07 is shown in Figure 5.1. Twelve sources with a detection significance `DETSIG`> 6 were found in that mosaic, with 4U 1909+07 being the fourth brightest source with ~2.6 cts s^{-1}. The data were extracted using the standard pipeline of the OSA 7.0 for spectra and images and using `ii_light` to obtain lightcurves with a higher temporal resolution. We extracted lightcurves with a resolution of 20 s as a trade-off between good S/N and good time resolution to measure the pulse period. We shifted the time to the barycenter of the solar system and corrected for the orbital motion of the neutron star, using the ephemeris given by Levine et al. (2004).

For phase resolved spectroscopy we used *RXTE* observations carried out in early 2003 which were previously analyzed by Levine et al. (2004). These data had a total exposure of 196 ksec. The only other *RXTE* data are from a shorter observation in 2000, which are not suitable for our study. Both major instruments of *RXTE*, PCA and HEXTE, were fully operational at the time of the observations in 2003. With a FoV of ~1° no other sources are visible to *RXTE*'s instrument while pointing at 4U 1909+07. *RXTE* data were reduced using the standard *HEASOFT* (v. 6.6), obtaining lightcurves of the PCA with 1 s resolution and pulse phase resolved spectra for PCA and HEXTE in the 4.5–150 keV energy range. The lightcurves were shifted to the barycenter of the solar system and corrected for the neutron star's orbital motion in the same way as the *INTEGRAL* data.

In order to take an even clearer look on the source we also obtained a 25 ksec *Suzaku* observation in AO5. With instruments being sensitive between 0.5–500 keV *Suzaku* provides a broad energy coverage and yet a good spectral resolution at the soft energies with the XIS CCD detectors. We extracted XIS, PIN, and GSO data using the standard pipeline as distributed with HEASOFT (v. 6.11). The FoV of the HXD is getting larger with increasing energy and above 100 keV source confusion with 4U 1907+09 is likely. We therefore ignored data above that energy. In GSO the source was not significantly detected so that we only present XIS data between 1.1–10 keV and PIN data between 15–90 keV here. No lightcurves were extracted.

5.3 Timing Analysis

So far only two measurements of the pulse period exist, taken in 2001 and 2003. At both times a period of $P \approx 604.7$ s was measured (Levine et al., 2004), indicating a stable pulse period. Such a stable period is very unlikely in an accreting system, as the accreted matter transfers angular momentum onto the neutron star, thereby changing its pulse period. Depending on the accretion type, i.e., if disk or wind accretion is dominant, different evolutions of the pulse period would be expected. For disk accretion a steady spin-up or spin-down trend is predicted, while for wind accretion random changes in the period should be measured (Ghosh & Lamb, 1979a). To distinguish between these accretion types, a monitoring of the pulse period over a long period of time is necessary. This monitoring is possible with the *INTEGRAL* data as presented in Section 5.3.1. In Section 5.3.2 the energy dependence of the pulse profile is studied, which has not been done in that detail before. We find that the profile changes strongly with energy, which lays the foundation for the study of the pulse phase resolved spectra presented in Section 5.4.2.

5.3.1 Pulse period evolution

Using the archival *INTEGRAL* data we could perform measurements of the pulse period between 2003 and 2008, largely extending the two *RXTE* measurements, and allowing to follow its evolution. We split the IBIS/ISGRI lightcurve into segments between 300 ksec and 800 ksec length, providing a good balance between accurate pulse period determination and temporal resolution, and used the epoch folding technique (Leahy, 1987, see also Section 3.8.2) with 24 phase bins to determine the pulse period for each of these segments individually.

The counting statistics in ISGRI smear out the single pulses in the lightcurve and make them invisible to the naked eye, see, e.g., Figure 5.2. Only after folding ≈500–1000 pulse periods, a stable pulse profile emerges which allows for a reliable determination of the pulse period. This profile is remarkably stable over our data set and not time dependent.

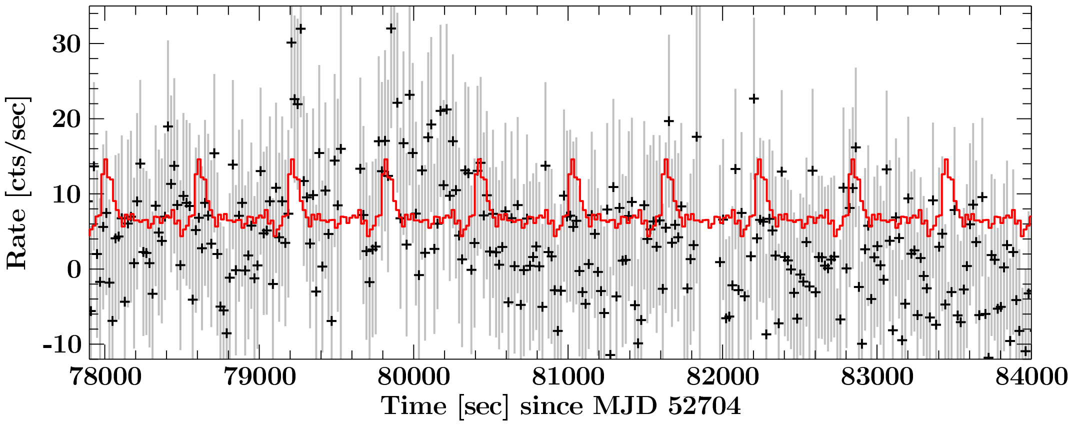

Figure 5.2.: Small part of the lightcurve in the 20–40 keV energy band as measured with IBIS/ISGRI. Data are shown as black stars with gray bars indicating the uncertainties. Time resolution is 20 s. The red curve shows the folded pulse profile over the whole data set.

The pulse period evolution between 2001 and 2007 is shown in Figure 5.3. The uncertainties of the pulse period were estimated by fitting a Gaussian distribution to the χ^2 distribution of the epoch folding results. The width of the best-fit Gaussian is a good estimate for the uncertainty of the measurement.

For the pulse period determination we assumed the pulse period to be constant during each individual segment. This assumption is justified, as the average $\dot{P}$ in our data between two consecutive data points is only $\dot{P} \approx 1.3 \times 10^{-8}\,\mathrm{s\,s^{-1}}$, very close to the value given by Levine et al. (2004). With the individual lightcurves being on average shorter than 50 days, the change between start and end of a lightcurve would be only $\Delta P \approx 0.05$ s. This change is on the order of the uncertainty we obtained from the Gaussian fits. Even when assuming a larger value of $\dot{P} = 1\,\mathrm{s\,yr^{-1}} = 3.17 \times 10^{-8}\,\mathrm{s\,s^{-1}}$ the obtained pulse profiles did not change significantly in shape, making a distinction impossible.

The circles in Figure 5.3 are *RXTE* measurements taken from Levine et al. (2004) and indicate an almost unchanged pulse period between January 2001 and December 2002. Starting with the *INTEGRAL* data, shown as crosses in Figure 5.3, a spin-up trend between March 2003 and September 2005 is visible from $P \approx 604.7$ s to $P \approx 603.9$ s. This trend is broken after September 2005 and the pulse period varies around $P = 604.0$ s. These changing trends make the overall behavior consistent with a random walk. To confirm this observation, we used the algorithm proposed by de Kool & Anzer (1993). It evaluates the relative change in pulse period over different time intervals δt between single measurements. To simplify the calculations the pulse period is converted to angular velocity $\omega = 2\pi/P$ and its change is expressed as the average value of absolute differences:

$$\delta\omega(\delta t) = \langle|\omega(t+\delta t) - \omega(t)|\rangle$$

Each pair $(\omega(t+\delta t), \omega(t))$ is additionally weighted in order to account for the data being grouped in clusters, see de Kool & Anzer (1993) for a detailed description. The results of

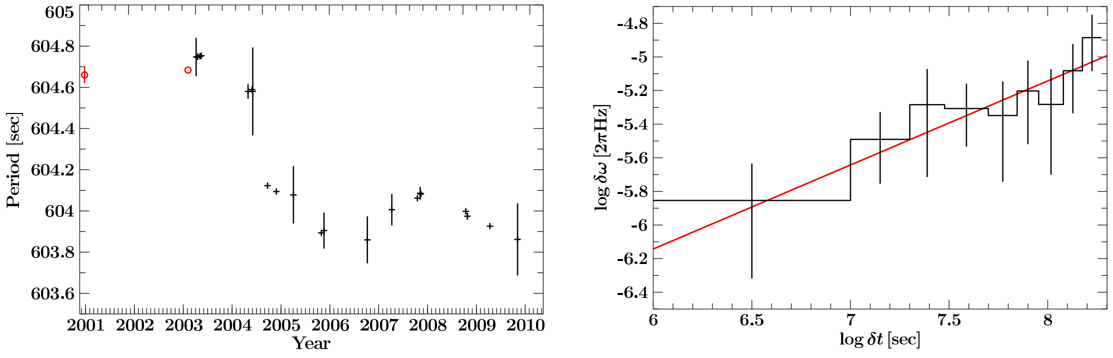

(a) Time-period space

(b) $\log \delta\omega - \log \delta t$ space

Figure 5.3.: (a): Evolution of the pulse period from 2001 until end of 2009. The historic *RXTE* data points of Levine et al. (2004) are shown as red circles, the new measurements obtained with *INTEGRAL* are shown as crosses. **(b)** Evolution in $\log \delta\omega - \log \delta t$ space, as proposed by de Kool & Anzer (1993). An ideal random walk process would show a slope of 0.5 in this plot. The data follow this slope closely, as shown by the red straight line with a slope of 0.5.

this analysis are shown in Figure 5.3b.

If the data are compatible with a random walk, they will follow a straight line with a slope of 0.5 in $\log \delta\omega - \log \delta t$ space. To test if the data are consistent with such a straight line, we fitted a function of the form

$$\log(\delta\omega(\delta t)) = A + 0.5 \cdot \log(\delta t)$$

where the free parameter A describes the noise level of the data. The best fit, superimposed in Figure 5.3b, has a Pearson's correlation coefficient of $r \approx 0.95$ and clearly shows that the pulse period evolution is consistent with a random walk. It gives a noise level of $A = -9.1$, fully in agreement with the expected value for a source with a luminosity of $L \approx 2.8 \times 10^{36}\,\mathrm{erg\,s^{-1}}$, assuming wind accretion with a turbulent accretion wake (de Kool & Anzer, 1993, and references therein).

The uncertainties of the $\delta\omega$-values are originating not only in the determination of the pulse period but also in the uneven and coarse sampling of the pulse period evolution. To estimate the latter effect, we chose a Monte Carlo approach and simulated 10 000 pulse period evolutions which followed a perfect random walk and sampled these with the same rate as the real data (see de Kool & Anzer, 1993). The standard deviation in each δt bin from these simulations gives an estimate of the uncertainty in each δt bin of the data and is roughly of the same order of magnitude as the uncertainties from the pulse period determination.

5.3.2 Pulse profiles

As Levine et al. (2004) showed in their Figure 2, the average pulse profile between 3.7–17 keV shows two distinct peaks, with the second one being slightly broader

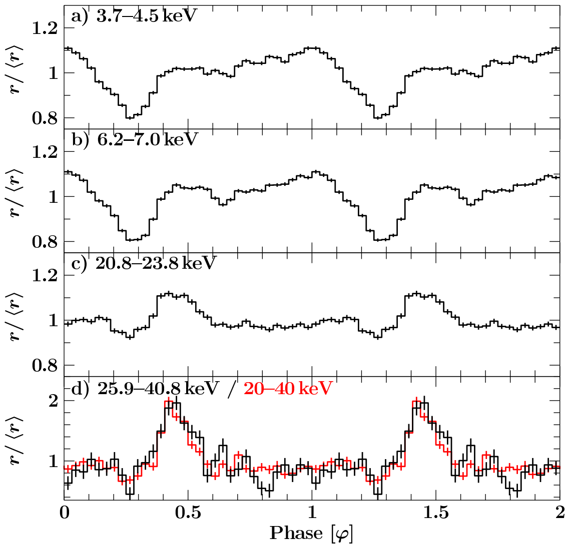

Figure 5.4.: Energy resolved pulse profiles with *RXTE*/PCA (a-c) and *RXTE*/HEXTE (d). The profiles are shown twice for clarity. In panel d) the *INTEGRAL*/ISGRI pulse profile in the 20–40 keV energy range is shown in red for comparison. Note that the *INTEGRAL* profile is shifted by hand to match the peak in the *RXTE* profile, but that the profiles are not phase aligned. The y-axis shows the count rate r in units of its average value $\langle r\rangle$.

than the first one and exhibiting a complex shape with two subpeaks. With higher energy resolution a remarkable and strong energy dependence becomes evident, clearly seen in pulse profiles extracted from *RXTE* data with a sampling period of $P = 604.685$ s and 32 phase bins. Thanks to the large effective area of the instrument, very good pulse profiles with a high S/N could be extracted in 30 narrow energy bands. Three examples are shown in the upper panels of Figure 5.4. At very low energies below 5 keV a broad plateau is visible, with increasing intensity at later orbital phases (Figure 5.4*a*). With increasing energy this plateau separates clearly into two peaks, while the second peak is getting dimmer compared to the first one (Figure 5.4*b*). The relative power of the secondary peak keeps declining up to ~20 keV (Figure 5.4*c*) and it is not visible anymore above 20 keV (Figure 5.4*d*). Despite the strong evolution with energy of the pulse profile, the deep minimum around phase $\phi = 0.3$ is not energy dependent. The IBIS/ISGRI pulse profile, which was extracted from the average data of the first 100 days of measurement in 2003, is shown in Figure 5.4*d* for comparison. We used the same epoch as for the *RXTE* analysis, but a period of $P = 604.747$ s, as determined in our analysis of the data. The pulse profile at energies above 20 keV is consistent between IBIS/ISGRI and *RXTE*/HEXTE.

To make the shape transition of the pulse profile at low and medium energies better visible, we plotted them in a color coded map (see Figure 5.5). The x-axis shows the pulse phase, the logarithmically scaled y-axis displays the energy in keV and the mean count rate is color-coded. The extensions of the pixels in y-direction represent the energy band of the given pulse profile. A smooth transition from the broad, two peaked structure to the single peaked structure is clearly seen. The minimum around phase $\phi = 0.3$ in black stays very stable.

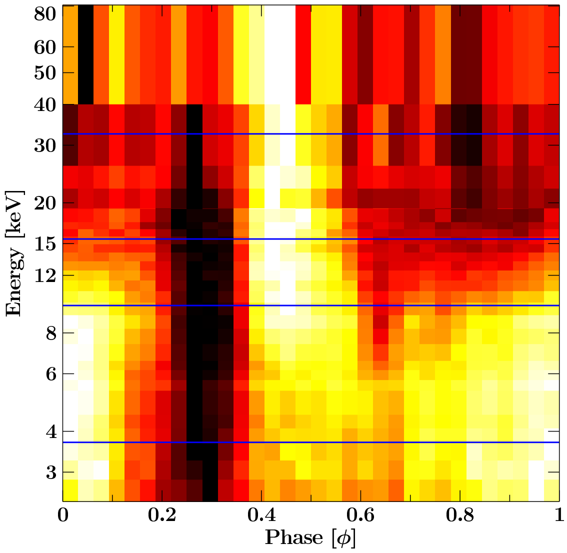

Figure 5.5.: Color coded pulse profile map of PCA and HEXTE data. The color indicates the mean countrate in each bin, ranging from black (lowest) to white (highest). The two highest energy bins are from HEXTE data. The four horizontal blue lines indicate the energies for which the pulse profiles are shown in Figure 5.4. The map shows one pulse only.

5.4 Spectral analysis

The spectrum of 4U 1909+07 shows a powerlaw shape, with a turnover at high energies, and is attenuated by photoabsorption at low energies, as common to many neutron star binary sources. Levine et al. (2004) used a phenomenological cutoff powerlaw and a bremsstrahlung model and found that both models describe the data well. We confirm this result in Section 5.4.1 and show that also the *INTEGRAL* and *Suzaku* data can be described by this kind of model. In Section 5.4.2 we performed pulse phase resolved analysis of the *RXTE* data, to investigate the changes of the spectrum with pulse phase. As indicated by the strong energy dependence of the pulse profile (Section 5.3.2) we expect strongly variable spectral parameters. These changes provide an insight into the physical conditions in the accretion column under different viewing angles.

5.4.1 Phase averaged spectrum

Various kinds of phenomenological continuum models exist to describe the overall spectral shape of accreting neutron stars in HMXBs. Among the most widely used models are the cutoff-powerlaw `cutoffpl`, with a smooth turnover at higher energies (determined by the folding energy E_{fold}), the `highecut` model, where the turnover begins suddenly at a given energy E_{cut} (White et al., 1983, and references therein) and the Comptonization model `compTT` (Hua & Titarchuk, 1995) with more free parameters to describe the temperature and optical thickness of the Comptonizing plasma. Levine et al. (2004) modeled the spectra using a cutoff powerlaw and a bremsstrahlung model, which incorporates only the temperature to describe the spectral shape. They found that both models fit the data equally well. We applied all four models, `cutoffpl`, `highecut`, `compTT`, and `bremss` to the *RXTE* and *INTEGRAL* data simultaneously, using ISIS 1.6.0-

3 and discarding all observations between orbital phase $0.88 < \phi_{\mathrm{orb}} < 0.12$, where the N_{H} is dramatically increased (Levine et al., 2004). The photoabsorption at low energies was modeled using a revised version of the `tbabs` model[1] with abundances by Wilms et al. (2000) and cross-sections by Verner et al. (1996). A strong iron line close to the energy of neutral iron of 6.4 keV is also present in the spectrum (Levine et al., 2004), and was modeled for all continuum models using a Gaussian emission line.

All continuum models described the data very well, except for the bremsstrahlung model, which only gave a best fit value of $\chi^2_{\mathrm{red}} = 1.75$. We ascribe this to the fact that the hard X-ray spectrum of 4U 1909+07 cannot be modeled accurately with the `bremss` model, noticeable only thanks to the improved statistics with the additional IBIS/ISGRI data. These data were not available to Levine et al. (2004). The best fit parameters and χ^2_{red} values of the other models are presented in Table 5.2 and Figure 5.6*a* shows the *RXTE* and IBIS/ISGRI spectra together with the best fit `cutoffpl`. The absorbed 5–100 keV flux of the data was $\mathscr{F} = 5.0 \times 10^{-10}\,\mathrm{erg\,s^{-1}\,cm^{-2}}$.

The χ^2_{red} values are below 1.5 for all models presented in Table 5.2, indicating a statistically acceptable fit. A look at the residuals in Figure 5.6*b*, however, shows that the models do not describe the data satisfactorily below 10 keV. These residuals can be eliminated by adding a blackbody component (Figure 5.6c and Table 5.2). The `cutoffpl` and the `highecut` model give similar blackbody temperatures between $kT \approx 1.4$–1.7 keV, whereas in the `compTT` model the temperature increased to $kT = 3.1 \pm 0.4$ keV. As the χ^2 of the `compTT + bbody` model is not as good as the χ^2 of the other two models, a temperature around $kT \approx 1.5$ keV seems most realistic.

We applied all three models also to the *Suzaku* data to check for consistency. The results presented here are preliminary and should be taken with the appropriate care. The flux in the *Suzaku* data was a bit lower than in the *RXTE/INTEGRAL* data with $\mathscr{F} = 4.5 \times 10^{-10}\,\mathrm{erg\,s^{-1}\,cm^{-2}}$ and taken between $\phi_{\mathrm{orb}} = 0.50$–$0.81$, i.e., outside of the high N_{H} phases. The N_{H} values are by a factor of $\sim$2 lower than in the *RXTE/INTEGRAL* data. The best fit values are given in Table 5.3, the data together with the best fit `cutoffpl` is shown in Figure 5.7. Besides the reduced N_{H} and flux, it is also clear that the continuum shape has changed drastically, with significantly smaller photon indices Γ (always ≤ 0.94 compared to always ≥ 1.03 for the old data) and smaller folding energies (always ≤ 15 keV compared to always ≥ 18 keV). This reduces the flux drastically at high energies. The blackbody component is only marginally improving the fit and not required to achieve acceptable χ^2_{red} values. Furthermore it is strongly correlated with the continuum model, so that the continuum flux is only very weakly constrained. The inclusion of the blackbody thus seems to be physical not relevant in the *Suzaku* data. The iron line was found to be consistent with the energy of neutral iron and could be modeled with a single Gaussian. We found no evidence for a Compton shoulder as detected by Torrejón et al. (2010) in *Chandra*, probably due to the worse spectral resolution of the XISs.

---

[1] see `http://pulsar.sternwarte.uni-erlangen.de/wilms/research/tbabs/`

Table 5.2.: Fit parameters for the phase averaged *RXTE* and *INTEGRAL* spectra with different models. No significant width of the iron line could be measured for the `highecut + bbody` and the `compTT` model and Fe σ was consequently frozen to 0.1 keV. Not shown are the cross calibration factors and the renormalization of the PCA background, which are similar for all models and close to 1.

Model parameter	cutoffpl	cutoffpl +bbody	highecut	highecut +bbody	compTT	compTT +bbody
N_H [10^{22} cm^{-2}]	20.6 ± 1.5	14 ± 2	15 ± 2	15 ± 2	$10.3^{+1.8}_{-1.9}$	9 ± 2
A_cont [ph@1 keV]	$0.084^{+0.012}_{-0.011}$	$0.029^{+0.009}_{-0.007}$	$0.057^{+0.009}_{-0.011}$	$0.036^{+0.011}_{-0.009}$	$(0.54 \pm 0.03) \times 10^{-2}$	$(4.8 \pm 0.4) \times 10^{-3}$
Γ	1.59 ± 0.07	1.15 ± 0.12	$1.56^{+0.06}_{-0.08}$	$1.36^{+0.11}_{-0.13}$	–	–
E_fold [keV]	28 ± 3	20 ± 2	27 ± 3	23 ± 3	–	–
E_cutoff [keV]	–	–	7.8 ± 0.5	$7.5^{+0.7}_{-1.0}$	–	–
T_0 [keV]	–	–	–	–	1.19 ± 0.04	1.15 ± 0.06
kT [keV]	–	–	–	–	$9.7^{+0.2}_{-0.5}$	10.1 ± 0.3
τ	–	–	–	–	$3.01^{+0.13}_{-0.01}$	$3.00^{+0.11}_{-0.00}$
Fe σ [keV]	$0.9^{+0.1}_{-0.2}$	$0.19^{+0.17}_{-0.19}$	0.41 ± 0.17	0.1	0.1	$0.15^{+0.16}_{-0.15}$
Fe Energy [keV]	6.76 ± 0.15	6.47 ± 0.07	$6.43^{+0.07}_{-0.09}$	$6.42^{+0.10}_{-0.05}$	$6.44^{+0.07}_{-0.06}$	6.44 ± 0.06
Fe A [ph/s/cm^2]	$(0.74^{+0.16}_{-0.15}) \times 10^{-3}$	$(4.3^{+1.2}_{-0.9}) \times 10^{-4}$	$(0.6^{+0.2}_{-0.1}) \times 10^{-3}$	$(3.9^{+0.8}_{-0.7}) \times 10^{-4}$	$(3.4^{+0.5}_{-0.4}) \times 10^{-4}$	$(4.5^{+1.0}_{-0.7}) \times 10^{-4}$
bbody kT [keV]	–	$1.65^{+0.11}_{-0.08}$	–	$1.4^{+0.2}_{-0.1}$	–	3.1 ± 0.4
bbody norm	–	$(0.71^{+0.15}_{-0.14}) \times 10^{-3}$	–	$(5 \pm 2) \times 10^{-4}$	–	$(3.7^{+1.4}_{-1.3}) \times 10^{-4}$
χ^2/dof (χ^2_red)	147.4/100 (1.47)	94.6/98 (0.97)	102.7/99 (1.04)	85.4/98 (0.87)	124.5/100 (1.25)	98.8/97 (1.02)

Table 5.3.: Same as Table 5.2, but for the *Suzaku* data. Not shown are the cross-calibration factors between XIS0, 1, 3 and PIN which were all close to 1. Fe σ could not be constrained with the data and was consequently frozen to 0.01 keV for all models.

Model parameter	cutoffpl	cutoffpl +bbody	highecut	highecut +bbody	compTT	compTT +bbody
N_H [$10^{22}\,\mathrm{cm}^{-2}$]	9.21 ± 0.18	7.6 ± 0.5	8.91 ± 0.20	$7.6^{+0.6}_{-0.5}$	6.09 ± 0.17	$8.3^{+0.4}_{-0.5}$
A_cont [ph@1 keV]	$0.0159^{+0.0010}_{-0.0009}$	$(0.6 \pm 0.3) \times 10^{-2}$	0.0150 ± 0.0011	$(0.5^{+0.4}_{-0.3}) \times 10^{-2}$	$(0.64^{+0.04}_{-0.05}) \times 10^{-2}$	≤ 19
Γ	$0.67^{+0.05}_{-0.06}$	0.4 ± 0.3	$0.90^{+0.04}_{-0.05}$	0.4 ± 0.5	–	–
E_fold [keV]	$11.4^{+1.0}_{-0.9}$	12^{+3}_{-2}	$13.9^{+1.1}_{-1.0}$	12^{+3}_{-2}	–	–
E_cutoff [keV]	–	–	5.4 ± 0.2	6.0 ± 0.4	–	–
T_0 [keV]	–	–	–	–	1.20 ± 0.04	$0.2^{+0.1}_{-0.2}$
kT [keV]	–	–	–	–	$6.9^{+0.5}_{-0.4}$	$6.0^{+0.6}_{-0.4}$
τ	–	–	–	–	4.4 ± 0.3	$7.4^{+1.6}_{-1.3}$
Fe σ [keV]	0.01	0.01	0.01	0.01	0.01	0.01
Fe Energy [keV]	6.406 ± 0.009	6.407 ± 0.010	6.407 ± 0.010	6.409 ± 0.010	$6.408^{+0.010}_{-0.009}$	6.407 ± 0.010
Fe A 10^{-4} [ph/s/cm^2]	(2.00 ± 0.17)	(1.84 ± 0.17)	(1.90 ± 0.17)	$(1.77^{+0.18}_{-0.19})$	(1.88 ± 0.17)	(1.82 ± 0.17)
bbody kT [keV]	–	$1.67^{+0.19}_{-0.13}$	–	$1.32^{+0.14}_{-0.07}$	–	$1.81^{+0.15}_{-0.12}$
bbody norm	–	$(0.96 \pm 0.15) \times 10^{-3}$	–	$(0.7^{+0.4}_{-0.3}) \times 10^{-3}$w	–	$(1.44^{+0.15}_{-0.13}) \times 10^{-3}$
χ^2/dof (χ^2_red)	747.1/537 (1.39)	617.2/535 (1.15)	637.9/536 (1.19)	608.5/534 (1.14)	636.0/536 (1.19)	622.1/534 (1.17)

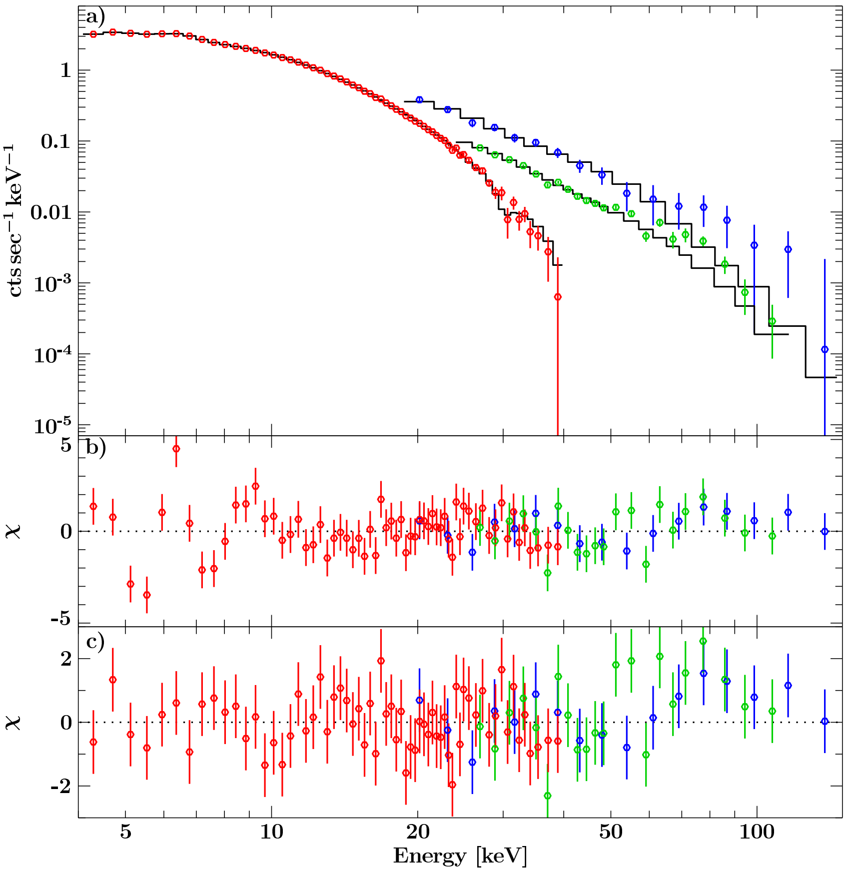

Figure 5.6.: *a)* Combined *RXTE*/PCA (red), HEXTE (green) and *INTEGRAL*/ISGRI (blue) spectra. The best fit `cutoffpl`-model with a blackbody component is shown in black. *b)* Residuals of the best fit model without a blackbody. *c)* Residuals of the best fit model with a blackbody.

5.4.2 Phase resolved spectra

DUE to the rotation of the neutron star, the accretion columns and hot-spots are seen under a constantly changing viewing angle. Since the physical conditions cannot be assumed to be constant throughout the emission regions, the X-ray spectrum can change significantly with pulse phase. These dramatic changes are indicated in the energy dependence of the pulse profile (Figures 5.4 and 5.5). Pulse phase resolved spectroscopy allows us to disentangle the contributions from the different physical components (see, e.g., Kreykenbohm et al., 2004). To perform phase resolved spectral analysis, we divided the *RXTE*/PCA and *RXTE*/HEXTE data into 7 phase bins, as indicated in Figure 5.8*a*. The IBIS/ISGRI data did not provide good enough statistics for high resolution phase resolved spectroscopy. The *Suzaku* data showed a clearly different spectral shape and could therefore not be combined with the *RXTE* data. Their phase resolved spectral analysis will be presented in a forthcoming publication and is beyond the scope of this work. A `cutoffpl`, a `highecut`, and a `compTT` model, each improved by photoabsorption, an

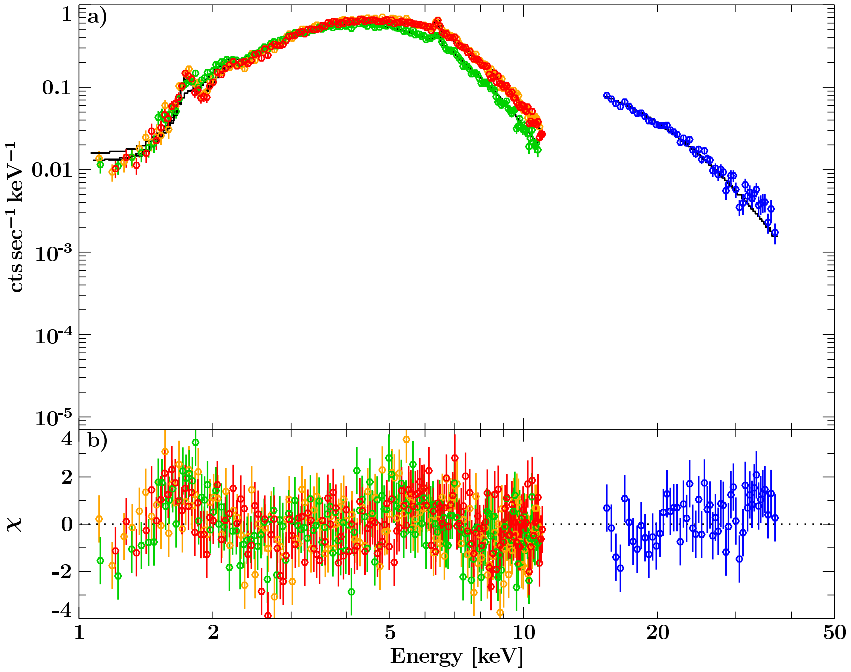

Figure 5.7.: *a)* XIS0 (red), XIS1 (green), XIS3 (orange), and PIN (blue) spectra together with the best fit `cutoffpl` model *b)* Residuals of the best fit model.

iron line, and a blackbody were fitted to all phase bins. All three models showed similar behavior as function of pulse phase. In terms of χ^2_{red}, however, the `highecut` failed in most phase bins very clearly, even though it gave the best χ^2_{red} values for the phase averaged spectrum. A possible explanation for this effect is that the phase averaged spectrum is a superposition of the different spectra at different phases and that this superposition is best described with the `highecut` model. To check this assumption, we simulated a spectrum consisting of a superposition of the best fit `cutoffpl` models for the individual phasebins, each parameter weighted by the respective count rate in the respective phase bin. The emerging spectrum could be described significantly better with a `highecut` model ($\chi^2_{\text{red}} = 0.72$) than with the `cutoffpl` model ($\chi^2_{\text{red}} = 0.82$). This result shows that the superposition of the simpler `cutoffpl` models introduces new features in the phase averaged spectrum, which are not source intrinsic. The `cutoffpl` model gave the best fits over all phasebins and only those results are presented here.

Describing the spectra without a blackbody component resulted in good χ^2_{red} values only for phase bins A, B, C, and G, but returned formally unacceptable χ^2_{red} values for phase bins D, E, and F, i.e., for spectra during the secondary peak. As discussed in the previous section the phase averaged spectrum can also be fitted relatively well without a blackbody component, but the inclusion of such a component improves the χ^2 value. This effect can now be explained by viewing the phase averaged spectrum as a superposition of spectra with and without a prominent blackbody component, and consequently showing only comparatively weak evidence for this component. Phase resolved analysis disentangles this superposition and gives more information on the real physical behavior of the source.

A close analysis of all spectra revealed that the folding energy and the photon index of the `cutoffpl` model depend strongly on each other and that the statistics of the spectra do not allow us to separate the influence of these two parameters. We consequently carried out two independent fits, one with the folding energy frozen to its value in the phase averaged fit and one with a frozen photon index, also set to the value of the phase averaged fit. Both models gave very good results in terms of χ^2_{red}. To further reduce the number of variable parameters, we also froze the energy of the Gaussian iron line to 6.47 keV, the value of the phase averaged fit. The iron line energy was consistent with that value in all phase bins when allowed to vary. Overall the free parameters of the fit were: the normalization of the `cutoffpl`, the column of the photo absorption, the normalization and temperature of the blackbody, the normalization and width of the iron line, and either the folding energy or the photon index of the `cutoffpl`.

The evolution of the spectral parameters is shown in Figure 5.8, the left panel shows the values for a frozen photon index, the right one for a frozen folding energy. It is clearly seen that for both models neither the photoabsorption N_{H} nor the power of the iron line seem to vary much over the pulse phase. The strong spectral changes indicated in the energy resolved pulse profiles are thus mainly due to a change in the continuum of the `cutoffpl` model, either due to a shift of the folding energy to higher energies (Figure 5.8*e*, left) or due to an increase in the photon index (Figure 5.8*d*, right). The folding energy is highest in the primary peak during phase bins A and B, making its spectrum distinctly harder than the rest of the pulse phase. In the secondary pulse the folding energy moves to values as low as ~14 keV, forcing a strong attenuation of the spectrum above this energy.

The behavior of the blackbody component is also very interesting in both models. Panels *f* and *g* of Figure 5.8 show the normalization of the blackbody component and its temperature, respectively. While the temperature varies insignificantly with pulse phase, the normalization, expressing the contribution of the blackbody component to the overall flux, shows a strong dependency on pulse phase with variation up to a factor of 3. The blackbody is strongest in phase bin D, i.e., during the beginning of the secondary pulse, and lowest in phase bin A, i.e., during the rise and maximum of the primary peak. As there is an indication for a broadening of the iron line during the phase bins where the blackbody is weakest, one might speculate about a compensation of the blackbody component by the Gaussian. Confidence contours between the two parameters, however, showed no such correlation. The indicated broadening of the iron line is more likely due to a change in the iron edge or an iron Kβ line, which cannot be resolved with *RXTE*/PCA. By using spectra with higher energy resolution, like the *Suzaku* data, a more in depth study of the iron line behavior with pulse phase will be possible.

The normalization of the powerlaw clearly reflects the pulse profile in the model where the photon index was frozen (see Figure 5.8*c*, left). In the model with the frozen folding energy, on the other hand, this correlation is not so clear (see Figure 5.8*c*, right). It rather seems that in this case a combination of the photon index and the power law normalization models not only the spectral change, but also the brightness variation. Because of this entanglement, the model with the variable folding energy seems the more realistic description of the spectrum.

We calculated confidence contours for the phase averaged spectrum for the blackbody normalization versus the photon index as well as for the blackbody normalization versus the folding energy, based on the models with frozen folding energy and frozen photon index, respectively, in order to exclude strong dependencies between these parameters. Figure 5.9 shows the confidence contour for the model with the variable photon index, i.e., the frozen folding energy, together with the best fit value as a bright cross. The contours are indicating only a very weak correlation between the blackbody normalization and the photon index. In the background the best fit value of the normalization of the Gaussian iron line is shown in gray-scale for every relevant point in the blackbody normalization – photon index space. The scale on the right of the plot gives its corresponding values. With increasing blackbody power and spectral softening a weaker iron line is necessary. Within the best fit contours, however, the iron line is not changing dramatically, thus ruling out a substitution of the blackbody with a stronger iron line for formally acceptable χ^2_{red} values.

Additionally to the phase averaged contour, Figure 5.9 shows the best fit values for all 7 phase bins as dark crosses, labeled with the respective letter. As can be clearly seen, in phase bins A and B the spectrum is hardest, while the blackbody component is weakest. Phase bins C–F are clustered together in a regime with a slightly softer spectrum and stronger blackbody than the phase averaged spectrum. Phase bin G, describing the minimum between two consecutive pulses shows only very weak portions of the blackbody and an intermediate spectral hardness. This distribution makes very clear that both, the photon index and the blackbody component change significantly over the pulse phase in a way which seems to indicate a correlation between them. This correlation is most likely of physical origin and not introduced due to improper modeling of the spectrum, as the confidence contour of the phase averaged spectrum showed no correlation between these parameters.

Figure 5.10 shows the same plot as Figure 5.9 but for the model with a variable folding energy, i.e., a frozen photon index. As for the variable photon index, the iron line does not change significantly within the acceptable χ^2 contours and is only a weak function of both parameters. The best fit phase resolved values show a similar distribution as in Figure 5.9. It is clearly seen that phase bin A shows the hardest spectrum with a negligible blackbody component, while phase bin B moves a bit to a softer spectrum with a stronger blackbody. Phase bins C–F are again clustered together and phase bin G shows intermediate spectral hardness with a very weak blackbody. This distribution of the phase resolved data indicates an anti-correlation between the blackbody normalization and the folding energy. As in the other model, this correlation is most likely intrinsic to the source as the phase averaged confidence contours rule out a model dependent correlation.

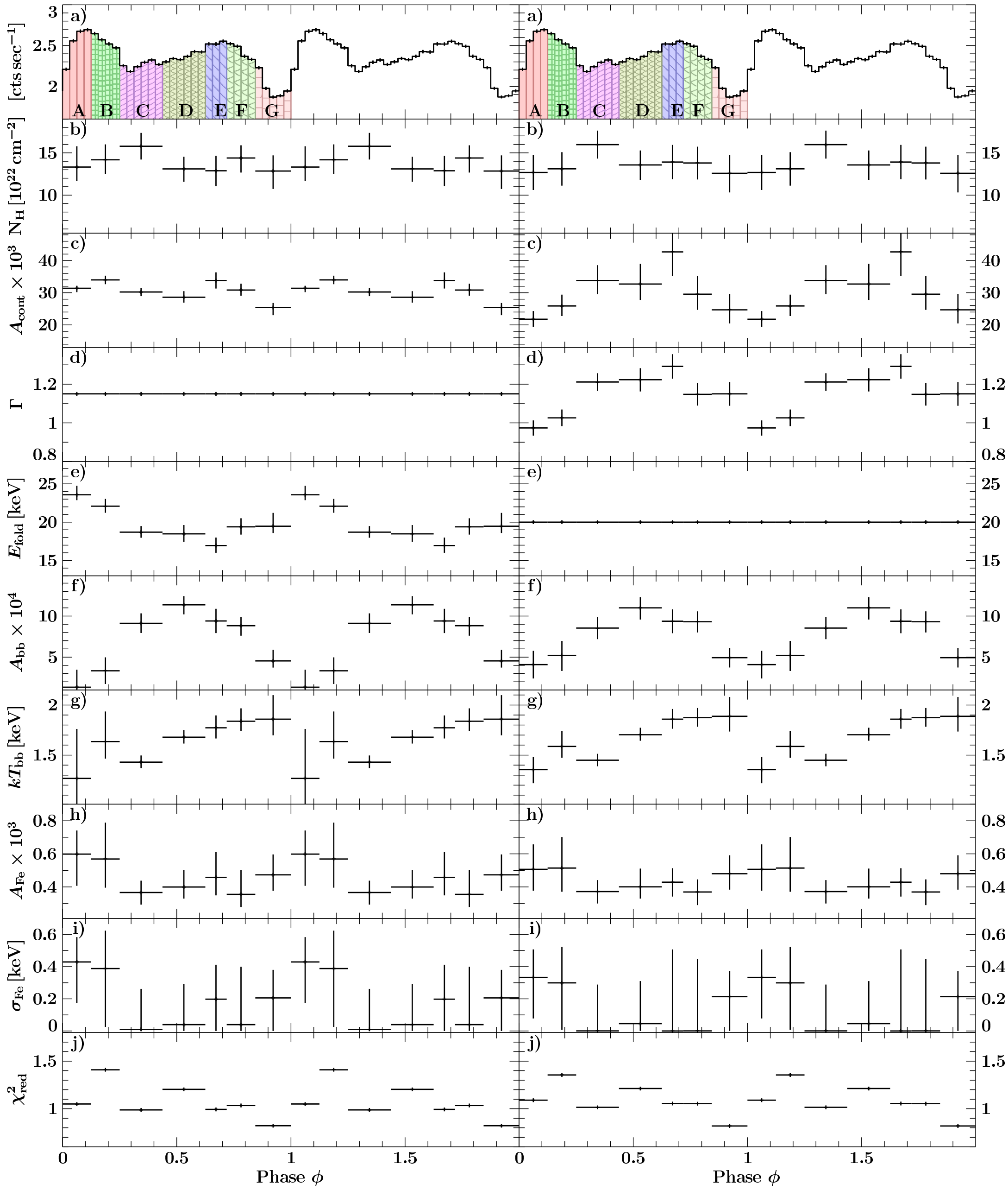

Figure 5.8.: Parameters of the phase-resolved spectra fitted with the `cutoffpl` model. For the left panels the photon index was frozen to $\Gamma = 1.15$, for the right panels the folding energy was frozen to $E_{\text{fold}} = 20.0\,\text{keV}$. *a)* Pulse profile in the 13.2–14.5 keV energy range. The different shaded areas indicate the phase bins used to extract the spectra. *b)* Photo electric absorption column N_{H}, *c)* power law normalization, *d)* power law index Γ, *e)* folding energy, *f)* blackbody normalization, *g)* blackbody temperature, *h)* iron line normalization, *i)* iron line width, and *j)* χ^2_{red}-value.

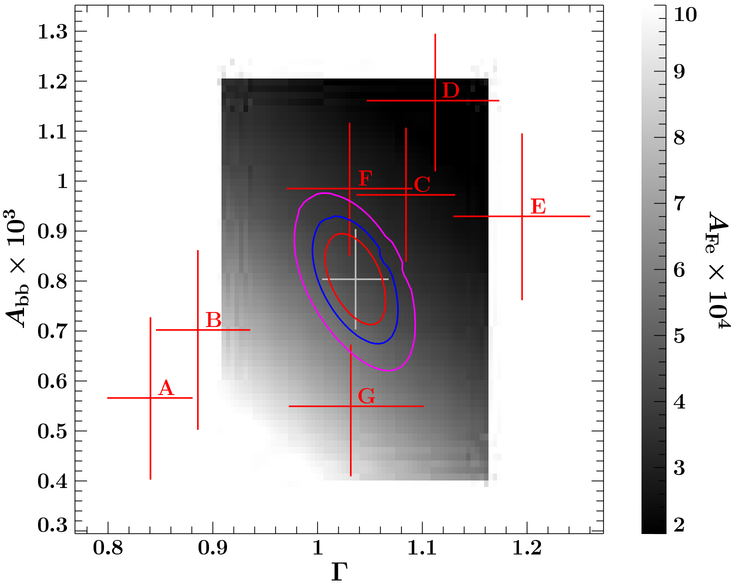

Figure 5.9.: Confidence contour and best fit value for the phase averaged spectrum between the photon index of the powerlaw and the normalization of the blackbody component, when fitted with a frozen folding energy. The contour lines show from the center outwards the 68% (1σ), 90% and 99% confidence level. Gray-scaled is the normalization of the Gaussian iron line for the best-fit model at every given photon index – blackbody normalization point. The points labeled A through G are the best fit values of the respective phase bins and their uncertainties in the same space and for the same model.

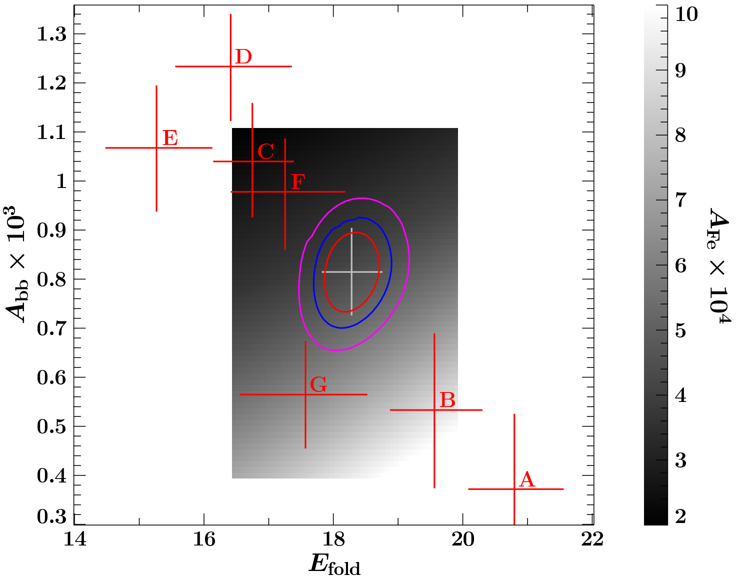

Figure 5.10.: Same as Figure 5.9 but for the folding energy of the power law versus the normalization of the blackbody, while the photon index of the `cutoffpl` model was frozen.

5.5 Discussion & Conclusion

We have presented the first detailed study with *INTEGRAL*, *RXTE*, and *Suzaku* of 4U 1909+07 and have shown that the pulse period evolution shows strong indications for a random walk like behavior. Such a behavior has been seen in other HMXBs like Vela X-1 and is a strong indicator for a wind accreting source without a persistent accretion disk (Ghosh & Lamb, 1979a). An accretion disk would provide a more constant transfer of angular momentum and thus a long-term spin-up or spin-down trend, as seen in other sources like 4U 1907+09 (Fritz et al., 2006). Accretion disks form to fulfill the conservation of angular momentum of the accreted wind, but in a system with a strongly magnetized neutron star the ionized matter will couple to the magnetic field lines before a stable disk can form. This requires field strengths on the order of 10^{12} G, not unusual for this kind of system (see Section 2.2). In these strong magnetic fields, CRSFs (“cyclotron lines”) can form, seen in many other sources, e.g., Vela X-1 (Kreykenbohm et al., 1999), 4U 0115+63 (Santangelo et al., 1999), or MXB 0656−072 (McBride et al., 2006) (see also Section 2.3.2). We found no evidence for a CRSF in the spectra of 4U 1909+07, which can be well described by a phenomenological absorbed cutoff-powerlaw or Comptonization model. As shown by Schönherr et al. (2007) this does not rule out a strong magnetic field, as CRSFs can be filled by photon spawning and their shapes and depths depend strongly on the geometry of the accretion column and on the viewing angle (see also Schwarm, 2010). Further investigations with high S/N data will allow a more thorough search for a CRSF in 4U 1909+07.

A strong magnetic field in 4U 1909+07 is supported by the strongly pulsed flux, as the X-ray flux is believed to be produced in a very small region above the hot-spots on the neutron star surface, where the surface is penetrated by the magnetic field lines and the matter is accreted onto the neutron star (Lamb et al., 1973). In the accretion column above the hot-spots, the density and temperatures are highest and the most X-rays are produced through Comptonization of the thermal photons from the thermal mound on the neutron star surface (Becker & Wolff, 2005a,b, see also Section 2.3). If the magnetic axis is not aligned with the rotational axis of the neutron star, the hot spots and the accretion columns move in and out of sight of the observer, resulting in a pulsed X-ray flux.

The hot spots and the accretion column are visible in the soft X-ray spectrum and described by a blackbody component. We have seen that in the *Suzaku* data a blackbody component is not required, contrary to the *RXTE* data. Together with the strong changes in the continuum parameters between the two data sets this difference indicates that the structure and physical conditions of the accretion column are very variable. A flux dependent change of the accretion column has been observed in other sources like A 0335+26 (Caballero et al., 2007) where the energy of the CRSF is changing. Whether the observed changes are indeed correlated with luminosity or are rather random changes can only be checked with further observations at different luminosity levels.

The exact geometry of the accretion column depends strongly on the way the matter couples to the magnetic field and cannot be constrained from our measurements (Basko

& Sunyaev, 1976; Mészáros, 1984). Besides the simple filled funnel other possible configurations include a hollow or a partly hollow funnel. With an average luminosity of $\sim 2.8 \times 10^{36}\,\mathrm{erg\,s^{-1}}$ between 4.5–200 keV the system can host accretion rates that are large enough for a shock to form in the accretion column, due to the radiation pressure from the material close to the neutron star surface. This shock prevents escape of the Comptonized photons parallel to the magnetic field lines, so that they can only emerge from the sides of the accretion column in a so-called "fan beam" (Mészáros, 1984). If the accretion rate is lower, no shock will form and the radiation can escape along the accretion column in a "pencil beam".

5.5.1 Classical picture

In a classical assumption the two distinct peaks in the pulse profile at low energies hint at the fact that accretion happens onto both magnetic poles of the neutron star, but under different physical conditions. These differences can explain the diverse spectra in the two peaks. The secondary peak shows a distinctly lower folding energy which corresponds roughly to the temperature of the electron gas in the accretion column. A misalignment between the magnetic center and the gravitational center of the neutron star could lead to different sizes of the accretion column and thus to other densities and temperatures.

We have also seen that the blackbody component of the spectrum of 4U 1909+07 is phase shifted with respect to the two peaks in the pulse profiles. It is likely that the blackbody originates from the thermal photons of the thermal mound at the hot spot. Through the rotation of the neutron star, the hot spot is only visible at certain pulse phases. Assuming a hollow funnel accretion geometry, with a large enough accretion rate to form a shock, we can argue that we see the thermal mound only at the phases were we look along the hollow accretion column, while the most hard X-ray flux is only visible when we see the sides of the accretion column, due to the "fan beam" geometry. As we averaged every phase bin over a large range of time, we can neither rule out nor investigate a change of the accretion geometry.

5.5.2 Strongly relativistic picture

Caution has to be taken, however, with these simple classical models as the behavior of plasma in magnetic fields on the order of $B \approx 10^{12}$ G is still not well understood and all models are based on strong simplifications. Additionally gravitational light bending must be taken into account when analyzing pulse profiles and their origin (Kraus et al., 2003; Mészáros & Nagel, 1985b). Close to the surface of a canonical neutron star of mass $M = 1.4\,\mathrm{M}_\odot$ and radius $R = 10\,\mathrm{km}$, i.e., a radius only 2.4 times the Schwarzschild radius, light bending leads to a visible surface of the neutron star of 83%. This huge amount of always visible surface reduces the pulsed flux from the two hot-spots. Assuming a "fan-beam" emission characteristic of the accretion column, gravitational light bending can increase the pulsed flux dramatically, especially at phases where one column would be hidden behind the neutron star in the classical picture (Riffert & Mészáros, 1988). In a very special configuration where the rotational axis takes an angle of 45° to both the observer and the magnetic axis, pulse profiles very similar to the high energetic pulse profile of 4U 1909+07 (Figure 5.4*d*) can emerge, in which only one sharp peak is visible (compare Figure 5 of Riffert & Mészáros, 1988). In the simple models of Riffert & Mészáros (1988) the emission characteristic of the accretion column is taken to be isotropic and independent of energy, so that a direct translation to 4U 1909+07 is not easily made. Attempts to decompose the pulse profile for other sources were made by Kraus et al. (2003) and Sasaki et al. (2010), among others. These decompositions prove difficult due to the many free parameters, like emission pattern, geometry of the accretion column, configuration of the magnetic field, and equation of state which cannot be closely constrained. Nonetheless the sharp peaked pulse profile of 4U 1909+07 above 20 keV is a hint that the hard X-ray emission is produced in a "fan-beam" accretion column and that during the rotation of the neutron star one column vanishes behind the star and its emission is bent around and focused due to the strong gravitation.

More detailed models for pulse decomposition will be applied to 4U 1909+07 in the future, together with a thorough analysis of the *Suzaku* data. With these data a detailed investigation of the long term variability of 4U 1909+07 is also possible as well as a comparative study of the pulse phase dependence of the spectral parameters.

“Excellent!” I cried. “Elementary,” said he.

(Arthur C. Doyle – Watson and Holmes in “The Crooked Man”)

6

Concerning GX 301−2

Contrary to 4U 1909+07, the topic of the previous Chapter, the source discussed here is much more famous: GX 301−2.[1] Similar to 4U 1909+07 it is a persistent HMXB, but additionally to the irregular flaring common to these sources, it shows large X-ray outbursts occurring regularly once per orbit. Presumably these regular flares are the main reason for the strong interest in the source, on the observational as well as on the theoretical site. In this Chapter the analysis of two separate data sets of GX 301−2, one from *XMM-Newton* and one from *Suzaku* are presented. The *XMM-Newton* analysis has been published by Fürst et al. (2011c), the *Suzaku* analysis by Suchy et al. (2011a). Major parts of this Chapter are taken almost verbatim from these publications. I try to combine both analyses, pointing out how the different data sets require different approaches to obtain the most information about the source. The reduction and modeling of the *Suzaku* data has mainly been performed by Slawomir Suchy, while I was responsible for the *XMM-Newton* analysis. The interpretation of the data was done jointly and started during my stay at UCSD.

This Chapter starts with an introduction to the GX 301−2 system in Section 6.1 followed by a description of the data used in Section 6.2. The scientific analysis starts in Section 6.3 with the timing behavior of GX 301−2, an investigation mainly based on the *XMM-Newton* data. Section 6.4 presents the spectral analysis, split into different subsections covering different approaches. While the *XMM-Newton* data were used to perform pulse-to-pulse spectroscopy (Section 6.4.3), *Suzaku* data were utilized for pulse phase resolved spectroscopy (Section 6.4.4). Finally Section 6.5 summarizes the analysis, and gives a physical interpretation of the results.

As in the previous Chapters, this Chapter is based on a scientific publication and therefore uses the common “we” style.

---

[1] More than 50 papers exist mentioning GX 301−2 in their title, compared to only 4 for 4U 1909+07. If the number of papers referring to a given source in their title is a good indicator for the source’s fame, Cyg X-1 is maybe the most famous HMXB, with more than 1100 papers.

6.1 Introduction

An X-ray flare at the coordinates of GX 301−2 was first detected in 1969 during a balloon experiment (Lewin et al., 1971). During further balloon flights McClintock et al. (1971) found that the source is persistent and named it GX 301−2. Since then it has been observed by most X-ray instruments and has risen a lot of interest in the community as it shows a strongly variable flux and a huge absorption column. White et al. (1976) detected a stable period at ~700 s, which could be identified as the pulse period of a neutron star. An orbital period of ~40 d was detected later (White et al., 1978) and then refined to 41.5 d (Watson et al., 1982). These authors used the regular X-ray outbursts of GX 301−2 to determine its orbit and found that the orbit is quite eccentric with $e = 0.47$. The same technique was used by Koh et al. (1997), refining the values from Sato et al. (1986) using data from the *Burst and Transient Source Experiment (BATSE)* aboard the *Compton Gamma Ray Observatory (CGRO)*. These authors obtained an orbital period $P_\mathrm{orb} = 41.498 \pm 0.002\,\mathrm{d}$. A thorough analysis of pulse arrival times in *INTEGRAL* data from 2007 by Doroshenko et al. (2010) resulted in a slightly shorter orbital period, which is in agreement with Sato et al. (1986) and Koh et al. (1997) when allowing for a secular period change of $\dot{P}_\mathrm{orb} = (-3.7 \pm 0.5) \times 10^{-6}\,\mathrm{s\,s^{-1}}$.

The neutron star accretes matter from its optical companion, which was identified as the B-type giant Wray 977 (Vidal, 1973). Its exact type and distance were disputed for a long time. Parkes et al. (1980) found a distance of $1.8 \pm 0.4\,\mathrm{kpc}$ identifying it as a B2 Iae star. Be stars have a circumstellar disk, through which the neutron star passes once or twice per orbit (depending on the size of the disk and the eccentricity of the orbit). During these passages, the accretion rate increases dramatically, resulting in large X-ray outbursts. Many transient HMXBs with Be-type companions are known, like A 0535+26 or XTE J1946+274 (Caballero et al., 2007; Wilson et al., 2003; Müller et al., 2011a). Kaper et al. (1995) stated that for the optical companion of GX 301−2 the spectral type B1 Ia+ is more likely, i.e., a star without a circumstellar disk. This classification implies a distance of 5.3 kpc and makes Wray 977 one of the most luminous and massive stars in our galaxy. The most recent measurements by Kaper et al. (2006) indicate a distance of 3 kpc using the same spectral type as before, a stellar-radius of $62\,\mathrm{R}_\odot$, and a mass of $43 \pm 10\,\mathrm{M}_\odot$. We adopt these values throughout the paper, as the X-ray accretion models by Leahy & Kostka (2008), which do not need a circumstellar disk, also seem to indicate similar values.

The regular X-ray flares of GX 301−2 were found to occur ~1.4 d prior to periastron, i.e., before the neutron star reaches the densest part of the stellar wind. Standard, symmetric wind accretion models fail to explain this pre-periastron flare. Pravdo & Ghosh (2001) suggested a model based on the Be classification of Wray 977. If its circumstellar disk is not aligned with the orbital plane of the neutron star, such a flare could be observed. More recent calculations (Leahy, 2002; Leahy & Kostka, 2008), based on the B1 Ia+ classification, show that it is also possible that the neutron star is trailed by an accretion stream, which it overtakes shortly before periastron. This model self-consistently explains the observed dependence of flux and column density on the orbital phase.

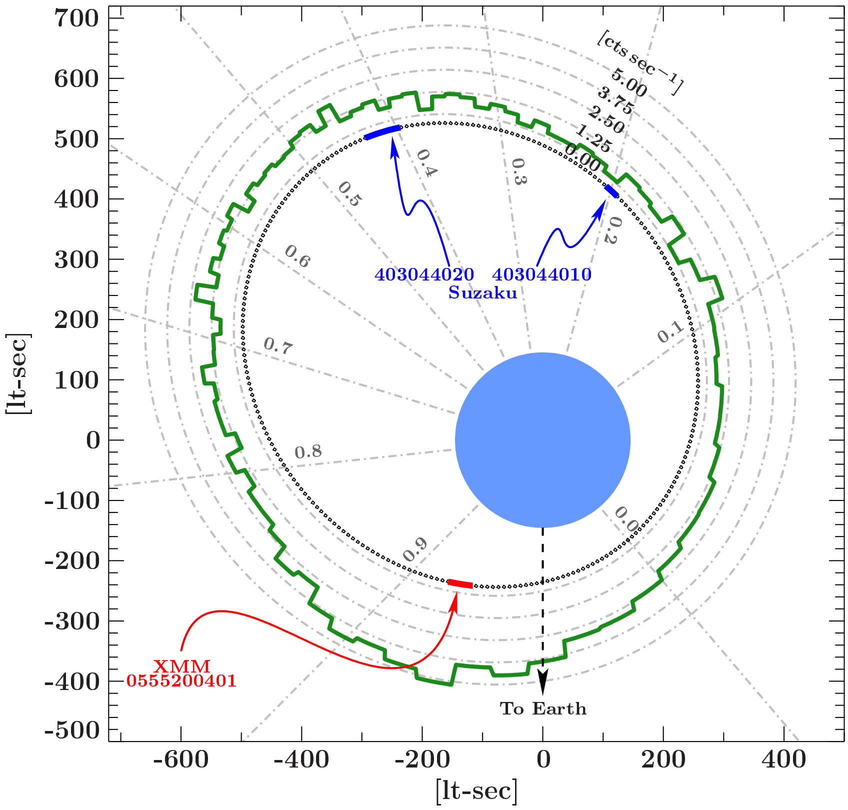

Figure 6.1.: Sketch of the orbit of GX 301−2, using the parameters given by Doroshenko et al. (2010). The green line shows the average *RXTE*/ASM light curve as function of orbital phase. The phases of the *XMM-Newton* observation discussed here are highlighted in red, the of *Suzaku* in blue.

It is the regular pre-periastron flare which distinguishes GX 301−2 from most other HMXBs. During the flare the X-ray flux increases by up to a factor of 25 (Pravdo et al., 1995; Rothschild & Soong, 1987), reaching luminosities of up to 1 Crab in the 15–50 keV band and some 100 mCrab in the softer 2–10 keV band. X-rays with energies below ~5 keV are less variable over the orbit as they are strongly affected by scattering and absorption due to the high column density (Leahy & Kostka, 2008).

Figure 6.1 shows the orbit of GX 301−2 and the *RXTE*/ASM light curve folded onto an orbital period of 41.5 d using the ephemeris by Doroshenko et al. (2010). Clearly visible is the pre-periastron flare, peaking around phase $\varphi = 0.91$. The plot assumes a size of $62\,R_\odot$ for the optical companion (Kaper et al., 2006) .

The broad-band X-ray spectrum of GX 301−2 can be described by an absorbed power law with a high-energy cutoff around 20 keV and a CRSF around 37 keV (Mihara et al., 1995; Endo et al., 2002). The continuum does not show strong variation in the intrinsic parameters (Γ, E_cut, and E_fold) with orbital phase (Mukherjee & Paul, 2004), as seen in two data sets from *RXTE*, taken in 1996 and 2000, sampling most phases of the binary orbit. The absorption column is highly variable between 10^{22}–$10^{24}\,\mathrm{cm}^{-2}$, but also seems to be uncorrelated with the orbit (Mukherjee & Paul, 2004; Leahy & Kostka, 2008).

Kreykenbohm et al. (2004) showed that the spectral parameters, e.g., the energy of the CRSF, vary with pulse phase, and therefore concluded that the X-rays are most likely produced in an accretion mound close to the neutron star surface. Furthermore, they showed that the CRSF centroid energy and width are correlated. These authors could also rule out a claim that a CRSF at ~ 20 keV is present, which would reduce the measured magnetic field strength in the accretion column (Orlandini et al., 2000). In the softer X-rays a very strong Fe Kα fluorescent emission line is visible, as well as fluorescent Kα lines from nickel and lighter elements (Leahy et al., 1988, 1989). The flux in these lines varies strongly with luminosity, indicating that the lines are produced in matter close to the neutron star (Mukherjee & Paul, 2004). Using *Chandra* data, Watanabe et al. (2003) detected a fully resolved Compton shoulder at the low-energy flank of the Fe Kα line. These authors could model the shoulder by simulating the Compton scattering of photons in a dense, cold gas-stream.

The slow pulse period of GX 301−2 is strongly variable over long timescales (Pravdo & Ghosh, 2001; Evangelista et al., 2010). It was first detected with $P \sim 700$ s, but changed in the last 40 years to values as low as 675 s and is today around $P \sim 685$ s. Independent of the variability of its period, GX 301−2 usually shows clear pulsations throughout its orbit. Recently, however, Göğüş et al. (2011) discovered a dip in an *RXTE* X-ray light curve during which GX 301−2 ceased to display pulsations. The data showed that exactly one pulse was missing and that the pulsed fraction was gradually reduced before and gradually increased after the dip. Interestingly, the spectrum softened significantly during that dip, contradicting the common picture that a very dense blob, absorbing all soft X-rays, was passing through the line of sight. Göğüş et al. (2011) speculate that due to the cessation of accretion the black body radiation from the polar cap became visible, effectively softening the spectrum and reducing the pulsed fraction, as the polar cap is larger and undergoes stronger gravitational light bending than the accretion column. Similar dips have already been observed in the light curves of other HMXBs like Vela X-1 and 4U 1907+09 (Kreykenbohm et al., 2008; in 't Zand et al., 1997), but never before in GX 301−2.

The strong absorption during the bright pre-periastron flare makes GX 301−2 an ideal object to study the X-ray producing and absorbing regions around a neutron star, especially focusing on the many fluorescent lines. *XMM-Newton* is the ideal instrument for this observation, with its large effective area and good spectral resolution. We obtained a $\sim$47 ksec *XMM-Newton* observation of which the results are presented here together with the analysis of a ~ 60 ksec long *Suzaku* observation. The broad-band capabilities of *Suzaku* enhance our view of GX 301−2 further, by allowing to also study the CRSFs at energies above 20 keV.

6.2 Data & Observations

We present data taken with *XMM-Newton* and *Suzaku*. The *XMM-Newton* data were taken on July 12th, 2009 (MJD 55024.103 – 55024.643, ObsID 0555200401) at orbital phase ∼0.91 of GX 301−2, i.e., during the pre-periastron flare. The exposure was 46.6 ksec, covering only a small part of the flare (see Figure 6.1). The X-ray flux was strongly variable during the observation, with values between $3.67 \times 10^{-10}\,\mathrm{erg\,s^{-1}\,cm^{-2}}$ and $2.47 \times 10^{-9}\,\mathrm{erg\,s^{-1}\,cm^{-2}}$ in the 2–10 keV energy band. Due to the expected high flux, the EPIC-MOS detectors were turned off to provide more telemetry for the EPIC-pn camera, which was operated in timing mode. For a detailed description of the instruments and their operation modes see Section 3.2. As GX 301−2 shows very strong absorption no usable information can be gained from RGS, which is mainly sensitive below 2.5 keV (Ness, 2011). We used the standard *Science Analysis System (SAS)* 10.0.0 to extract light curves and spectra. We tested for pile-up using the tool `epatplot`, but found no severe pile-up. The source data were extracted from EPIC-pn columns 35–40 and background data were obtained from columns 10–17 and 53–60. As high photon fluxes change the CTI of the CCD detector (see also Section 3.8.1), we also extracted spectra with the tool `epfast`, which takes these changes into account. We found, however, no significant differences to the standard pipeline.

Timing and spectral analysis of the *XMM-Newton* data was performed using ISIS 1.6.1 (Houck, 2002).

Observations by *Suzaku* were performed on 2008 August 25 with an exposure time of ∼ 10 ks (MJD 54703.552–54704.004, ObsID 403044010, orbital phase 0.19). The first observation was cut short by a set of ToO observations and was continued on 2009 January 5, acquiring an additional ∼ 60 ks exposure time (MJD 54836.440–54838.042, ObsID 403044020, obital phase 0.38). The 2–10 keV absorbed flux was measured to be $1.6 \times 10^{-10}\,\mathrm{erg\,s^{-1}\,cm^{-2}}$ during the first, short observation and clearly higher during the second observation, but with $\sim 8 \times 10^{-10}\,\mathrm{erg\,s^{-1}\,cm^{-2}}$ still lower than the flux during the *XMM-Newton* observation. As the second observation was also longer it provides much better statistics and in the *Suzaku* analysis presented here we will concentrate on this data set. See Suchy et al. (2011a) for an analysis and comparison of both data sets. Both main instruments, the XIS and HXD, were used in these observations which were performed with HXD nominal pointing to enhance the sensitivity of the HXD.

To minimize possible pile-up, the XIS instruments were operated with the 1/4 window mode with a readout time of 2 s. Data were taken in both 3 × 3 and 5 × 5 editing modes, which were extracted individually with the *Suzaku FTOOLS* version 16 as part of HEASOFT 6.9 as detailed in Suchy et al. (2011a). The unfiltered XIS data were reprocessed with the most recent calibration files available and then screened with the standard selection criteria as described by the *Suzaku* ABC guide[2]. The RMFs and ARFs were weighted according to the exposure times of the different editing modes. The XIS data were then grouped with the number of channels per energy bin corresponding to the half width half maximum of the spectral resolution, i.e., grouped by 8, 12, 14, 16, 18,

---

[2] `http://heasarc.gsfc.nasa.gov/docs/suzaku/analysis/abc/`

20, and 22 channels starting at 0.5, 1, 2, 3, 4, 5, 6, and 7 keV, respectively (M. A. Nowak, 2010, priv. comm.). During spectral modelling we found that the calculated responses of the XIS detectors showed a "leakage" emission level (Matsumoto et al., 2006) below 2 keV, which stemmed from the instrument characteristics. The "leakage" became relevant due to the large difference between the flux at the iron line energy and the flux at softer energies below 2 keV. To avoid uncertainties introduced by this calibration issue, we used the XIS data only in the energy range of 2–10 keV. For a detailed discussion of this issue see Suchy et al. (2011a).

To determine the PIN background, the *Suzaku* HXD team provides the tuned PIN non X-ray background for each individual observation. In addition, the cosmic X-ray background was simulated following the example in the ABC guide and both backgrounds were added together. The PIN data were grouped by a factor of 3 throughout the whole energy range. GSO data were extracted and binned following the *Suzaku* ABC guide. For the phase averaged analysis the PIN data were used between 15–60 keV, the GSO data between 50–90 keV. Due to the short exposure times, no GSO data were used in the phase resolved analysis.

For the spectral analysis of the *Suzaku* data *XSPEC* 12 (Arnaud, 1996) was used.

Both data sets, the *XMM-Newton* and the *Suzaku* one, were barycentric and binary corrected, using the ephemeris provided by Doroshenko et al. (2010).

6.3 Timing Analysis

During the pre-periastron flare GX 301−2 is highly variable, exhibiting strong flares superimposed on the variation introduced by the rotation of the neutron star. Compared to this violent behavior, the flux is much less variable close to apastron, where the *Suzaku* data were obtained. In these data the only visible variation is the pulse and no significant changes between pulses are evident. The analysis in Section 6.3.1 therefore concentrates on the *XMM-Newton* data, while in Section 6.3.2 also pulse profiles from *Suzaku* are presented, reaching to higher energies than possible with the *XMM-Newton* data alone.

6.3.1 Light curve

The top panel of Figure 6.2 shows the 20 s resolution, 2–10 keV, *XMM-Newton* light curve of GX 301−2. The light curve shows clear flaring behavior, with a smaller flare in the beginning and a large flare starting ∼30 ksec after the start of the observation. Clearly visible are also the sub-peaks induced by the pulse period of ∼685 s. We performed a search for the pulse period via epoch folding and found a period of $P = 685.0 \pm 0.1$ s, consistent with the monitoring data from the *Fermi*/GBM Pulsar Project (Finger et al., 2009). In search for changes of the pulse period during the observation, we performed epoch folding and phase connecting on parts of the light curve as short as 15 ksec. We did not find a significant change of the pulse period, consistent with

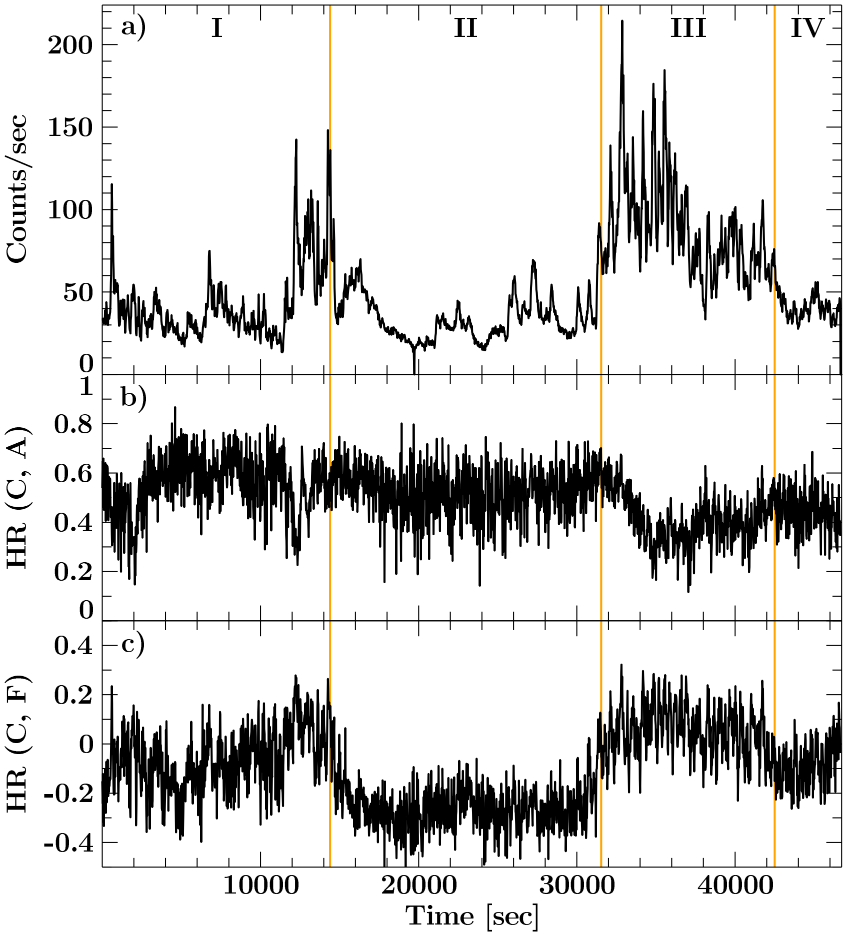

Figure 6.2.: *a)* Lightcurve of GX 301−2 with 20 s resolution in the 0.5–10.0 keV energy band. Vertical lines indicate the time regimes I–IV used in the later analysis. *b)* Hardness ratio between the continuum energy band *C* (8.5–10.0 keV) and the absorbed energy band *A* (4.0–5.0 keV). *c)* Hardness ratio between *C* and the Fe Kα line band *F* (6.3–6.5 keV).

Fermi/GBM data which show that the pulse period was only slowly changing during that time.

A close-up view of the light curve reveals that albeit the pulsations are clearly visible, strong pulse-to-pulse variations are also present. The individual pulse shapes range from simple two-peaked profiles to more complex shapes, with multiple minor peaks superimposed on the general shape. An example of two different profiles is shown in Figure 6.3 using light curves with 1 s and 20 s resolution. It becomes clear that the average pulse profile, also shown in Figure 6.3, is highly complex. Additionally brightness changes independent of the pulses are visible in the light curve. These changes can be on the same order of magnitude with respect to luminosity and duration as the variability due to the pulsation.

Stronger and sudden changes in luminosity are also seen in the light curve and differ-

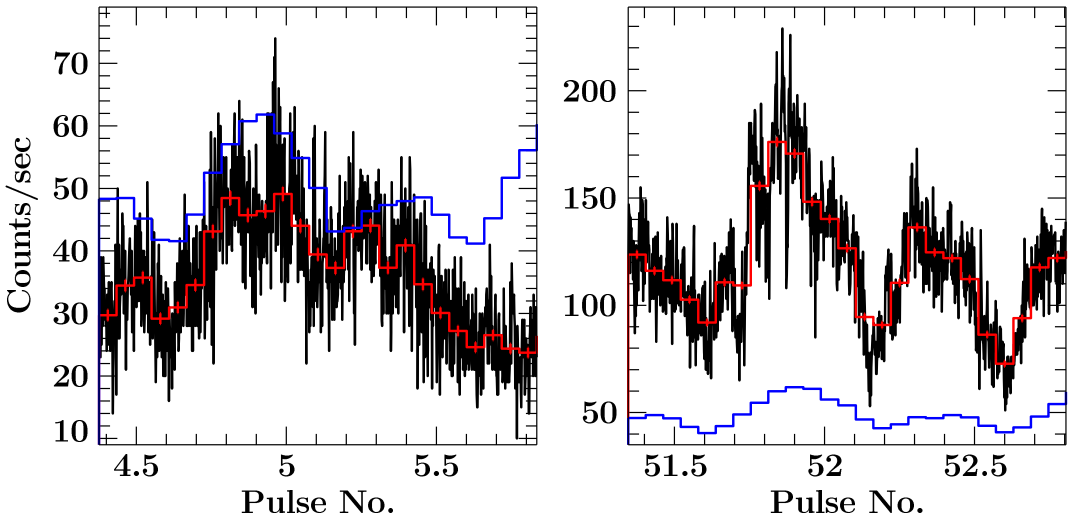

Figure 6.3.: Two examples of the variability of the pulse shape, left an example early in the observation, right one close to the end of the observation. Shown in black is the 1 s light curve, in red a 20 s light curve. The blue profile is the average pulse profile over the complete observation. Note that the y-axes are not the same scale.

ent luminosity levels are marked as regions I–IV in Figure 6.2. These changes are also accompanied by changes in the pulse profile and the pulsed fraction. To investigate this behavior in more detail, we folded each regime I–IV separately on the pulse period of $P = 685.0\,\mathrm{s}$ and studied the normalized distribution of the countrate in each phase bin. As the overall countrate is different for every region we also normalized each light curve to its maximum countrate. The mean of the distribution in each phase bin gives the value of the pulse profile in that bin. Figure 6.4 shows the results for all four regimes in a color-coded map. Region III shows the clearest pulse profile, where the mean countrate as well as the whole distribution is changing with phase. This behavior is different in region I. Here the pulse profile is also visible in the mean values but the values measured most often (shown in red in Figure 6.4) are only weakly phase dependent. The two peaks of the profile result from strong outliers and flares at the respective phases. In region II a similar effect is seen, but the overall pulsations are weaker. Region IV has a very short duration and therefore provides barely enough statistics for an interpretation. The behavior seems similar to the one seen in region III, but the pulse profile is not that well pronounced.

Region II seems to be the region with the weakest pulsations and shows a very different behavior compared to region III. To investigate these differences further, we took a closer look at the 5 s light curve during region II, as shown in Figure 6.5. In the beginning the pulse is visible but it vanishes almost completely during the decline of the luminosity for ∼3 rotations. Around $t = 21000\,\mathrm{s}$ a sudden increase of the luminosity is accompanied by weak pulses but these disappear again after ∼4 rotations of the neutron star, also during a dip in the brightness. Looking at the hardness ratio during that time (Figure 6.2, lower two panels) allows us to deduce the spectral shape. The hardness ratio was calculated

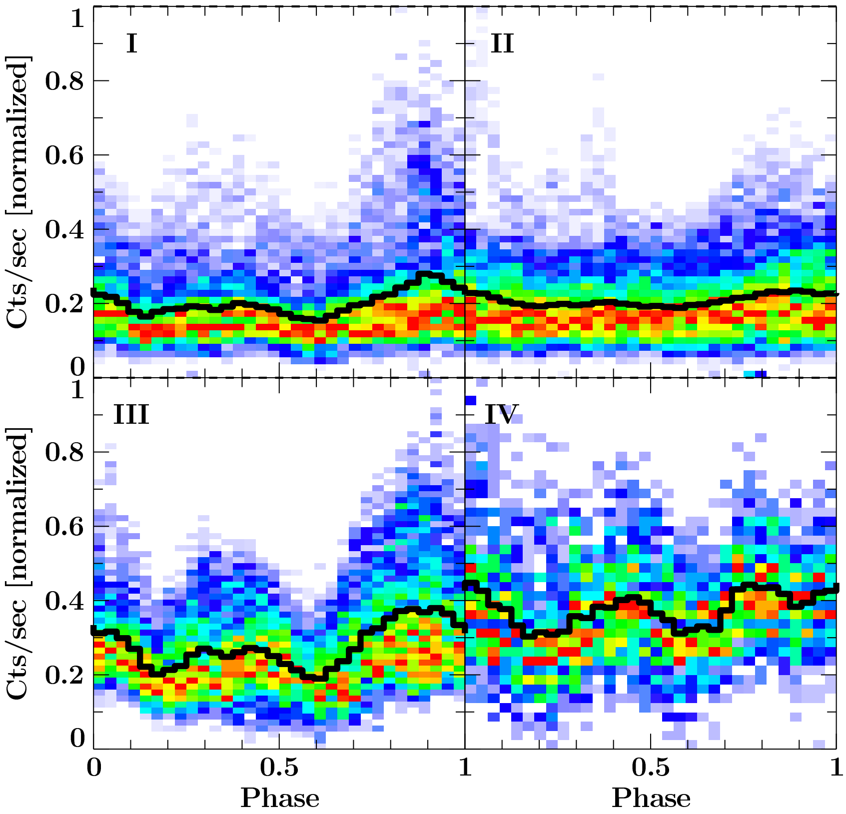

Figure 6.4.: Color-coded maps of the pulse phase distribution of normalized countrates in regions I–IV as indicated in Figure 6.2. See text for details. Color represents the number of measurements for each countrate in the respective phase bin. Each phase bin was normalized to itself, so that they have all comparable color-codes. Colors are ranging from violet, corresponding to zero, to red, corresponding to one. The superimposed black line shows the mean value, i.e., the pulse profile.

as $\mathrm{HR}(H,S) = (H-S)/(H+S)$, with H indicating the count rate in the harder and S in the softer energy band. When comparing the count rate in the 8.5–10 keV continuum band C to the count rate in the strongly absorbed energy band A between 4–5 keV, no significant variability of the hardness $\mathrm{HR}(C,A)$ can be measured during region II. Neither is a change compared to region I visible, indicating that the reduced flux is not due to increased absorption, which would primarily absorb the soft X-rays and would thereby make the spectrum overall harder. Contrary to that we see that the hardness $\mathrm{HR}(C,F)$ between the count rate in the continuum band and in the iron line energy band F between 6.3–6.5 keV changes dramatically in region II. The strong drop of the hardness indicates that the flux of the iron line is not reduced as strongly as the continuum flux.

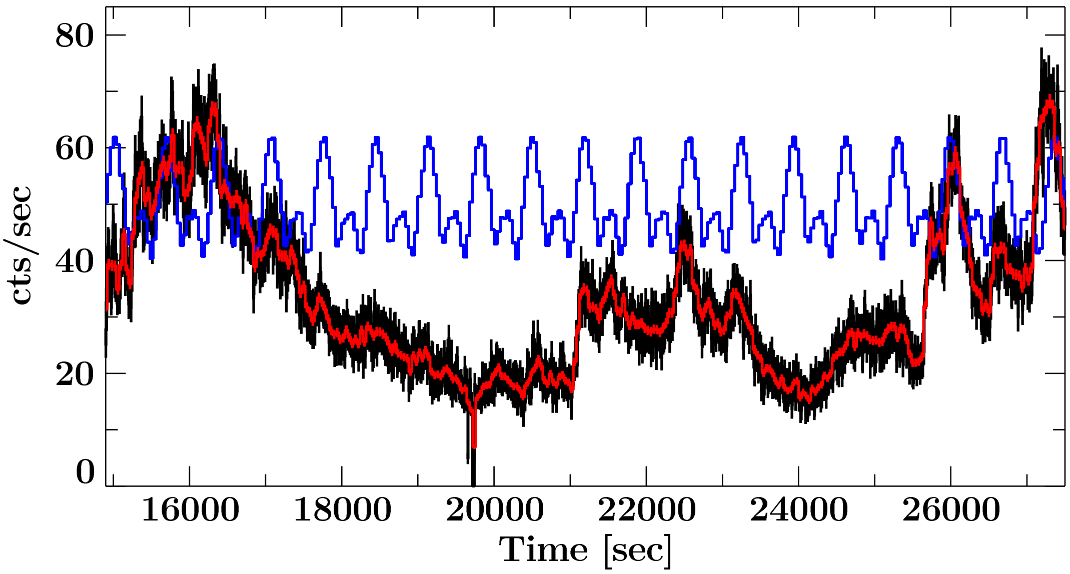

Figure 6.5.: Small part of the light curve between 0.3–12.0 keV, showing a vanishing of the pulsations. In black the light curve with 5 s resolution is shown, in red with 40 s resolution. Superimposed in blue is the average pulse profile for the whole observation.

6.3.2 Pulse profiles and pulsed fraction

Earlier observations with *RXTE* and *BeppoSAX* have already shown that the pulse profile of GX 301−2 is strongly energy dependent (Kreykenbohm et al., 2004; La Barbera et al., 2005). It is exhibiting a double peak shape in which the main peak (P1) is broader below 10 keV. The second peak (P2) stays rather constant in width, but increases its relative intensity toward higher energies. This behavior is confirmed in the *Suzaku* data, as shown in Figure 6.6. The *Suzaku* data were folded onto a period $P = 685.75$ sec, as obtained from the *Fermi*/GBM monitoring (Finger, 2011, priv. comm.) and consistent with $P = 685.4 \pm 0.9$ sec found from epoch folding of the lightcurve. The average *XMM-Newton* pulse profile is only weakly energy dependent and very similar to the XIS one.

Endo et al. (2002) and Tashiro et al. (1991) have shown that the pulsed fraction in the iron line energy band is significantly smaller than in other neighboring energy bands. Analysis of *XMM-Newton* data confirms this behavior, indicating that the matter producing the fluorescent iron line is distributed homogeneously around the X-ray producing region. The pulsed fraction f was calculated using

$$f = \frac{\max(P) - \min(P)}{\max(P) + \min(P)} \tag{6.1}$$

with P denoting the pulse profile. The pulsed fraction is plotted in Figure 6.7 for the four different regions defined above. Common to all four regions is the fact that the pulsations in the iron line band are notably reduced. In region IV the dip is least prominent, probably due to the overall low pulsations and the short duration of this region. The same effect of

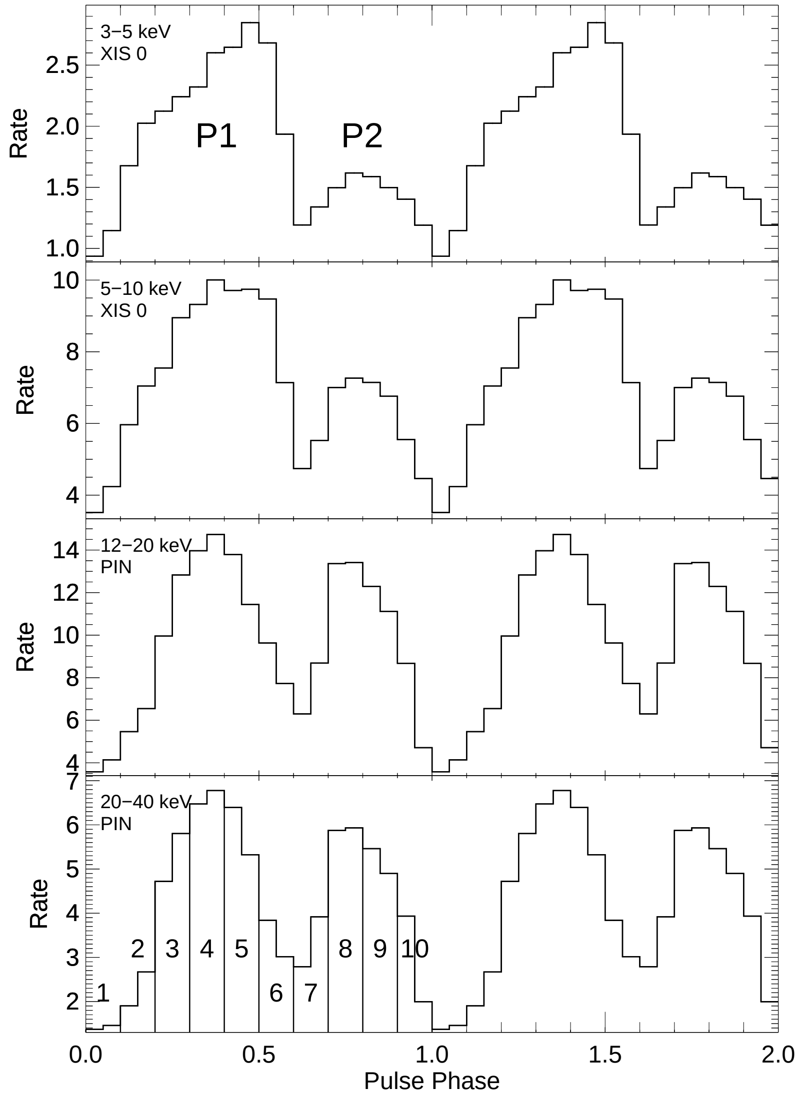

Figure 6.6.: Pulse profiles in different energy bands, as measured with *Suzaku*. From top to bottom: 3–5 kev with XIS, 5–10 keV with XIS, 12–20 keV with PIN, and 20–40 keV with PIN. The two peaks are labeld in the top panel. The bottom panel shows the selection of phase bins which are used for phase resolved spectroscopy (Section 6.4.4) (Suchy et al., 2011a).

a less pulsed iron line is also seen in the *Suzaku* data, albeit at a lower energy resolution due to the lower count rate (see Figure 6.8).

Figure 6.7 also clearly shows that the pulsed fraction is variable with time, dropping significantly during region II, as already seen in Figures 6.4 and 6.5. Some residual pulsed fraction is still measurable outside of the iron line band, but as the iron line band dominates the whole spectrum during that interval, almost no pulsations are visible in the broad band light curve. The lowest energy bin, between 0.5–4.0 keV is dominated by the strong absorption, smearing out the pulsations and reducing the S/N. With increasing

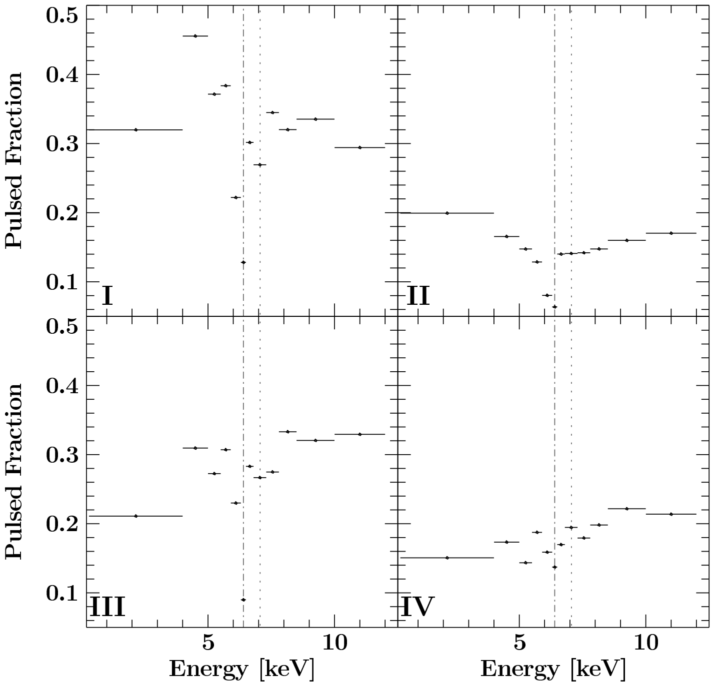

Figure 6.7.: Pulsed fraction from the *XMM-Newton* observation for different energy bands and for the 4 different regions I–IV. The dashed vertical line marks 6.4 keV, the energy of the Fe Kα line, the dotted one 7.1 keV, the energy of the Fe Kβ line.

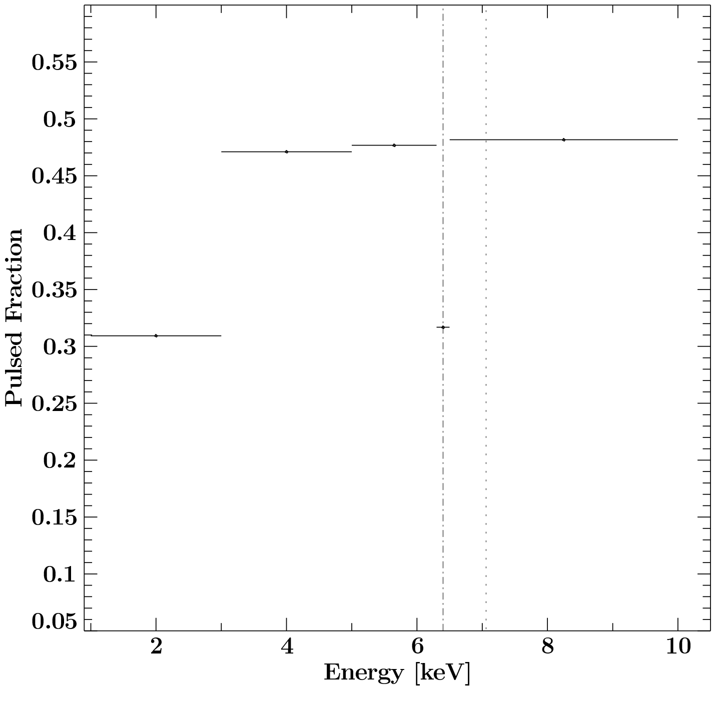

Figure 6.8.: Same as Figure 6.7, but for the whole *Suzaku* observation using five energy bands and only XIS 0 data.

energy the pulsed fraction increases above 6.4 keV, with exception of the energy bin covering the Fe Kβ line at 7.1 keV. The Fe Kβ line is strong enough to contribute significantly to the flux in that bin, and the line is, similar to the Fe Kα line, only very weakly pulsed.

6.4 Spectral analysis

SPECTRAL measurements of point sources are always a superposition of spectra originating in different regions under a different physical environment. For example, the magnetic field strength in the accretion column depends on the altitude above the neutron star (Becker & Wolff, 2007), and as the altitude of the measured line producing region is changing with accretion rate and pulse phase, different CRSF energies are present in an averaged spectrum. By reducing the exposure time in each spectrum as far as S/N allows or by performing pulse phase resolved spectroscopy, this superposition can be lessened. The first approach was applied to the *XMM-Newton* data, and they were first split by luminosity and hardness state (Section 6.4.2). In a second step, we wanted to directly measure the changes between each pulse and we extracted spectra with only 685.0 s exposure time and performed “pulse-to-pulse” spectroscopy (Section 6.4.3). The changes between individual pulses proved to be stronger than the changes throughout the pulse, so that no pulse phase resolved spectroscopy of the *XMM-Newton* data was performed. The *Suzaku* data were much less variable so that pulse phase resolved spectroscopy could give valuable insight in the geometry of the accretion column (Section 6.4.4).

Even though the overall averaged spectrum is a superposition, it still is a good starting point for spectral modelling as it provides the best statistics. Thereby it allows to search for weak, but relatively constant features, and constrains the applicable model parameters. To do so, the average *XMM-Newton* and *Suzaku* spectra are first of all presented in Section 6.4.1 and the applied models are explained.

6.4.1 Phase averaged spectrum

WHEN looking at the averaged X-ray spectrum of GX 301$-$2 (see Figures 6.9*a* and 6.10*a* for the *XMM-Newton* and *Suzaku* one, respectively) a large iron Kα fluorescent emission line is visible, as well as an equally large absorption column, which reduces the countrate to effectively zero below 2 keV. The *XMM-Newton* EPIC-pn 2–10 keV spectrum can be reasonably well described by a partially covered power law, with additional lines at the Fe Kα, Fe Kβ, Ni Kα, Ca Kα, Ar Kα, and S Kα fluorescent line energies. These lines are unusal strong for a HMXB and directly evident in the spectrum, probably due to the high column density. Using a Gaussian model for the fluorescent lines provides a good description of their residuals, the only exception being the Fe Kα line, as discussed later. An exponential cut-off, as used in the literature (e.g. Endo et al., 2002) was not necessary, as the cutoff energy lies above the energy range of *XMM-Newton* (but see Equation 6.4

for the description of the *Suzaku* data). We used a model of the form:

$$N_{\mathrm{H}}^{\mathrm{gal}} \times \Big(\big(cN_{\mathrm{H},1} + (1-c)\, N_{\mathrm{H},2} \big) \times \text{power law} + \text{Gaussian lines} \Big) \tag{6.2}$$

Where $N_{\mathrm{H},1}$ and $N_{\mathrm{H},2}$ are the two different parts of the partial coverer and $0 \leq c \leq 1$ is the covering fraction. We applied the `tbnew` absorption model (Wilms et al., 2011, in prep.)[3] for both elements of the partial coverer. For the large column densities measured in GX 301−2 the plasma becomes optically thick and some flux is scattered out of the line of sight. This effect is taken into account with the `cabs` model, described by

$$\mathtt{cabs}(E) = \exp\big(-N_{\mathrm{H}}\, \sigma_{\mathrm{T}}(E) \big) \tag{6.3}$$

where $\sigma_{\mathrm{T}}(E)$ is the Thomson cross section and N_{H} is the equivalent hydrogen column. Both components of the partial coverer were multiplied by the `cabs` model using the same column densities, $N_{\mathrm{H},1}$ and $N_{\mathrm{H},2}$, respectively.

The Gaussian components used to model the fluorescent lines were only photo-electrically absorbed using a galactic $N_{\mathrm{H}}^{\mathrm{gal}} = 1.7 \times 10^{22}\,\mathrm{cm}^{-2}$ (Kalberla et al., 2005), i.e., they were modeled as they appear outside the absorber.[4] This description was chosen because the spectrum shows clear Ar and S Kα lines at 2.3 and 2.9 keV, respectively, which cannot be as strong as observed if they have to pass through an absorption column of $\sim 10^{24}\,\mathrm{cm}^{-2}$, as is necessary to describe the continuum. For a discussion on self-absorption and intrinsic strength of the lines, see Section 6.5.2. Spectral parameters can be found in Table 6.2 and a plot of the spectrum with the separate components and the residuals in Figure 6.9. In Table 6.2 $N_{\mathrm{H},1}$ gives the absorption column which is multiplied by the covering fraction (CF), while $N_{\mathrm{H},2}$ is multiplied by $(1-\mathrm{CF})$. The normalization and the photon index of the power law continuum are given in rows “norm” and “photon index Γ”, respectively.

The Fe Kα line shows strong residuals when fitted with a single Gaussian. Watanabe et al. (2003) have shown that the Fe Kα line shows an extended *Compton shoulder (CS)* at its lower energy side, but the resolution of EPIC-pn does not allow for an unique identification of this feature. Bianchi et al. (2002) have shown that the CS can be described with a box-shaped model. We included such a box in our model, which extends the Gaussian shaped Fe Kα line to lower energies and starts at the centroid energy of the line. This model gives a very good description of the line, as evident in Figure 6.9. In Table 6.2 the row “CS E_1” gives the low energy end of the box, while “CS A” gives its area. The ratio of the flux between the Fe Kα line and the CS is in good agreement with the ratio expected for photons transmitted through a dense absorption column on the order of $10^{23}\,\mathrm{cm}^{-2}$ (Matt, 2002).

The best fit χ^2 obtained with this model was 769 with 376 *degrees of freedom (dof)* ($\chi^2_{\mathrm{red}} = 2.04$). Still snake-like residuals between 5.0–5.5 keV were visible, see panel *b* of Figure 6.9. We identified these residuals with the Kα line of neutral chromium at 5.41 keV (Kaastra & Mewe, 1993; Kortright & Thompson, 2001), and adding a Gaussian emission line in this energy range resulted in an improvement of the fit to $\chi^2 = 713$ with

---

[3] see also `http://pulsar.sternwarte.uni-erlangen.de/wilms/research/tbabs/`

[4] DL value obtained with `nh` (`HEASOFT v6.10`), provided by HEASARC, at the coordinates of GX 301−2

374 dof ($\chi^2_{\text{red}} = 1.91$). The center of the line was found at $5.425^{+0.005}_{-0.030}$ keV in agreement with theory. Still residuals remain around 5.6 keV in absorption, see panel *c* of Figure 6.9. These residuals are in the energy range of the plateau between the iron lines and their escape peaks in the silicon of the detector. The escape peaks and the plateau are clearly visible in the model of the Gaussian components of the Fe Kα and Fe Kβ line in Figure 6.9 due to the large flux of these lines. The residuals could be very well described with a broad Gaussian absorption feature, improving the fit further to $\chi^2 = 488$ with 371 dof ($\chi^2_{\text{red}} = 1.32$) and called "Abs. Feat." in Table 6.2. Using only this absorption feature, and leaving out the Cr Kα line to model the residuals, does not adequately describe the spectrum, and gives a χ^2 of only 562 for 373 dof ($\chi^2_{\text{red}} = 1.51$), see panel *d* of Figure 6.9.

Finally strong residuals remained around 8.3 keV, very close to the energy of the nickel Kβ line at 8.26 keV (Palmeri et al., 2008a). A Gaussian shaped line centered at that energy was used to model the residuals and improved the fit clearly. This last addition resulted in our best fit model, with $\chi^2 = 448$ for 369 dof ($\chi^2_{\text{red}} = 1.214$), of which the residuals are shown in Figure 6.9*f*.

To our knowledge, this is the first time that clear evidence for a Cr Kα as well as a Ni Kβ emission line was found in the X-ray spectrum of a HMXB. Cr has been observed in absorption in other sources before, e.g., in GRO J1655−40 (Miller et al., 2008). These authors found, however, no evidence for fluorescence lines and Cr as well as all other Fe-like elements were found to be highly ionized.

Even though the spectrum was only used above 2 keV, as all bins below are clearly background dominated, the continuum in the energy range between 2–3 keV cannot be accurately described by the partial covering model only. A constant DC level is needed additionally, to lift the continuum in the lowest energy bins. Without this DC component the best fit provides only a χ^2-value of 737 with 370 dof. Values of the DC level are given in Table 6.2 in the row labeled "DC level". The DC level might originate from a low energy response of the large Fe Kα line below the escape peak, which is not fully taken into account in the RMF. A similar effect is known to be present in XIS data from *Suzaku* (Matsumoto et al., 2006) and has also been observed in our *Suzaku* data (see Section 6.2).

The *Suzaku* data between 2–90 keV can be described with a very similar spectral model, but due the extended high energy range, an exponential cut-off needs to be included. This cut-off was represented using the *Fermi-Dirac cut-off spectral model (*`fdcut`*)* proposed by Tanaka (1986) which was multiplied to the powerlaw continuum:

$$I_{\text{cont}}(E) \propto \frac{E^{-\Gamma}}{\exp(E - E_{\text{cut}}/E_{\text{fold}}) + 1} \tag{6.4}$$

Here E_{cut} is the cutoff energy, and E_{fold} is the folding energy of the Fermi-Dirac cut-off. With a value of $29.2^{+13.5}_{-2.1}$ keV, E_{cut} was significantly higher than the ~ 20 keV value measured in previous *RXTE* (Mukherjee & Paul, 2004) and *BeppoSAX* (La Barbera et al., 2005) observations. The folding energy $E_{\text{fold}} = 5.7^{+0.4}_{-2.5}$ keV is consistent with the *RXTE* data for the pre-periastron flare and the periastron passage (Kreykenbohm, 2004; Suchy et al., 2011a).

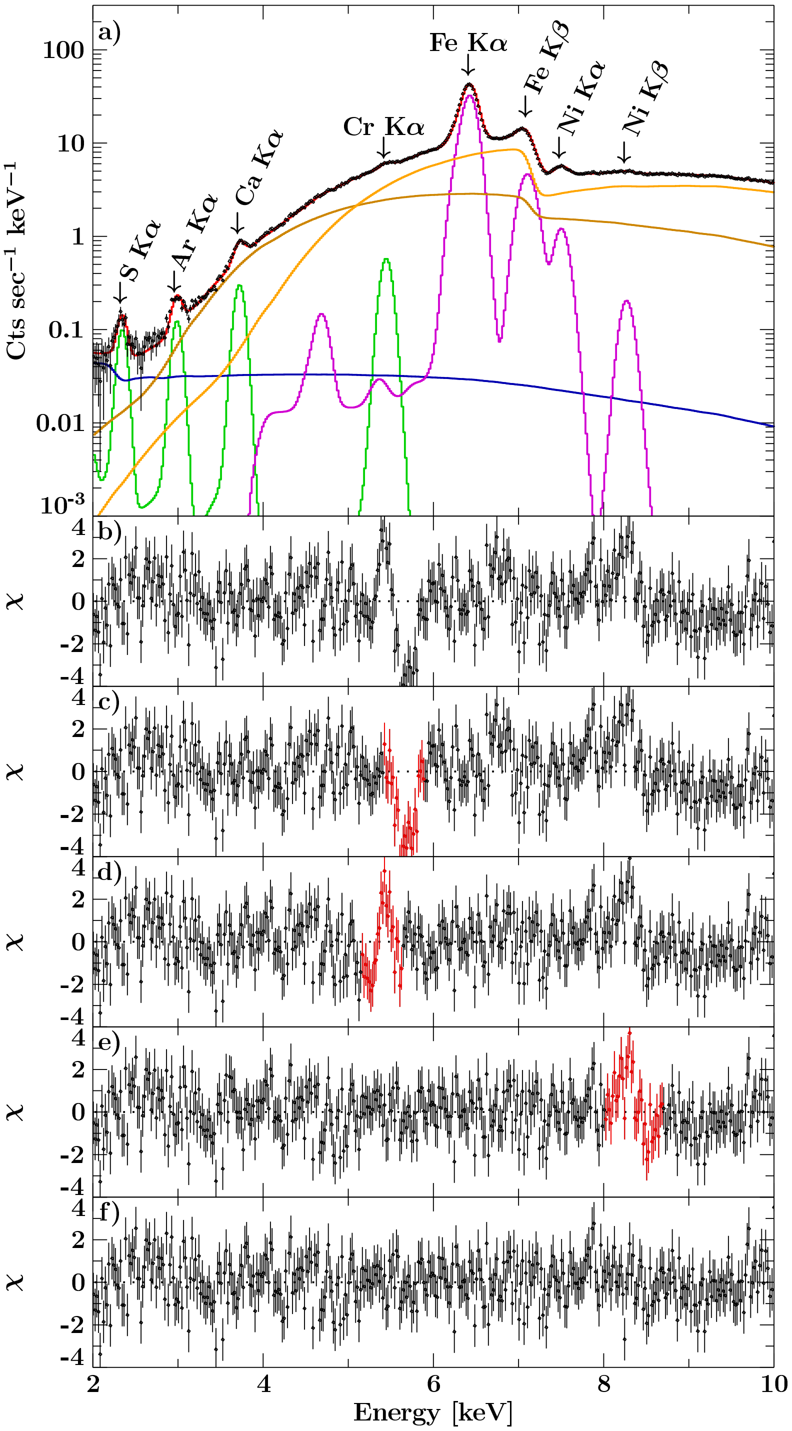

Figure 6.9.: *a)*: Phase and time averaged *XMM-Newton* spectrum in the 2–10 keV energy range of EPIC-pn. The components of the spectral model are shown in different colors, see text for a detailed description. *b)* Residuals with neither an absorption feature nor an Cr Kα line around 5.4 keV. *c)* Residuals with a Cr Kα line, but without an absorption feature. *d)* Residuals with an absorption feature, but without a Cr Kα line. *e)* Residuals without a Ni Kβ line. *f)* Best fit residuals.

The implementation of the model was done in a slightly different way than for the *XMM-Newton* data, because XSPEC instead of ISIS was used to analyze the data. The model had the form:

$$N_{\mathrm{H},1}\left(\text{power law}_1 + N_{\mathrm{H},2} \times \text{power law}_2\right) \times \text{fdcut} \times \text{CRSF line} + \text{Gaussian lines} \tag{6.5}$$

The photon indices Γ_i of the power laws were tied to each other, but the respective normalizations A_1 and A_2were left independent. The covering fraction (c in Equation 6.2) is then calculated as

$$c = \frac{A_2}{A_1 + A_2} \quad . \tag{6.6}$$

From the technical description of the XIS instruments[5], it is known that small discrepancies, e.g., in fitted power law slope, have been observed between Front Illuminated (FI) and Back Illuminated (BI) XIS instruments. Due to the higher sensitivity of the FI XIS instruments above 2 keV, we concentrated our discussion on the results obtained with the two FI instruments, XIS 0 and 3. For a comparison between the BI and FI instruments see Suchy et al. (2011a).

As the *Suzaku* data were taken during a lower flux state than the *XMM-Newton* data, no evidence for a Cr Kα, a Ni Kβ line, nor the Compton shoulder of the Fe Kα line could be found. All other fluorescent lines from the *XMM-Newton* model are visible (see Table 6.1), with the energies of the lines consistent with emission from neutral elements (Kaastra & Mewe, 1993).

A very good description of the *Suzaku* spectrum was obtained using the abundances of Wilms et al. (2000), however, some residuals were visible around the K-edges of Fe and Ca. Allowing the abundances of these elements to vary, smoother residuals were obtained with marginally increased abundances (see Table 6.1). The other continuum parameters did not show significantly different values (Suchy et al., 2011a).

Using this model, residuals in the 35 – 40 keV energy range are visible (panel *b* of Figure 6.10), which we interpret as the previously observed CRSF (Mihara et al., 1995; Kreykenbohm, 2004). Modeling these residuals with an absorption line at $E_\mathrm{CRSF} = 35.2^{+1.4}_{-0.9}$ keV with a Gaussian optical depth (`gabs`) improved the residuals significantly (see panel *c* of Figure 6.10). The magnetic field strength is then calculated, using Equation 2.9, to be $4.10^{+0.15}_{-0.10} \times 10^{12}$ G, consistent with *RXTE* data (Kreykenbohm, 2004), but lower than observed during the pre-periastron flare (La Barbera et al., 2005; Doroshenko et al., 2010). The energy of the CRSF can change with luminosity, as the altitude of the line production region in the accretion column changes (see, e.g., Staubert et al., 2007, and Section 2.3.2). Direct comparison of the line energy with older publications is, however, difficult as different spectral models were applied. For a more detailed discussion see Suchy et al. (2011a).

The CRSF can alternatively be described with the Lorenzian shaped `cyclabs` model (Mi-

---

[5] `http://heasarc.nasa.gov/docs/suzaku/prop_tools/suzaku_td/`

hara et al., 1990), defined by[6]

$$I_{\mathrm{CRSF}}(E) = \exp\left(-\tau_{\mathrm{CRSF}}\frac{(\sigma_{\mathrm{CRSF}}/E_{\mathrm{CRSF}})^2 \times E^2}{(E - E_{\mathrm{CRSF}})^2 - \sigma^2_{\mathrm{CRSF}}}\right) \tag{6.7}$$

with the variable parameters being the centroid energy E_{CRSF}, the width σ_{CRSF}, and the resonance depth τ_{CRSF}, similar to the `gabs` parameters. The best fit continuum parameters are consistent with the best fit values determined with the `gabs` component. The observed centroid energies of $31.6^{+1.0}_{-0.5}$ keV are of the order of ∼ 10% lower than the energy obtained with the `gabs` model. This discrepancy stems from a different calculation of the line centroid energy and is described in detail in Nakajima et al. (2010). The best fit using the `cyclabs` model gave $\chi^2 = 548$ with 267 dof ($\chi^2_{\mathrm{red}} = 2.05$) and thus showed no significant improvement compared to the `gabs` model. For the final discussion we use the values determined by the `gabs` model. Table 6.1 shows the best fit values for the continuum with a `gabs` CRSF line where the given errors are 90% confidence values.

The best description of the spectrum was achieved with the two separate absorption columns of the partial coverer having very similar values. This fact might indicate that a partial covering model is not necessary to describe the data, but as visible in panel *c* of Figure 6.10, residuals between 2–3 keV remain when allowing for only one absorption column. As the absorption columns are highly variable (see, e.g., Mukherjee & Paul, 2004, and Section 6.4.3), it is possible that the *Suzaku* observation was taken during a state were both observers showed similar column densities but were still present separately.

The *Suzaku* data were taken using four separate instruments. To accommodate for cross-calibration flux issues between them, we included instrument dependent constants. The constants were used with respect to the XIS 0 data and are labeled $C_{\mathrm{XIS\,3}}$, C_{PIN}, and C_{GSO}, respectively in Table 6.1.

6.4.2 Time resolved spectra

We have seen in the variability of the light curves, pulsed fractions, and hardness ratios that the overall *XMM-Newton* spectrum will only provide a very inadequate description of the physics of the neutron star, as many different accretion regimes are mixed together. The *Suzaku* data on the other hand were more constant and we could find no indication for changing spectral parameters during the observation. Sacrificing S/N we decided to split the *XMM-Newton* spectrum according to the four regimes I–IV defined in Section 6.3 and indicated in Section 6.2 to quantify the observed changes. These states show the strongest differences in the light curve and hardness ratio and are therefore expected to show different spectra. This Section is consequently exclusively based on *XMM-Newton* data.

All spectra were rebinned to a S/N of 12 up to 3.5 keV, of 36 up to 6 keV, of 60 up to 8.5 keV and of 48 above. Additionally, at least 4 channels were combined to account for the real energy resolution of the instrument. This binning resulted in different amounts

---

[6] the original definition includes a secondary line at twice the energy, which was omitted by setting its depth τ to zero during fitting.

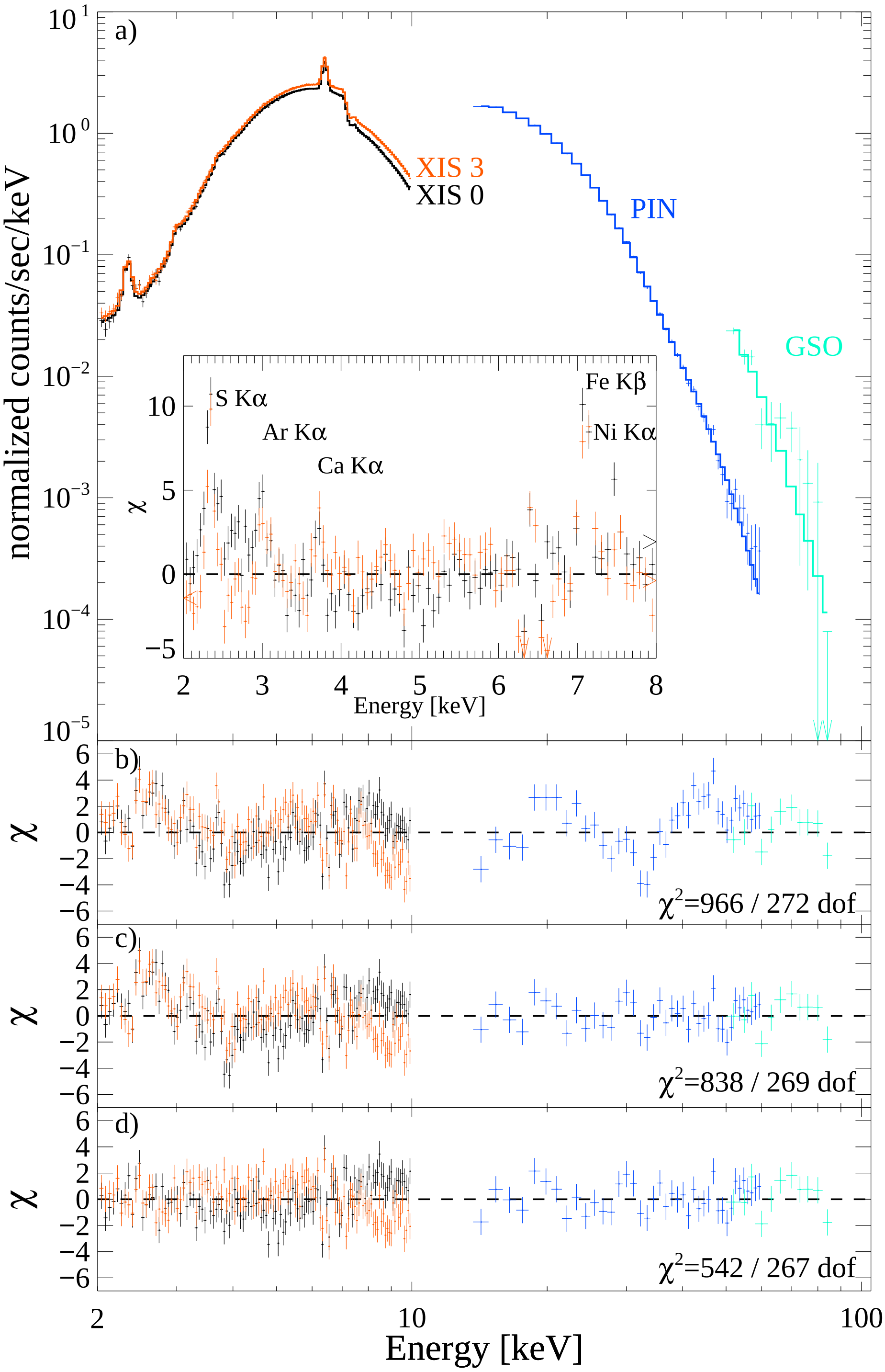

Figure 6.10.: *a)* Phase and time averaged *Suzaku* spectrum. The inset shows the residuals for the different emission lines observed in XIS data, where the Fe Kα line is already included in the model. *b)* shows the residuals without partial covering and the CRSF, *c)* has only the CRSF added and *d)* has both components included (Suchy et al., 2011a).

Table 6.1.: Phase averaged spectral parameters with the `gabs` model component for the best fit *Suzaku* spectrum. Uncertainties are given at the 90% confidence level (Suchy et al., 2011a).

Parameter	Value	Parameter	Value
$N_{\mathrm{H},1}[10^{22}\ \mathrm{cm}^{-2}]$	$20.9^{+3.5}_{-3.3}$	Ca $\mathrm{K}\alpha$ A $[10^{-5}]^2$	$4.72^{+0.95}_{-0.99}$
Abund Ca	$1.55^{+0.39}_{-0.18}$	Ca $\mathrm{K}\alpha$ E [keV]	$3.70^{+0.02}_{-0.01}$
Abund Fe	$1.17^{+0.04}_{-0.03}$	Ca $\mathrm{K}\alpha$ EQW^3 [eV]	14^{+10}_{-8}
$N_{\mathrm{H},2}[10^{22}\ \mathrm{cm}^{-2}]$	$28.4^{+1.0}_{-1.0}$	Fe $\mathrm{K}\alpha$ A$[10^{-4}]^2$	$19.20^{+0.29}_{-0.30}$
Γ	$0.96^{+0.06}_{-0.04}$	Fe $\mathrm{K}\alpha$ E [keV]	$6.409^{+0.003}_{-0.001}$
A_1 $[10^{-3}]^1$ fully covered	$1.1^{+1.1}_{-0.5}$	Fe $\mathrm{K}\alpha\ \sigma$ [eV]	< 5
A_2 $[10^{-3}]^1$ part. covered	$215.5^{+25.1}_{-8.9}$	Fe $\mathrm{K}\alpha$ EQW^3 [eV]	133^{+27}_{-4}
E_{cut} [keV]	$29.2^{+13.5}_{-2.1}$	Fe $\mathrm{K}\beta$ A$[10^{-4}]^2$	$2.65^{+0.27}_{-0.25}$
E_{fold} [keV]	$5.7^{+0.4}_{-2.5}$	Fe $\mathrm{K}\beta$ E [keV]	$7.09^{+0.01}_{-0.01}$
E_{CRSF} [keV]	$35.2^{+1.4}_{-0.9}$	Fe $\mathrm{K}\beta$ EQW^3 [eV]	21^{+7}_{-5}
σ_{CRSF} [keV]	$7.8^{+1.1}_{-0.9}$	Ni $\mathrm{K}\alpha$ A$[10^{-4}]^2$	$1.57^{+0.25}_{-0.25}$
τ_{CRSF}	$12.0^{+37.7}_{-4.5}$	Ni $\mathrm{K}\alpha$ E [keV]	$7.46^{+0.02}_{-0.02}$
S $\mathrm{K}\alpha$ A $[10^{-5}]^2$	$5.36^{+0.50}_{-0.50}$	Ni $\mathrm{K}\alpha$ EQW^3 [eV]	15^{+9}_{-7}
S $\mathrm{K}\alpha$ E [keV]	$2.33^{+0.01}_{-0.01}$	$\mathscr{F}_{2-10\,\mathrm{keV}}{}^4$	$7.98^{+0.00}_{-1.42}$
S $\mathrm{K}\alpha$ EQW^3 [eV]	671^{+491}_{-172}	$\mathscr{F}^{\mathrm{unabs}}_{2-10\,\mathrm{keV}}{}^4$	$31.8^{+1.3}_{-0.2}$
Ar $\mathrm{K}\alpha$ A $[10^{-5}]^2$	$2.74^{+0.55}_{-0.54}$	$C_{\mathrm{XIS\,3}}$	$0.951^{+0.003}_{-0.003}$
Ar $\mathrm{K}\alpha$ E [keV]	$3.00^{+0.01}_{-0.02}$	C_{PIN}	$1.31^{+0.02}_{-0.02}$
Ar $\mathrm{K}\alpha$ EQW^3 [eV]	38^{+29}_{-21}	C_{GSO}	$1.39^{+0.12}_{-0.12}$

$\chi^2/\mathrm{dof} = 542\ /\ 267 \quad \chi^2_{\mathrm{red}} = 2.03$

(1) Units are ph $\mathrm{keV}^{-1}\,\mathrm{s}^{-1}\,\mathrm{cm}^{-2}$, (2) Units are ph $\mathrm{s}^{-1}\,\mathrm{cm}^{-2}$

(3) Values of EQWs are determined relative to the absorbed continuum

(4) Absorbed and unabsorbed flux units are $[10^{-10}\ \mathrm{erg}\,\mathrm{s}^{-1}\,\mathrm{cm}^{-2}]$

of dof for each of the four spectra. We fitted the same model as to the overall spectrum to each one and obtained very good χ^2_{red} values ∼1 for all of them.

The best fit parameters are listed in Table 6.2. It can be seen that the absorption is highest during part II in which the countrate drops very low and the pulsations vanish. During that time the absorption is increased by ∼20% compared to part I. The underlying power law continuum softens at the same time, resulting in comparable hardness ratios. The unabsorbed flux is also highest during part II (see row $\mathscr{F}^{\mathrm{unabs}}_{2-10\,\mathrm{keV}}$ in Table 6.2), so that the observed drop in count rate can be attributed solely to the very high absorption column.

The width, σ, of the Fe Kα line was in all parts around 40 eV, larger than the energy resolution of EPIC-pn. If this width is due to Doppler shifts from turbulence in the fluorescent medium, speeds in excess of $1000\,\mathrm{km}\,\mathrm{s}^{-1}$ would be necessary. In GX 301−2, observational evidence and models suggest that a wind speed of only $300\,\mathrm{km}\,\mathrm{s}^{-1}$ is reached at the position of the neutron star (Kaper et al., 2006; Leahy & Kostka, 2008), which can account for significantly lesser broadening of only ∼10 eV. During accretion the wind will

Table 6.2.: Fit parameters for the best fit model for the overall spectrum and the spectra of the four states I–IV, respectively. For details on the model see text. Uncertainties are given at the 90% limit. The two lowest values are obtained when using a gainshift kernel, as discussed in the text.

Parameter	all	I	II	III	IV
Cov. Frac.	$0.935^{+0.005}_{-0.001}$	$0.943^{+0.011}_{-0.012}$	$0.9796^{+0.0019}_{-0.0018}$	$0.89^{+0.02}_{-0.03}$	$0.968^{+0.010}_{-0.019}$
$N_{\mathrm{H},1}$ [10^{22} atoms cm^{-2}]	141^{+3}_{-2}	147 ± 6	175^{+5}_{-4}	114 ± 5	$130^{+1.2}_{-8}$
$N_{\mathrm{H},2}$ [10^{22} atoms cm^{-2}]	53.7 ± 1.6	59 ± 4	47 ± 2	53^{+3}_{-4}	42^{+9}_{-6}
Norm [keV^{-1} s^{-1} cm^{-2}]	$1.15^{+0.00}_{-0.06}$	$1.19^{+0.18}_{-0.15}$	$2.2^{+0.3}_{-0.1}$	$1.02^{+0.09}_{-0.10}$	$1.1^{+0.4}_{-0.2}$
Photo Index Γ	0.90 ± 0.02	0.93 ± 0.04	1.10 ± 0.04	0.78 ± 0.03	$1.05^{+0.08}_{-0.03}$
Fe Kα A [ph s^{-1} cm^{-2}]	$\left(1.04^{+0.02}_{-0.03}\right) \times 10^{-2}$	$\left(0.82^{+0.04}_{-0.05}\right) \times 10^{-2}$	$\left(1.10^{+0.03}_{-0.04}\right) \times 10^{-2}$	$\left(1.27^{+0.06}_{-0.07}\right) \times 10^{-2}$	$\left(0.78^{+0.09}_{-0.13}\right) \times 10^{-2}$
Fe Kα E [keV]	$6.4227^{+0.0016}_{-0.0001}$	6.413 ± 0.003	6.407 ± 0.002	6.453 ± 0.003	$6.417^{+0.008}_{-0.006}$
Fe Kα σ [keV]	$0.0426^{+0.0016}_{-0.0018}$	0.040 ± 0.004	0.040 ± 0.003	$0.032^{+0.003}_{-0.004}$	$0.029^{+0.008}_{-0.013}$
CS E$_1$ [keV]	6.205 ± 0.009	$6.199^{+0.017}_{-0.019}$	$6.181^{+0.013}_{-0.015}$	$6.249^{+0.015}_{-0.017}$	$6.23^{+0.03}_{-0.04}$
CS A [ph s^{-1} cm^{-2}]	$(2.0 \pm 0.3) \times 10^{-3}$	$\left(2.4^{+0.4}_{-0.5}\right) \times 10^{-3}$	$\left(2.2^{+0.4}_{-0.3}\right) \times 10^{-3}$	$\left(3.3^{+0.7}_{-0.6}\right) \times 10^{-3}$	$\left(1.3^{+0.7}_{-0.6}\right) \times 10^{-3}$
Fe Kβ A [ph s^{-1} cm^{-2}]	$(2.32 \pm 0.05) \times 10^{-3}$	$(1.76 \pm 0.08) \times 10^{-3}$	$(2.04 \pm 0.07) \times 10^{-3}$	$\left(3.68^{+0.11}_{-0.10}\right) \times 10^{-3}$	$\left(1.53^{+0.15}_{-0.14}\right) \times 10^{-3}$
Fe Kβ E [keV]	7.095 ± 0.002	7.087 ± 0.005	$7.070^{+0.003}_{-0.004}$	$7.12669^{+0.00009}_{-0.00016}$	7.063 ± 0.009
Fe Kβ σ [keV]	$0.0675^{+0.0011}_{-0.0002}$	0.069 ± 0.006	0.063 ± 0.005	0.052 ± 0.005	$0.058^{+0.012}_{-0.013}$
Ni Kα A [ph s^{-1} cm^{-2}]	$\left(0.57^{+0.03}_{-0.04}\right) \times 10^{-3}$	$\left(4.4^{+0.5}_{-0.4}\right) \times 10^{-4}$	$\left(0.66^{+0.05}_{-0.04}\right) \times 10^{-3}$	$(0.69 \pm 0.07) \times 10^{-3}$	$\left(0.42^{+0.15}_{-0.12}\right) \times 10^{-3}$
Ni Kα E [keV]	7.491 ± 0.005	$7.484^{+0.005}_{-0.011}$	$7.473^{+0.004}_{-0.000}$	$7.515^{+0.015}_{-0.001}$	7.50 ± 0.03
Ni Kα σ [keV]	$0.036^{+0.010}_{-0.012}$	≤ 0.04	$0.053^{+0.011}_{-0.012}$	≤ 0.03	$0.06^{+0.05}_{-0.06}$
Ca Kα A [ph s^{-1} cm^{-2}]	$(0.73 \pm 0.06) \times 10^{-4}$	$(0.47 \pm 0.09) \times 10^{-4}$	$(0.82 \pm 0.09) \times 10^{-4}$	$(1.03 \pm 0.18) \times 10^{-4}$	$(0.8 \pm 0.2) \times 10^{-4}$
Ca Kα E [keV]	$3.71^{+0.02}_{-0.01}$	$3.71^{+0.03}_{-0.00}$	$3.716^{+0.004}_{-0.011}$	$3.735^{+0.015}_{-0.009}$	$3.69^{+0.02}_{-0.03}$
Ar Kα A [ph s^{-1} cm^{-2}]	$(3.2 \pm 0.3) \times 10^{-5}$	$(1.9 \pm 0.5) \times 10^{-5}$	$(3.1 \pm 0.5) \times 10^{-5}$	$(0.47 \pm 0.09) \times 10^{-4}$	$\left(0.48^{+0.16}_{-0.14}\right) \times 10^{-4}$
Ar Kα E [keV]	$2.973^{+0.012}_{-0.002}$	$2.969^{+0.016}_{-0.014}$	$2.955^{+0.015}_{-0.000}$	3.000 ± 0.015	2.96 ± 0.02
S Kα A [ph s^{-1} cm^{-2}]	$(3.3 \pm 0.4) \times 10^{-5}$	$(2.1 \pm 0.5) \times 10^{-5}$	$(3.0 \pm 0.5) \times 10^{-5}$	$(0.61 \pm 0.10) \times 10^{-4}$	$\left(2.9^{+1.7}_{-1.8}\right) \times 10^{-5}$
S Kα E [keV]	$2.336^{+0.008}_{-0.004}$	2.35 ± 0.02	2.315 ± 0.011	2.348 ± 0.012	2.36 ± 0.06
Abs. Feat. A [ph s^{-1} cm^{-2}]	$\left(-0.52^{+0.09}_{-0.10}\right) \times 10^{-3}$	$\left(-3.3^{+1.1}_{-1.2}\right) \times 10^{-4}$	$\left(-2.3^{+0.6}_{-1.9}\right) \times 10^{-4}$	$(-1.5 \pm 0.5) \times 10^{-3}$	$\left(-0.8^{+0.3}_{-0.5}\right) \times 10^{-3}$
Abs. Feat. E [keV]	5.61 ± 0.03	$5.57^{+0.06}_{-0.05}$	$5.67^{+0.03}_{-0.02}$	$5.70^{+0.00}_{-0.09}$	$5.56^{+0.10}_{-0.08}$
Abs. Feat. σ [keV]	0.26 ± 0.03	$0.18^{+0.06}_{-0.05}$	$0.12^{+0.11}_{-0.05}$	$0.45^{+0.09}_{-0.12}$	$0.32^{+0.16}_{-0.12}$
Cr Kα A [ph s^{-1} cm^{-2}]	$(1.5 \pm 0.2) \times 10^{-4}$	$(1.2 \pm 0.5) \times 10^{-4}$	$\left(0.9^{+0.7}_{-0.3}\right) \times 10^{-4}$	$\left(1.9^{+0.6}_{-0.5}\right) \times 10^{-4}$	$(1.9 \pm 0.7) \times 10^{-4}$
Cr Kα E [keV]	$5.430^{+0.015}_{-0.000}$	$5.45^{+0.04}_{-0.02}$	5.42 ± 0.03	5.44 ± 0.03	$5.44^{+0.02}_{-0.03}$
Ni Kβ A [ph s^{-1} cm^{-2}]	$(1.2 \pm 0.3) \times 10^{-4}$	$(0.8 \pm 0.5) \times 10^{-4}$	$(1.2 \pm 0.4) \times 10^{-4}$	$(1.9 \pm 0.8) \times 10^{-4}$	$\left(0.8^{+0.9}_{-0.8}\right) \times 10^{-4}$
Ni Kβ E [keV]	$8.26^{+0.04}_{-0.02}$	$8.28^{+0.06}_{-0.08}$	$8.22^{+0.03}_{-0.04}$	$8.27^{+0.05}_{-0.04}$	$8.2^{+0.3}_{-0.2}$
DC Level [keV^{-1} s^{-1} cm^{-2}]	$(0.48 \pm 0.04) \times 10^{-4}$	$(3.9 \pm 0.6) \times 10^{-5}$	$(3.4 \pm 0.6) \times 10^{-5}$	$(0.74 \pm 0.11) \times 10^{-4}$	$\left(0.4^{+0.3}_{-0.2}\right) \times 10^{-4}$
Ratio Fe	$0.223^{+0.007}_{-0.006}$	$0.214^{+0.014}_{-0.013}$	$0.186^{+0.008}_{-0.007}$	$0.283^{+0.020}_{-0.016}$	$0.20^{+0.04}_{-0.02}$
Ratio Ni	0.20 ± 0.05	0.18 ± 0.11	0.18 ± 0.06	0.23 ± 0.14	0.2 ± 0.2
Fe Ions	–	XII–XIII	VI–XI	≥XIV	IX–XI
χ^2/d.o.f(χ^2_{red})	448.02/369 (1.214)	113.69/122 (0.932)	136.13/120 (1.134)	129.76/131 (0.991)	91.72/90 (1.019)
$\mathscr{F}_{2\text{–}10\,\mathrm{keV}}$ [erg sec^{-1} cm^{-2}]	1.043×10^{-9}	8.863×10^{-10}	7.127×10^{-10}	1.852×10^{-9}	8.048×10^{-10}
$\mathscr{F}^{\mathrm{unabs}}_{2\text{–}10\,\mathrm{keV}}$ [erg sec^{-1} cm^{-2}]	1.617×10^{-8}	1.624×10^{-8}	2.151×10^{-8}	1.797×10^{-8}	1.350×10^{-8}
Gainshift	1.00396 ± 0.00017	$1.0023^{+0.0003}_{-0.0004}$	$1.0010^{+0.0003}_{-0.0002}$	1.0082 ± 0.0003	$1.0019^{+0.0006}_{-0.0005}$
χ^2/d.o.f(χ^2_{red})	468.08/375 (1.248)	129.48/128 (1.012)	172.64/126 (1.370)	133.93/137 (0.978)	101.12/96 (1.053)

become turbulent, however, and thereby possibly locally increasing the wind speed to values high enough to explain the broadening (Mauche et al., 2008). Turbulent flows in the accretion stream are theoretically not yet well understood. A more likely source of apparent line broadening comes from the fact that the Fe Kα line is not a single line, but a superposition of different Kα lines of differently strongly ionized iron (Kallman et al., 2004). This effect can account for a width of 20–30 eV of the observed line, as the single lines cannot be resolved with the spectral resolution of EPIC-pn. Together with broadening in the wind, the observed width of Fe Kα seems realistic. The Fe Kβ line is even broader with values around 65 eV. As the Fe Kβ complex is not as broad as the Fe Kα complex (Kallman et al., 2004), this broadening might be mainly due to confusion with the strong Fe K-edge at 7.1 keV, very close to the line. EPIC-pn's resolution does not allow to completely separate these two features, but attempts to fit the spectra with a narrow Fe Kβ line led to unacceptable χ^2_{red} values.

The centroid energy of the Fe Kα line is changing with time and can be as high as 6.45 keV in part III, where the brightest flare occurred. This energy corresponds to Fe XIX or higher ionized iron, which does not emit a Fe Kβ line, as all M-shell electrons are already stripped from the ion. Still the spectrum of part III shows clear evidence for a Fe Kβ line at 7.127 keV, corresponding roughly to Fe XIII to XIV (Kallman et al., 2004). For the Ni Kα and Ni Kβ lines a similar discrepancy emerges regarding the best fit values: the best fit Ni Kβ centroid energy is very close to the one of neutral nickel (Palmeri et al., 2008a), while the Ni Kα centroid energy requires at least Ni X or higher. The uncertainties of the Ni Kβ energy, allow, however, also for ionization states of this order.

We obtain strongly varying flux ratios between Fe Kβ/Fe Kα = 0.186 – 0.283. The Ni Kβ/Ni Kα ratio seems to be less variable with values between 0.18 – 0.23, and the individual uncertainties are much larger so that they are all consistent with each other (see Table 6.2, rows “Ratio Fe“ and “Ratio Ni“). These values are clearly above the theoretical ones for neutral elements from Kaastra & Mewe (1993), which give Fe Kβ/Fe Kα = 0.125 and Ni Kβ/Ni Kβ = 0.105. Measurements in solid state metals give higher numbers of Fe Kβ/Fe Kα = 0.132 and Ni Kβ/Ni Kα = 0.133 (Han & Demir, 2009). The Ni Kβ/Ni Kα ratio is marginally consistent with all these values within its uncertainties, but the measured iron ratio is clearly higher. Other measurements and calculations for neutral iron give figures of the same order with Fe Kβ/Fe Kα $\approx$ 0.13 (see, e.g., Palmeri et al., 2003, and references therein).

It is conceivable that the fluorescence lines originate from the dense absorbing material. If this is the case, self-absorption is not negligible (Inoue, 1985). For a column density of $N_\text{H} \approx 140 \times 10^{22}\,\text{cm}^{-2}$ the optical depth at the energy of the Fe Kα line is only $\approx$ 60% of the depth at the energy of the Fe Kβ line. If the whole absorption column would act on the lines, the intrinsic ratios are drastically reduced to values between Fe Kβ/Fe Kα = 0.114 – 0.173, much closer to the theoretical values. Such a strong effect is, however, unlikely, as the fluorescence lines at softer energies from elements like S and Ar would vanish completely. The line ratio also depends strongly on the viewing angle and the geometry of the absorber (Molendi et al., 2003, and references therein). Simulations have shown that for certain viewing angles around 45° of a dense slab absorber in transmission the measured ratios are reduced, while softer fluorescence lines, especially the Cr Kα line, are still clearly detected (Barragán et al., 2011, in prep.). A detailed investigation will be presented in a forthcoming publication. For further discussion of the absorption of the fluorescence lines see also Section 6.5.2.

The line energies as well as the flux ratio is expected to change with the ionization state of iron (Palmeri et al., 2003). Allowing for a mixture of different ionizations during each part and using the energies and yields from Mendoza et al. (2004), we found that ions between Fe VI to Fe XIV can explain the observed energies and ratios (see Table 6.2, row "Fe Ions"). Here we neglected self-absorption, as we cannot confine its effect on the ratios. Additionally the Fe Kβ line is superimposed on the iron K-edge and the Gaussian model component can be artificially increased due to a correlation with the edge. The real ionization states are therefore likely to be lower, but changes are still clearly present. We find an indication that the ionization state is correlated with the luminosity of the source but that overall the ionization state stays around intermediate values. In the *Suzaku* data we found an iron flux ratio of Fe Kβ/Fe K$\alpha = 0.14 \pm 0.01$, very close to the neutral value. The overall flux in the *Suzaku* observation was also lower, supporting the weak flux dependence of the ionization state.

It is furthermore possible that the energy calibration of *XMM-Newton* is slightly off and that a small shift in energy depending on the count-rate is present, leading to an apparent shift of the observed line energies. The most likely effect causing such a behavior is either a change in the CTI of the CCD or a gainshift due to X-ray loading. The CTI is decreasing with higher photon flux when impurities in the CCD are filled up with electrons (Strüder et al., 1997), while X-ray loading causes more electrons than expected (see also Section 3.8.2). If these changes are not taken into account correctly, they lead to a shift of measured energies depending on the source flux. The expected uncertainties of the calibration of these effects in EPIC-pn are below ±0.5% (Guainazzi, 2011, priv. comm.).

To investigate the possibility of such a shift we froze the line energies of all measured elements to the values of their respective neutral line energy, with values taken from Palmeri et al. (2008b) for S, Ar, and Ca, Kaastra & Mewe (1993) for Cr, Kallman et al. (2004) for Fe, and Palmeri et al. (2008a) for Ni. We then applied a gainshift kernel, shifting the model counts spectrum energy grid according to $E_{\mathrm{new}}(c) = E_{\mathrm{old}}(c)/\mathrm{gainshift}$ (see also Section 3.8.1, Equation 3.14). The obtained best fits were only marginally worse than with free energies of the lines and the shifts were on the order of 1.001–1.008 (0.1–0.8%), see bottom lines of Table 6.2. These values are only marginally higher than expected from calibration uncertainties but also include unknown source intrinsic energy shifts. The continuum parameters of the spectral model did not change significantly due to the gainshfit, but the fluxes of the fluorescence lines were slightly altered to values marginally consistent with the ones shown in Table 6.2. Especially the Fe Kβ line flux was decreased, possibly due to a better separation from the iron K-edge. This effect influenced also the Fe Kβ/Fe Kα ratio by decreasing it slightly to values ≤ 0.2 at all times, which is closer to the values expected for neutral iron. No significant change of the ratio with luminosity could be observed.

Using the gainshift kernel we can explain the measured line energy shifts stemming purely from detector effects while the physical condition of the plasma in GX 301−2 does not change significantly during our observation.

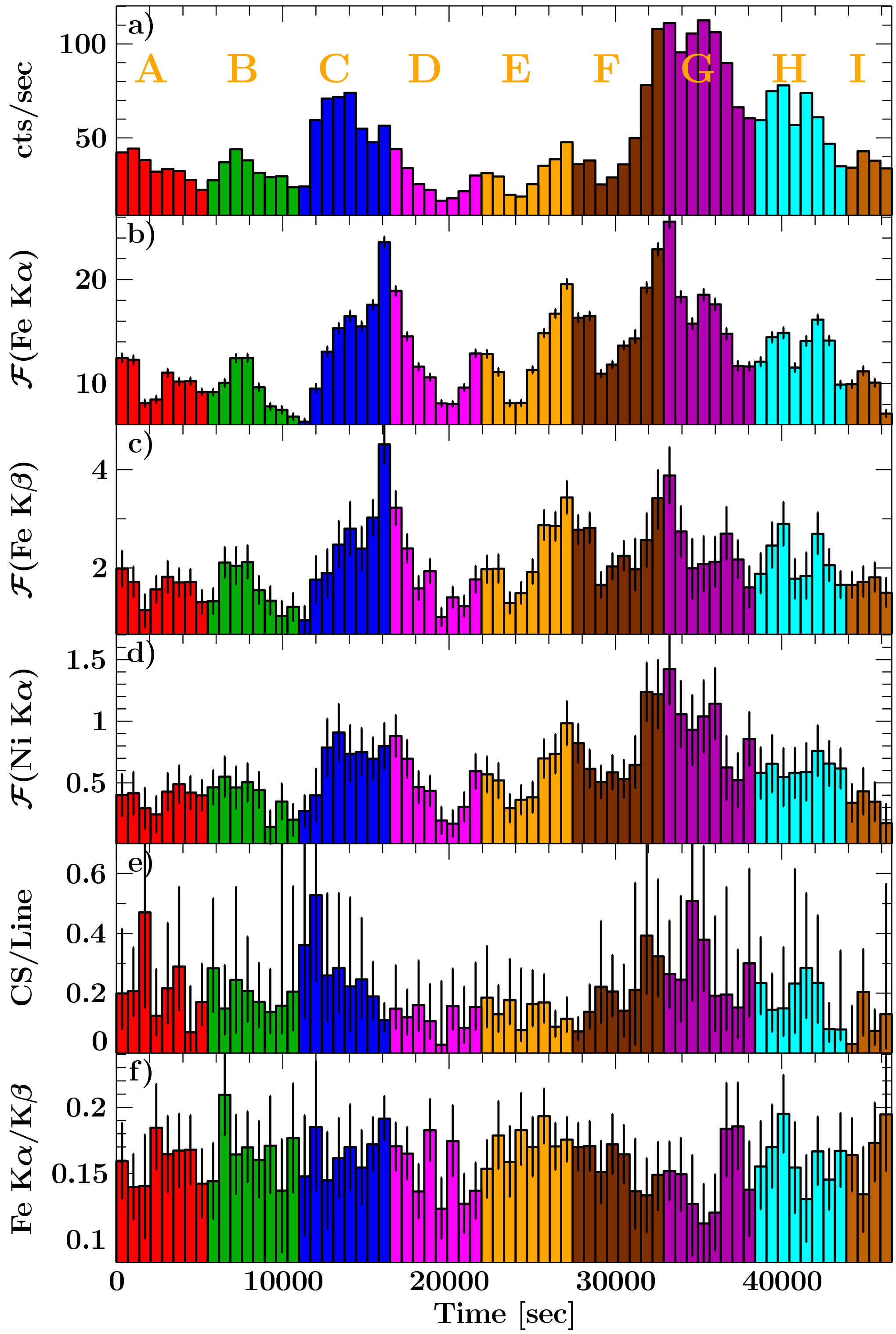

Figure 6.11.: Evolution of the spectral parameters of individual pulses. *a)* Light curve between 0.5–10 keV , *b)* Fe Kα flux (including the Compton shoulder), *c)* Fe Kβ flux, *d)* Ni Kα flux, *e)* ratio between the Compton shoulder and the Gaussian shaped Fe Kα line, and *f)* ratio between the Fe Kα and the Fe Kβ flux. The fluxes of the lines are given in photons $\mathrm{s}^{-1}\,\mathrm{cm}^{-2} \times 10^{-3}$.

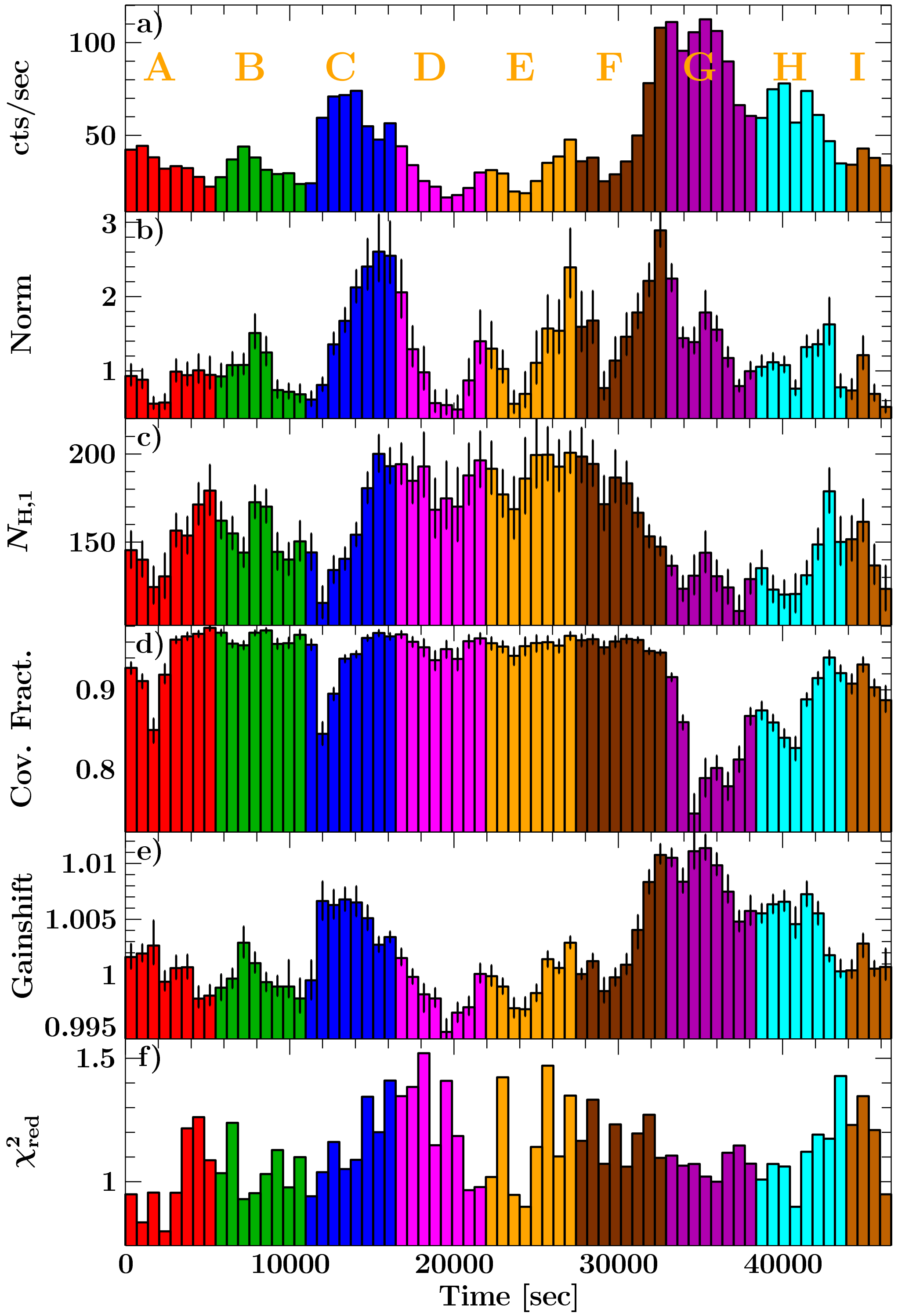

Figure 6.12.: Evolution of the spectral parameters of individual pulses. *a)* Light curve between 0.5–10 keV, *b)* continuum norm in photons $\mathrm{keV}^{-1}\,\mathrm{s}^{-1}\,\mathrm{cm}^{-2}$, *c)* main absorption column in $10^{22}\,\mathrm{cm}^{-2}$, *d)* covering fraction, *e)* gainshift slope, and *f)* χ^2_{red} of the best fit.

6.4.3 Pulse to pulse spectroscopy

IN an approach to understand the time variability of the spectral parameters, especially the iron line complex, in more detail, we extracted spectra for individual pulses from the *XMM-Newton* data, leading to 69 spectra with an exposure time of 685.0 s each. The S/N in the *Suzaku* data did not allow to perform a similar analysis. The resulting model parameters are presented in Figures 6.11 and 6.12. The data are grouped by color into 9 parts labeled A–I to facilitate orientation. We applied a reduced version of the time averaged spectral model and included only the Fe Kα line with its Compton shoulder, the Fe Kβ, and the Ni Kα line. All other fluorescent lines could not be identified in these short exposure spectra. Additionally we had to fix the photon index $\Gamma = 0.90$ and the secondary absorption column $N_{\mathrm{H},2} = 5.37 \times 10^{23}\,\mathrm{cm}^{-2}$ because neither could be constrained well with the data. When leaving the centroid energy of the emission lines free, we found a strong correlation between these energies and the average count rate, as already indicated in the previous Section. This correlation is clearly stronger than expected from ionization (Kallman et al., 2004) and is therefore likely a detector effect. As described in the previous Section, these calibration uncertainties can be modeled with a gainshift kernel. We also checked the spectra extracted using `epfast`, but they showed the same systematic effects.

With fixed energies for the fluorescent lines and for the iron K-edge the use of a gainshift kernel leads to a very good description of the individual spectra. As expected the gainshift is directly correlated to the incident countrate, see Figure 6.12*e*.

The flux of the Fe Kα line and its Compton shoulder is mostly, but not always, correlated with the count rate in the 0.5–10 keV energy band, as seen in Figure 6.11. Especially in the second, main flare (part G) the iron line flux starts to rise with the light curve but breaks down around the maximum of the flare and stays low for the remainder of the observation. A better correlation is observed with the normalization of the power law continuum (Figure 6.12). The Fe Kβ and the Ni Kα lines show a very similar behavior and are strongly correlated with the Fe Kα line flux, with a *Pearson's correlation coefficient* of 0.92 and 0.89, respectively. As discussed in the previous Section, the Fe Kα and Fe Kβ lines required a finite width σ, with an average value of 40 eV and 71 eV, respectively. The widths did not show a significant correlation with time or flux. The width of the Ni Kα was frozen to 10^{-4} keV, to be clearly below the spectral resolution of EPIC-pn.

The absorption column is also strongly changing over the course of the observation, varying by more than 50% (see panel *c* of Figure 6.12). It is increasing during the first flare in part C and stays high until the onset of the second, main flare (parts F and G), where a strong drop is registered. After the flare it is increasing again gradually. The covering fraction is very high throughout the observation, with an average of ∼92%, reducing the secondary absorption column to almost negligible values. It is only during the bright flare in part G where the covering fraction suddenly drops as low as 74%, around the time when the Fe Kα line flux dips.

A typical spectrum with an exposure time of one pulse is shown in Figure 6.13. The Fe Kα and Fe Kβ lines, as well as the iron K-edge, are clearly seen. The Ni Kα line is also visible

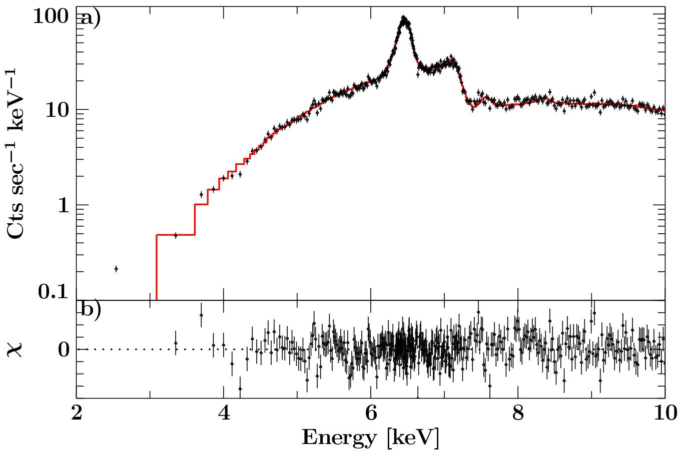

Figure 6.13.: Typical spectrum with 685.0 sec exposure time, i.e., one pulse. The upper panel shows the data and the best fit spectrum, the lower panel shows the respective residuals. For details about the spectral model see text.

on close inspection, but below 3 keV no significant excess over the background can be measured anymore due to the huge absorption column. The Ca, Ar, S, and Cr Kα lines and the Ni Kβ line are not significantly detected.

Assuming the absorbing matter is the same as responsible for the fluorescent iron emission and that it is distributed spherically symmetric around the X-ray source, the equivalent width of the Fe Kα line is proportional to the overall absorbing column (Inoue, 1985). Furthermore, self-shielding should be negligible and the matter is assumed to be cold and neutral. We can see this behavior during most of the *XMM-Newton* observation, even at very large N_H values, see Figure 6.14. The average Pearson's correlation coefficient over all parts except part D is 0.91. During part D, corresponding to the off-state seen in the light curve (Figures 6.2 and 6.5), this correlation is not visible. Instead indication for an anti-correlation with a correlation coefficient of −0.67 exists. During that state the equivalent width of the Fe Kα line reaches its highest values, whereas the N_H stays in a regime around $1.8\times10^{24}\,\mathrm{cm}^{-2}$, lower than the maximal measured value. The overall N_H value is quite high, as expected from the analysis of region II from Section 6.4.2 (corresponding to parts D, E, and F) which showed the highest overall absorption value. But the off-state is happening during part D only, a part which does not stand out for its increased absorption column when compared to parts E and F. This invariance of the N_H value clearly shows that the off-state is not due to a increased absorption, which was already indicated by the softening during that state (see Figure 6.2).

6.4.4 Phase resolved analysis

Using only the *Suzaku* data we performed phase resolved spectral analysis. The data were divided into 10 equally spaced phase bins and individual spectra were extracted for the XIS and PIN instruments. Figure 6.6 shows the individual phase bins in the lowest panel. This division resulted in an exposure time in each phase bin of $\sim 5-6$ ksec for each individual instrument. No GSO data were used in this analysis due to the reduced exposure time per phase bin. For spectral analysis, the phase averaged *Suzaku* model was applied to all phase bins, resulting in best fit values shown in Fig-

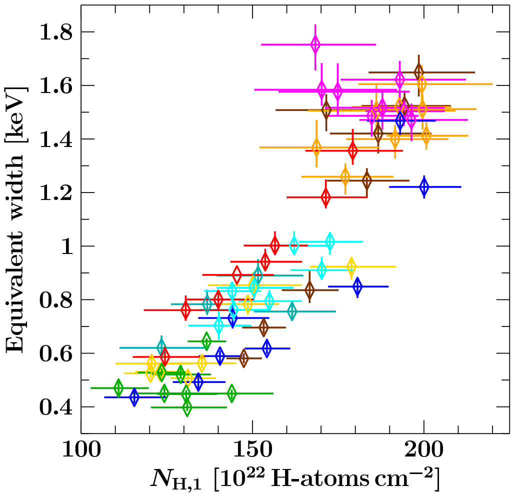

Figure 6.14.: Equivalent width of the Fe Kα line as function of the main absorption column $N_{\mathrm{H},1}$. Colors are the same as in Figure 6.12 and are indicating the time.

ure 6.15. The cutoff energy was frozen to the phase averaged value of 29.2 keV to avoid a degeneracy with E_{CRSF} (Suchy et al., 2011a).

The two absorbing components, $N_{\mathrm{H},1}$ from the smooth stellar wind and $N_{\mathrm{H},2}$ from the partial coverer vary between 20–40×10^{22} cm^{-2}, but show an anti-correlated trend throughout the first peak. Although the error bars are rather large, an indication that $N_{\mathrm{H},1}$ follows the flux in P1 can be seen, whereas the $N_{\mathrm{H},2}$ value dips at the same time (panels *b* and *c* in Figure 6.15).

In contrast to Kreykenbohm (2004), the power law index Γ is varying strongly with phase. The values are 0.9–1.3 throughout the first peak and drop suddenly to 0.6–0.8 for the second peak (panel *d* of Figure 6.15). Measuring the second peak to be significantly harder than the first peak supports the behavior seen in the pulse profile, where the intensity of P2 increases at higher energies until becoming similar to the intensity in P1. Power law normalizations are relatively small and badly constrained for the first power law component (panel *e* in Figure 6.15). The partially covered power law normalization seems to follow the flux, showing a higher value throughout the first peak (panel *f* in Figure 6.15). The folding energy does not vary significantly throughout the pulse and shows values between 5 and 6 keV (not shown in Figure 6.15).

The CRSF energy varies between 30–40 keV (panel *h* of Figure 6.15), similar to the values observed in the *RXTE* data (Kreykenbohm, 2004). The addition of the cyclotron line in the individual spectra improved the χ^2 for most of the phase bins, except in phase bin 6, which falls in the gap between both P1 and P2. Phase bins 1 and 7, also minima in the pulse profile, only showed a small improvement in the best fit when the CRSF was included. In all other bins the addition of the CRSF significantly improved the fit. The CRSF energy changes very smoothly throughout the pulse and does not follow explicitly the observed flux in each phase bin. The visible outliers in phase bins 1 and 6 are not very well constrained due to lack of statistics and are ignored in the discussion. The CRSF energy increases during the main peak and reaches the maximum at the falling flank of P1. During P2 the CRSF energy decreases until it reaches a minimum at the dip between P2 and P1.

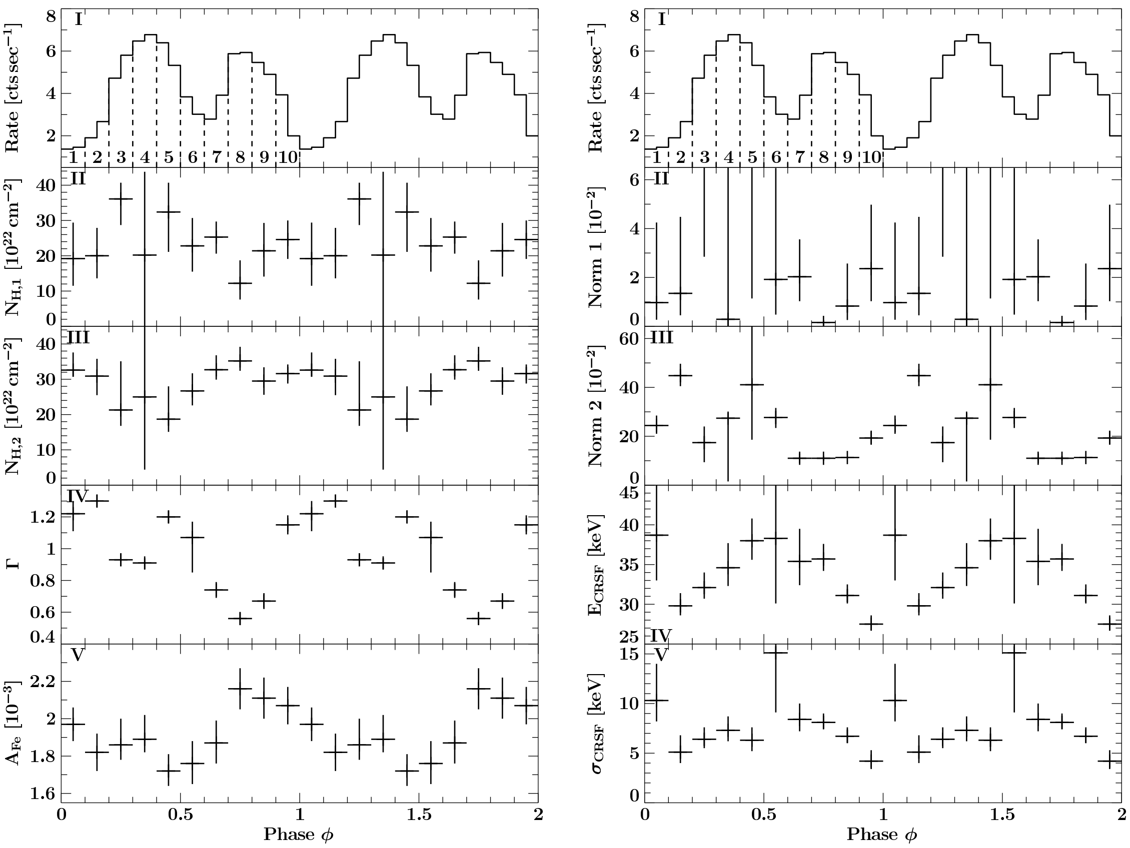

(a) Absorption, photon index, and iron line

(b) Normalizations and CRSF parameters

Figure 6.15.: Phase resolved spectral parameters. **(a)**: (I) 20 − 40 keV pulse profile, with the individual phase bins numbered, (II) absorption column of the smooth component, (III) absorption column of the clumpy wind component, (IV) powerlaw index, (V) flux of the Fe Kα line in ph cm^{-2} s^{-1}. **(b)**: (II) normalization of main powerlaw component in ph keV^{-1} cm^{-2} s^{-1}, (III) normalization of the partially covered powerlaw component in ph keV^{-1} cm^{-2} s^{-1}, (IV) centroid energy of the CRSF, (V) width of the CRSF. For clarity, two pulses are shown (Suchy et al., 2011a).

To check for the significance of the CRSF in the phase resolved spectra we selected phase bin 2 as a good example for a shallow CRSF and phase bin 5 as an example for a high flux phase. For both phase bins we created 10 000 spectra in a Monte Carlo simulation using the respective spectral parameters without the CRSF and distributing them following a Gaussian distribution within their respective uncertainties. All simulated spectra were fitted with and without a CRSF and we analyzed how strongly the inclusion of a line, with an optical depth larger than the lower limit of the observed one, improves the fit. We found that the measured improvement in χ^2 is ruled out with over 99% ($\sim 3\sigma$) to be from stochastic fluctuations, making the CRSF sufficient significant for the interpretation and discussion in Sect 6.5.5.

6.5 Discussion & Conclusion

We have presented a detailed timing and spectral analysis of GX 301−2 during its pre-periastron flare using the EPIC-pn camera of *XMM-Newton* as well as data taken with the *Suzaku* satellite close to apastron. The 2–10 keV spectrum can be described with a partially covered, strongly absorbed power law model enhanced by several Gaussian emission lines from S, Ar, Ca, Fe, and Ni. We found evidence that the Kα line from Cr is also present as well as the Kβ line from Ni. To our knowledge this is the first detection of these lines in a HMXB. In the spectrum above 10 keV, a Fermi-Dirac cutoff and a CRSF at $\sim$ 35 keV are present. In order to account for the different states of activity visible in the *XMM-Newton* light curve we separated the data according to these states, labeling them I–IV. During the sub-flares (parts I and III) regular pulsations with $P = 685.0 \pm 0.1$ s were clearly detected and a double peaked pulse profile is visible. During the off-state II these pulsations vanished almost completely and the countrate dropped to very low values of ~10% of the peak count rate. *XMM-Newton* still detected the source clearly. In the *Suzaku* data a slightly slower period of 685.4 ± 0.9 s was measured and we have seen that the secondary peak of the pulse profile is more prominent at higher energies, indicating a harder spectrum. In phase resolved spectral analysis we confirmed this assumption and found that the secondary peak shows a clearly harder powerlaw continuum. Additionally the energy and width of the CRSF vary almost sinusoidal throughout the pulse. By separating the *XMM-Newton* data into individual spectra for every rotation of the neutron star, we were able to perform a detailed spectral analysis of the off-state. We found that although the absorbing column is very large, it is not drastically increased during that state, compared to values measured shortly before and after it. Instead a softening of the spectra is observed in which the Fe Kα line is even more important than at other times.

We have shown that the absorption column is larger than $10^{23}\,\mathrm{cm}^{-2}$ at all times during our observations and even larger than 10^{24} during the pre-periastron flare. GX 301−2 is not the only source showing absorption columns of this magnitude. *INTEGRAL*, for example, discovered more than 10 highly absorbed HMXBs, which might form a new class of objects (Kuulkers, 2005; Walter et al., 2006). Among them are sources like IGR J16318−4848 (Matt & Guainazzi, 2003; Barragán et al., 2009) or IGR J17252−3616 (Manousakis & Walter, 2011) which show very prominent Fe Kα and Fe Kβ lines, as well as Ni Kα lines. The flux of these sources is, however, usually lower than that of GX 301−2, decreasing the S/N drastically below 4 keV and thereby not allowing for studies of softer fluorescence lines. Results from the iron line energies and Fe Kα/Kβ ratios also indicate only mildly ionized iron. GX 301−2 could therefore be a brighter example of these sources and help to understand this class of HMXBs.

Our analysis also shows a strong variability of the absorption column, on timescales as short as a few 100 s but also long-term changes on the orbital timescale or longer. This variability has also been seen in former studies (e.g., Mukherjee & Paul, 2004) and could also be observed in IGR J17252−3616 (Manousakis & Walter, 2011). We see indications that the X-ray flux is lower with a lower absorption column density. If this is also the case for the other highly absorbed sources, further studies of variable absorption columns might be difficult, due to the intrinsic lower flux of these sources.

Comparing the fluxes with the photon indices of the four parts of the *XMM-Newton* observation as well as from the *Suzaku* observation, an anti-correlation is visible. This softening of the power law index Γ with increased luminosity is in agreement with the basic model of the accretion column predicting that the plasma temperature decreases with height. With increased luminosity, the rate of accreted material increases and with that the amount of soft photons created by the lateral walls of the relatively taller column increases as well, leading to a softer spectrum (Becker & Wolff, 2005a).

6.5.1 Fluorescence region size

To estimate the distance between the X-ray producing region and the fluorescent medium, we extracted *XMM-Newton* light curves with 1 s resolution for the iron line energy band between 6.3–6.5 keV and the harder continuum band between 7.3–8.5 keV. The *Suzaku* data did not provide a good enough S/N ratio to perform this kind of analysis. The countrate between 6.3–6.5 keV is completely dominated by the Fe Kα line and any variability of it must be due to the reaction of the fluorescent line to changes in the continuum flux. We compared both light curves using Fourier transformation as well as cross-correlation techniques and could not find a significant time delay between both curves in the range of 2–5000 s. This finding is in agreement with the size of the fluorescence region being smaller than 10^{10} cm, i.e., 0.3 lt-sec, as given by Endo et al. (2002). The count rate in the narrow energy bands was not high enough to achieve a time resolution sufficient to see a delay of the fluorescence lines on that order. For IGR J17252−3616 Manousakis & Walter (2011) also found that the emission line region is compact and not larger than the accretion radius. However, during the off-state (part D in Figure 6.11) the iron line is still clearly visible, although the luminosity of the continuum has significantly decreased. This leads to the largest equivalent widths for the Fe Kα line measured in the whole observation (Figure 6.14) and seems to indicate that the fluorescence line is partly reacting rather slowly on changes in the continuum. A possible explanation is that the weaker part of the partial coverer is located further out, and thereby reacting much slower to any changes in the X-ray continuum flux. The X-ray flux was low for ~4500 s and we can assume this scale as an upper limit of the light travel time to the absorber. On a direct path, this would place the absorbing medium almost 10 times the average orbital diameter of the system away. Through scattering in the dense medium, with an optical depth $\tau = 1.2 N_{\mathrm{H},1} \times \sigma_{\mathrm{T}} \approx 1$, the effective light-path is increased, so that a size of 2000 lt-sec or less is plausible[7]. A similar geometry was already proposed by Mukherjee & Paul (2004). Through scattering in the inner absorber the outer absorber receives a much less pulsating X-ray flux and transforms it into fluorescence lines, which are consequently also pulsating much less. This effect can explain the reduced pulsed fraction in the Fe Kα and Fe Kβ line band (Figure 6.7). A secondary absorber further out can also explain the dip in N_{H} and in the covering fraction during the large flare in part G (Figure 6.12).

---

[7] assuming 1.2 electrons per H-atom as typical for galactic abundances

Here the inner absorber is almost completely ionized and transparent to soft X-rays. The visible absorption is then primarily due to the still cold outer absorber. The present data do not allow to distinguish between the lines formed in the different absorbers, and as they are both variable it is hard to disentangle the effects. The indications we obtain from the data do, however, support this absorption geometry. If both columns of the partial covering model would be located close to the neutron star, where the large column describes the clumpy stellar wind and the other the smooth part of the wind, neither the large equivalent width nor the strong dip in covering fraction during the large flare are easily explainable. The measured widths of the Fe Kα and Fe Kβ lines as well as their ratio (Section 6.4.2) can also be understood in this geometry as a superposition of cold and neutral iron in the outer absorber and higher ionized iron in the inner one. As stated before, the spectral resolution of EPIC-pn does not allow to separate different iron lines, but we would expect to see an only slowly variable Fe Kα line of neutral iron and many variable lines from the different ionized species from the inner absorber.

In the *Suzaku* data a much smaller flux and equivalent width, together with a much smaller absorption column was measured. A comparison to the *XMM-Newton* data provides only little insight, as the absorber density and geometry is strongly variable in GX 301−2 and the *Suzaku* data were taken almost one year earlier and at a different orbital phase. However, in a more extensive analysis of the *Suzaku* data, using a bigger data set, Suchy et al. (2011a) propose that the fluorescent medium should at least partially be located relatively far away from the X-ray source, as they could find no direct correlation between continuum flux and line flux. This finding is in agreement with the effect we see in the *XMM-Newton* data.

6.5.2 Fluorescence and abundances

EMISSION lines of Fe Kα, Fe Kβ, Ni Kα, S Kα, Ca Kα, Ar Kα are evident in the spectrum of GX 301−2, and can be modelled consistently between *XMM-Newton* and *Suzaku*. Thanks to the better S/N in the *XMM-Newton* data also a Ni Kβ and a Cr Kα line are visible. To perform a further consistency check of our model, especially regarding the Cr Kα line, we applied our model to the *Chandra* HETG data presented by Watanabe et al. (2003) and taken during the pre-periastron flare in January 2001. The model describes the data very well in its overall shape. Neither a Cr Kα nor a Ni Kβ line is significantly detected, but lines with the same flux and width as in the *XMM-Newton* spectrum are also not ruled out by the data and could vanish due to the worse S/N of the *Chandra* data.

In our description of the spectrum we used a model in which the fluorescent lines were only absorbed by the galactic absorption column of $N_\mathrm{H}^\mathrm{gal} = 1.7 \times 10^{22}\,\mathrm{cm}^{-2}$ to accommodate for the observed fluxes of the Kα lines of S and Ar, see Section 6.4.1. The flux of the lines indicates, however, that they originate in a dense absorber and that therefore self-absorption must be taken into account. Additionally timing analysis has shown that the main producing region of the iron line must be very close to the X-ray source and it is likely that this is true for the other lines as well. It is thus conceivable that the photons emitted from the fluorescent ions are also absorbed by material relatively close to the neutron star with a column density in excess of $N_{\mathrm{H}}^{\mathrm{gal}}$, e.g., by the stellar wind of the companion.

In order to estimate how strongly these lines are absorbed we performed the following simple sanity check, assuming the solar abundances given by Wilms et al. (2000) for all elements: for each element, where a fluorescent line was observed, we calculated how many photons were absorbed by this element alone above its respective K-shell, applying the cross-sections by Verner et al. (1996). Using the fluorescence yields for near neutral ions from Kaastra & Mewe (1993) we calculated how many of these photons were reemitted in the respective Kα and Kβ lines. As we do not know the geometry of the fluorescent medium and hence can not tell how many of these reemitted photons reach us, we calculated the fluxes of all lines relative to Fe Kα. We compared these relative fluxes to the fluxes as measured by the Gaussian lines in our model of the *XMM-Newton* data. The relative fluxes of the Gaussian lines are strongly correlated with the absorption column applied, especially for the soft S and Ar lines. By changing the absorption column we can find the best agreement between measurement and calculation. We find that consistency can be achieved with an overall absorption column around $20 \times 10^{22}\,\mathrm{cm}^{-2}$, i.e., a factor of ~6 less than the continuum absorption and consistent with the above assumptions. Systematic uncertainties outweigh any statistical uncertainties in this analysis and are estimated to be on the order of $\pm 5 \times 10^{22}\,\mathrm{cm}^{-2}$. An drastic improvement on this estimate can be achieved using Monte Carlo simulations of different absorber geometries, but this investigation is beyond the scope of this work (see Barragán et al., 2011, in prep.).

6.5.3 The chromium line

We have reported the detection of an emission line at 5.43 keV in the *XMM-Newton* data, compatible with the Kα line energy of neutral chromium. This line is weak and only visible because of the large absorption column of GX 301−2 making it bright enough to be visible over the continuum. The highly absorbed IGR sources mentioned in the beginning of this Section are typically not bright enough to provide enough S/N to allow searches for a Cr line. In Supernova Remnants (SNRs) evidence for fluorescent chromium K lines was found, most notably in W49B (Hwang et al., 2000; Miceli et al., 2006) but also in Tycho, Cas A, and Kepler (Yang et al., 2009). Cr is a decay product of Fe in supernovae, and thus a high iron abundance is accompanied by a high chromium abundance. The ratio of Cr to Fe is ~1% for solar abundances. In supernovae the ratio depends on the explosion model and can be 2% or larger for delayed detonation models (see, e.g., Iwamoto et al., 1999). The SNRs investigated by Yang et al. (2009) show different abundance ratios between 0.63%–3.6%, leading the authors to suspect that they originate from different types of supernovae explosions. Using the method described in the previous Section to calculate the relative strengths and therewith the relative abundances of Cr to Fe we obtain a value of 1.4%, very well within the expected values. Taking only the ratio of the measured photons in the Cr Kα and Fe Kα line, we obtain higher values of ~6.4%, but this value neglects the fact that the K-edge for Cr is lower than the one of Fe and that consequently more photons are able to ionize Cr. With our measurement we cannot infer possible explosion models or production channels of the GX 301−2 system. The measured relative line flux does, however, agree with predicted fluorescence yields and element abundances.

6.5.4 Accretion during the off-state

The off-state is perhaps the single most puzzling feature of the *XMM-Newton* data. A similar off-state was only recently discovered by Göğüş et al. (2011) in *RXTE* data. *RXTE*'s spectral resolution does not allow for a detailed analysis of the iron line region but provides a larger broad band coverage compared to *XMM-Newton*. Göğüş et al. (2011) fitted individual spectra with exposure times of one pulse period each, keeping the iron line fixed and letting the photon index of the power law continuum vary. They found that the photon index is drastically increased during the dip, making the overall spectrum much softer. It thus seems very likely that the accretion was switched off during that time and that only weak Comptonization in the accretion columns was possible, while most of the X-ray flux originated from the blackbody on the neutron star's surface. This result is in accordance with a theory developed to explain similar off-states in Vela X-1 (Kreykenbohm et al., 2008, and references therein). According to this theory, accretion ceases during the off-state and the source enters the propeller-regime, i.e., a regime in which the Alfvén radius is larger than the co-rotating radius (Lamb et al., 1973). This transition is triggered by a strong decrease in the mass accretion rate, possibly due to a strongly structured or clumped wind (Oskinova et al., 2007; Kreykenbohm et al., 2008; Fürst et al., 2010). Even though GX 301−2 is not directly accreting from the wind in the pre-periastron flare but rather from an accretion stream (Leahy & Kostka, 2008), strong density variations are evident through the flaring behavior of the light-curve (Figure 6.2). Other observational evidence for a clumpy wind around Wray 977 was put forward by Mukherjee & Paul (2004) who studied in detail the time variability of the absorption column on short and long timescales.

All our results indicate that the observed off-state was caused by a cessation of accretion and not by an optically-thick clump moving through the line of sight. A clump in the line of sight would also lead to drastically reduced pulsations and flux, as the X-ray flux is scattered in the absorber and thereby smearing out the pulsations (Makino et al., 1985). In the spectral analysis, however, we would expect that the spectrum gets harder, as softer X-rays are affected stronger by absorption than harder X-rays. We would also expect to see a drastic increase of the absorption column. Both are not the case, as seen in Figure 6.12.

We investigated the overall behavior of the pulsed fraction as function of N_H, and found almost no correlation (Figure 6.16), contradictory to the results by Makino et al. (1985). It is thus very unlikely that the complete disappearance of pulses in part D is to be caused by larger N_H values, as scattering in the absorption medium seems to be influencing the pulsed flux only marginally. The variation in the pulsed fraction seems to originate from different accretion rates, as expected from a clumpy accretion medium. This influence is also supported by the variability of the individual pulse profiles, as shown in Figure 6.3. We do not see a weaker pulsed flux with essentially the same shape causing the lower pulsed fraction, but rather a clear change in the overall pulse profile caused by a different accretion rate.

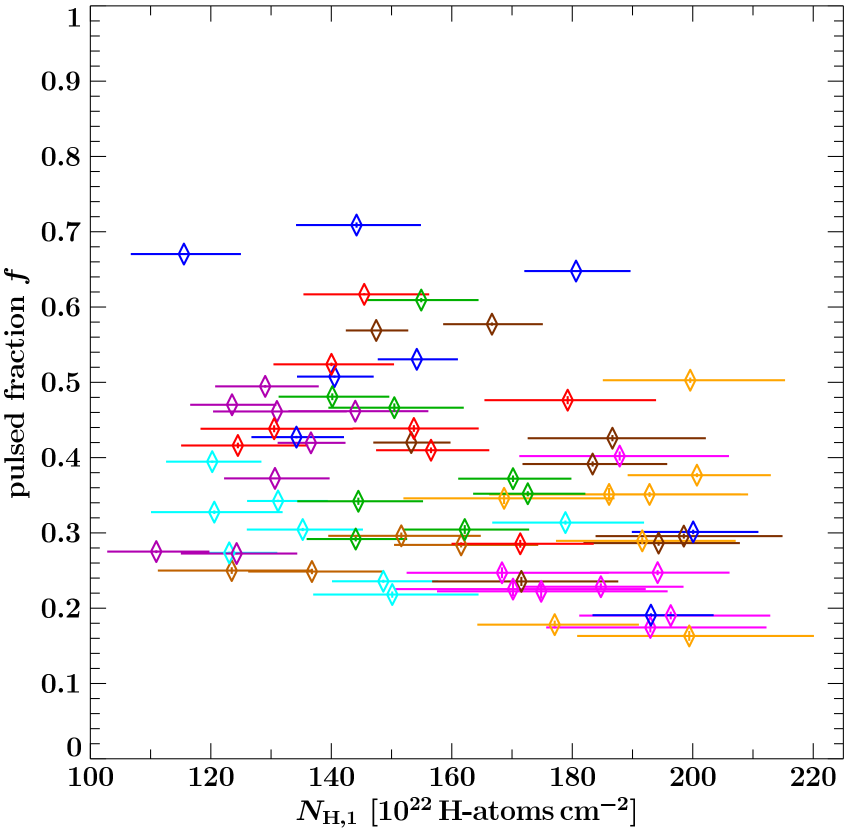

Figure 6.16.: Pulsed fraction as function of $N_{\mathrm{H},1}$. Color code is the same as in Figure 6.12.

From results at harder X-rays (Evangelista et al., 2010) a decrease of the pulsed fraction with decreased luminosity would be expected. In a simple toy model this can be explained by a change in altitude of the X-ray producing region in the accretion column (Lutovinov & Tsygankov, 2009). Such a change would also be visible in a change of the energy of the CRSF (Doroshenko et al., 2010). We did not find a correlation between the pulsed flux and the luminosity in the *XMM-Newton* data and also no significant change of the CRSF centroid energy could be found in *Suzaku* (Suchy et al., 2011a). The pulsed fraction during the pre-periastron flare is the lowest over the whole orbit and is also much lower in the soft than in the hard X-rays (Evangelista et al., 2010). It is thus possible that a change in the accretion column might not be visible in the pulsed fraction of the 2–10 keV band.

Assuming that the off-state was caused by a cessation of accretion, possibly because the neutron star entered the propeller regime, the remaining X-ray flux is mainly coming from the still fluorescent absorbing medium around the neutron star, as described in Section 6.5.1.

As shown in Figure 6.14 during the normal states the equivalent width of the Fe Kα is correlated with the $N_{\mathrm{H},1}$ value. This correlation is explained by the assumption that the fluorescent medium is the same as the absorbing medium. As a result, a higher absorption column leads also to a brighter fluorescence line as more atoms in the absorber are ionized by the X-ray continuum. During the off-state, the X-ray continuum is drastically reduced leading to a reduced Fe Kα line from the main absorber in the line of sight. The off-state indicates a very clumpy medium, so that the absorption in the line of sight is not necessarily an indicator for the overall density of the medium surrounding the X-ray source. The observed break-down of the correlation between equivalent width of the Fe Kα line and the $N_{\mathrm{H},1}$ value can thus be explained by a complex structure of the medium around the neutron star. For example, fluorescence from a dense medium behind the neutron star could arrive simultaneously with the reduced continuum flux at the observer due to different light-travel times. The remaining continuum flux during the off-state could also be due to Compton reflection from a dense medium around the neutron star, similar to the scenario proposed by Rea et al. (2005) to explain a long low-intensity state in the LMXB GX 1+4. These authors analyzed broad band *BeppoSAX* spectra and found that they could be described by a cut-off power law plus a reflection component, the latter becoming more important during the low intensity state. In this state also the Fe Kα line reached the highest equivalent widths, similar to GX 301−2. Rea et al. (2005) found that although the pulsations vanished below 7 keV they could still be seen in the harder X-rays, an effect we cannot investigate with the *XMM-Newton* data but which is not evident in the *RXTE*/PCA data presented by Göğüş et al. (2011). If the reflecting surface is not as well defined as in the geometry proposed for GX 1+4, all pulsations can be smeared out over a broad energy range, so that the reflected continuum flux is also unpulsed when escaping the medium around the system. More observations in a broader energy range are necessary to understand the geometry further. A sufficient energy range is provided by *Suzaku*, but during our observation no off-state occurred.

6.5.5 Geometrical constraints of the magnetic field

PHASE resolved analysis of the *Suzaku* observation showed that several spectral parameters vary strongly throughout the pulse profile. As previously observed by Kreykenbohm et al. (2004), the CRSF centroid energy varies by $\sim 30\%$ where the highest energy is detected at the peak and the falling flank of P1. Such behavior has been observed in multiple other sources, e.g., Vela X-1 (La Barbera et al., 2003), 4U 0352+309 (Coburn et al., 2001), and Her X-1 (Klochkov et al., 2008). A model for the CRSF variations is based upon the change in the viewing angle throughout the pulse and thus different heights of the accretion column are probed, yielding a different local magnetic field observed for each phase bin.

A simple approach to derive a possible geometry for the neutron star and the magnetic field uses the variation in the observed magnetic field throughout the pulse phase. In this case the very smooth and sinusoidal variation (Figure 6.17) can be modeled as a simple dipole where the total magnetic moment μ is calculated from the phase averaged CRSF value, and then geometrical angles are fitted. The dipole was modeled through the center of the neutron star. The three free parameters are Θ, the viewing angle between line of sight and the neutron star spin axis, the inclination angle α of the magnetic moment with respect to the spin axis, and the angle β, indicating the 'lag' of the B-field plane with respect to the ephemeris, i.e., the observed shift in pulse phase. The magnetic moment

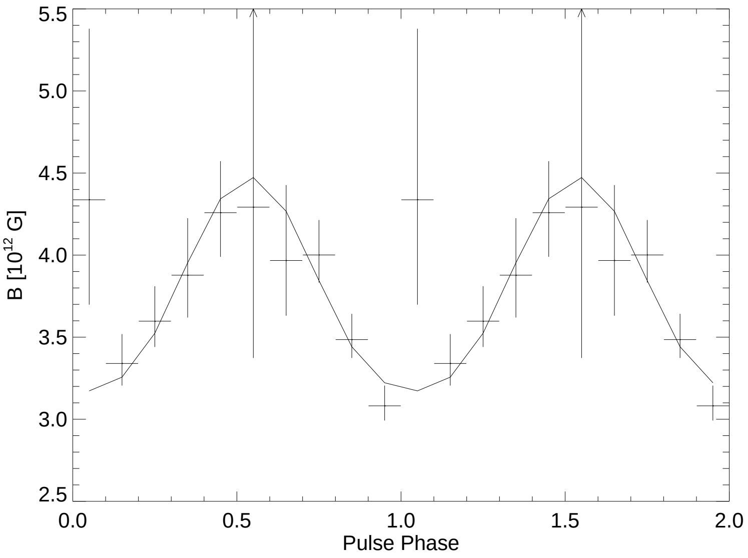

Figure 6.17.: Calculated phase resolved magnetic fields from the CRSF energy and the best fit for a simple magnetic dipole model (Suchy et al., 2011a).

was calculated and combined with the viewing angle of the dipole for each individual phase bin. Figure 6.17 shows the calculated magnetic field values from the CRSF centroid energies and the theoretical values for B from the best fit angles for a simple dipole model with $\Theta = 67°$, $\alpha = -14.6°$ and $\beta = -4.6°$. The best fit values for β were either $-5°$ or $175°$, where the latter value is equivalent to the former when the dipole polarity is flipped. The angles α and Θ showed a very strong interdependence, and the best fit Θ/α pairs were: $-14.6°/67°$, $14.6°/113°$, $67°/-14.6°$, and $113°/14.6°$. All best fit values have a $\chi^2 \approx 4$ with 7 dof. These pairs do show a degeneracy of $0 \pm 14.6°$ and $90 \pm 23°$, which can be explained with a geometrical symmetry, when calculating the magnetic field for each individual phase bin. The first and last two pairs can each be treated as the same geometry, rotated by 180 degrees.

The phase resolved energy and width of the CRSF show a strong correlation, where the width varies in phase with the CRSF energy (Figure. 6.15). Kreykenbohm (2004) observed a similar correlation, where the magnetic pole was observed under different viewing angles Φ, where Φ is the angle between the line of sight and the magnetic pole. Mészáros & Nagel (1985a) showed that the anisotropic velocity field of the electrons in the accretion column leads to a fractional line width of:

$$\frac{\sigma_{\mathrm{CRSF}}}{E_{\mathrm{CRSF}}} \approx \sqrt{8\ln 2 \frac{kT_{\mathrm{e}}}{m_{\mathrm{e}}c^2}}\,|\cos\Phi| = k\,|\cos\Phi|\,. \tag{6.8}$$

The $\sigma_{\mathrm{CRSF}}/E_{\mathrm{CRSF}}$ ratios vary in the 0.16 – 0.24 range, corresponding to variations of ±20% throughout the pulse orbit. The two outliers with large errors in phase bin 1 and 6 were ignored. The variation of Φ can be estimated as $\Theta - \alpha$ and $\Theta + \alpha$ throughout one pulse orbit, where the magnetic pole rotates around the neutron star spin axis, tilted by Θ with respect to the line of sight.

Using the average ratio of 0.2, we calculated the two values of k for the two geometries of $\Theta = -14.6°$ ($k = 0.21$) and $\Theta = 67°$ ($k = 0.51$). For each geometry, we used the variation of the $\sigma_{\mathrm{CRSF}}/E_{\mathrm{CRSF}}$ ratio (± 0.04) to calculate the variation in Φ, resulting in values of $\Phi = 15° \pm 25°$ and $\Phi = 67° \pm 5°$. These variations are smaller than the values expected from the geometrical discussion, but show a similar behavior, where the variation of the angle is larger for the smaller value of Φ. From Equation 6.8, we were also able to estimate a possible plasma temperature for the two geometries from the calculated values of k. The plasma temperature of $kT \sim 4\,\mathrm{keV}$ for $\Theta = 15°$ is very similar to the observed folding energy E_{fold}, which is an indication of the plasma temperature (Burderi et al., 2000, and references therein). The value of $kT \sim 24\,\mathrm{keV}$ for the $\Theta = 67°$ geometry is much larger and is not consistent with the observed E_{fold}. Assuming that the neutron star spin axis is aligned with the inclination of the binary system, a value of $\Theta = 15°$ would put the inclination at $i \sim 75°$, a value which is only marginally above the upper limit of 72°, as determined by Kaper et al. (2006).

6.5.6 Outlook

OFF-STATES are seen in an increasingly number of sources, like Vela X-1 and GX 1+4 and can provide interesting insight in the structure of the accreted material as well as the configuration of the accretion and absorption region. For GX 301−2 we propose that two absorbers exists, a very dense but clumpy primary one close to the neutron star, and a weaker and smoother secondary one farther away. Fluorescence lines from the secondary absorber are much weaker than the ones from the primary and only visible during the off-state. High-resolution spectra of the off-states from *Chandra* HETG or future missions will help to investigate them in more detail by allowing for better measurements of the ionization state and the geometry of the absorber. The discovery of a Cr Kα line in the spectrum of GX 301−2 leads to interesting new questions about the abundances of the iron family atoms, including Cr and Ni. With higher effective areas in future missions, more sources might be found showing a Cr Kα line and in comparing these findings to GX 301−2 more insight into the production of HMXBs and the preceding supernova can be achieved. The observed variance of the CRSF centroid energy throughout the pulse is consistent with a dipole magnetic field. We could loosely constrain the magnetic field alignment with respect to the neutron star spin axis and orbital inclination. More complex models describing the energy dependent pulse profile, taking also gravitational light bending into account, could further constrain the geometry (Kraus et al., 2003). Such models have been already successfully applied to other HMXBs like A 0535+26 (Caballero et al., 2011). As discussed in Section 2.3.3 these models are computationally very extensive and therefore beyond the scope of this work. The data and analysis presented here has already enhanced our view of GX 301−2. With the availability of data with higher spectral and timing resolution, as possible with missions like *Athena*, our understanding can be further improved. The geometry of the different absorbers as well as the emission geometry in the accretion column will be better understood. All this information combined will complete the picture of GX 301−2 and possibly also of the other highly absorbed sources.

They dined on mince, and slices of quince,
Which they ate with a runcible spoon.

(Edward Lear — "The Owl and the Pussycat")

7

Conclusion & Outlook

STUDYING the X-rays emitted by compact objects in binary systems means to directly study the interaction between matter and very strong gravitational and electro-magnetic fields. In this thesis three neutron star X-ray binaries were analyzed, namely 3A 1954+319, 4U 1909+07, and GX 301−2. All of them are observable in X-rays because they transfer gravitational energy of matter into radiation, by means of accretion. In all sources the accreted matter originates from their companion star, to whom they are gravitational bound. All of them also show regular pulsations in the X-ray lightcurve, due to the rotation of the neutron star and their strong magnetic field, which forces the accreted matter into accretion columns above the magnetic poles. Furthermore all of them are embedded in the stellar wind of their companion, as seen by their intrinsic absorption. Despite these many similarities, they also show very distinctive features, making each source unique. In the following paragraphs I briefly summarize the results of the analyses and point out the main points.

3A 1954+319 has, with 5.3 h, the longest pulse period of all known neutron stars in binaries, only the isolated pulsar in the SNR RCW 103 rotates slower (De Luca et al., 2006). It belongs to the class of SyXBs with only 7 other members, characterized by an M-type companion. I have analyzed *INTEGRAL* and *Swift*/BAT data, studying an outburst in November 2008 in great detail. 3A 1954+319 shows a very fascinating pulse period evolution, with rapid spin-up episodes on the order of $1.8\times10^{-4}\,\mathrm{s\,s^{-1}}$ during bright X-ray flares and slower spin-down episodes during quieter times. A possible explanation for this behavior is that accretion takes place via quasi-spherical accretion in which a hot shell forms and mediates the transfer of angular momentum (Shakura et al., 2011). Long term studies, especially during quiet phases, will allow to verify this model. The spectrum of 3A 1954+319 can be described well with a Comptonization model, very similar to many HMXBs sources, indicating that X-rays are produced in a similar way in accretion columns above the magnetic poles.

4U 1909+07 is a persistent HMXB close to other well studied sources like 4U 1907+09 (see, e.g., Rivers et al., 2010) and GRS 1915+105 (see, e.g., van Oers et al., 2010), but has not received very much attention. The spectrum as measured with *RXTE*, *INTEGRAL*, and *Suzaku* can be fitted with a Comptonization model similar to 3A 1954+319, but a better description was obtained using a cutoff-powerlaw model. I found evidence in the *RXTE* data that a blackbody component is visible at soft energies. In the preliminary analysis of the *Suzaku* data this blackbody was not required, indicating that it is strongly variable. The investigation presented here was the first to perform pulse phase resolved analysis, clearly showing that the spectral hardness and the flux of the blackbody component are strongly changing throughout the pulse. It is possible that the accretion column is hollow, allowing a less obscured view onto the hot-spot at phases when we look along the column. 4U 1909+07 shows a pulse period evolution which is consistent with a random walk like behavior, indicating that no accretion disk is present.

GX 301−2 is the most strongly absorbed source of the sample presented here, and one of the most strongly absorbed bright binaries known. With an equivalent hydrogen column density of more than $10^{24}\,\mathrm{cm}^{-2}$ it is hidden behind the dense matter from its companion. We analyzed observations taken with *XMM-Newton* and *Suzaku*. The strong absorption leads to very prominent fluorescence lines, among which a Cr Kα line could be observed for the first time. The very bright Fe Kα line showed an asymmetric shape, interpreted as a Compton shoulder widening its low energy flank (Watanabe et al., 2003). GX 301−2 is also the only source presented in this thesis which shows a CRSF, allowing to directly measure its surface magnetic field to be $\sim 4\times10^{12}\,\mathrm{G}$. The variability of the centroid energy of the CRSF can be explained by different viewing angles of a dipole magnetic field. In the *XMM-Newton* lightcurve a very peculiar state was measured, in which the source ceased to show pulsations for ~2000 s. It was still clearly detected in *XMM-Newton* and the equivalent width of the iron line increased to very high values. This state was probably triggered by a strong reduction of the accretion, the residual flux measured originating from reflected X-rays in the dense absorber.

7.1 Pulse profiles

Pulse profiles provide information about the structure of the accretion column and its physical conditions. The pulse profiles in all three sources show two separated peaks, possibly originating from the two accretion columns above the north and the south magnetic pole (Figure 7.1). The peaks are separated by two minima, one clearly deeper than the other one. Keeping in mind that the flux in each peak is a strong function of viewing angle, geometry, and physical conditions in the accretion column, it is surprising how similar the pulse profiles of these different sources look. The main differences visible in Figure 7.1 are the relative strengths and exact shapes of the peaks. In the energy bands displayed, 4U 1909+07 shows a symmetric profile, with both peaks of comparable flux. In 3A 1954+319 the peak before the deep minimum is the brighter one, in GX 301−2 it is the one after the minimum.

However, these strengths are also strongly depending on the energy band (see, e.g., Section 5.3.2 for 4U 1909+07) and in this dependence the biggest difference between the sources is found. While for 3A 1954+319 no energy dependence could be found, most likely due to the missing coverage of the soft energies, the relative strength in the pro-

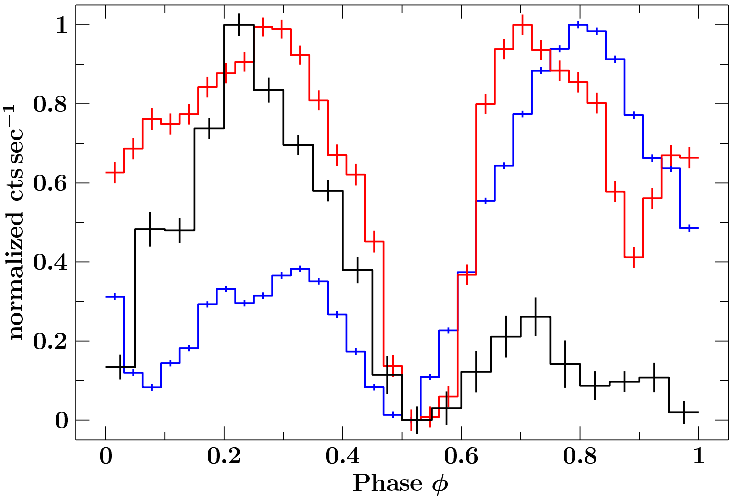

Figure 7.1.: Pulse profiles of 3A 1954+319 (black, 20–40 keV), 4U 1909+07 (red, 6–12 keV), and GX 301−2 (blue, 2–10 keV). The profiles were individually normalized and shifted to align the phases of lowest countrate.

files changes drastically for GX 301−2 and 4U 1909+07. In GX 301−2 we have seen that the secondary peak gets relatively stronger, compared to the primary one, with increasing energy (Figure 6.6). In 4U 1909+07 on the other hand, the secondary vanishes completely at the highest energies (Figure 5.4). This different behavior is also seen in the variation of the spectral parameters. In 4U 1909+07 the photon index is highest during the secondary peak, while in GX 301−2 the highest index is measured during the minimum. In other words, there seems to be no common correlation between spectral shape or hardness and flux throughout the pulse, indicating that the emission geometry is different in all sources. An exhaustive analysis of the pulse profiles allows consequently to investigate the detailed structure of the magnetic field and the accretion column. The investigation of the phase dependence of the CRSF energy, as performed for GX 301−2 (Section 6.5.5) is a first step in that direction.

7.2 Structures in the wind

ALL sources presented in this thesis show a strongly variable flux with time. As they are all producing X-rays by transforming kinetic energy of accreted material into radiation, the variable flux carries information about the structure of the accreted medium. As detailed in Section 2.1.2 the winds of O- and B-type stars are highly structured or “clumpy”, a possible origin for the structure of the accreted medium. Additionally the neutron star is disrupting the stellar wind to a large extend, e.g., a accretion shock can form in front of it (see, e.g., Blondin et al., 1991; Mauche et al., 2008). Fürst et al. (2010) have shown that these effects can explain the observed brightness distribution of Vela X-1. The structured wind is also responsible for a large part of the observed intrinsic absorption of the sources, which is also variable on short timescales as seen in GX 301−2 (Section 6.4.4).

In the most extreme case, density variations are so large that the neutron star eventually encounters a region of very thin material, e.g., a hole in the stellar wind. In this hole the accretion rate will drop drastically, resulting in a strongly reduced X-ray flux or "off-state", in which no pulsations are visible, as we have observed in GX 301−2 (see Section 6.3.1). Neither 4U 1909+07 nor 3A 1954+319 have shown such an off-state yet. For 3A 1954+319 with its very long pulse period such a cessation of pulsations will be difficult to see, as the flux varies erratically on shorter timescales. In 4U 1909+07 a period is not visible directly in the *INTEGRAL* lightcurve, due to the low flux of the source, rendering off-states indistinguishable from normal states. Dedicated observations with sensitive instruments are typically short and will only by chance capture an off-state. Estimates on how often off-states occur are hard to give for a specific source. There are numerous other sources for which off-states have been observed, among them Vela X-1 (Kreykenbohm et al., 2008), 4U 1907+09 (in 't Zand et al., 1997), and GX 1+4 (Rea et al., 2005). For 4U 1907+09 in 't Zand et al. (1997) observed that it is spending ~20% in an off- or dip-state, while Vela X-1 shows off-states only in < 1% of all observations (Kreykenbohm, 2011, priv. comm.). In the GX 301−2 *XMM-Newton* observation the off-state had a duration of $\lesssim$10% of the observation time and $\lesssim$3% when also including the *Suzaku* data. Further monitoring is therefore necessary to observe and compare the off-states of different sources, also with regard to their spectral behavior. If the highly structured wind, for which evidence in all sources exist, is responsible for the off-states, every source should show them.

7.3 Outlook

Our understanding of neutron stars and HMXBs is far from being complete. X-ray astronomy has already come a long way from the first observations in the 1960s, and very detailed spectra and lightcurves can be obtained. We have direct evidence for very strong magnetic fields in neutron stars by measuring the CRSFs and can probe the ionization state of the surrounding medium by studying the fluorescence lines. Through precise timing, the evolution of the orbit and pulse ephemeris can be followed. Nonetheless many observations are still puzzling and difficult to explain theoretically. To name but a few examples are the timing properties of 3A 1954+319 or the changing spectral parameters with pulse phase in 4U 1909+07 and GX 301−2. These effects depend strongly on the internal structure of the neutron star, and thereby its mass, radius, and magnetic field as well as on the behavior and physical condition of the material in the accretion column. With upcoming observatories like *ASTRO-H*, *LOFT*, or *Athena* more precise and detailed investigations will be possible. For example, the XRT of *Athena* with its very high spectral resolution will allow to follow the ionization state of the Fe Kα line in GX 301−2 on timescales of a few 100 s, thereby revealing how and how fast it reacts on changes in the continuum luminosity. It will also be possible to investigate other fluorescence lines, among them the Cr Kα line, in more detail, allowing to constrain abundances and the geometry of the observer. The large effective area of *LOFT* allows to investigate sources even during quiescence or off-states, exposing how in these states the accretion behavior differs from brighter phases.

But even further observations with currently working X-ray satellites will be a great asset to our understanding of X-ray binaries. For 3A 1954+319, *Chandra* and *XMM-Newton* observations will for the first time allow to investigate the behavior in the absorber and its correlation with luminosity. A more in depth study of the *Suzaku* data of 4U 1909+07 will show how the blackbody has changed compared to the *RXTE/INTEGRAL* observations and thereby allow to draw conclusions on the hot spot and the temperature in the accretion column.

I hope that with the analyses presented in this thesis I have contributed a little to our knowledge about X-ray binaries and their behavior. Through the combined effort of observers, theorists, and instrument teams, working together in international collaborations our understanding of the X-ray sky and the behavior of matter under extreme circumstances will continue to increase. With each new discovery, some questions will be answered and others raised, and the curiosity of scientists will always demand better data to provide better insight.

Not from the stars do I my judgment pluck;
And yet methinks I have astronomy

(W. Shakespeare – Sonnet XIV)

Acknowledgements

Official

I acknowledge support by the Bundesministerium für Wirtschaft und Technologie through DLR grant 50 OR 0808 and via a DAAD fellowship. I have been partially funded by the European Commission under the 7th Framework Program under contract ITN 215212 "Black Hole Universe". For this work I have made use of NASA's Astrophysics Data System. This work is based on observations obtained with *XMM-Newton*, an ESA science mission with instruments and contributions directly funded by ESA Member States and NASA and on observations with *INTEGRAL*, an ESA project with instruments and science data centre funded by ESA member states (especially the PI countries: Denmark, France, Germany, Italy, Switzerland, Spain), Czech Republic and Poland, and with the participation of Russia and the USA. I made use of results provided by the ASM/*RXTE* teams at MIT and at the *RXTE* SOF and GOF at NASA's GSFC. This research has made use of data obtained from the *Suzaku* satellite, a collaborative mission between the space agencies of Japan (JAXA) and the USA (NASA). I used the ISIS software package provided by MIT for this work. I especially like to thank J. C. Houck and J. E. Davis for their restless work to improve ISIS and S-Lang.

Personal

First of all I would like to thank everybody who supported and helped me during the work on this thesis. Without all of you, I would not have made it to the finish line.[1] Especially, I want to thank Jörn Wilms for giving me the opportunity to work at the Remeis-observatory in his group, for his great commitment, encouragement, and his helpful feedback. I think the German term "Doktorvater" describes Jörn much better than the simple word "advisor". I also like to thank Ingo Kreykenbohm very much, for his great insight in the physics of neutron stars, his help over all the years, and for keeping the computers running.

Of course, I am thankful to the whole Remeis-gang (even including the stellar and black-hole people!) for being a great group and making the time here very enjoyable and interesting. Particularly I would like to thank my Co-PhD-students Moritz Böck and Christian

---

[1] this is especially true for everybody who proof-read my thesis. Thanks!

Schmid for all the interesting discussions and help with strange physics and weird ISIS problems (and for the late working nights). This is also and especially true for Manfred Hanke, who also demonstrated that finishing is possible. Thank you! I would like to thank Michael Wille for being a great office- and observing-mate (never give up in trying to capture that perfect picture!), Sebastian Müller for joining the neutron star group, questioning all my stupid assumptions, and the very enjoybale business trips through Europe, and Matthias Kühnel for all the discussions, scripts, and observing nights. Special thanks to Laura Barragán for always having an open ear and great ideas, even though I didn't see her nearly often enough.

Thanks to Nela Müller and Thomas Dauser for the very funny and enjoyable car rides to and from Bamberg and for all the rest. Also thanks to Eva Ziegerer for joining the commuter club. I would also like to thank Victoria Grinberg, for her *INTEGRAL* knowledge as well as for her engagement for the coffee machine. I'd like to thank Natalie Hell for not running away during her Bachelor thesis, as well as Aisha Mahmoud for helping me out over the summer. Thanks also to all the other RISE students for creating an international atmosphere. Thanks to Fritz Schwarm for his patience in explaining torque and cyclo-lines. I would like to thank Stephan Geier for the jolly good times, as well as Andreas Irrgang, Florian Schiller, and Markus Firnstein and all the other players for the many volleyball and DotA matches.

Thanks also to Edith Day for keeping the observatory running and never complaining too loud when I again lost my "Dienstreiseantrag". Thanks also to Uli Heber and Horst Drechsel for signing the "Dienstreiseanträge" I forgot to hand in in time and for making sure that we have functional telescopes at the observatory.

Thanks to the whole ECAP-Erlangen gang, I very much enjoyed working in the PI offices. Special thanks to Markus Holler and Peter Eger for the company in Rhode Island, and Sebastian Heinz for sharing some frustrating days. Thanks of course also to Kora Stycz and the rest of the lunch table.

Leaving Germany and looking over the Atlantic, I would like to thank all the colleagues at UCSD and GSFC for their hospitality. Especially Rick E. Rothschild for inviting me to San Diego, as well as Alex Markowitz and Liz Rivers for the nice lunches on the balcony. Many thanks to Slawo Suchy for being a great flat-, office-, and boatmate! Thanks also to Neil Gehrels for supporting my stay at Goddard, and many, many thanks to Katja Pottschmidt for showing me Washington and Greenbelt, for letting me stay at her place, and for her great support. I also like to thank Diana Marcu for the ride and for being great to work with.

Thanks to all the everybody else from the MAGNET-group, especially Peter Kretschmar, Isa Caballero, Carlo Ferrigno, Dima Klochkov, and Gabi Schönherr for the helpful discussions.

Personally I like to thank all my friends in Erlangen and Nürnberg, who are too numerous to name. Thanks for being there!

I would like to express my endless gratitude to my dad, who always supported me and stood at my side.

Thanks to Neli Schulz for giving me the best 5 years of my life.

A

Appendix

Glossary

- **absorption edge** feature at which the →photo-electric absorption cross section of an element increases suddenly, as electrons from a stronger bound shell can be liberated from the atom
- **AGN** Active Galactic Nuclei
- **Alfvén radius** radius at which the magnetic pressure equals the ram pressure from the accreted material
- **AO** Announcement of Opportunity
- **ARF** Ancillary Response Function
- ***ASTRO-H*** Successor of →*Suzaku*, planned for launch end of 2013
- ***Athena*** Advanced Telescope for High ENergy Astrophysics
  - **WFI** Wide-Field Imager
  - **XMS** X-ray Microcalorimeter Spectrometer
    - **TES** Transition Edge Sensor
- **AXP** Anomalous X-ray Pulsar

- ***BeppoSAX*** “Beppo” Satellite per Astronomia X
- **bremsstrahlung** radiation produced by accelerating electrons in the Coulomb field of ions

- **CCD** Charge Coupled Device
- ***CGRO*** Compton Gamma Ray Observatory
  - **BATSE** Burst and Transient Source Experiment
- ***Chandra*** Chandra X-ray Observatory, one of NASA’s “Great Observatories”
- **Chandrasekhar mass** mass limit above which a dense core will collapse into a neutron star
- **Compton effect** acceleration of cold electrons at hot photons, in the inverse Compton effect, cold photons are accelerated by relativistic electrons
- **Crab nebula** →SNR of a supernova which occurred in the year 1054, hosting a pulsar. It is bright throughout the electromagnetic spectrum and is often used as a standard candle in high energy astrophysics. Fluxes are often given in units of →mCrab.
- **CRSF** Cyclotron Resonance Scattering Feature
- **CS** Compton shoulder: excess photons at the low energy side of a strong emission line due to Compton scattering of the line photons in a dense medium
- **CTI** Charge Transfer Inefficency

Dirac equation quantum-mechanical description of a relativistic particle
dof degrees of freedom
Doppler effect the blue or red shift of light depending on the speed of the source relative to the observer. In a broader sense each shift of a frequency or period due to movement of the emitting body can be described by the D.

ECAP Erlangen Centre for Astroparticle Physics
Eddington luminosity the luminosity at which the radiation pressure equals the ram or gravitational pressure of the infalling matter
Einstein The second *High Energy Astrophysical Observatories (HEAO)* satellite (*HEAO-2*), renamed *Einstein* after launch
EoS equation of state
eV electron volt; used as a measure of energy: $1\text{eV} = 1.602 \times 10^{-12}$ erg

`fdcut` Fermi-Dirac cut-off spectral model
Fermi Fermi Gammay-ray Space Telescope; formerly known as Gamma-ray Large Area Space Telescope (GLAST)
FFT Fast Fourier Transformation
FITS Flexible Image Transfer System
fluorescence emission of a photon when an electron falls back from an excited to a lower shell
FoV Field of View
FTOOLS software to display and manipulate →FITS files, distributed by the *High Energy Astrophysics Science Archive Research Center (HEASARC)*

GOF Guest Observer Facility
GRB Gamma-Ray Burst
GSFC Goddard Space Flight Center

Hartree-Fock iterative method to calculate a mutli-electron Hamiltonian
Harvard Classification stellar classification scheme according to the temperature of the stars, denoted with capitalized letters
HEAO High Energy Astrophysical Observatories
HEASARC High Energy Astrophysics Science Archive Research Center
HEASOFT Software package relased by →HEASARC, containing the →FTOOLS, among others
HMXB High Mass X-ray Binary
hyperon heavy baryon with strangeness like Σ^- and Λ

INTEGRAL *INTErnational Gamma-Ray Laboratory*
- **IBIS** Imager on Board the *INTEGRAL* Satellite
  - **ISGRI** *INTEGRAL* Soft Gamma-Ray Imager
  - **MURA** Modified Uniformly Redundant Array
  - **PICsIT** PIxelated Caesium Iodide (CsI) Telescope
- **JEM-X** Joint European X-ray Monitor
- **OMC** Optical Monitoring Camera

- **OSA** Offline Scientific Analysis
- **ScW** Science Window
- **SPI** Spectrometer on *INTEGRAL*
  - **GeD** Germanium detectors

ISIS Interactive Spectral Interpretation System
- **S-Lang** multi-platform programmer's library and interpreter

ISS International Space Station
IXO International X-ray Observatory

JAXA Japan Aerospace eXploration Agency

Kepler equation equations describing the behavior of two bodies of mass in their mutual gravitational potential

Landau level quantized energy levels of electrons perpendicular to a strong magnetic field
LEO Low Earth Orbit
LMXB Low Mass X-ray Binary
LOFT Large Observatory For x-ray Timing

magnetar A neutron star with a magnetic field $B > 10^{14}$ G, showing bright X-ray flares
mass-function function describing the relative masses of the two stars of a binary system
mCrab unit for fluxes defined as 1/1000 of the flux of the →Crab nebula in the respective energy band.
MHD Magnetohydrodynamics
MIT Massachusetts Institute of Technology
MPE Max-Planck-Institut für extraterrestrische Physik

NASA National Aeronautics and Space Administration

Oppenheimer-Volkov mass limit above which a dense star will collapse into a black hole

Pauli exclusion principle quantum mechanical finding that no two fermions can have the exact same quantum state
Pearson's correlation coefficient a very commonly used estimator on the linear correlation between two data sets, ranging from +1 (fully correlated) to −1 (fully anti-correlated)
photo-electric absorption absorption of a photon by an atom, thereby freeing an electron
Planck's Law of blackbody radiation energy output of a blackbody as a function of wavelength and temperature
PMT Photo-Multiplier Tube
PSD Power Spectral Density

QCD Quantum-Chromo Dynamics

RMF Redistribution Matrix Function

- **Roche lobe** maximal surface which is still bound to one component in a rotating binary system; its size depends on the orbital period and the masses of the two components. If one component fills its R., mass flows over to the other component of the system.
- ***RXTE*** *Rossi X-ray Timing Explorer*
  - **ASM** All Sky Monitor
    - **SSC** Scanning Shadow Camera
  - **HEXTE** High Energy X-ray Timing Experiment
  - **PCA** Proportional Counter Array
    - **PCU** Proportional Counter Unit

- **S/N** signal-to-noise ratio
- **SAA** South Atlantic Anomaly
- **SAS** Science Analysis System
- **SFXT** Supergiant Fast X-ray Transient
- **SGR** Soft Gamma-Ray Repeater
- **Siegbahn notation** historic notation of atomic transitions, still wildly used in X-ray spectroscopy
- **Snell's law** describes the directional change of a light ray when passing between two media
- **SNR** Supernova Remnant
- **SRG** Spectrum-X-Gamma
  - **eROSITA** extended ROentgen Survey with an Imaging Telescope Array
- **SRON** Netherlands Institute for Space Research, formally known as Stichting RuimteOnderzoek Nederland
- ***Suzaku*** Joint →JAXA/→NASA mission, formerly called ASTRO-E2
  - **HXD** Hard X-ray Detector
    - **BGO** Bismuth Germanate
    - **GSO** Gadolinium Silicate
    - **PIN** silicon diode detector of HXD
  - **XIS** X-ray Imaging Spectrometer
  - **XRS** X-ray Spectrometer
- ***Swift*** X-ray satellite built to investigate GRBs
  - **BAT** Burst Alert Telescope
  - **UVOT** UV/Optical Telescope
  - **XRT** X-ray Telescope
- **SyXB** Symbiotic X-ray Binary

- **TeV** tera electronvolts; 10^9 →*eV*
- **Thomson scattering** classical description of elastic photon-electron scattering
- **ToO** Target of Opportunity; observation only performed if certain prerequistes are met, like an outburst of the source in question

- **UCSD** University of California, San Diego
  - **CASS** Center for Astrophysics & Space Sciences
- ***Uhuru*** First satellite dedicated exclusively to X-ray astronomy

Wien's Displacement Law law describing the effect that the color of a blackbody gets bluer with increasing temperature

XEUS X-Ray Evolving Universe Spectrometer Mission

xfig a freeware vector graphics drawing programm, see `http://www.xfig.org/`

XMM-Newton *X-ray Multi Mirror Mission*

- **EPIC** European Photon Imaging Camera
  - **MOS** Metal Oxide Semi-conductor
  - **pn** Positive-Negative CCD
- **OM** Optical Monitor
- **RGS** Reflection Grating Spectrometers

XSPEC An X-Ray Spectral Fitting Package distributed by →HEASARC

Yerkes Spectral Classification enhancement of the →Harvard Classification, adding subtypes and luminosity classes

List of Figures

2. Neutron Stars in X-ray Binaries

3. Satellites & Data Analysis

4. The symbiosis of 3A 1954+319

5. 4U 1909+07: an overlooked source

6. Concerning GX 301−2

7. Conclusion & Outlook

List of Tables

3. Satellites & Data Analysis

4. The symbiosis of 3A 1954+319

5. 4U 1909+07: an overlooked source

6. Concerning GX 301−2

References

Airapetian V., Carpenter K.G., Ofman L., 2010, ApJ 723, 1210

Als-Nielsen J., McMorrow D., 2011, Elements of Modern X-ray Physics, John Wiley & Sons Ltd., Chichester, UK, 2nd edition

Arnaud K.A., 1996, In: Jacoby G.H., Barnes J. (eds.) Astronomical Data Analysis Software and Systems V, Vol. 101. Astronomical Society of the Pacific Conference Series, p.17

Aschenbach B., 2009, Experimental Astronomy 26, 95

Attié D., Cordier B., Gros M., et al., 2003, A&A 411, L71

Ayers L., 1996, S-Lang Applications for Linux, The Linux Gazette, 12, http://linuxgazette.net/issue12/slang.html

Barragán L., Wilms J., Pottschmidt K., et al., 2009, A&A 508, 1275

Barthelmy S.D., Barbier L.M., Cummings J.R., et al., 2005, Space Sci. Rev. 120, 143

Basko M.M., Sunyaev R.A., 1976, MNRAS 175, 395

Becker P.A., 1998, ApJ 498, 790

Becker P.A., Wolff M.T., 2005a, ApJ 621, L45

Becker P.A., Wolff M.T., 2005b, ApJ 630, 465

Becker P.A., Wolff M.T., 2007, ApJ 654, 435

Bélanger G., 2011, IBIS Observer's Manual INT/OAG/11-0345/Dc, INTEGRAL Science Data Centre, ISOC/ESAC, Villanueva de la Cañada, Spain

Belcher J.W., 1971, ApJ 168, 509

Bianchi S., Matt G., Fiore F., et al., 2002, In: G. Branduardi-Raymont (ed.) High Resolution X-ray Spectroscopy with XMM-Newton and Chandra, Proc. of the international workshop held at the Mullard Space Science Laboratory of University College London, Holmbury St Mary, Dorking, Surrey, UK.

Blondin J.M., Kallman T.R., Fryxell B.A., Taam R.E., 1990, ApJ 356, 591

Blondin J.M., Stevens I.R., Kallman T.R., 1991, ApJ 371, 684

Bodaghee A., Tomsick J.A., Rodriguez J., 2011, In: Proc. of the 4th International MAXI Workshop held in Tokyo, The First Year of MAXI: Monitoring Variable X-ray Sources.

Bombaci I., 1996, A&A 305, 871

Boyd P.T., Roming P., Mason K.O., et al., 2005, In: American Astronomical Society Meeting Abstracts, Vol. 37. Bulletin of the American Astronomical Society, p. 153.05

Bradt H.V., Rothschild R.E., Swank J.H., 1993, A&AS 97, 355

Burderi L., Di Salvo T., Robba N.R., et al., 2000, ApJ 530, 429

Burrows D.N., Hill J.E., Nousek J.A., et al., 2000, In: K. A. Flanagan & O. H. Siegmund (ed.) Society of Photo-Optical Instrumentation Engineers (SPIE) Conference Series, Vol. 4140. Presented at the Society of Photo-Optical Instrumentation Engineers (SPIE) Conference, p.64

Caballero I., 2009, Ph.D. thesis, Institut für Astronomie und Astrophysik, Uni Tübingen

Caballero I., Kraus U., Santangelo A., et al., 2011, A&A 526, 131

Caballero I., Kretschmar P., Santangelo A., et al., 2007, A&A 465, L21

Caballero-García M.D., Domingo A., Rísquez D., Mas-Hesse J.M., 2006, In: A. Wilson (ed.) The X-ray Universe 2005, Vol. 604. ESA Special Publication, p. 249

Cappelluti N., Predehl P., Boehringer H., et al., 2010, Memorie della Societa Astronomica Italiana Supplement (astro-ph:1004.5219) 17, 159

Carter J.A., Read A.M., 2007, A&A 464, 1155

Castor J.I., Abbott D.C., Klein R.I., 1975, ApJ 195, 157

Chiosi C., Bertelli G., Bressan A., 1992, Rev. Astron. 30, 235

Clayton D.D., 1984, Principles of stellar evolution and nucleosynthesis, 2nd edition, The University of Chicago Press, Chicago - London

Coburn W., Heindl W.A., Gruber D.E., et al., 2001, ApJ 552, 738

Cohen-Tannoudji C., Diu B., Laloe F., 1978, Quantum Mechanics, Volume 1, Wiley-Interscience, 1 edition

Compton A.H., 1923, Phys. Rev. 21, 483

Corbet R., Barbier L., Barthelmy S., et al., 2006a, ATEL 797, 1

Corbet R., Barbier L., Barthelmy S., et al., 2006b, The Astronomer's Telegram 779, 1

Corbet R.H.D., Sokoloski J.L., Mukai K., et al., 2008, ApJ 675, 1424

Coursey J., Schwab D., Tsai J., Dragoset R., 2010, Atomic Weights and Isotopic Compositions (version 3.0), online (2011/03/18), Gaithersburg, MD

Cui W., Smith B., 2004, ApJ 602, 320

Davis J.E., 2001, ApJ 562, 575

Davis J.E., 2001, ApJ 548, 1010

de Kool M., Anzer U., 1993, MNRAS 262, 726

de Korte P.A.J., van Baar J.J., Baars N.H.R., et al., 2004, In: A. D. Holland (ed.) Society of Photo-Optical Instrumentation Engineers (SPIE) Conference Series, Vol. 5501. Presented at the Society of Photo-Optical Instrumentation Engineers (SPIE) Conference, p.167

De Luca A., Caraveo P.A., Mereghetti S., et al., 2006, Sci 313, 814

Demtröder W., 2008, Experimentalphysik 2: Elektrizität und Optik, Springer Berlin Heidelberg, 5., überarb. u. erw. Aufl.

den Herder J.W., Brinkman A.C., Kahn S.M., et al., 2001, A&A 365, L7

den Herder J.W., Kelley R.L., Mitsuda K., et al., 2010, In: Society of Photo-Optical Instrumentation Engineers (SPIE) Conference Series, Vol. 7732. Presented at the Society of Photo-Optical Instrumentation Engineers (SPIE) Conference

Dessart L., 2004, A&A 423, 693

Dessart L., Owocki S.P., 2005, A&A 437, 657

Di Cocco G., Bianchin V., Foschini L., et al., 2007, In: ESA Special Publication, Vol. 622. ESA Special Publication, p.619

Doppler C., 1842, In: Studnicka F. (ed.) Abhandlungen der k. böhm. Gesellschaft der Wissenschaften (V. Folge, Bd. 2)., Verlag der Königl. Böhm. Gesellschaft der Wissenschaften, Prague, p.465

Doroshenko V., Santangelo A., Suleimanov V., et al., 2010, A&A 515, A10

Drude P., 1900, Annalen der Physik 306, 566

Ebert U., 2010, Physik Journal 12, 39

Einstein A., 1905, Annalen der Physik 322, 891

Einstein A., 1916, Annalen der Physik 354, 769

Endo T., Ishida M., Masai K., et al., 2002, ApJ 574, 879

Espey B.R., Crowley C., 2008, In: Proc. of the Conference on RS Ophiuchi (2006) and the Recurrent Nova Phenomenon, Vol. 401., Astronomical Society of the Pacific, San Francisco, p. 166

Evangelista Y., Feroci M., Costa E., et al., 2010, ApJ 708, 1663

Fermi E., 1949, Phys. Rev. 75, 1169

Feroci M., Stella L., van der Klis M., et al., 2011, Exp. Astron. 39

Ferrigno C., Becker P.A., Segreto A., et al., 2009, A&A 498, 825

Ferrigno C., Segreto A., Santangelo A., et al., 2007, A&A 462, 995

Finger M.H., Beklen E., Narayana Bhat P., et al., 2009, arXiv:0912.3847

Forman W., Jones C., Cominsky L., et al., 1978, A&AS 38, 357

Frank J., King A., Raine D.J., 2000, Accretion Power in Astrophysics, Cambridge, UK, 2nd edition

Fritz S., Kreykenbohm I., Wilms J., et al., 2006, A&A 458, 885

Fürst F., Kreykenbohm I., Pottschmidt K., et al., 2010, A&A 519, A37

Fürst F., Kreykenbohm I., Suchy S., et al., 2011a, A&A 525, A73

Fürst F., Marcu D.M., Pottschmidt K., et al., 2011b, In: Proc. of the 8th INTEGRAL Workshop., Dublin, Ireland

Fürst F., Suchy S., Kreykenbohm I., et al., 2011c, A&A in press (DOI 10.1051/0004-6361/201117665)

Fürst F., Wilms J., Rothschild R., et al., 2009, Earth Planet. Sci. Lett. 281, 125

Gaensler B.M., Slane P.O., 2006, Astron. Astrophys. Rev. 44, 17

Gehrels N., Chincarini G., Giommi P., et al., 2004, ApJ 611, 1005

Ghosh P., Lamb F.K., 1979a, ApJ 232, 259

Ghosh P., Lamb F.K., 1979b, ApJ 234, 296

Ghosh P., Pethick C.J., Lamb F.K., 1977, ApJ 217, 578

Giacconi R., Gursky H., Paolini F.R., Rossi B.B., 1962, Phys. Rev. Let. 9, 439

Giacconi R., Murray S., Gursky H., et al., 1974, A&AS 27, 37

Giacconi R., Rossi B., 1960, J. Geophys. Res. 65, 773

Glasser C.A., Odell C.E., Seufert S.E., 1994, IEEE Transactions on Nuclear Science 41, 1343

Glendenning N.K., 2000, Compact Stars: Nuclear Physics, Particle Physics and General Relativity, Springer, 2nd edition

Goldwurm A., David P., Foschini L., et al., 2003, A&A 411, L223

González-Galán A., Kuulkers E., Kretschmar P., et al., 2011, In: Proc. of the 8th INTEGRAL Workshop., Dublin, Ireland

Götz O., Mereghetti S., Hurley K., et al., 2007, In: ESA Special Publication, Vol. 622. ESA Special Publication, p.533

Göğüş E., Kreykenbohm I., Belloni T.M., 2011, A&A 525, L6

Grinberg V., Marcu D., Pottschmidt K., et al., 2011, In: Proc. of the 8th INTEGRAL Workshop., Dublin, Ireland

Gruenspecht H., 2010, International Energy Outlook 2010 (IEO2010)

Güver T., Wroblewski P., Camarota L., Özel F., 2010, ApJ 719, 1807

Haensel P., Potekhin A.Y., Yakovlev D.G., 2007, Neutron Stars 1: Equation of State and Structure, Vol. 326 of *Astrophysics and space science library*, Astrophysics and space science library, Springer, New York

Halm I., Wiebicke H.J., Christensen F.E., et al., 1998, In: O. H. Siegmund & M. A. Gummin (ed.) Society of Photo-Optical Instrumentation Engineers (SPIE) Conference Series, Vol. 3445. Presented at the Society of Photo-Optical Instrumentation Engineers (SPIE) Conference, p.132

Hamann W.R., Feldmeier A., Oskinova L.M., (eds.) 2008, Clumping in hot-star winds

Han I., Demir L., 2009, Phys. Rev. A 80, 052503

Hanke M., 2007, Diploma thesis, Dr. Karl Remeis-Sternwarte Bamberg & ECAP, University Regensburg

Hanke M., 2011, Ph.D. thesis, Dr. Karl Remeis-Sternwarte Bamberg & ECAP, FAU Erlangen-Nürnberg

Hanke M., Wilms J., Nowak M.A., et al., 2009, ApJ 690, 330

Harding A.K., 1994, In: S. Holt & C. S. Day (ed.) The Evolution of X-ray Binariese, Vol. 308. American Institute of Physics Conference Series, p.429

Harding A.K., Kirk J.G., Galloway D.J., Meszaros P., 1984, ApJ 278, 369

Harding A.K., Lai D., 2006, Rep. Prog. Phys. 69, 2631

Hartmann L., MacGregor K.B., 1980, ApJ 242, 260

Heindl W.A., Coburn W., Gruber D.E., et al., 2000, In: M. L. McConnell & J. M. Ryan (ed.) AIP Conference Series, Vol. 510. AIP Conference Series, p.173

Hilditch R.W., 2001, An Introduction to Close Binary Stars, An Introduction to Close Binary Stars, by R. W. Hilditch, Cambridge, UK: Cambridge University Press, March 2001.

Houck J.C., 2002, In: G. Branduardi-Raymont (ed.) High Resolution X-ray Spectroscopy with XMM-Newton and Chandra.

Hua X., Titarchuk L., 1995, ApJ 449, 188

Hwang U., Petre R., Hughes J.P., 2000, ApJ 532, 970

Iben I.J., 1991, ApJS 76, 55

Ikhsanov N.R., 2007, MNRAS 375, 698

in ’t Zand J.J.M., Heise J., Jager R., 1994, A&A 288, 665

in ’t Zand J.J.M., Strohmayer T.E., Baykal A., 1997, ApJ 479, L47

Inoue H., 1985, Space Sci. Rev. 40, 317

Inoue H., 2003, In: J. E. Truemper & H. D. Tananbaum (ed.) Society of Photo-Optical Instrumentation Engineers (SPIE) Conference Series, Vol. 4851., p.289

Iwamoto K., Brachwitz F., Nomoto K., et al., 1999, ApJS 125, 439

Jackson J.D., 2006, Klassische Elektrodynamik, Walter de Gruyter GmbH & Co. KG, Berlin, 4th edition

Jahoda K., Markwardt C.B., Radeva Y., et al., 2006, ApJS 163, 401

Jahoda K., Swank J.H., Giles A.B., et al., 1996, In: O. H. Siegmund & M. A. Gummin (ed.) Society of Photo-Optical Instrumentation Engineers (SPIE) Conference Series, Vol. 2808. Society of Photo-Optical Instrumentation Engineers (SPIE) Conference Series, p.59

Jansen F., Lumb D., Altieri B., et al., 2001, A&A 365, 6

Jensen P.L., Clausen K., Cassi C., et al., 2003 411, L7

Joss P.C., Rappaport S.A., 1984, Rev. Astron. 22, 537

Judge P.G., Stencel R.E., 1991, ApJ 371, 357

Kaastra J.S., Mewe R., 1993, A&AS 97, 443

Kalberla P.M.W., Burton W.B., Hartmann D., et al., 2005, A&A 440, 775

Kallman T.R., Palmeri P., Bautista M.A., et al., 2004, ApJS 155, 675

Kaper L., Lamers H.J.G.L.M., Ruymaekers E., et al., 1995, A&A 300, 446

Kaper L., van der Meer A., Najarro F., 2006, A&A 457, 595

Karttunen H., Krüger P., Oja H., et al., (eds.) 2007, Fundamental Astronomy, Fundamental Astronomy, Edited by H. Karttunen, P. Krüger, H. Oja, M. Poutanen, and K.J. Donner. Berlin: Springer, 2007.

Keenan P.C., 1985, In: D. S. Hayes, L. E. Pasinetti, & A. G. D. Philip (ed.) Calibration of Fundamental Stellar Quantities, Vol. 111. IAU Symposium, p.121

Kippenhahn R., Weigert A., 1994, Stellar Structure and Evolution, Astronomy and Astrophysics Library, Springer Verlag, Berlin Heidelberg

Kirkpatrick J.D., 2005, Rev. Astron. 43, 195

Kirkpatrick J.D., Reid I.N., Liebert J., et al., 1999, ApJ 519, 802

Kirsch M.G., Briel U.G., Burrows D., et al., 2005, In: O. H. W. Siegmund (ed.) Society of Photo-Optical Instrumentation Engineers (SPIE) Conference Series, Vol. 5898. Society of Photo-Optical Instrumentation Engineers (SPIE) Conference Series, p.22

Klebesadel R.W., Strong I.B., Olson R.A., 1973, ApJ 182, L85

Klochkov D., Staubert R., Postnov K., et al., 2008, A&A 482, 907

Knoll G.F., 2010, Radiation detection and measurement, Wiley, New York, 4th edition

Koh D.T., Bildsten L., Chakrabarty D., et al., 1997, ApJ 479, 933

Kortright J.B., Thompson A.C., 2001, X-ray emission energies. In: Thompson A., Vaughan D. (eds.) X-ray data booklet. Lawrence Berkeley National Laboratory, 2nd edition

Koyama K., Tsunemi H., Dotani T., et al., 2007, PASJ 59, 23

Kraus U., Nollert H., Ruder H., Riffert H., 1995, ApJ 450, 763

Kraus U., Zahn C., Weth C., Ruder H., 2003, ApJ 590, 424

Kreykenbohm I., 2004, Ph.D. thesis, Eberhard-Karls-Universität Tübingen

Kreykenbohm I., Kretschmar P., Wilms J., et al., 1999, A&A 341, 141

Kreykenbohm I., Wilms J., Coburn W., et al., 2004, A&A 427, 975

Kreykenbohm I., Wilms J., Kretschmar P., et al., 2008, A&A 492, 511

Krivosheyev Y.M., Bisnovatyi-Kogan G.S., Cherepashchuk A.M., Postnov K.A., 2009, In: Choliy V.Y., Ivashchenko G. (eds.) YSC'16 Proceedings of Contributed Papers., p.49

Kühnel M., 2011, *Master's thesis*, Dr. Karl Remeis-Sternwarte Bamberg & ECAP, FAU Erlangen-Nürnberg

Kuulkers E., 2005, In: L. Burderi, L. A. Antonelli, F. D'Antona, T. di Salvo, G. L. Israel, L. Piersanti, A. Tornambè, & O. Straniero (ed.) Interacting Binaries: Accretion, Evolution, and Outcomes, Vol. 797. American Institute of Physics Conference Series, p.402

Kuśmierek K., Madej J., Kuulkers E., 2011, MNRAS 415, 3344

La Barbera A., Santangelo A., Orlandini M., Segreto A., 2003, A&A 400, 993

La Barbera A., Segreto A., Santangelo A., et al., 2005, A&A 438, 617

Labanti C., Di Cocco G., Ferro G., et al., 2003, A&A 411, L149

Lamb F.K., Pethick C.J., Pines D., 1973, ApJ 184, 271

Lamers H.J.G.L.M., Cassinelli J.P., 1999, Introduction to Stellar Winds, Cambridge University Press, Cambridge, UK

Lattimer J.M., Prakash M., 2001, ApJ 550, 426

Leahy D.A., 1987, A&A 180, 275

Leahy D.A., 2002, A&A 391, 219

Leahy D.A., Elsner R.F., Weisskopf M.C., 1983, ApJ 272, 256

Leahy D.A., Kostka M., 2008, MNRAS 384, 747

Leahy D.A., Matsuoka M., Kawai N., Makino F., 1989, MNRAS 237, 269

Leahy D.A., Nakajo M., Matsuoka M., et al., 1988, PASJ 40, 197

Lebrun F., Leray J.P., Lavocat P., et al., 2003, A&A 411, L141

Levine A.M., Bradt H., Cui W., et al., 1996, ApJ 469, L33

Levine A.M., Rappaport S., Remillard R., Savcheva A., 2004, ApJ 617, 1284

Lewin W.H.G., Ricker G.R., McClintock J.E., 1971, ApJ 169, L17

Lewin W.H.G., van Paradijs J., Taam R.E., 1993, Space Sci. Rev. 62, 223

Liu Q.Z., van Paradijs J., van den Heuvel E.P.J., 2000, A&AS 147, 25

Liu Q.Z., van Paradijs J., van den Heuvel E.P.J., 2007, A&A 469, 807

Lucy L.B., Solomon P.M., 1970, ApJ 159, 879

Lum K.S.K., Canizares C.R., Clark G.W., et al., 1992, ApJS 78, 423

Lund N., Budtz-Jørgensen C., Westergaard N.J., et al., 2003, A&A 411, L231

Lutovinov A.A., Tsygankov S.S., 2009, Astron. Let. 35, 433

Makino F., Leahy D.A., Kawai N., 1985, Space Sci. Rev. 40, 421

Manchester R.N., Hobbs G.B., Teoh A., Hobbs M., 2005, AJ 129, 1993

Manousakis A., Walter R., 2011, A&A 526, A62

Marcu D.M., Fürst F., Pottschmidt K., et al., 2011, ApJ in press

Mariska J.T., 2006, ApJ 639, 484

Mas-Hesse J.M., Giménez A., Culhane J.L., et al., 2003, A&A 411, L261

Masetti N., Orlandini M., Palazzi E., et al., 2006, A&A 453, 295

Masetti N., Rigon E., Maiorano E., et al., 2007, A&A 464, 277

Mason K.O., Breeveld A., Much R., et al., 2001, A&A 365, L36

Matsumoto H., Nakajima H., Yamaguchi H., et al., 2006, In: Turner M.J.L., Hasinger G. (eds.) SPIE Conf. Ser., Vol. 6266., p. 626641

Matt G., 2002, MNRAS 337, 147

Matt G., Guainazzi M., 2003, MNRAS 341, L13

Mattana F., Götz D., Falanga M., et al., 2006, A&A 460, L1

Mauche C.W., Liedahl D.A., Akiyama S., Plewa T., 2008, In: Axelsson M. (ed.) Cool Discs, Hot Flows: The Varying Faces of Accreting Compact Objects, AIP Conference Proceedings 1054., Stockholm, Sweden, p.3

McBride V.A., Wilms J., Coe M.J., et al., 2006, A&A 451, 267

McClintock J.E., Ricker G.R., Lewin W.H.G., 1971, ApJ 166, L73

Meidinger N., Andritschke R., Ebermayer S., et al., 2010, Nuclear Instruments and Methods in Physics Research A 624, 321

Mendoza C., Kallman T.R., Bautista M.A., Palmeri P., 2004, A&A 414, 377

Mereghetti S., Chiarlone L., Israel G.L., Stella L., 2002, In: W. Becker, H. Lesch, & J. Trümper (ed.) Neutron Stars, Pulsars, and Supernova Remnants., p. 29

Mészáros P., 1984, Space Sci. Rev. 38, 325

Mészáros P., Nagel W., 1985a, ApJ 298, 147

Mészáros P., Nagel W., 1985b, ApJ 299, 138

Miceli M., Decourchelle A., Ballet J., et al., 2006, A&A 453, 567

Mihara T., Makishima K., Nagase F., 1995, In: 187th AAS Meeting, Vol. 187., p. 1434

Mihara T., Makishima K., Ohashi T., et al., 1990, Nat 346, 250

Mihara T., Terada Y., Nakajima M., et al., 2007, Prog. Theor. Phys. 169, 191

Miller J.M., Raymond J., Reynolds C.S., et al., 2008, ApJ 680, 1359

Mitsuda K., Bautz M., Inoue H., et al., 2007, PASJ 59, 1

Mitsuda K., Kelley R.L., Boyce K.R., et al., 2010, In: Arnaud M., Murray S., Takahashi T. (eds.) SPIE Conf. Ser., Vol. 7732., p.773211

Miškovičová I., Hanke M., Wilms J., et al., 2011, In: Proc. of the Integral/Bart Workshop Karlsbad, CZ, Acta Polytechnica, 51-2, 85.

Molendi S., Bianchi S., Matt G., 2003, MNRAS 343, L1

Morel T., Grosdidier Y., 2005, MNRAS 356, 665

Morgan W.W., Keenan P.C., Kellman E., 1943, An atlas of stellar spectra, with an outline of spectral classification, The University of Chicago press, Chicago, Ill.

Mukherjee U., Paul B., 2004, A&A 427, 567

Müller S., Kühnel M., Caballero I., et al., 2011a, A&A in prep.

Müller S., Obst M., Kreykenbohm I., et al., 2011b, In: J.-U. Ness & M. Ehle (ed.) Proc. of The X-ray Universe 2011, held in Berlin, Germany, 27-30 June 2011., p.283

Nagase F., Hayakawa S., Sato N., et al., 1986, PASJ 38, 547

Nakajima M., Mihara T., Makishima K., 2010, ApJ 710, 1755

Negueruela I., Torrejon J.M., Reig P., et al., 2008, In: Bandyopadhyay R. (ed.) A Population Explosion: The Nature & Evolution of X-ray Binaries in Diverse Environments. AIP Conference Proceedings 1010., St. Petersburg Beach, Florida, p.252

Nelson R.W., Bildsten L., Chakrabarty D., et al., 1997, ApJ 488, L117

Nespoli E., Fabregat J., Mennickent R.E., 2009, A&A 516, A94

Ness J.U., 2011, XMM-Newton Users Handbook, XMM-Newton Community Support Team, issue 2.9 edition

Noble M.S., Nowak M.A., 2008, PASP 120, 821

Nowak M., 2010, "Basics of X-ray Spectra ", Lecture at the 2nd Summer School on Multiwavlength Astronomy, 28 June – 9 July, Amsterdam

Orlandini M., dal Fiume D., Frontera F., et al., 2000, Adv. Space Res. 25, 417

Oskinova L.M., Hamann W., Feldmeier A., 2007, A&A 476, 1331

Oskinova L.M., Hamann W.R., Feldmeier A., 2008, In: Hamann W.R., Feldmeier A., Oskinova L.M. (eds.) Clumping in Hot-Star Winds., p.203

Palmeri P., Mendoza C., Kallman T.R., et al., 2003, A&A 410, 359

Palmeri P., Quinet P., Mendoza C., et al., 2008a, ApJS 179, 542

Palmeri P., Quintet P., Mendoza C., et al., 2008b, ApJS 177, 408

Parkes G.E., Culhane J.L., Mason K.O., Murdin P.G., 1980, MNRAS 191, 547

Patel S.K., Zurita J., Del Santo M., et al., 2007, ApJ 657, 994

Pearlman A.B., Corbet R.H.D., Pottschmidt K., Skinner G.K., 2011, ApJ, in prep.

Perna R., Bozzo E., Stella L., 2006, ApJ 639, 363

Planck M., 1900, Annalen der Physik 306, 719

Porter F.S., Beiersdorfer P., Brown G.V., et al., 2009, J. Phys.: Conf. Ser. 163, 012105

Postnov K., Shakura N., González-Galán A., et al., 2011, In: Proc. of the 8th INTEGRAL Workshop (PoS(INTEGRAL 2010)015)., Dublin, Ireland, arXiv:1110.1156

Pottschmidt K., Rothschild R.E., Gasaway T., et al., 2006, In: Bulletin of the American Astronomical Society, Vol. 38. Bulletin of the American Astronomical Society, p. 384

Pradhan A.K., Nahar S.N., 2011, Atomic Astrophysics and Spectroscopy, Cambridge University Press, Cambridge, UK

Pravdo S.H., Day C.S.R., Angelini L., et al., 1995, ApJ 454, 872

Pravdo S.H., Ghosh P., 2001, ApJ 554, 383

Puls J., Vink J.S., Najarro F., 2008, Astron. Astrophys. Rev. 16, 209

Rea N., Esposito P., 2011, In: Rea N., Torres D.F. (eds.) ASS Proc. High-Energy Emission from Pulsars and their Systems., Springer, Berlin, Heidelberg, p. 247

Rea N., Stella L., Israel G.L., et al., 2005, MNRAS 364, 1229

Riffert H., Mészáros P., 1988, ApJ 325, 207

Rivers E., Markowitz A., Pottschmidt K., et al., 2010, ApJ 709, 179

Rodriguez J., Hannikainen D.C., Shaw S.E., et al., 2008, ApJ 675, 1436

Roming P.W.A., Hunsberger S.D., Nousek J.A., et al., 2004, AIP Conference Proceedings 727, 651

Roques J.P., Schanne S., von Kienlin A., et al., 2003, A&A 411, L91

Rothschild R.E., Blanco P.R., Gruber D.E., et al., 1998, ApJ 496, 538

Rothschild R.E., Soong Y., 1987, ApJ 315, 154

Roy J., Agrawal P.C., Paul B., Duorah K., 2011, MNRAS 412, 1011

Salvaterra R., Della Valle M., Campana S., et al., 2009, Nat 461, 1258

Santangelo A., Segreto A., Giarrusso S., et al., 1999, ApJ 523, L85

Santos-Lleo M., Schartel N., Tananbaum H., et al., 2009, Nat 462, 997

Sasaki M., Klochkov D., Kraus U., et al., 2010, A&A 517, 8

Sato N., Hayakawa S., Nagase F., et al., 1986, PASJ 38, 731

Sato N., Nagase F., Kawai N., et al., 1986, ApJ 304, 241

Schartel N., Santos-Lleo M., Parmar A., Clavel J., 2010, ESA Bulletin 141, 2

Schönherr G., Wilms J., Kretschmar P., et al., 2007, A&A 472, 353

Schwarm F., 2010, Diploma thesis, Dr Karl Remeis-Sternwarte Bamberg & ECAP, FAU Erlangen-Nürnberg

Schwarzenberg-Czerny A., 1989, MNRAS 241, 153

Seward F.D., Charles P.A., 2010, Exploring the X-ray Universe, Cambridge University Press, 2nd edition

Shakura N., Postnov K., Kochetkova A., Hjalmarsdotter L., 2011, MNRAS, in press (arXiv:1110.3701v1)

Sidoli L., 2008, In: 37th COSPAR Scientific Assembly, Vol. 37., p.2892

Skinner G.K., 2004, New Astron. Rev 48, 205

Skinner G.K., Ponman T.J., 1994, MNRAS 267, 518

Smith D.M., Markwardt C.B., Swank J.H., Negueruela I., 2011, In: HEAD Meeting #12., Bulletin of the AAS, vol. 43, no. 6

Sobolev V.V., 1960, Moving envelopes of stars, Harvard University Press, Cambridge, MI

Staubert R., Klochkov D., Postnov K., et al., 2009, A&A 494, 1025

Staubert R., Shakura N.I., Postnov K., et al., 2007, A&A 465, L25

Steiner A.W., Lattimer J.M., Brown E.F., 2010, ApJ 722, 33

Stephen J.B., Caroli E., Malizia A., et al., 2003, A&A 411

Strohmayer T.E., Zhang W., Swank J.H., et al., 1996, ApJ 469, L9

Strüder L., Bräuninger H., Briel U., et al., 1997, Rev. Sci. Instrum. 68, 4271

Strüder L., Briel U., Dennerl K., et al., 2001, A&A 365, L18

Sturner S.J., Shrader C.R., Weidenspointner G., et al., 2003, A&A 411, L81

Suchy S., Fürst F., Pottschmidt K., et al., 2011a, ApJ subm.

Suchy S., Pottschmidt K., Rothschild R.E., et al., 2011b, ApJ 733, 15

Suzuki T.K., 2007, ApJ 659, 1592

Suzuki T.K., 2011, Space Sci. Rev. 158, 339

Swank J., Rothschild R., Bradt H., et al., 1995, The RXTE technical appendix F, NASA/GSFC

Takahashi T., Abe K., Endo M., et al., 2007, PASJ 59, 35

Tanaka Y., 1986, In: Mihalas D., Winkler K.H.A. (eds.) Radiation Hydrodynamics in Stars and Compact Objects, Vol. 255. Proc. IAU Colloq. 89

Tashiro M., Makishima K., Ohashi T., et al., 1991, MNRAS 252, 156

Tiengo A., Galloway D.K., di Salvo T., et al., 2005, A&A 441, 283

Titarchuk L., Lyubarskij Y., 1995, ApJ 450, 876

Torrejón J.M., Schulz N.S., Nowak M.A., Kallman T.R., 2010, ApJ 715, 947

Turner M.J.L., Abbey A., Arnaud M., et al., 2001, A&A 365, L27

Tweedy R.W., Warwick R.S., Remillard R., 1989, In: Hunt J., Battrick B. (eds.) Two Topics in X-ray Astronomy: Vol. 1 (ESA-SP-296)., p.661

Ubertini P., Lebrun F., Di Cocco G., et al., 2003, A&A 411, L131

Unsöld A., 2005, Der neue Kosmos, Springer, Berlin [u.a.]

Uttley P., Wilkinson T., Cassatella P., et al., 2011, MNRAS 414, L60

Vallée J.P., 2008, AJ 135, 1301

van Oers P., Markoff S., Rahoui F., et al., 2010, MNRAS 409, 763

Vedrenne G., Roques J.P., Schönfelder V., et al., 2003, A&A 411, L63

Verner D.A., Ferland G.J., Korista K.T., Yakovlev D.G., 1996, ApJ 465, 487

Vidal N.V., 1973, ApJ 186, L81

Walsh D., Carswell R.F., Weymann R.J., 1979, Nat 279, 381

Walter R., Zurita-Heras J., 2007, A&A 476, 335

Walter R., Zurita Heras J., Bassani L., et al., 2006, A&A 453, 133

Warwick R.S., Marshall N., Fraser G.W., et al., 1981, MNRAS 197, 865

Watanabe S., Sako M., Ishida M., et al., 2003, ApJ 597, L37

Watson M.G., Warwick R.S., Corbet R.H.D., 1982, MNRAS 199, 915

Wen L., Remillard R.A., Bradt H.V., 2000, ApJ 532, 1119

White N.E., Mason K.O., Huckle H.E., et al., 1976, ApJ 209, L119

White N.E., Mason K.O., Sanford P.W., 1978, MNRAS 184, 67P

White N.E., Swank J.H., Holt S.S., 1983, ApJ 270, 711

Williams D.R., 2011, Earth Fact Sheet, online, retrieved 2011/09/23

Wilms J., 1998, Ph.D. thesis, Universität Tübingen, Wilhelmstr. 32, 72074 Tübingen

Wilms J., 2008, "X-ray Astronomy I", Lecture notes at the FAU Erlangen-Nürnberg

Wilms J., Allen A., McCray R., 2000, ApJ 542, 914

Wilson C.A., Finger M.H., Coe M.J., Negueruela I., 2003, ApJ 584, 996

Wilson-Hodge C.A., Cherry M.L., Case G.L., et al., 2011, ApJ 727, L40

Winkler C., 2001, In: Battrick B. (ed.) Exploring the gamma-ray universe. Proceedings of the Fourth INTEGRAL Workshop, 4-8 September 2000, Alicante, Spain, Vol. 459., p.471

Winkler C., Courvoisier T.J.L., Di Cocco G., et al., 2003, A&A 411, L1

Wolter H., 1952, Annalen der Physik 445, 286

Yang X.J., Tsunemi H., Lu F.J., Chen L., 2009, ApJ 692, 894

Zasche P., 2011, New Astronomy 16, 157

Zavlin V.E., Pavlov G.G., 2002, In: W. Becker, H. Lesch, & J. Trümper (ed.) Neutron Stars, Pulsars, and Supernova Remnants., p. 263

Özel F., 2006, Nat 441, 1115

Özel F., Güver T., Psaltis D., 2009, ApJ 693, 1775